

This is an introductory textbook for graduate students and researchers from various fields of science who wish to learn about carbon nanotubes. The field is still at an early stage, and progress continues at a rapid rate. This book focuses on the basic principles behind the physical properties and gives the background necessary to understand the recent developments. Some useful computational source codes which generate coordinates for carbon nanotubes are also included in the appendix.

About the Authors

Riichiro Saito studied physics at the University of Tokyo and got his Dr Sc in 1985. Since 1990, he has been an associate professor at the University of Electro-Communications, in Tokyo. He was a visiting scientist at MIT in 1992 where he did pioneering work on carbon nanotubes with Professor Gene Dresselhaus and Professor Mildred S Dresselhaus. He was visiting associate professor at the University of Tokyo, three times, in 1991, 1994, and 1997. His major subjects are solid state theory and the materials science of carbon.

Gene Dresselhaus studied physics at the University of California, Berkeley, where he worked with Kittel and Kip on the early cyclotron resonance experiments on semiconductors and semimetals. His early postdoctoral work was at the University of Chicago and then a junior faculty position at Cornell University for four years. The major part of his professional career has been at MIT, first at the MIT Lincoln Laboratory and later at The Francis Bitter National Magnet Laboratory. He is a Fellow of the American Physical Society.

Mildred S Dresselhaus completed her PhD degree at the University of Chicago. After a postdoctoral fellowship at Cornell University, she joined the MIT Lincoln Laboratory and subsequently joined the MIT Faculty in 1968. She is a fellow of the American Physical Society, the AAAS and served as president of both these organizations. She is a member of the National Academy of Sciences and of the National Academy of Engineering. She coauthored a book on the *Science of Fullerenes and Carbon Nanotubes* with G Dresselhaus and P C Eklund.

Imperial College Press



SAITO
DRESSELHAUS
DRESSELHAUS

Physical Properties of Carbon Nanotubes

ICP

Physical Properties of Carbon Nanotubes

R SAITO
G DRESSELHAUS
M S DRESSELHAUS

Imperial College Press

Physical Properties of Carbon Nanotubes

R SAITO
G DRESSELHAUS
M S DRESSELHAUS

SAITO
DRESSELHAUS
DRESSELHAUS

Physical Properties of Carbon Nanotubes



ISBN 1-86094-093-5

Imperial College Press

P080 hc

Imperial College Press

Physical Properties of Carbon Nanotubes

Physical Properties of Carbon Nanotubes

R SAITO

UNIVERSITY OF ELECTRO-COMMINUCATIONS, TOKYO

G DRESSELHAUS & M S DRESSELHAUS

MIT

Published by

Imperial College Press
203 Electrical Engineering Building
Imperial College
London SW7 2BT

Distributed by

World Scientific Publishing Co. Pte. Ltd.
P O Box 128, Farrer Road, Singapore 912805
USA office: Suite 1B, 1060 Main Street, River Edge, NJ 07661
UK office: 57 Shelton Street, Covent Garden, London WC2H 9HE

British Library Cataloguing-in-Publication Data
A catalogue record for this book is available from the British Library.

PHYSICAL PROPERTIES OF CARBON NANOTUBES

Copyright © 1998 by Imperial College Press

All rights reserved. This book, or parts thereof, may not be reproduced in any form or by any means, electronic or mechanical, including photocopying, recording or any information storage and retrieval system now known or to be invented, without written permission from the Publisher.

For photocopying of material in this volume, please pay a copying fee through the Copyright Clearance Center, Inc., 222 Rosewood Drive, Danvers, MA 01923, USA. In this case permission to photocopy is not required from the publisher.

ISBN 1-86094-093-5

This book is printed on acid-free paper.

Printed in Singapore by Uto-Print

Preface

A carbon nanotube is a honeycomb lattice rolled into a cylinder. The diameter of a carbon nanotube is of nanometer size and the length of the nanotube can be more than $1\mu\text{m}$. The nanotube diameter is much smaller in size than the most advanced semiconductor devices obtained so far. Thus the availability of carbon nanotubes may have a large impact on semiconductor physics because of its very small size and the special electronic properties that are unique to carbon nanotubes. Because of the large variety of possible helical geometries known as chirality, carbon nanotubes provide a family of structures with different diameters and chiralities. One of the most significant physical properties of carbon nanotubes is their electronic structure which depends only on their geometry, and is unique to solid state physics. Specifically, the electronic structure of a single-wall carbon nanotube is either metallic or semiconducting, depending on its diameter and chirality, and does not require any doping. Thus we can imagine that the smallest possible semiconductor devices are likely to be based on carbon nanotubes. Further, the energy gap of semiconducting carbon nanotubes can be varied continuously from 1 eV to 0 eV, by varying the nanotube diameter. Thus, in principle, it may be possible to specify the desired semiconducting properties using only carbon atoms with a specified geometric structure.

The purpose of this book is to define the structure of carbon nanotubes as clearly as possible, starting from basic physics and chemistry. Since the uniqueness in the electronic structure comes directly from the uniqueness of the electronic structure of graphite, this volume provides background information about the structure and properties of graphite and related carbon materials. From our definition of the structure of carbon nanotubes, we can explain the electronic structure and phonon dispersion relations based on simple physical models, which the reader can follow with a pen and paper. Thus the contents of the book are rather theoretically oriented, and experimental results are used primarily to provide evidence for the validity of the theory. This is actually the

way that the field of carbon nanotubes developed. At an early stage, the theory stimulated experiments in carbon nanotube physics, since obtaining sufficient quantities of pure carbon nanotubes has been difficult in practice. The early experiments were made through electron microscope observation. The direct evidence provided by electron microscopy for the existence of carbon nanotubes was sensational to many physicists and chemists, and because of this fascination, the field of carbon nanotubes has grown explosively, with many active research groups worldwide working independently or in collaborative research projects.

In this book, using basic ideas of the lattice, electronic and phonon structures, the physical properties are discussed in the terminology of carbon nanotubes, which are characterized by the chiral index (n, m) . The chiral index (n, m) consists of a set of integers which specify each carbon nanotube uniquely. Since quantum effects are prominent in nanotube physics, the magnetic and transport quantum effects are very significant. Although progress in the field is still at an early stage, the book focuses on the basic principles behind the physical properties. Another unique property of a carbon nanotube is its stiffness, corresponding to the upper limit of the best carbon fibers, which are commonly used as a strong light-weight material. The special properties of carbon nanotubes are explained in the various chapters in this book.

Thus the physical properties of carbon nanotubes provide a new dimension for solid state physics, based on the great variety of possible geometries that are available for carbon nanotubes. In order to expand this field into the future, many researchers in different fields of science should contribute to this field. The authors hope that readers from any field of science can read this book without any special background requirements. This book is not intended to be a collection of all activities on carbon nanotubes worldwide because this field is already so extensive, and is moving forward so rapidly at the present time. When this book was started three years ago, the present status of the field could not have been anticipated. Thus future progress is beyond our imagination. We hope that through this book, we will find many new friends in this field. So please enjoy the book and please communicate to the authors any comments you might have about this book.

The authors would like to acknowledge many carbon nanotube researchers who have contributed to the contents of the book. The authors also thank the New Energy Development Organization (NEDO) of the Japanese Ministry for

International Trade and Industry (MITI), Japan Society for the Promotion of Science (JSPS), and their generous support for international collaboration which made the writing of this book possible. The authors especially thank Ms. Junko Yamamoto and Ms. Laura Doughty for their help in preparing the indexes and figures of the book.

Finally the authors wish to say to readers: "Welcome to Carbon Nanotube Physics."

R. Saito, Tokyo

M.S. Dresselhaus, Cambridge, Massachusetts

G. Dresselhaus, Cambridge, Massachusetts

Contents

1 Carbon Materials	1
1.1 History	1
1.2 Hybridization in A Carbon Atom	4
1.2.1 sp Hybridization: Acetylene, $\text{HC}\equiv\text{CH}$	5
1.2.2 sp^2 Hybridization: Polyacetylene, $(\text{HC}=\text{CH}-)_n$	7
1.2.3 sp^3 Hybridization: Methane, (CH_4)	8
1.2.4 Carbon $1s$ Core Orbitals	9
1.2.5 Isomers of Carbon	11
1.2.6 Carbynes	13
1.2.7 Vapor Grown Fibers	14
2 Tight Binding Calculation of Molecules and Solids	17
2.1 Tight Binding Method for a Crystalline Solid	17
2.1.1 Secular Equation	17
2.1.2 Procedure for obtaining the energy dispersion	21
2.2 Electronic Structure of Polyacetylene	22
2.3 Two-Dimensional Graphite	25
2.3.1 π Bands of Two-Dimensional Graphite	26
2.3.2 σ Bands of Two-Dimensional Graphite	29
3 Structure of a Single-Wall Carbon Nanotube	35
3.1 Classification of carbon nanotubes	35
3.2 Chiral Vector: C_h	37
3.3 Translational Vector: T	39
3.4 Symmetry Vector: R	41
3.5 Unit Cells and Brillouin Zones	45
3.6 Group Theory of Carbon Nanotubes	48
3.7 Experimental evidence for nanotube structure	53

4 Electronic Structure of Single-Wall Nanotubes	59
4.1 One-electron dispersion relations	59
4.1.1 Zone-Folding of Energy Dispersion Relations	59
4.1.2 Energy Dispersion of Armchair and Zigzag Nanotubes . .	61
4.1.3 Dispersion of chiral nanotubes	65
4.2 Density of States, Energy gap	66
4.3 Effects of Peierls distortion and nanotube curvature	70
5 Synthesis of Carbon Nanotubes	73
5.1 Single-Wall Nanotube Synthesis	73
5.2 Laser Vaporization Synthesis Method	74
5.3 Arc Method of Synthesizing Carbon Nanotubes	77
5.4 Vapor Growth and Other Synthesis Methods	79
5.4.1 Vapor Growth Method	80
5.4.2 Other Synthesis Methods	82
5.5 Purification	83
5.6 Nanotube Opening, Wetting, Filling and Alignment	84
5.6.1 Nanotube Opening	84
5.6.2 Nanotube Wetting	85
5.6.3 Nanotube Filling	85
5.6.4 Alignment of Nanotubes	86
5.7 Nanotube Doping, Intercalation, and BN/C Composites	86
5.8 Temperature Regimes for Carbonization and Graphitization . .	87
5.9 Growth Mechanisms	89
6 Landau Energy Bands of Carbon Nanotubes	95
6.1 Free Electron in a Magnetic Field	95
6.2 Tight Binding in a Magnetic Field	98
6.3 Cosine Band in a Magnetic Field	100
6.4 Landau Energy Bands	104
6.5 Landau Energy Bands: Aharonov-Bohm	108
6.6 Landau Energy Bands: Quantum-Oscillation	111
7 Connecting Carbon Nanotubes	115
7.1 Net Diagrams of a Junction	115
7.2 The Rule for Connecting Two Nanotubes	119

7.3	Shape of a Junction	120
7.4	Tunneling Conductance of a Junction	123
7.5	Coiled Carbon Nanotubes	130
8	Transport Properties of Carbon Nanotubes	137
8.1	Quantum transport in a one-dimensional wire	137
8.1.1	A ballistic conductor ($L \ll L_m, L_\varphi$)	142
8.1.2	Classic transport, $L_\varphi \ll L_m \ll L$	144
8.1.3	Localization, ($L_m \ll L_\varphi \ll L$)	145
8.1.4	Universal Conductance Fluctuations	148
8.1.5	Negative Magnetoresistance	151
8.2	Transport experiments on carbon nanotubes	152
8.2.1	Attaching Contacts	153
8.2.2	An Individual Single-Wall Nanotube	154
8.2.3	An Individual Rope of Single-Wall Nanotubes	158
8.2.4	Magneto-Transport in Multi-Wall Nanotubes	159
9	Phonon Modes of Carbon Nanotubes	163
9.1	Dynamical matrix for phonon dispersion relations	163
9.2	Phonon dispersion relations for two-dimensional graphite	165
9.3	Phonon dispersion relations for nanotubes	171
9.3.1	Zone folding method	171
9.3.2	Force constant tensor of a carbon nanotube	173
9.3.3	Force constant corrections due to curvature of 1D nanotubes	178
10	Raman Spectra of Carbon Nanotubes	183
10.1	Raman or infrared active modes of carbon nanotubes	183
10.2	Raman experiments on single-wall nanotubes	187
10.3	Bond Polarizability Theory of Raman Intensity for Carbon Nanotubes	192
10.4	Raman Spectra of Nanotubes with Random Orientations	195
10.4.1	Lower Frequency Raman Spectra	196
10.4.2	Higher Frequency Raman Modes	198
10.4.3	Medium Frequency Raman Modes	201
10.5	Sample Orientation Dependence	203

11 Elastic Properties of Carbon Nanotubes	207
11.1 Overview of Elastic Properties of Carbon Nanotubes	207
11.2 Strain Energy of Carbon Nanotubes	210
11.3 The Peierls Instability of Nanotubes	213
11.3.1 Bond Alternation	213
11.3.2 Peierls Distortion of graphite and carbon nanotubes . . .	217
11.4 Properties of Multi-Wall Nanotubes	221
References	239
Index	253

CHAPTER 1.

Carbon Materials

Carbon materials are found in variety forms such as graphite, diamond, carbon fibers, fullerenes, and carbon nanotubes. The reason why carbon assumes many structural forms is that a carbon atom can form several distinct types of valence bonds, where the chemical bonds refer to the *hybridization* of orbitals by physicists. This chapter introduces the history of carbon materials and describes the atomic nature of carbon.

1.1 History

We provide here a brief review of the history of carbon fibers, which are the macroscopic analog of carbon nanotubes. The early history of carbon fibers was stimulated by needs for materials with special properties, both in the 19th century and more recently after World War II. The first carbon fiber was prepared by Thomas A. Edison to provide a filament for an early model of an electric light bulb. Specially selected Japanese Kyoto bamboo filaments were used to wind a spiral coil that was then pyrolyzed to produce a coiled carbon resistor, which could be heated ohmically to provide a satisfactory filament for use in an early model of an incandescent light bulb [1]. Following this initial pioneering work by Edison, further research on carbon filaments proceeded more slowly, since carbon filaments were soon replaced by a more sturdy tungsten filament in the electric light bulb. Nevertheless research on carbon fibers and filaments proceeded steadily over a long time frame, through the work of Schützenberger and Schützenberger (1890) [2], Pelabon [3], and others. Their efforts were mostly directed toward the study of vapor grown carbon filaments, showing filament growth from the thermal decomposition of hydrocarbons.

The second applications-driven stimulus to carbon fiber research came in

the 1950's from the needs of the space and aircraft industry for strong, stiff light-weight fibers that could be used for building lightweight composite materials with superior mechanical properties. This stimulation led to great advances in the preparation of continuous carbon fibers based on polymer precursors, including rayon, polyacrylonitrile (PAN) and later mesophase pitch. The late 1950's and 1960's was a period of intense activity at the Union Carbide Corporation, the Aerospace Corporation and many other laboratories worldwide. This stimulation also led to the growth of a carbon whisker [4], which has become a benchmark for the discussion of the mechanical and elastic properties of carbon fibers. The growth of carbon whiskers was also inspired by the successful growth of single crystal whisker filaments at that time for many metals such as iron, non-metals such as Si, and oxides such as Al_2O_3 , and by theoretical studies [5], showing superior mechanical properties for whisker structures [6]. Parallel efforts to develop new bulk synthetic carbon materials with properties approaching single crystal graphite led to the development of highly oriented pyrolytic graphite (HOPG) in 1962 by Ubbelohde and co-workers [7,8], and HOPG has since been used as one of the benchmarks for the characterization of carbon fibers.

While intense effort continued toward perfecting synthetic filamentary carbon materials, and great progress was indeed made in the early 60's, it was soon realized that long term effort would be needed to reduce fiber defects and to enhance structures resistive to crack propagation. New research directions were introduced because of the difficulty in improving the structure and microstructure of polymer-based carbon fibers for high strength and high modulus applications, and in developing graphitizable carbons for ultra-high modulus fibers. Because of the desire to synthesize more crystalline filamentous carbons under more controlled conditions, synthesis of carbon fibers by a catalytic chemical vapor deposition (CVD) process proceeded, laying the scientific basis for the mechanism and thermodynamics for the vapor phase growth of carbon fibers in the 1960's and early 1970's.[9] In parallel to these scientific studies, other research studies focused on control of the process for the synthesis of vapor grown carbon fibers,[10]–[13] leading to current commercialization of vapor grown carbon fibers in the 1990's for various applications. Concurrently, polymer-based carbon fiber research has continued worldwide, mostly in industry, with emphasis on greater control of processing steps to achieve carbon fibers with ever-increasing modulus and strength, fibers with special characteristics, while decreasing costs

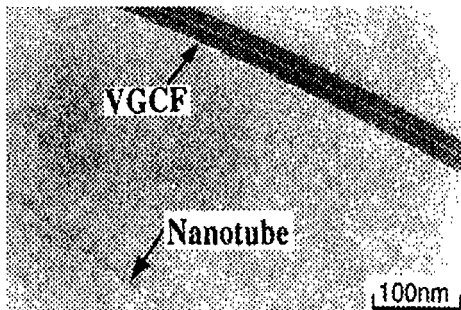


Fig. 1.1: High resolution TEM micrograph showing carbon nanotubes with diameters less than 10 nm [14–17].

of the commercial products.

As research on vapor grown carbon fibers on the micrometer scale proceeded, the growth of very small diameter filaments, such as shown in Fig. 1.1, was occasionally observed and reported [14, 15], but no detailed systematic studies of such thin filaments were carried out. In studies of filamentous carbon fibers, the growth of the initial hollow tube and the subsequent thickening process were reported.[16, 17] An example of a very thin vapor grown tubules ($< 100 \text{ \AA}$) is shown in the bright field TEM image of Fig. 1.1 [14–17].

Reports of such thin filaments inspired Kubo [18] to ask whether there was a minimum dimension for such filaments. Early work [14, 15] on vapor grown carbon fibers, obtained by thickening filaments such as the fiber denoted by VGCF (vapor grown carbon fiber) in Fig. 1.1, showed very sharp lattice fringe images for the inner-most cylinders corresponding to a vapor grown carbon fiber (diameter $< 100 \text{ \AA}$). Whereas the outermost layers of the fiber have properties associated with vapor grown carbon fibers, there may be a continuum of behavior of the tree rings as a function of diameter, with the innermost tree rings perhaps behaving like carbon nanotubes.

Direct stimulus to study carbon filaments of very small diameters more systematically [19] came from the discovery of fullerenes by Kroto and Smalley [20]. In December 1990 at a carbon-carbon composites workshop, papers were given on the status of fullerene research by Smalley [21], the discovery of a new synthesis method for the efficient production of fullerenes by Huffman [22], and a review of carbon fiber research by M.S. Dresselhaus [23]. Discussions at the workshop stimulated Smalley to speculate about the existence of carbon nanotubes of dimensions comparable to C_{60} . These conjectures were later followed

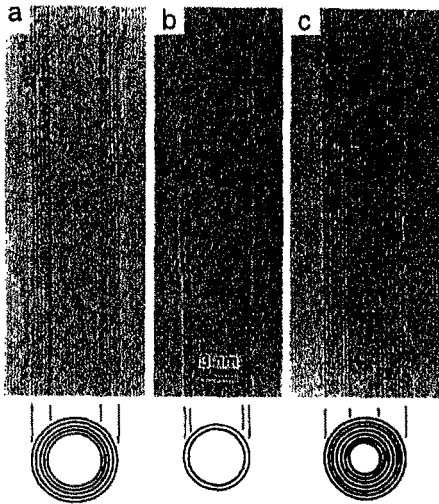


Fig. 1.2: The observation by TEM of multi-wall coaxial nanotubes with various inner and outer diameters, d_i and d_o , and numbers of cylindrical shells N : reported by Iijima using TEM: (a) $N = 5$, $d_o = 67\text{\AA}$, (b) $N = 2$, $d_o = 55\text{\AA}$, and (c) $N = 7$, $d_i = 23\text{\AA}$, $d_o = 65\text{\AA}$ [19].

up in August 1991 by an oral presentation at a fullerene workshop in Philadelphia by Dresselhaus [24] on the symmetry proposed for carbon nanotubes capped at either end by fullerene hemispheres, with suggestions on how zone folding could be used to examine the electron and phonon dispersion relations of such structures. However, the real breakthrough on carbon nanotube research came with Iijima's report of experimental observation of carbon nanotubes using transmission electron microscopy (see Fig. 1.2) [19]. It was this work which bridged the gap between experimental observation and the theoretical framework of carbon nanotubes in relation to fullerenes and as theoretical examples of 1D systems. Since the pioneering work of Iijima [19], the study of carbon nanotubes has progressed rapidly.

1.2 Hybridization in A Carbon Atom

Carbon-based materials, clusters, and molecules are unique in many ways. One distinction relates to the many possible configurations of the electronic states of a carbon atom, which is known as the hybridization of atomic orbitals. In this section we introduce the hybridization in a carbon atom and consider the family of carbon materials.

Carbon is the sixth element of the periodic table and is listed at the top

of column IV. Each carbon atom has six electrons which occupy $1s^2$, $2s^2$, and $2p^2$ atomic orbitals.* The $1s^2$ orbital contains two strongly bound electrons, and they are called core electrons. Four electrons occupy the $2s^22p^2$ orbitals, and these more weakly bound electrons are called valence electrons. In the crystalline phase the valence electrons give rise to $2s$, $2p_x$, $2p_y$, and $2p_z$ orbitals which are important in forming covalent bonds in carbon materials. Since the energy difference between the upper $2p$ energy levels and the lower $2s$ level in carbon is small compared with the binding energy of the chemical bonds,[†] the electronic wave functions for these four electrons can readily mix with each other, thereby changing the occupation of the $2s$ and three $2p$ atomic orbitals so as to enhance the binding energy of the C atom with its neighboring atoms. This mixing of $2s$ and $2p$ atomic orbitals is called hybridization, whereas the mixing of a single $2s$ electron with $n = 1, 2, 3$ [‡] $2p$ electrons is called sp^n hybridization [9].

In carbon, three possible hybridizations occur: sp , sp^2 and sp^3 ; other group IV elements such as Si, Ge exhibit primarily sp^3 hybridization. Carbon differs from Si and Ge insofar as carbon does not have inner atomic orbitals except for the spherical $1s$ orbitals, and the absence of nearby inner orbitals facilitates hybridizations involving only valence s and p orbitals for carbon. The lack of sp and sp^2 hybridization in Si and Ge might be related to the absence of “organic materials” made of Si[§] and Ge.

1.2.1 *sp Hybridization: Acetylene, $HC\equiv CH$*

In sp hybridization, a linear combination of the $2s$ orbital and one of the $2p$ orbitals of a carbon atom, for example $2p_x$, is formed. From the two-electron orbitals of a carbon atom, two hybridized sp orbitals, denoted by $|sp_a\rangle$ and $|sp_b\rangle$, are expressed by the linear combination of $|2s\rangle$ and $|2p_x\rangle$ wavefunctions of the carbon atom,

$$\begin{aligned} |sp_a\rangle &= C_1|2s\rangle + C_2|2p_x\rangle \\ |sp_b\rangle &= C_3|2s\rangle + C_4|2p_x\rangle \end{aligned} \quad (1.1)$$

*The ground state of a free carbon atom is 3P ($S = 1, L = 1$) using the general notation for a two-electron multiplet.

[†]In the free carbon atom, the excited state, $2s2p^3$ which is denoted by 5S is 4.18 eV above the ground state.

[‡]Because of the electron-hole duality, $n = 4$ and 5 are identical to $n = 2$ and 1, respectively.

[§]It should be mentioned that the “organic chemistry” for Si is becoming an active field today.

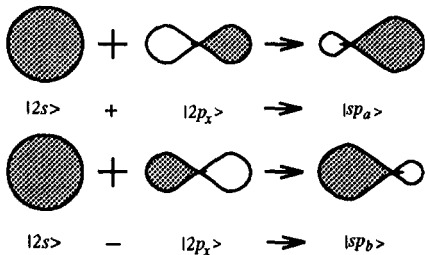


Fig. 1.3: sp hybridization. The shading denotes the positive amplitude of the wavefunction. $|2s\rangle + |2p_x\rangle$ is elongated in the positive direction of x (upper panel), while that of $|2s\rangle - |2p_x\rangle$ is elongated in the negative direction of x (lower panel).

where C_i are coefficients. Using the ortho-normality conditions $\langle sp_a|sp_b\rangle = 0$, $\langle sp_a|sp_a\rangle = 1$, and $\langle sp_b|sp_b\rangle = 1$, we obtain the relationship between the coefficients C_i :

$$\begin{aligned} C_1C_3 + C_2C_4 &= 0, & C_1^2 + C_2^2 &= 1, \\ C_3^2 + C_4^2 &= 1, & C_1^2 + C_3^2 &= 1. \end{aligned} \quad (1.2)$$

The last equation is given by the fact that the sum of $|2s\rangle$ components in $|sp_a\rangle$ and $|sp_b\rangle$, is unity. The solution of (1.2) is $C_1 = C_2 = C_3 = 1/\sqrt{2}$ and $C_4 = -1/\sqrt{2}$ so that

$$\begin{aligned} |sp_a\rangle &= \frac{1}{\sqrt{2}} \left(|2s\rangle + |2p_x\rangle \right) \\ |sp_b\rangle &= \frac{1}{\sqrt{2}} \left(|2s\rangle - |2p_x\rangle \right). \end{aligned} \quad (1.3)$$

In Fig. 1.3 we show a schematic view of the directed valence of the $|sp_a\rangle$ (upper panel) and $|sp_b\rangle$ (lower panel) orbitals. The shading denotes a positive amplitude of the wavefunction. The wavefunction of $|2s\rangle + |2p_x\rangle$ is elongated in the positive direction of x , while that of $|2s\rangle - |2p_x\rangle$ is elongated in the negative direction of x . Thus when nearest-neighbor atoms are in the direction of x axis, the overlap of $|sp_a\rangle$ with the wavefunction at $x > 0$ becomes large compared with the original $|2p_x\rangle$ function, which gives rise to a higher binding energy. If we select $|2p_y\rangle$ for $|2p_x\rangle$, the wavefunction shows a directed valence in the direction of y axis.

It is only when an asymmetric shape of the wavefunction (see Fig. 1.3) is desired for forming a chemical bond that a mixing of $2p$ orbitals with $2s$ orbitals occurs. The mixing of only $2p$ orbitals with each other gives rise to the rotation of $2p$ orbitals, since the $2p_x$, $2p_y$ and $2p_z$ orbitals behave like a vector, (x, y, z) . A wavefunction $C_x|2p_x\rangle + C_y|2p_y\rangle + C_z|2p_z\rangle$, where $C_x^2 + C_y^2 + C_z^2 = 1$, is the $2p$

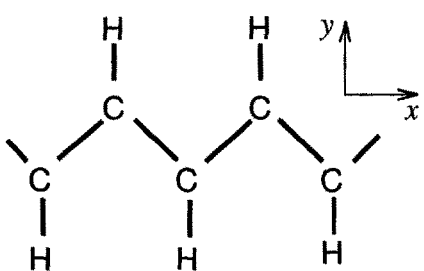


Fig. 1.4: *trans*-polyacetylene, $(HC=CH-)_n$, the carbon atoms form a zigzag chain with an angle of 120° , through sp^2 hybridization. All σ bonds shown in the figure are in the plane, and in addition, one π orbital per carbon atom exists perpendicular to the plane.

wavefunction whose direction of positive amplitude is the direction (C_x, C_y, C_z) . The $2p$ wavefunctions of Eq. (1.3) correspond to $(C_x, C_y, C_z) = (1, 0, 0)$ and $(C_x, C_y, C_z) = (-1, 0, 0)$, respectively.

A simple carbon-based material showing sp hybridization is acetylene, $HC\equiv CH$, where \equiv is used by chemists to denote a triple bond between two carbon atoms. The acetylene molecule $HC\equiv CH$ is a linear molecule with each atom having its equilibrium position along a single axis and with each carbon atom exhibiting sp hybridization. The hybridized $|sp_a\rangle$ orbital of one of the carbon atoms in $HC\equiv CH$ forms a covalent bond with the $|sp_b\rangle$ orbital of the other carbon atom, called a σ bond. The $2p_y$ and $2p_z$ wavefunctions of each carbon atom are perpendicular to the σ bond, and the $2p_y$ and $2p_z$ wavefunctions form relatively weak bonds called π bonds with those of the other carbon atom. Thus, one σ bond and two π bonds yields the triple bond of $HC\equiv CH$.

1.2.2 sp^2 Hybridization: Polyacetylene, $(HC=CH-)_n$

In sp^2 hybridization, the $2s$ orbital and two $2p$ orbitals, for example $2p_x$ and $2p_y$, are hybridized. An example of sp^2 hybridization is polyacetylene, $(HC=CH-)_n$ as is shown in Fig.1.4, where carbon atoms form a zigzag chain with an angle of 120° . All σ bonds shown in the figure are in a (xy) plane, and, in addition, a π orbital for each carbon atom exists perpendicular to the plane. Since the directions of the three σ bonds of the central carbon atom in Fig.1.4 are $(0, -1, 0)$, $(\sqrt{3}/2, 1/2, 0)$, and $(-\sqrt{3}/2, 1/2, 0)$, the corresponding sp^2 hybridized

orbitals $|sp_i^2\rangle$ ($i = a, b, c$) are made from $2s$, $2p_x$, and $2p_y$ orbitals as follows:

$$\begin{aligned} |sp_a^2\rangle &= C_1|2s\rangle - \sqrt{1-C_1^2}|2p_y\rangle \\ |sp_b^2\rangle &= C_2|2s\rangle + \sqrt{1-C_2^2}\left\{\frac{\sqrt{3}}{2}|2p_x\rangle + \frac{1}{2}|2p_y\rangle\right\} \\ |sp_c^2\rangle &= C_3|2s\rangle + \sqrt{1-C_3^2}\left\{-\frac{\sqrt{3}}{2}|2p_x\rangle + \frac{1}{2}|2p_y\rangle\right\}. \end{aligned} \quad (1.4)$$

We now determine the coefficients C_1 , C_2 , and C_3 . From the orthonormal requirements of the $|sp_i^2\rangle$ and $|2s\rangle$, $|2p_{x,y}\rangle$ orbitals, we obtain three equations for determining the coefficients, C_i ($i = 1, \dots, 3$):

$$\begin{aligned} C_1^2 + C_2^2 + C_3^2 &= 1 \\ C_1C_2 - \frac{1}{2}\sqrt{1-C_1^2}\sqrt{1-C_2^2} &= 0 \\ C_1C_3 + \frac{1}{2}\sqrt{1-C_1^2}\sqrt{1-C_3^2} &= 0, \end{aligned} \quad (1.5)$$

yielding the solution of Eq. (1.5) given by $C_1 = C_2 = 1/\sqrt{3}$ and $C_3 = -1/\sqrt{3}$. The sp^2 orbitals thus obtained have a large amplitude in the direction of the three nearest-neighbor atoms, and these three-directed orbitals are denoted by *trigonal* bonding. There are two kinds of carbon atoms in polyacetylene, as shown in Fig. 1.4, denoting different directions for the nearest-neighbor hydrogen atoms. For the upper carbon atoms in Fig. 1.4, the coefficients of the $|2p_y\rangle$ terms in Eq. (1.4) are positive, but are changed to $-|2p_y\rangle$ for the lower carbon atoms in the figure.

1.2.3 sp^3 Hybridization: Methane, (CH_4)

The carbon atom in methane, (CH_4), provides a simple example of sp^3 hybridization through its tetragonal bonding to four nearest neighbor hydrogen atoms which have the maximum spatial separation from each other. The four directions of tetrahedral bonds from the carbon atom can be selected as $(1,1,1)$, $(-1,-1,1)$, $(-1,1,-1)$, $(1,-1,1)$. In order to make elongated wavefunctions to these directions, the $2s$ orbital and three $2p$ orbitals are mixed with each other, forming an sp^3 hybridization. Using equations similar to Eq. (1.4) but with the four unknown coefficients, C_i , ($i = 1, \dots, 4$), and orthonormal atomic

wavefunctions, we obtain the sp^3 hybridized orbitals in these four directions:

$$\begin{aligned} |sp_a^3\rangle &= \frac{1}{2} \{|2s\rangle + |2p_x\rangle + |2p_y\rangle + |2p_z\rangle\} \\ |sp_b^3\rangle &= \frac{1}{2} \{|2s\rangle - |2p_x\rangle - |2p_y\rangle + |2p_z\rangle\} \\ |sp_c^3\rangle &= \frac{1}{2} \{|2s\rangle - |2p_x\rangle + |2p_y\rangle - |2p_z\rangle\} \\ |sp_d^3\rangle &= \frac{1}{2} \{|2s\rangle + |2p_x\rangle - |2p_y\rangle - |2p_z\rangle\}. \end{aligned} \quad (1.6)$$

In general for sp^n hybridization, $n+1$ electrons belong to the carbon atom occupied in the hybridized σ orbital and $4-(n+1)$ electrons are in π orbital. In the case of sp^3 hybridization, the four valence electrons occupy $2s^1$ and $2p^3$ states as σ bonding states. The excitation of $2s^1$ and $2p^3$ in the solid phase from the $2s^22p^2$ atomic ground state requires an energy approximately equal to the energy difference between the $2s$ and $2p$ (~ 4 eV) levels. However the covalent bonding energy for σ orbitals is larger ($3 \sim 4$ eV per *bond*) than the $2s-2p$ energy separation.

It is important to note that the directions of the three wavefunctions in the sp^3 hybridization are freely determined, while the remaining fourth direction is determined by orthonormal conditions imposed on the $2p$ orbitals. This fact gives rise to possible sp^2 hybridization of a planar pentagonal (or heptagonal) carbon ring and $sp^{2+\eta}$ ($0 < \eta < 1$) hybridization* which is found in fullerenes. A general $sp^{2+\eta}$ hybridization is expected to have a higher excitation energy than that of the symmetric sp^2 hybridization discussed here because of the electron-electron repulsion which occurs in the hybridized orbital.

1.2.4 Carbon 1s Core Orbitals

Carbon 1s core orbitals do not generally affect the solid state properties of carbon materials, since the energy position of the 1s core levels is far from the Fermi energy compared with the valence levels. Because of the small overlap between the 1s orbitals on adjacent atomic sites in the solid, the energy spectrum of the 1s core levels in carbon materials is sharp and the core level energies lie close to that of an isolated carbon atom. Using X-ray photoelectron spectroscopy (XPS), the energy of the 1s core level is measured relative to the position of the

*This notation denotes an admixture of sp^2 and sp^3 hybridization.

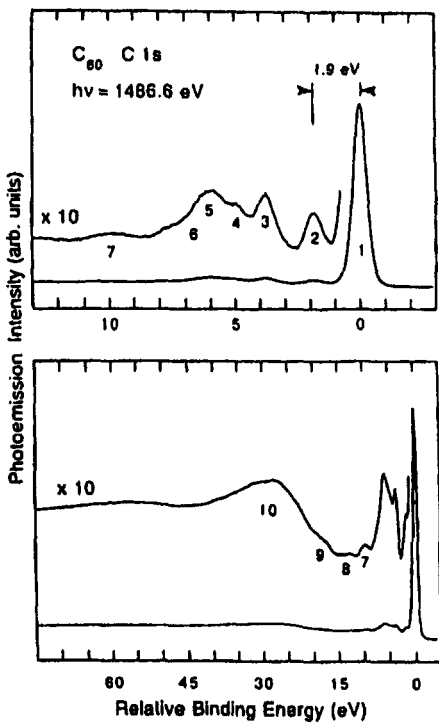


Fig. 1.5: X-ray photoelectron spectra (XPS) for the carbon 1s-derived satellite structures for C_{60} films [25]. The sharp feature 1 is the fundamental XPS line, while the downshifted features 2–10 refer to C_{60} excitations (see text). The XPS data are shown on two energy scales to emphasize features near E_F (upper spectrum) and features farther away in energy (lower spectrum) [25].

vacuum level, and this energy difference is especially sensitive to the transfer of electric charge between carbon atoms. Specifically, the 1s core level shifts in energy relative to the vacuum level by an amount depending on the interaction with nearest-neighbor atoms, and this effect is known as the chemical shift of XPS.

Furthermore, XPS refers to the photoelectron spectroscopy (PES) process when the excitation photon is in the x-ray range and the electron excitation is from a core level. XPS spectra have been obtained for the unoccupied orbitals for a variety of fullerenes. For example, Fig. 1.5 shows the XPS spectrum for C_{60} [25]. In this spectrum, we can see well-defined peaks which show an intense, narrow main line (peak #1 in Fig. 1.5) identified with the emission of a photo-excited electron from the carbon 1s state, which has a binding energy of 285.0 eV and a very small linewidth of 0.65 eV at half-maximum intensity [25].

Table 1.1: Isomers made of carbon

Dimension	0-D	1-D	2-D	3-D
isomer	C ₆₀ fullerene	nanotube carbyne	graphite fiber	diamond amorphous
hybridization	sp^2	sp^2 (sp)	sp^2	sp^3
density [g/cm ³]	1.72	1.2-2.0 2.68-3.13	2.26 ~ 2	3.515 2-3
Bond Length [Å]	1.40(C=C) 1.46(C-C)	1.44(C=C)	1.42(C=C) 1.44(C=C)	1.54(C-C)
electronic properties	semiconductor	metal or semiconductor	semimetal	insulating $E_g = 5.47\text{eV}$

The sharpest side-band feature in the downshifted XPS spectrum (labeled 2) is identified with an on-site molecular excitation across the HOMO-LUMO gap at 1.9 eV [25]. Features 3, 4 and 5 are the photoemission counterparts of electric dipole excitations seen in optical absorption, while features 6 and 10 represent intramolecular plasmon collective oscillations of the π and σ charge distributions. Plasma excitations are also prominently featured in core level electron energy loss spectra (EELS).

1.2.5 Isomers of Carbon

The sp^n hybridization discussed in the previous section is essential for determining the dimensionality of not only carbon-based molecules, but also carbon-based solids. Carbon is the only element in the periodic table that has isomers from 0 dimensions (0D) to 3 dimensions (3D), as is shown in Table 1.1. Here we introduce possible structures of carbon materials in the solid phase, which are closely related to the sp^n hybridization.

In sp^n hybridization, $(n + 1)$ σ bonds per carbon atom are formed, these σ bonds making a skeleton for the local structure of the n -dimensional structure. In sp hybridization, two σ bonds make only a one-dimensional chain structure, which is known as a ‘carbyne’. A three-dimensional solid is formed by gathering these carbyne chains. In sp^3 hybridization, four σ bonds defining a regular tetrahedron are sufficient to form a three-dimensional structure known as the diamond structure. It is interesting that sp^2 hybridization which forms a planar structure in two-dimensional graphite also forms a planar local structure in

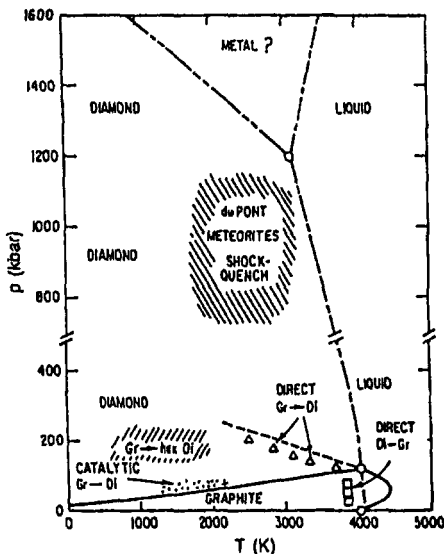


Fig. 1.6: One version of the phase diagram of carbon suggested by Bundy [26]. The diamond (Di) and graphite (Gr) phases are emphasized in this figure. Other phases shown in the diagram include hexagonal diamond and a high temperature-high pressure phase, denoted in the diagram by du Pont, meteorites and shock-quench, which has not been studied in much detail and may, in part, be related to carbynes. Liquid carbon, which has been studied at low pressures and high temperatures, and an unexplored high pressure phase, which may be metallic, are also indicated on the figure.

the closed polyhedra (0-dimensional) of the fullerene family and in the cylinders (1-dimensional) called carbon nanotubes. Closely related to carbon nanotubes are carbon fibers which are macroscopic one-dimensional materials, because of their characteristic high length to diameter ratio. A carbon fiber, however, consists of many graphitic planes and microscopically exhibits electronic properties that are predominantly two-dimensional. Amorphous carbon is a disordered, three-dimensional material in which sp^2 and sp^3 hybridization are both present, randomly. Amorphous graphite, which consists mainly of sp^2 hybridization, is a graphite with random stacking of graphitic layer segments. Because of the weak interplanar interaction between two graphitic planes, these planes can move easily relative to each other, thereby forming a solid lubricant. In this sense, amorphous graphite can behave like a two-dimensional material.

Under ambient conditions and in bulk form, the graphite phase with strong in-plane trigonal bonding is the stable phase, as indicated by the phase diagram of Fig. 1.6 [26–28]. Under the application of high pressure and high temperature (both of which are somewhat reduced when catalyst particles like iron or nickel

are used), transformation to the diamond structure takes place. Once the pressure is released, diamond remains essentially stable under ambient conditions although, in principle, it will very slowly transform back to the thermodynamically stable form of solid carbon, which is graphite. When exposed to various perturbations, such as irradiation and heat, diamond will quickly transform back to the equilibrium graphite phase.

Hereafter we introduce the ‘one-dimensional’ isomers, carbynes and carbon fibers, which are related to nanotubes, as the subject of the following chapters.

1.2.6 Carbynes

Linear chains of carbon which have *sp* bonding have been the subject of research for many years [29].

A polymeric form of carbon consisting of chains $[\cdots -C\equiv C-\cdots]_n$ for $n > 10$ has been reported in rapidly quenched carbons and is referred to as “carbynes.” This carbon structure is stable at high temperature and pressure as indicated in the phase diagram of Fig. 1.6 as shock-quenched phases. Carbynes are silver-white in color and are found in meteoritic carbon deposits, where the carbynes are mixed with graphite particles. Synthetic carbynes have also been prepared by sublimation of pyrolytic graphite [30, 31]. It has been reported that carbynes are formed during very rapid solidification of liquid carbon, near the surface of the solidified droplets formed upon solidification [32]. Some researchers [31–35] have reported evidence that these linearly bonded carbon phases are stable at temperatures in the range $2700 < T < 4500$ K.

Carbynes were first identified in samples found in the Ries crater in Bavaria [36] and were later synthesized by the dehydrogenation of acetylene [31, 37]. The carbynes have been characterized by x-ray diffraction, scanning electron microscopy (TEM), ion micro-mass analysis, and spectroscopic measurements which show some characteristic features that identify carbynes in general and specific carbyne polymorphs in particular. The crystal structure of carbynes has been studied by x-ray diffraction through identification of the Bragg peaks with those of synthetic carbynes produced from the sublimation of pyrolytic graphite [33, 37]. In fact, two polymorphs of carbynes (labeled α and β) have been identified, both being hexagonal and with lattice constants $a_\alpha = 8.94$ Å, $c_\alpha = 15.36$ Å; $a_\beta = 8.24$ Å, $c_\beta = 7.68$ Å [31]. Application of pressure converts the

α phase into the β phase. The numbers of atoms per unit cell and the densities are, respectively, 144 and 2.68 g/cm^3 for the α phase and 72 and 3.13 g/cm^3 for the β phase [38]. These densities determined from x-ray data [31] are in rough agreement with prior estimates [39, 40]. It is expected that other less prevalent carbyne polymorphs should also exist. In the solid form, these carbynes have a hardness intermediate between diamond and graphite. Because of the difficulty in isolating carbynes in general, and specific carbyne polymorphs in particular, little is known about their detailed physical properties.

1.2.7 Vapor Grown Fibers

Vapor-grown carbon fibers can be prepared over a wide range of diameters (from less than 1000 \AA to more than $100 \mu\text{m}$) and these fibers have hollow cores [9]. In fact vapor-grown fibers with diameters less than 100\AA were reported many years ago [41–43]. The preparation of these fibers is based on the growth of a thin hollow tube of about 1000 \AA diameter from a transition metal catalytic particle ($\sim 100 \text{ \AA}$ diameter) which has been super-saturated with carbon from a hydrocarbon gas present during fiber growth at 1050°C . The thickening of the vapor-grown carbon fiber occurs through an epitaxial growth process whereby the hydrocarbon gas is dehydrogenated and sticks to the surface of the growing fiber. Subsequent heat treatment to $\sim 2500^\circ\text{C}$ results in carbon fibers with a tree ring concentric cylinder morphology [44]. Vapor-grown carbon fibers with micrometer diameters and lengths of $\sim 30 \text{ cm}$ provide a close analogy to carbon nanotubes with diameters of nanometer dimensions and similar length to diameter ratios (see Chapter 5).

Carbon fibers represent an important class of graphite-related materials from both a scientific and commercial viewpoint. Despite the many precursors that can be used to synthesize carbon fibers, each having different cross-sectional morphologies [9, 44], the preferred orientation of the graphene planes is parallel to the fiber axis for all types of carbon fibers, thereby accounting for the high mechanical strength and high modulus of carbon fibers [9]. As-prepared vapor-grown fibers have an “onion skin” or “tree ring” morphology [Fig. 1.7(a)], and after heat treatment to about 3000°C , they form facets [Fig. 1.7(b)]. Of all carbon fibers [9], these faceted fibers are closest to crystalline graphite in both crystal structure and properties. The commercial pitch and PAN fibers with other

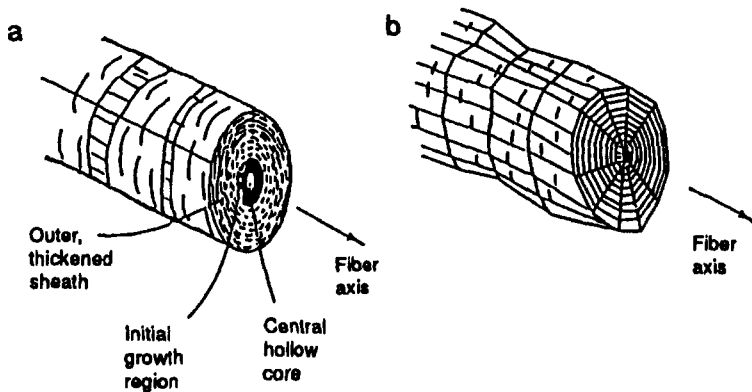


Fig. 1.7: Sketch illustrating the morphology of vapor-grown carbon fibers (VGCF): (a) as-deposited at 1100°C [9], (b) after heat treatment to 3000°C [9].

morphologies (not shown), are exploited for their extremely high bulk modulus and high thermal conductivity, while the commercial PAN (polyacrylonitrile) fibers with circumferential texture are widely used for their high strength [9]. The high modulus of the mesophase pitch fibers is related to the high degree of *c*-axis orientation of adjacent graphene layers, while the high strength of the PAN fibers is related to defects in the structure, which inhibit the slippage of adjacent planes relative to each other. Typical diameters for these individual commercial carbon fibers are $\sim 10 \mu\text{m}$, and since the fibers are produced in a continuous process, they can be considered to be infinite in length. These fibers are woven into bundles called tows and are then wound up as a continuous yarn on a spool. The remarkable high strength and modulus of carbon fibers are responsible for most of the commercial interest in these fibers [9, 44].

CHAPTER 2.

Tight Binding Calculation of Molecules and Solids

In carbon materials except for diamond, the π electrons are valence electrons which are relevant for the transport and other solid state properties. A tight binding calculation for the π electrons is simple but provides important insights for understanding the electronic structure of the π energy levels or bands for graphite and graphite-related materials.

2.1 Tight Binding Method for a Crystalline Solid

In this section we explain the tight binding method for a crystalline solid. In the following sections, we show some examples of energy bands for carbon materials discussed in the Chapter 1.

2.1.1 Secular Equation

Because of the translational symmetry of the unit cells in the direction of the lattice vectors, \vec{a}_i , ($i = 1, \dots, 3$), any wave function of the lattice, Ψ , should satisfy Bloch's theorem

$$T_{\vec{a}_i} \Psi = e^{i\vec{k} \cdot \vec{a}_i} \Psi, \quad (i = 1, \dots, 3), \quad (2.1)$$

where $T_{\vec{a}_i}$ is a translational operation along the lattice vector \vec{a}_i , and \vec{k} is the wave vector[45, 46]. There are many possible functional forms of Ψ which satisfy Eq. (2.1). The most commonly used form for Ψ is a linear combination of plane waves. The reason why plane waves are commonly used is that: (1) the integration of the plane wave wavefunction is easy and can be done analytically, (2) the numerical accuracy only depends on the number of the plane waves used. However, the plane wave method also has limitations: (1) the scale of the

computation is large, and (2) it is difficult to relate the plane wave wavefunction to the atomic orbitals in the solid.

Another functional form which satisfies Eq. (2.1) is based on the j -th atomic orbital in the unit cell (or atom). A tight binding, Bloch function $\Phi_j(\vec{k}, \vec{r})$ is given by,

$$\Phi_j(\vec{k}, \vec{r}) = \frac{1}{\sqrt{N}} \sum_{\vec{R}}^N e^{i\vec{k} \cdot \vec{R}} \varphi_j(\vec{r} - \vec{R}), \quad (j = 1, \dots, n). \quad (2.2)$$

Here \vec{R} is the position of the atom and φ_j denotes the atomic wavefunction in state j . The number of atomic wavefunctions in the unit cell is denoted by n , and we have n Bloch functions in the solid for a given \vec{k} . To form $\Phi_j(\vec{k}, \vec{r})$ in Eq. (2.2), the φ_j 's in the N ($\sim 10^{24}$) unit cells are weighted by the phase factor $\exp(i\vec{k} \cdot \vec{R})$ and are then summed over the lattice vectors \vec{R} of the whole crystal. The merits of using atomic orbitals in Bloch functions are as follows: (1) the number of basis functions, n , can be small compared with the number of plane waves, and (2) we can easily derive the formulae for many physical properties using this method.* Hereafter we consider the tight binding functions of Eq. (2.2) to represent the Block functions.

It is clear that Eq. (2.2) satisfies Eq. (2.1) since

$$\begin{aligned} \Phi_j(\vec{k}, \vec{r} + \vec{a}) &= \frac{1}{N} \sum_{\vec{R}}^N e^{i\vec{k} \cdot \vec{R}} \varphi_j(\vec{r} + \vec{a} - \vec{R}) \\ &= e^{i\vec{k} \cdot \vec{a}} \frac{1}{N} \sum_{\vec{R}-\vec{a}}^N e^{i\vec{k} \cdot (\vec{R}-\vec{a})} \varphi_j(\vec{r} - (\vec{R} - \vec{a})) \\ &= e^{i\vec{k} \cdot \vec{a}} \Phi_j(\vec{k}, \vec{r}), \end{aligned} \quad (2.3)$$

where we use the periodic boundary condition for the $M \equiv N^{-1/3}$ unit vectors in each \vec{a}_i direction,

$$\Phi_j(\vec{k}, \vec{r} + M\vec{a}_i) = \Phi_j(\vec{k}, \vec{r}) \quad (i = 1, \dots, 3), \quad (2.4)$$

consistent with the boundary condition imposed on the translation vector $T_M \vec{a}_i = 1$. From this boundary condition, the phase factor appearing in Eq. (2.2) satisfies $\exp\{ikM\vec{a}_i\} = 1$, from which the wave number k is related by the integer

*The limitations of the tight binding method are that: (1) there is no simple rule to improve the numerical accuracy and (2) atomic orbitals do not describe the interatomic region.

p ,

$$k = \frac{2p\pi}{Ma_i}, \quad (p = 0, 1, \dots, M-1), \quad (i = 1, \dots, 3). \quad (2.5)$$

In three dimensions, the wavevector \vec{k} is defined for the x , y and z directions, as k_x , k_y and k_z . Thus $M^3 = N$ wave vectors exist in the first Brillouin zone, where the k_i can be considered as continuum variables.

The eigenfunctions in the solid $\Psi_j(\vec{k}, \vec{r})$ ($j = 1, \dots, n$), where n is the number of Bloch wavefunctions, are expressed by a linear combination of Bloch functions $\Phi_{j'}(\vec{k}, \vec{r})$ as follows:

$$\Psi_j(\vec{k}, \vec{r}) = \sum_{j'=1}^n C_{jj'}(\vec{k}) \Phi_{j'}(\vec{k}, \vec{r}), \quad (2.6)$$

where $C_{jj'}(\vec{k})$ are coefficients to be determined. Since the functions $\Psi_j(\vec{k}, \vec{r})$ should also satisfy Bloch's theorem, the summation in Eq. (2.6) is taken only for the Bloch orbitals $\Phi_{j'}(\vec{k}, \vec{r})$ with the same value of \vec{k} .

The j -th eigenvalue $E_j(\vec{k})$ ($j = 1, \dots, n$) as a function of \vec{k} is given by

$$E_j(\vec{k}) = \frac{\langle \Psi_j | \mathcal{H} | \Psi_j \rangle}{\langle \Psi_j | \Psi_j \rangle} = \frac{\int \Psi_j^* \mathcal{H} \Psi_j d\mathbf{r}}{\int \Psi_j^* \Psi_j d\mathbf{r}} \quad (2.7)$$

where \mathcal{H} is the Hamiltonian of the solid. Substituting Eq. (2.6) into Eq. (2.7) and making a change of subscripts, we obtain the following equation,

$$E_i(\vec{k}) = \frac{\sum_{j,j'=1}^n C_{ij}^* C_{ij'} \langle \Phi_j | \mathcal{H} | \Phi_{j'} \rangle}{\sum_{j,j'=1}^n C_{ij}^* C_{ij'} \langle \Phi_j | \Phi_{j'} \rangle} \equiv \frac{\sum_{j,j'=1}^n \mathcal{H}_{jj'}(\vec{k}) C_{ij}^* C_{ij'}}{\sum_{j,j'=1}^n \mathcal{S}_{jj'}(\vec{k}) C_{ij}^* C_{ij'}} \quad (2.8)$$

where the integrals over the Bloch orbitals, $\mathcal{H}_{jj'}(\vec{k})$ and $\mathcal{S}_{jj'}(\vec{k})$ are called transfer integral matrices and overlap integral matrices, respectively, which are defined by

$$\mathcal{H}_{jj'}(\vec{k}) = \langle \Phi_j | \mathcal{H} | \Phi_{j'} \rangle, \quad \mathcal{S}_{jj'}(\vec{k}) = \langle \Phi_j | \Phi_{j'} \rangle \quad (j, j' = 1, \dots, n). \quad (2.9)$$

When we fix the values of the $n \times n$ matrices $\mathcal{H}_{jj'}(\vec{k})$ and $\mathcal{S}_{jj'}(\vec{k})$ in Eq. (2.9) for a given \vec{k} value, the coefficient C_{ij}^* is optimized so as to minimize $E_i(\vec{k})$.

It is noted that the coefficient C_{ij}^* is also a function of \vec{k} , and therefore C_{ij}^* is determined for each \vec{k} . When we take a partial derivative for C_{ij}^* while fixing the other $C_{ij'}$, $C_{ij'}^*$, and C_{ij} coefficients,[†] we obtain zero for the local minimum condition as follows,

$$\frac{\partial E_i(\vec{k})}{\partial C_{ij}^*} = \frac{\sum_{j'=1}^N \mathcal{H}_{jj'}(\vec{k}) C_{ij'}}{\sum_{j,j'=1}^N \mathcal{S}_{jj'}(\vec{k}) C_{ij}^* C_{ij'}} - \frac{\sum_{j,j'=1}^N \mathcal{H}_{jj'}(\vec{k}) C_{ij}^* C_{ij'}}{\left(\sum_{j,j'=1}^N \mathcal{S}_{jj'}(\vec{k}) C_{ij}^* C_{ij'} \right)^2} \sum_{j'=1}^N \mathcal{S}_{jj'}(\vec{k}) C_{ij'} = 0. \quad (2.10)$$

When we multiply both sides of Eq. (2.10) by $\sum_{j,j'=1}^N \mathcal{S}_{jj'}(\vec{k}) C_{ij}^* C_{ij'}$ and substitute the expression for $E_i(\vec{k})$ of Eq. (2.8) into the second term of Eq. (2.10), we obtain

$$\sum_{j'=1}^N \mathcal{H}_{jj'}(\vec{k}) C_{ij'} = E_i(\vec{k}) \sum_{j'=1}^N \mathcal{S}_{jj'}(\vec{k}) C_{ij'}. \quad (2.11)$$

Defining a column vector,

$$\mathbf{C}_i = \begin{pmatrix} C_{i1} \\ \vdots \\ C_{iN} \end{pmatrix}, \quad (2.12)$$

Eq. (2.11) is expressed by

$$\mathcal{H}\mathbf{C}_i = E_i(\vec{k})\mathcal{S}\mathbf{C}_i. \quad (2.13)$$

Transposing the right hand side of Eq. (2.13) to the left, we obtain $[\mathcal{H} - E_i(\vec{k})\mathcal{S}]\mathbf{C}_i = 0$. If the inverse of the matrix $[\mathcal{H} - E_i(\vec{k})\mathcal{S}]$ exists, we multiply both sides by $[\mathcal{H} - E_i(\vec{k})\mathcal{S}]^{-1}$ to obtain $\mathbf{C}_i = 0$ (where 0 denotes the null vector), which means that no wavefunction is obtained. Thus the eigenfunction is given only when the inverse matrix does not exist, consistent with the condition given by

$$\det[\mathcal{H} - E\mathcal{S}] = 0, \quad (2.14)$$

where Eq. (2.14) is called the secular equation, and is an equation of degree n , whose solution gives all n eigenvalues of $E_i(\vec{k})$ ($i = 1, \dots, n$) for a given \vec{k} .

[†]Since C_{ij} is generally a complex variable with two degrees of freedom, a real and a complex part, both C_{ij} and C_{ij}^* can be varied independently.

Using the expression for $E_i(\vec{k})$ in Eqs. (2.7) and (2.11), the coefficients C_i as a function of \vec{k} are determined. In order to obtain the energy dispersion relations (or energy bands) $E_i(\vec{k})$, we solve the secular equation Eq. (2.14), for a number of high symmetry \vec{k} points.

2.1.2 Procedure for obtaining the energy dispersion

In the tight binding method, the one-electron energy eigenvalues $E_i(\vec{k})$ are obtained by solving the secular equation Eq. (2.14). The eigenvalues $E_i(\vec{k})$ are a periodic function in the reciprocal lattice, which can be described within the first Brillouin zone. In a two or three dimensional solid, it is difficult to show the energy dispersion relations over the whole range of \vec{k} values, and thus we plot $E_i(\vec{k})$ along the high symmetry directions in the Brillouin zone. The actual procedure of the tight binding calculation is as follows:

1. Specify the unit cell and the unit vectors, \vec{a}_i . Specify the coordinates of the atoms in the unit cell and select n atomic orbitals which are considered in the calculation.
2. Specify the Brillouin zone and the reciprocal lattice vectors, \vec{b}_i . Select the high symmetry directions in the Brillouin zone, and \vec{k} points along the high symmetry axes.
3. For the selected \vec{k} points, calculate the transfer and the overlap matrix element, \mathcal{H}_{ij} and \mathcal{S}_{ij} .*
4. For the selected \vec{k} points, solve the secular equation, Eq. (2.14) and obtain the eigenvalues $E_i(\vec{k})$ ($i = 1, \dots, n$) and the coefficients $C_{ij}(\vec{k})$.

Tight-binding calculations are not self-consistent calculations in which the occupation of an electron in an energy band would be determined self-consistently. That is, for given electron occupation, the potential of the Hamiltonian is calculated, from which the updated electron occupation is determined using, for example, Mulliken's gross population analysis [47]. When the input and the output of occupation of the electron are equal to each other within the desired accuracy, the eigenvalues are said to have been obtained self-consistently.

*When only the transfer matrix is calculated and the overlap matrix is taken as the unit matrix, then the Slater-Koster extrapolation scheme results.

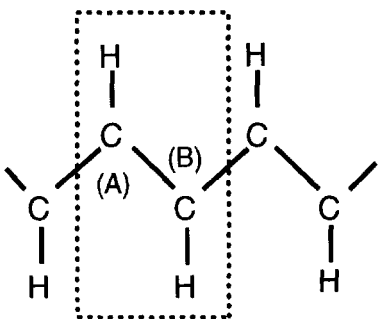


Fig. 2.1: The unit cell of *trans*-polyacetylene bounded by a box defined by the dotted lines, and showing two inequivalent carbon atoms, A and B, in the unit cell.

In applying these calculational approaches to real systems, the symmetry of the problem is considered in detail on the basis of a tight-binding approach and the transfer and the overlap matrix elements are often treated as parameters selected to reproduce the band structure of the solid obtained either experimentally or from first principles calculations. Both extrapolation methods such as $\vec{k} \cdot \vec{p}$ perturbation theory or interpolation methods using the Slater–Koster approach are commonly employed for carbon-related systems such as a 2D graphene sheet or 3D graphite [9].

2.2 Electronic Structure of Polyacetylene

A simple example of π -energy bands for a one-dimensional carbon chain is polyacetylene (see Sect. 1.2.2). In Fig. 2.1 we show, within the box defined by the dotted lines, the unit cell for *trans*-polyacetylene (CH_x), which contains two inequivalent carbon atoms, A and B, in the unit cell. As discussed in Sect. 1.2.2, there is one π -electron per carbon atom, thus giving rise to two π -energy bands called bonding and anti-bonding π -bands in the first Brillouin zone.

The lattice unit vector and the reciprocal lattice vector of this one-dimensional molecule are given by $\vec{a}_1 = (a, 0, 0)$ and $\vec{b}_1 = (a/2\pi, 0, 0)$, respectively. The Brillouin zone is the line segment $-a/\pi < k < a/\pi$. The Bloch orbitals consisting of A and B atoms are given by

$$\Phi_j(r) = \frac{1}{\sqrt{N}} \sum_{R_\alpha} e^{i\mathbf{k}R_\alpha} \varphi_j(r - R_\alpha), \quad (\alpha = \text{A}, \text{B}) \quad (2.15)$$

where the summation is taken over the atom site coordinate R_α for the A or B

carbon atoms in the solid.

The (2×2) matrix Hamiltonian, $\mathcal{H}_{\alpha\beta}$, ($\alpha, \beta = A, B$) is obtained by substituting Eq. (2.15) into Eq. (2.9). When $\alpha = \beta = A$,

$$\begin{aligned}\mathcal{H}_{AA}(r) &= \frac{1}{N} \sum_{R, R'} e^{ik(R-R')} \langle \varphi_A(r-R') | \mathcal{H} | \varphi_A(r-R) \rangle \\ &= \frac{1}{N} \sum_{R=R'} \epsilon_{2p} + \frac{1}{N} \sum_{R=R' \pm a} e^{\pm ika} \langle \varphi_A(r-R') | \mathcal{H} | \varphi_A(r-R) \rangle \\ &\quad + (\text{terms equal to or more distant than } R = R' \pm 2a) \\ &= \epsilon_{2p} + (\text{terms equal to or more distant than } R = R' \pm a).\end{aligned}\quad (2.16)$$

In Eq. (2.16) the maximum contribution to the matrix element \mathcal{H}_{AA} comes from $R = R'$, and this gives the orbital energy of the $2p$ level, ϵ_{2p} .* The next order contribution to \mathcal{H}_{AA} comes from terms in $R = R' \pm a$, which will be neglected for simplicity. Similarly, \mathcal{H}_{BB} also gives ϵ_{2p} for the same order of approximation.

Next let us consider the matrix element $\mathcal{H}_{AB}(r)$. The largest contribution to $\mathcal{H}_{AB}(r)$ arises when atoms A and B are nearest neighbors. Thus, in the summation over R' , we only consider the cases $R' = R \pm a/2$ and neglect more distant terms to obtain

$$\begin{aligned}\mathcal{H}_{AB}(r) &= \frac{1}{N} \sum_R \left\{ e^{ika/2} \langle \varphi_A(r-R) | \mathcal{H} | \varphi_B(r-R-a/2) \rangle \right. \\ &\quad \left. + e^{-ika/2} \langle \varphi_A(r-R) | \mathcal{H} | \varphi_B(r-R+a/2) \rangle \right\} \\ &= 2t \cos(ka/2)\end{aligned}\quad (2.17)$$

where the transfer integral t is the integral appearing in Eq. (2.17) and denoted by[†].

$$t = \langle \varphi_A(r-R) | \mathcal{H} | \varphi_B(r-R \pm a/2) \rangle. \quad (2.18)$$

It is stressed that t has a negative value. The matrix element $\mathcal{H}_{BA}(r)$ is obtained from $\mathcal{H}_{AB}(r)$ through the Hermitian conjugation relation $\mathcal{H}_{BA} = \mathcal{H}_{AB}^*$, but since \mathcal{H}_{AB} is real, we obtain $\mathcal{H}_{BA} = \mathcal{H}_{AB}$.

*Note that ϵ_{2p} is not simply the atomic energy value for the free atom, because the Hamiltonian contains a crystal potential.

[†]Here we have assumed that all the π bonding orbitals are equal (1.5 Å bonds). In the real $(\text{CH})_x$ compound, bond alternation occurs, in which the bond energy alternates between 1.7 Å and 1.3 Å bonds, and the two atomic integrations in Eq. (2.17) are not equal. Although the distortion of the lattice lowers the energy, the electronic energy always decreases more than the lattice energy in a one-dimensional material, and thus the lattice becomes deformed by a process called the Peierls instability. See details in Sect. 11.3.1

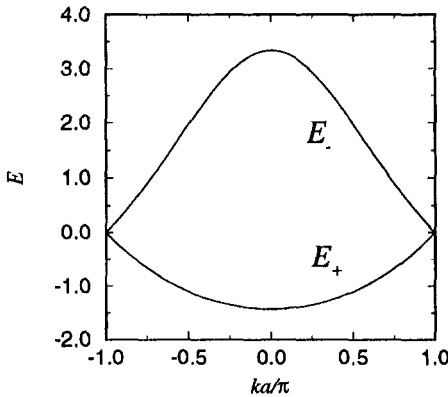


Fig. 2.2: The energy dispersion relation $E_{\pm}(\vec{k})$ for polyacetylene $[(CH)_x]$, given by Eq. (2.21) with values for the parameters $t = -1$ and $s = 0.2$. Curves $E_+(k)$ and $E_-(k)$ are called bonding π and antibonding π^* energy bands, respectively, and the plot is given in units of $|t|$.

The overlap matrix S_{ij} can be calculated by a similar method as used for H_{ij} , except that the intra-atomic integral yields the energy for the crystal Hamiltonian H_{ij} , but the overlap matrix rather yields unity for the case of S_{ij} , if we assume that the atomic wavefunction is normalized, $S_{AA} = S_{BB} = 1$ and $S_{AB} = S_{BA} = 2s \cos(ka/2)$, where s is the overlap integral between the nearest A and B atoms,

$$s = \langle \varphi_A(r - R) | \varphi_B(r - R \pm a/2) \rangle. \quad (2.19)$$

The secular equation for the $2p_z$ orbital of $[(CH)_x]$ is given by

$$\begin{aligned} & \left| \begin{array}{cc} \epsilon_{2p} - E & 2(t - sE) \cos(ka/2) \\ 2(t - sE) \cos(ka/2) & \epsilon_{2p} - E \end{array} \right| \\ &= (\epsilon_{2p} - E)^2 - 4(t - sE)^2 \cos^2(ka/2) \\ &= 0, \end{aligned} \quad (2.20)$$

yielding the eigenvalues of the energy dispersion relations of Eq. (2.20) given by

$$E_{\pm}(\vec{k}) = \frac{\epsilon_{2p} \pm 2t \cos(ka/2)}{1 \pm 2s \cos(ka/2)}, \quad \left(-\frac{\pi}{a} < k < \frac{\pi}{a} \right) \quad (2.21)$$

in which the + sign defines one branch and the - sign defines the other branch, as shown in Fig. 2.2, where we use values for the parameters, $\epsilon_{2p} = 0$, $t = -1$, and $s = 0.2$. The levels E_+ and E_- are degenerate at $ka = \pm\pi$.

$E_+(k)$ and $E_-(k)$ are called bonding π and antibonding π^* energy bands, respectively. Since there are two π electrons per unit cell, each with a different

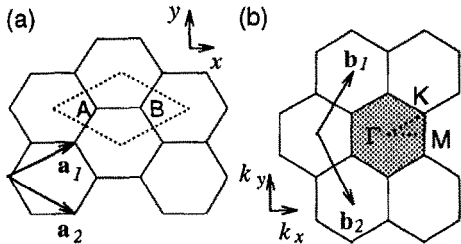


Fig. 2.3: (a) The unit cell and (b) Brillouin zone of two-dimensional graphite are shown as the dotted rhombus and the shaded hexagon, respectively. \vec{a}_i , and \vec{b}_i , ($i = 1, 2$) are unit vectors and reciprocal lattice vectors, respectively. Energy dispersion relations are obtained along the perimeter of the dotted triangle connecting the high symmetry points, Γ , K and M .

spin orientation, both electrons occupy the bonding π energy band, which makes the total energy lower than ϵ_{2p} .

2.3 Two-Dimensional Graphite

Graphite is a three-dimensional (3D) layered hexagonal lattice of carbon atoms. A single layer of graphite, forms a two-dimensional (2D) material, called 2D graphite or a graphene layer. Even in 3D graphite, the interaction between two adjacent layers is small compared with intra-layer interactions, since the layer-layer separation of 3.35\AA is much larger than nearest-neighbor distance between two carbon atoms, $a_{C-C}=1.42\text{\AA}$. Thus the electronic structure of 2D graphite is a first approximation of that for 3D graphite.

In Fig. 2.3 we show (a) the unit cell and (b) the Brillouin zone of two-dimensional graphite as a dotted rhombus and shaded hexagon, respectively, where \vec{a}_1 and \vec{a}_2 are unit vectors in real space, and \vec{b}_1 and \vec{b}_2 are reciprocal lattice vectors. In the x, y coordinates shown in the Fig. 2.3, the real space unit vectors \vec{a}_1 and \vec{a}_2 of the hexagonal lattice are expressed as

$$\vec{a}_1 = \left(\frac{\sqrt{3}}{2}a, \frac{a}{2} \right), \quad \vec{a}_2 = \left(\frac{\sqrt{3}}{2}a, -\frac{a}{2} \right), \quad (2.22)$$

where $a = |\vec{a}_1| = |\vec{a}_2| = 1.42 \times \sqrt{3} = 2.46\text{\AA}$ is the lattice constant of two-dimensional graphite. Correspondingly the unit vectors \vec{b}_1 and \vec{b}_2 of the recip-

reciprocal lattice are given by:

$$\vec{b}_1 = \left(\frac{2\pi}{\sqrt{3}a}, \frac{2\pi}{a} \right), \quad \vec{b}_2 = \left(\frac{2\pi}{\sqrt{3}a}, -\frac{2\pi}{a} \right) \quad (2.23)$$

corresponding to a lattice constant of $4\pi/\sqrt{3}a$ in reciprocal space. The direction of the unit vectors \vec{b}_1 and \vec{b}_2 of the reciprocal hexagonal lattice are rotated by 90° from the unit vectors \vec{a}_1 and \vec{a}_2 of the hexagonal lattice in real space, as shown in Fig. 2.3. By selecting the first Brillouin zone as the shaded hexagon shown in Fig. 2.3(b), the highest symmetry is obtained for the Brillouin zone of 2D graphite. Here we define the three high symmetry points, Γ , K and M as the center, the corner, and the center of the edge, respectively. The energy dispersion relations are calculated for the triangle ΓMK shown by the dotted lines in Fig. 2.3(b).

As discussed in Sect. 2.3.2, three σ bonds for 2D graphite hybridize in a sp^2 configuration, while, and the other $2p_z$ orbital, which is perpendicular to the graphene plane, makes π covalent bonds. In Sect. 2.3.1 we consider only π energy bands for 2D graphite, because we know that the π energy bands are covalent and are the most important for determining the solid state properties of graphite.

2.3.1 π Bands of Two-Dimensional Graphite

Two Bloch functions, constructed from atomic orbitals for the two inequivalent carbon atoms at A and B in Fig. 2.3, provide the basis functions for 2D graphite. When we consider only nearest-neighbor interactions, then there is only an integration over a single atom in \mathcal{H}_{AA} and \mathcal{H}_{BB} , as is shown in Eq. (2.16), and thus $\mathcal{H}_{AA} = \mathcal{H}_{BB} = \epsilon_{2p}$. For the off-diagonal matrix element \mathcal{H}_{AB} , we must consider the three nearest-neighbor B atoms relative to an A atom, which are denoted by the vectors \vec{R}_1 , \vec{R}_2 , and \vec{R}_3 . We then consider the contribution to Eq. (2.17) from \vec{R}_1 , \vec{R}_2 , and \vec{R}_3 as follows:

$$\begin{aligned} \mathcal{H}_{AB} &= t(e^{i\vec{k}\cdot\vec{R}_1} + e^{i\vec{k}\cdot\vec{R}_2} + e^{i\vec{k}\cdot\vec{R}_3}) \\ &= tf(k) \end{aligned} \quad (2.24)$$

where t is given by Eq. (2.18)* and $f(k)$ is a function of the sum of the phase factors of $e^{i\vec{k}\cdot\vec{R}_j}$ ($j = 1, \dots, 3$). Using the x, y coordinates of Fig. 2.3(a), $f(k)$ is given by:

$$f(k) = e^{ik_x a/\sqrt{3}} + 2e^{-ik_x a/2\sqrt{3}} \cos\left(\frac{k_y a}{2}\right). \quad (2.25)$$

Since $f(k)$ is a complex function, and the Hamiltonian forms a Hermitian matrix, we write $\mathcal{H}_{BA} = \mathcal{H}_{AB}^*$ in which * denotes the complex conjugate. Using Eq. (2.25), the overlap integral matrix is given by $\mathcal{S}_{AA} = \mathcal{S}_{BB} = 1$, and $\mathcal{S}_{AB} = sf(k) = \mathcal{S}_{BA}^*$. Here s has the same definition as in Eq. (2.19), so that the explicit forms for \mathcal{H} and \mathcal{S} can be written as:

$$\mathcal{H} = \begin{pmatrix} \epsilon_{2p} & tf(k) \\ tf(k)^* & \epsilon_{2p} \end{pmatrix}, \quad \mathcal{S} = \begin{pmatrix} 1 & sf(k) \\ sf(k)^* & 1 \end{pmatrix}. \quad (2.26)$$

Solving the secular equation $\det(\mathcal{H} - E\mathcal{S}) = 0$ and using \mathcal{H} and \mathcal{S} as given in Eq. (2.26), the eigenvalues $E(\vec{k})$ are obtained as a function $w(\vec{k})$, k_x and k_y :

$$E_{g2D}(\vec{k}) = \frac{\epsilon_{2p} \pm tw(\vec{k})}{1 \pm sw(\vec{k})}, \quad (2.27)$$

where the + signs in the numerator and denominator go together giving the bonding π energy band, and likewise for the - signs, which give the anti-bonding π^* band, while the function $w(\vec{k})$ is given by:

$$w(\vec{k}) = \sqrt{|f(\vec{k})|^2} = \sqrt{1 + 4 \cos \frac{\sqrt{3}k_x a}{2} \cos \frac{k_y a}{2} + 4 \cos^2 \frac{k_y a}{2}}. \quad (2.28)$$

In Fig. 2.4, the energy dispersion relations of two-dimensional graphite are shown throughout the Brillouin zone and the inset shows the energy dispersion relations along the high symmetry axes along the perimeter of the triangle shown in Fig. 2.3(b). Here we use the parameters $\epsilon_{2p} = 0$, $t = -3.033\text{eV}$, and $s = 0.129$ in order to reproduce the first principles calculation of the graphite energy bands [9, 48]. The upper half of the energy dispersion curves describes the π^* -energy anti-bonding band, and the lower half is the π -energy bonding band. The upper π^* band and the lower π band are degenerate at the K points through which

*We often use the symbol γ_0 for the nearest neighbor transfer integral. γ_0 is defined by a positive value.

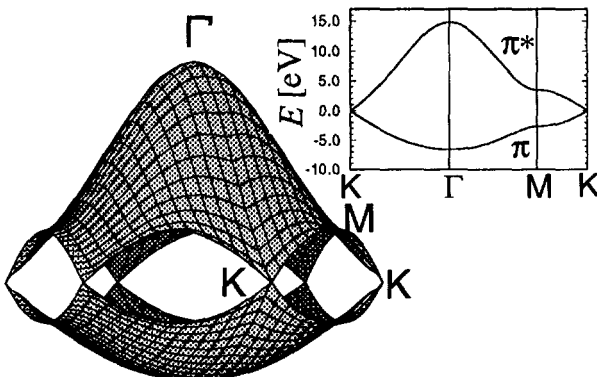


Fig. 2.4: The energy dispersion relations for 2D graphite are shown throughout the whole region of the Brillouin zone. The inset shows the energy dispersion along the high symmetry directions of the triangle ΓMK shown in Fig. 2.3(b) (see text).

the Fermi energy passes. Since there are two π electrons per unit cell, these two π electrons fully occupy the lower π band. Since a detailed calculation of the density of states shows that the density of states at the Fermi level is zero, two-dimensional graphite is a zero-gap semiconductor. The existence of a zero gap at the K points comes from the symmetry requirement that the two carbon sites A and B in the hexagonal lattice are equivalent to each other.[†] The existence of a zero gap at the K points gives rise to quantum effects in the electronic structure of carbon nanotubes, as shown in Chapter 3.

When the overlap integral s becomes zero, the π and π^* bands become symmetrical around $E = \epsilon_{2p}$, which can be understood from Eq. (2.27). The energy dispersion relations in the case of $s = 0$ (i.e., in the Slater–Koster scheme) are commonly used as a simple approximation for the electronic structure of a graphene layer:

$$E_{g2D}(k_x, k_y) = \pm t \left\{ 1 + 4 \cos\left(\frac{\sqrt{3}k_x a}{2}\right) \cos\left(\frac{k_y a}{2}\right) + 4 \cos^2\left(\frac{k_y a}{2}\right) \right\}^{1/2}. \quad (2.29)$$

[†]If the A and B sites had different atoms such as B and N, the site energy ϵ_{2p} would be different for B and N, and therefore the calculated energy dispersion would show an energy gap between the π and π^* bands.

In this case, the energies have the values of $\pm 3t$, $\pm t$ and 0, respectively, at the high symmetry points, Γ , M and K in the Brillouin zone. Thus the band width gives $|6t|$, which is consistent with the three connected π bonds. The simple approximation given by Eq. (2.29) is used in Sect. 4.1.2 to obtain a simple approximation for the electronic dispersion relations for carbon nanotubes.

2.3.2 σ Bands of Two-Dimensional Graphite

Finally let us consider the σ bands of two-dimensional graphite. There are three atomic orbitals of sp^2 covalent bonding per carbon atom, $2s$, $2p_x$ and $2p_y$. We thus have six Bloch orbitals in the 2 atom unit cell, yielding six σ bands. We will calculate these six σ bands using a 6×6 Hamiltonian and overlap matrix, and we will then solve the secular equation* for each \vec{k} point. For the eigenvalues thus obtained, three of the six σ bands are bonding σ bands which appear below the Fermi energy, and the other three σ bands are antibonding σ^* bands above the Fermi energy.

The calculation of the Hamiltonian and overlap matrix is performed analytically, using a small number of parameters. Hereafter we arrange the matrix elements in accordance with their atomic identity for the free atom: $2s^A$, $2p_x^A$, $2p_y^A$, $2s^B$, $2p_x^B$, $2p_y^B$. Then the matrix elements coupling the same atoms (for example A and A) can be expressed by a 3×3 small matrix which is a sub-block of the 6×6 matrix. Within the nearest neighbor site approximation given by Eq. (2.16), the small Hamiltonian and overlap matrices are diagonal matrices as follows,

$$\mathcal{H}_{AA} = \begin{pmatrix} \epsilon_{2s} & 0 & 0 \\ 0 & \epsilon_{2p} & 0 \\ 0 & 0 & \epsilon_{2p} \end{pmatrix}, \quad \mathcal{S}_{AA} = \begin{pmatrix} 1 & 0 & 0 \\ 0 & 1 & 0 \\ 0 & 0 & 1 \end{pmatrix}, \quad (2.30)$$

where ϵ_{2p} is defined by Eq. (2.16) and ϵ_{2s} is the orbital energy of the $2s$ levels.

The matrix element for the Bloch orbitals between the A and B atoms can be obtained by taking the components of $2p_x$ and $2p_y$ in the directions parallel or perpendicular to the σ bond. In Fig. 2.5, we show how to rotate the $2p_x$ atomic orbital and how to obtain the σ and π components for the rightmost

*Since the planar geometry of graphite satisfies the even symmetry of the Hamiltonian \mathcal{H} and of $2s$, $2p_x$ and $2p_y$ upon mirror reflection about the xy plane, and the odd symmetry of $2p_z$, the σ and π energy bands can be solved separately, because matrix elements of different symmetry types do not couple in the Hamiltonian.

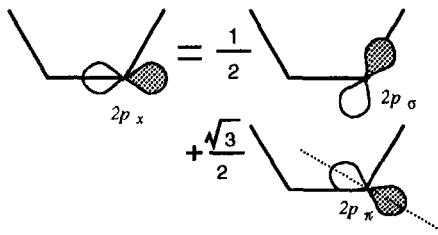


Fig. 2.5: The rotation of $2p_x$. The figure shows how to project the σ and π components along the indicated bond starting with the $2p_x$ orbital. This method is valid only for p orbitals.

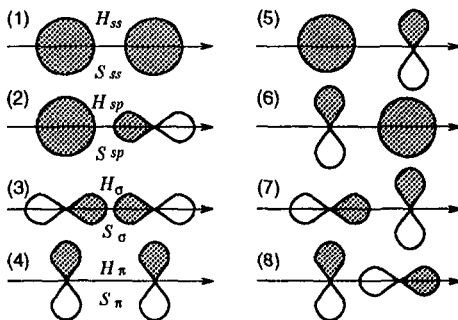


Fig. 2.6: The band parameters for σ bands. The four cases from (1) to (4) correspond to matrix elements having non-vanishing values and the remaining four cases from (5) to (8) correspond to vanishing matrix elements.

bond of this figure. In Fig. 2.5 the wavefunction of $|2p_x\rangle$ is decomposed into its σ and π components as follows:

$$|2p_x\rangle = \cos \frac{\pi}{3} |2p_\sigma\rangle + \sin \frac{\pi}{3} |2p_\pi\rangle. \quad (2.31)$$

This type of decomposition can be used to describe a bond in any general direction, which is discussed in Sect. 1.2. This procedure is also useful for fullerenes and carbon nanotubes, when we consider the curvature of their surfaces.

By rotating the $2p_x$ and $2p_y$ orbitals in the directions parallel and perpendicular to the desired bonds, the matrix elements appear in only 8 patterns as shown in Fig. 2.6, where shaded and not-shaded regions denote positive and negative amplitudes of the wavefunctions, respectively. The four cases from (1) to (4) in Fig. 2.6 correspond to non-vanishing matrix elements and the remaining four cases from (5) to (8) correspond to matrix elements which vanish because of symmetry. The corresponding parameters for both the Hamiltonian and the overlap matrix elements are shown in Fig. 2.6.

In Figs. 2.7(a) and (b) we show examples of the matrix elements of $\langle 2s^A | \mathcal{H} | 2p_x^B \rangle$ and $\langle 2p_x^A | \mathcal{H} | 2p_y^B \rangle$, respectively, obtained by the methods described above. In the case of Fig. 2.7 (a), there is only one non-vanishing contribution, and this

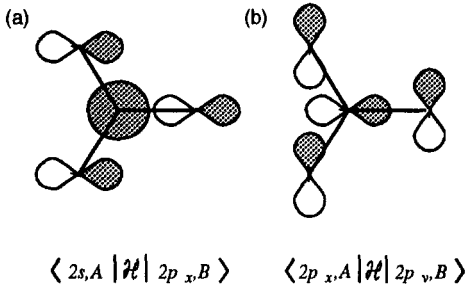


Fig. 2.7: Examples of the Hamiltonian matrix elements of σ orbitals, (a) $\langle 2s^A | \mathcal{H} | 2p_x^B \rangle$ and (b) $\langle 2p_x^A | \mathcal{H} | 2p_y^B \rangle$. By rotating the $2p$ orbitals, we get the matrix elements in Eq. (2.32) and Eq. (2.33), respectively.

comes from Fig. 2.6 (2). The other pertinent cases of Fig. 2.6 (5) or (6) give matrix elements that vanish by symmetry. Multiplying the phase factors for the three nearest neighbor B atoms with the matrix elements, we get the following result:

$$\langle 2s^A | \mathcal{H} | 2p_x^B \rangle = \mathcal{H}_{sp} \left(-e^{ik_x a / \sqrt{3}} + e^{-ik_x a / 2\sqrt{3}} \cos \frac{k_y a}{2} \right). \quad (2.32)$$

Similarly, in the case of Fig. 2.7 (b), the non-zero matrix elements correspond to the cases of Fig. 2.6 (3) and (4),

$$\begin{aligned} & \langle 2p_x^A | \mathcal{H} | 2p_y^B \rangle \\ &= \frac{\sqrt{3}}{4} (\mathcal{H}_\sigma + \mathcal{H}_\pi) e^{-ik_x a / 2\sqrt{3}} e^{ik_y a / 2} - \frac{\sqrt{3}}{4} (\mathcal{H}_\sigma + \mathcal{H}_\pi) e^{-ik_x a / 2\sqrt{3}} e^{-ik_y a / 2} \quad (2.33) \\ &= \frac{\sqrt{3}i}{2} (\mathcal{H}_\sigma + \mathcal{H}_\pi) e^{-ik_x a / 2\sqrt{3}} \sin \frac{k_y a}{2}. \end{aligned}$$

The resulting matrix element in Eq. (2.33) is a pure imaginary. However, the calculated results for the energy eigenvalues give real values.

When all the matrix elements of the 6×6 Hamiltonian and overlap matrices are calculated in a similar way, the 6×6 Hamiltonian matrix is obtained as a function of k_x and k_y . For given \vec{k} points we then calculate the energy dispersion of the σ bands from the secular equation of Eq. (2.14). The results thus obtained for the calculated σ and π energy bands are shown in Fig. 2.8. Here we have used the parameters listed in Table 2.1, yielding a fit of the functional form of the energy bands imposed by symmetry to the energy values obtained for the first principles band calculations at the high symmetry points [48].

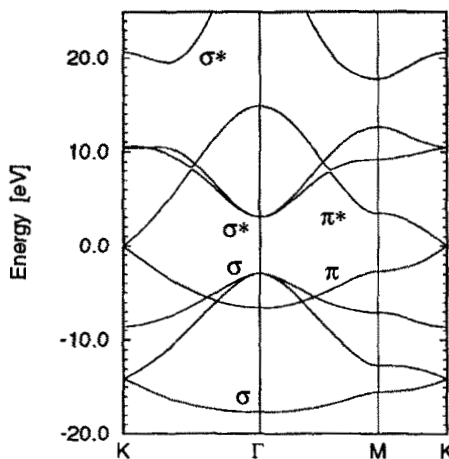


Fig. 2.8: The energy dispersion relations for σ and π bands of two-dimensional graphite. Here we used the parameters listed in Table 2.1.

Table 2.1: Values for the coupling parameters for carbon atoms in the Hamiltonian for π and σ bands in 2D graphite.

\mathcal{H}	value (eV)	\mathcal{S}	value
\mathcal{H}_{ss}	-6.769	\mathcal{S}_{ss}	0.212
\mathcal{H}_{sp}	-5.580	\mathcal{S}_{sp}	0.102
\mathcal{H}_σ	-5.037	\mathcal{S}_σ	0.146
$\mathcal{H}_\pi \equiv t$	-3.033	$\mathcal{S}_\pi \equiv s$	0.129
$\epsilon_{2s}^{(a)}$	-8.868		

(a) The value for ϵ_{2s} is given relative to setting $\epsilon_{2p} = 0$.

In the absence of more detailed experimental or theoretical information, these parameters can be used as a first approximation in describing the matrix elements for most sp^2 carbon materials for which the carbon-carbon distance is close to that of graphite, 1.42Å. Further, if the parameters are only slightly changed, the formulation can be used to describe the sp^3 diamond system and sp carbyne materials.

As is shown in Fig. 2.8, the π and the two σ bands cross each other (i.e., have different symmetries), as do the π^* and the two σ^* bands. However, because of the different group theoretical symmetries between σ and π bands, no band separation occurs at the crossing points. The relative positions of these crossings are known to be important for: (1) photo-transitions from σ to π^* bands and

from π to σ^* bands, which satisfy the selection rule for electric dipole transitions, and (2) charge transfer from alkali metal ions to graphene sheets in graphite intercalation compounds.

Using the basic concepts of two-dimensional graphite presented in Chapter 2, we next discuss the structure and electronic properties of single-wall carbon nanotubes in Chapters 3 and 4, respectively.

CHAPTER 3.

Structure of a Single-Wall Carbon Nanotube

A single-wall carbon nanotube can be described as a graphene sheet rolled into a cylindrical shape so that the structure is one-dimensional with axial symmetry, and in general exhibiting a spiral conformation, called *chirality*. The chirality, as defined in this chapter, is given by a single vector called the chiral vector. To specify the structure of carbon nanotubes, we define several important vectors, which are derived from the chiral vector.

3.1 Classification of carbon nanotubes

A single-wall nanotube is defined by a cylindrical graphene sheet with a diameter of about $0.7 - 10.0$ nm,* though most of the observed single-wall nanotubes have diameters < 2 nm. If we neglect the two ends of a carbon nanotube and focus on the large aspect ratio of the cylinder (i.e., length/diameter which can be as large as $10^4 - 10^5$), these nanotubes can be considered as one-dimensional nanostructures.

An interesting and essential fact about the structure of a carbon nanotube is the orientation of the six-membered carbon ring (hereafter called a hexagon) in the honeycomb lattice relative to the axis of the nanotube. Three examples of single-wall carbon nanotubes (SWCN's) are shown in Fig. 3.1. From this figure, it can be seen that the direction of the six-membered ring in the honeycomb lattice can be taken almost arbitrarily, without any distortion of the hexagons except for the distortion due to the curvature of the carbon nanotube. This fact provides many possible structures for carbon nanotubes, even though the basic

*Many carbon nanotubes that are observed experimentally are multi-wall structures which are discussed in Chapter 11. The synthesis of single-wall carbon nanotubes is discussed in Chapter 5.

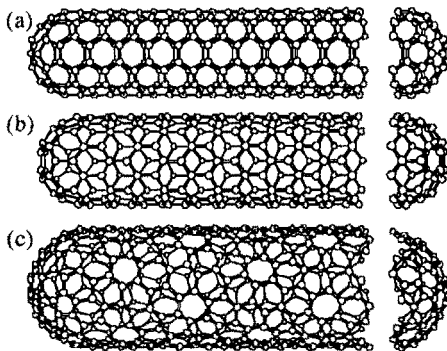


Fig. 3.1: Classification of carbon nanotubes: (a) armchair, (b) zigzag, and (c) chiral nanotubes. From the figure it can be seen that the orientation of the six-membered ring in the honeycomb lattice relative to the axis of the nanotube can be taken almost arbitrarily.

shape of the carbon nanotube wall is a cylinder.

In Fig. 3.1 we show the terminations of each of the three nanotubes. The terminations are often called caps or end caps and consist of a “hemisphere” of a fullerene. Each cap contains six pentagons and an appropriate number and placement of hexagons that are selected to fit perfectly to the long cylindrical section. In this chapter we focus on the periodic structure along the nanotube axis.

The primary symmetry classification of a carbon nanotube is as either being achiral (symmorphic) or chiral (non-symmorphic). An achiral carbon nanotube is defined by a carbon nanotube whose mirror image has an identical structure to the original one. There are only two cases of achiral nanotubes; armchair and zigzag nanotubes, as are shown in Fig. 3.1 (a) and (b), respectively. The names of armchair and zigzag arise from the shape of the cross-sectional ring, as is shown at the edge of the nanotubes in Fig. 3.1 (a) and (b), respectively. Chiral nanotubes exhibit a spiral symmetry whose mirror image cannot be superposed on to the original one. We call this tube a chiral nanotube, since such structures are called axially chiral in the chemical nomenclature. Axial chirality is commonly discussed in connection with optical activity. We have thus a variety of geometries in carbon nanotubes which can change diameter, chirality and cap structures. A classification of carbon nanotubes is given in Table 3.1 and is further discussed in Sect. 3.2 and Sect. 3.6.

Table 3.1: Classification of carbon nanotubes.

Type	$\theta^a)$	$C_h^b)$	Shape of cross section	Symmetry ^{c)}
armchair	30°	(n, n)	<i>cis</i> -type	
zigzag	0°	$(n, 0)$	<i>trans</i> -type	
chiral	$0^\circ < \theta < 30^\circ$	(n, m)	mixture of <i>cis</i> and <i>trans</i>	$C_d \otimes C_{N/d}$

^{a)} The chiral angle θ is defined by Eq. (3.4).

^{b)} The chiral vector is defined by Eq. (3.1), where n, m are integers $n \neq m$.

^{c)} The group theory of carbon nanotubes is discussed in Sect. 3.6.

3.2 Chiral Vector: C_h

The structure of a single-wall carbon nanotube is specified by the vector (\vec{OA} in Fig. 3.2) which corresponds to a section of the nanotube perpendicular to the nanotube axis (hereafter we call this section the equator of the nanotube). In Fig. 3.2, the unrolled honeycomb lattice of the nanotube is shown, in which \vec{OB} is the direction of the nanotube axis, and the direction of \vec{OA} corresponds to the equator. By considering the crystallographically equivalent sites O , A , B , and B' , and by rolling the honeycomb sheet so that points O and A coincide (and points B and B' coincide), a paper model of a carbon nanotube can be constructed.* The vectors \vec{OA} and \vec{OB} define the chiral vector C_h and the translational vector T of a carbon nanotube, respectively, as further explained below. The chiral vector C_h can be expressed by the real space unit vectors a_1 and a_2 (see Fig. 3.2) of the hexagonal lattice defined in Eq. (2.22):

$$C_h = n\mathbf{a}_1 + m\mathbf{a}_2 \equiv (n, m), \quad (n, m \text{ are integers}, 0 \leq |m| \leq n). \quad (3.1)$$

The specific chiral vectors C_h shown in Fig. 3.1 are, respectively, (a) $(5, 5)$, (b) $(9, 0)$ and (c) $(10, 5)$, and the chiral vector shown in Fig. 3.2 is $(4, 2)$. As is shown in Table 3.1, an armchair nanotube corresponds to the case of $n = m$, that is $C_h = (n, n)$, and a zigzag nanotube corresponds to the case of $m = 0$, or $C_h = (n, 0)$. All other (n, m) chiral vectors correspond to chiral nanotubes. Because of the hexagonal symmetry of the honeycomb lattice, we need to consider only $0 < |m| < n$ in $C_h = (n, m)$ for chiral nanotubes.

*The authors recommend that the readers copy Fig. 3.2 and then construct a paper model of a carbon nanotube. This construction exercise is very useful for understanding the nanotube structure.

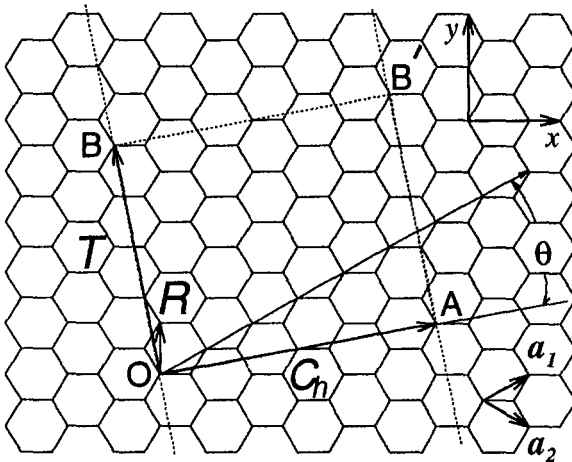


Fig. 3.2: The unrolled honeycomb lattice of a nanotube. When we connect sites O and A , and B and B' , a nanotube can be constructed. \vec{OA} and \vec{OB} define the chiral vector C_h and the translational vector T of the nanotube, respectively. The rectangle $OAB'B$ defines the unit cell for the nanotube. The vector R denotes a symmetry vector (see Sect. 3.4). The figure corresponds to $C_h = (4, 2)$, $d = d_R = 2$, $T = (4, -5)$, $N = 28$, $R = (1, -1)$.

The diameter of the carbon nanotube, d_t , is given by L/π , in which L is the circumferential length of the carbon nanotube:

$$d_t = L/\pi, \quad L = |C_h| = \sqrt{C_h \cdot C_h} = a\sqrt{n^2 + m^2 + nm}. \quad (3.2)$$

It is noted here that a_1 and a_2 are not orthogonal to each other and that the inner products between a_1 and a_2 yield:

$$a_1 \cdot a_1 = a_2 \cdot a_2 = a^2, \quad a_1 \cdot a_2 = \frac{a^2}{2}, \quad (3.3)$$

where the lattice constant $a = 1.44\text{\AA} \times \sqrt{3} = 2.49\text{\AA}$ of the honeycomb lattice is given in Eq. (2.22).[†] For example, the diameter of the armchair nanotube (5,5), whose end cap is a hemisphere of the fullerene C_{60} , is $d_t = 6.88\text{\AA}$.

[†]The C–C bond length of graphite is 1.42\AA . In the case of carbon nanotubes, the C–C bond length is known to be slightly larger than graphite: 1.44\AA .

The chiral angle θ (see Fig. 3.2) is defined as the angle between the vectors \mathbf{C}_h and \mathbf{a}_1 , with values of θ in the range $0 \leq |\theta| \leq 30^\circ$, because of the hexagonal symmetry of the honeycomb lattice. The chiral angle θ denotes the tilt angle of the hexagons with respect to the direction of the nanotube axis, and the angle θ specifies the spiral symmetry. The chiral angle θ is defined by taking the inner product of \mathbf{C}_h and \mathbf{a}_1 , to yield an expression for $\cos \theta$:

$$\cos \theta = \frac{\mathbf{C}_h \cdot \mathbf{a}_1}{|\mathbf{C}_h||\mathbf{a}_1|} = \frac{2n + m}{2\sqrt{n^2 + m^2 + nm}}, \quad (3.4)$$

thus relating θ to the integers (n, m) defined in Eq. (3.1). In particular, zigzag and armchair nanotubes correspond to $\theta = 0^\circ$ and $\theta = 30^\circ$, respectively.

3.3 Translational Vector: \mathbf{T}

The translation vector \mathbf{T} is defined to be the unit vector of a 1D carbon nanotube. The vector \mathbf{T} is parallel to the nanotube axis and is normal to the chiral vector \mathbf{C}_h in the unrolled honeycomb lattice in Fig. 3.2. The lattice vector \mathbf{T} shown as \overrightarrow{OB} in Fig. 3.2 can be expressed in terms of the basis vectors \mathbf{a}_1 and \mathbf{a}_2 as:

$$\mathbf{T} = t_1 \mathbf{a}_1 + t_2 \mathbf{a}_2 \equiv (t_1, t_2), \quad (\text{where } t_1, t_2 \text{ are integers}). \quad (3.5)$$

The translation vector \mathbf{T} corresponds to the first lattice point of the 2D graphene sheet through which the vector \overrightarrow{OB} (normal to the chiral vector \mathbf{C}_h) passes. From this fact, it is clear that t_1 and t_2 do not have a common divisor except for unity. Using $\mathbf{C}_h \cdot \mathbf{T} = 0$ and Eqs. (3.1), (3.3), and (3.5), we obtain expressions for t_1 and t_2 given by:

$$t_1 = \frac{2m + n}{d_R}, \quad t_2 = -\frac{2n + m}{d_R} \quad (3.6)$$

where d_R is the greatest common divisor (gcd) of $(2m + n)$ and $(2n + m)$. Also, by introducing d as the greatest common divisor of n and m , then d_R can be

related to d by*

$$d_R = \begin{cases} d & \text{if } n - m \text{ is not a multiple of } 3d \\ 3d & \text{if } n - m \text{ is a multiple of } 3d. \end{cases} \quad (3.7)$$

In the case of Fig. 3.2, where $C_h = (4, 2)$, we have $d = d_R = 2$, $\mathbf{T} = (4, -5)$. The length of the translation vector, T , is given by:

$$T = |\mathbf{T}| = \sqrt{3}L/d_R, \quad (3.8)$$

where the circumferential nanotube length L is given by Eq. (3.2). We note that the length T is greatly reduced when (n, m) have a common divisor or when $(n - m)$ is a multiple of $3d$. In fact, for the $C_h = (5, 5)$ armchair nanotube, we have $d_R = 3d = 15$, $\mathbf{T} = (1, -1)$ [Fig. 3.1(a)], while for the $C_h = (9, 0)$ zigzag nanotube we have $d_R = d = 9$, and $\mathbf{T} = (1, -2)$ [Fig. 3.1(b)].

The unit cell of the 1D carbon nanotube is the rectangle $OAB'B$ defined by the vectors C_h and \mathbf{T} (see Fig. 3.2), while the vectors a_1 and a_2 define the area of the unit cell of 2D graphite. When the area of the nanotube unit cell $|C_h \times \mathbf{T}|$ (where the symbol \times denotes the vector product operator) is divided by the area of a hexagon ($|a_1 \times a_2|$), the number of hexagons per unit cell N is obtained as a function of n and m in Eq. (3.1) as:[†]

$$N = \frac{|C_h \times \mathbf{T}|}{|a_1 \times a_2|} = \frac{2(m^2 + n^2 + nm)}{d_R} = \frac{2L^2}{a^2 d_R}, \quad (3.9)$$

where L and d_R are given by Eqs. (3.2) and (3.7), respectively, and we note that each hexagon contains two carbon atoms. Thus there are $2N$ carbon atoms (or $2p_z$ orbitals) in each unit cell of the carbon nanotube.

*This relation is obtained by repeated use of the fact that when two integers, α and β ($\alpha > \beta$), have a common divisor, γ , then γ is also the common divisor of $(\alpha - \beta)$ and β (Euclid's law). When we denote the greatest common divisor as $\gamma = gcd(\alpha, \beta)$, we get

$$d_R = gcd(2m + n, 2n + m) = gcd(2m + n, n - m) = gcd(3m, n - m) = gcd(3d, n - m),$$

which gives Eq. (3.7).

[†]For non-orthogonal unit vectors, the calculation using the vector product is easier than using the inner product, since the vector products of the unit vectors are:

$$\mathbf{a}_1 \times \mathbf{a}_1 = \mathbf{a}_2 \times \mathbf{a}_2 = \mathbf{0} \quad \text{and} \quad |\mathbf{a}_1 \times \mathbf{a}_2| = \sqrt{3}a^2/2$$

where $|\mathbf{a}_1 \times \mathbf{a}_2|$ corresponds to the area of the rhombus generated by \mathbf{a}_1 and \mathbf{a}_2 . The area of the rhombus is equal to that of the hexagon.

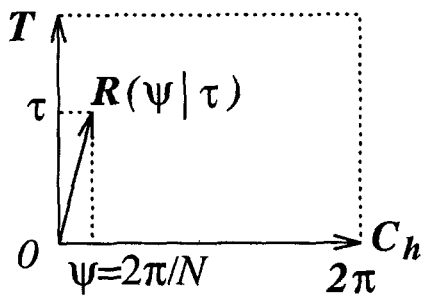


Fig. 3.3: Space group symmetry operation, $R = (\psi | \tau)$ in which ψ denotes the angle of rotation around the nanotube axis and τ is the translation in the direction of T as specified by the symmetry vector \mathbf{R} in Eq. (3.16). Note that $N\psi = 2\pi$ and $N\tau = MT$, which follow from Eqs. 3.16, 3.17, and 3.18.

3.4 Symmetry Vector: \mathbf{R}

We denote the carbon atom site vectors within the 1D nanotube unit cell by i times the vector \mathbf{R} , that is, $i\mathbf{R}$, where i is an integer ($i = 1 \dots N$). When $i\mathbf{R}$ goes out of the unit cell, we shift it to lie within the unit cell through translation by an integral number of C_h or T vectors, using periodic boundary conditions. The vector \mathbf{R} is used for generating the coordinates of carbon atoms in the nanotube. It is convenient to express the \mathbf{R} vector in terms of its projections on the orthogonal vectors C_h and T of the nanotube unit cell, as shown in Fig. 3.3. The symmetry vector \mathbf{R} is then defined as the site vector (shown by OR in Fig. 3.2) having the smallest component in the direction of C_h , and \mathbf{R} is expressed in terms of a_1 and a_2 as:

$$\mathbf{R} = p\mathbf{a}_1 + q\mathbf{a}_2 \equiv (p, q), \quad (p, q \text{ are integers}) \quad (3.10)$$

where p and q do not have a common divisor except for unity.* The C_h component of \mathbf{R} , or $C_h \cdot \mathbf{R}$, is proportional to the value of $T \times \mathbf{R}$ given by:[†]

$$T \times \mathbf{R} = (t_1 q - t_2 p) (\mathbf{a}_1 \times \mathbf{a}_2), \quad (3.11)$$

*If p and q were to have a common divisor, r , then, \mathbf{R}/r would have a smaller component in the direction of C_h than does \mathbf{R} .

[†]Hereafter we frequently use the relation between the inner product and vector product of a vector \mathbf{R} with the two orthogonal vectors C_h and T , to obtain:

$$\frac{C_h \cdot \mathbf{R}}{L} = \frac{|\mathbf{R} \times \mathbf{T}|}{T}, \quad \text{or} \quad \frac{\mathbf{T} \cdot \mathbf{R}}{T} = \frac{|\mathbf{C}_h \times \mathbf{R}|}{L},$$

where L and T are given by Eqs. (3.2) and (3.8), respectively. Here we assume that \mathbf{R} lies between C_h and T , as in Fig. 3.3.

where $(t_1q - t_2p)$ on the right hand side of Eq. 3.11 is an integer. We select p and q of \mathbf{R} to form the smallest site vector ($i = 1$), such that

$$t_1q - t_2p = 1, \quad (0 < mp - nq \leq N). \quad (3.12)$$

The solution of Eq. (3.12) for p and q is uniquely determined if t_1 and t_2 of Eq. (3.5) do not have a common divisor except for unity. The second condition in Eq. (3.12), $0 < mp - nq < N$, arises from the fact that \mathbf{R} exists within the 1D nanotube unit cell, so that

$$0 < \frac{\mathbf{R} \cdot \mathbf{T}}{T^2} = \frac{|\mathbf{C}_h \times \mathbf{R}|}{LT} = \frac{mp - nq}{N} < 1, \quad (3.13)$$

using Eqs. (3.2), (3.8), and (3.9). Similarly, using Eqs. (3.6) and (3.9), we obtain another necessary condition arising from \mathbf{R} being within the 1D unit cell:

$$0 < \frac{\mathbf{R} \cdot \mathbf{C}_h}{L^2} = \frac{|\mathbf{R} \times \mathbf{T}|}{LT} = \frac{t_1q - t_2p}{N} \leq 1, \quad (3.14)$$

and from Eq. (3.14), we get the condition,

$$0 < t_1q - t_2p \leq N. \quad (3.15)$$

Since the first condition of Eq. (3.12) satisfies Eq. (3.14), it is not necessary to add this condition to the definition of \mathbf{R} , as explained below.

To determine all N site location vectors $i\mathbf{R}$, ($i = 1 \dots N$) of the nanotube unit cell, we use the expression $i(t_1q - t_2p) = i$ for each i , and note that the maximum value of $i(t_1q - t_2p)$ becomes N . Using the fact[†] that the \mathbf{C}_h component of $N\mathbf{R}$ is always equal to $|\mathbf{C}_h| = L$, the vectors $i\mathbf{R}$ define N inequivalent sites in the nanotube unit cell, and will thus have different values for their projections along the direction of \mathbf{C}_h . Therefore $i\mathbf{R}$, ($i = 1 \dots N$), uniquely generates N different atom sites in the unit cell of the nanotube.[§]

[†]This fact can be shown as follows:

$$\frac{N\mathbf{R} \cdot \mathbf{C}_h}{L} = \frac{N|\mathbf{R} \times \mathbf{T}|}{T} = \frac{2L^2}{d_R a^2} \frac{\sqrt{3}a^2}{2} \frac{d_R}{\sqrt{3}L} = L,$$

where we made use of Eqs. (3.8) and (3.9).

[§]It is noted that the definition of \mathbf{R} is different from that by Jishi *et al.* [49]. The definition of \mathbf{R} given here is independent of whether or not $d = 1$. Further, Eq. (3.12) can be generalized to

$$t_1q - t_2p = Q, \quad (1 \leq Q \leq N)$$

where the integers Q and N do not have a common divisor except for unity. If Q and N would have a common divisor, d_Q , then $(N/d_Q)\mathbf{R}$ would become a site equivalent to O . The largest possible value of Q corresponds to the \mathbf{R} defined by Jishi *et al.* [49]. Here we use the notation for the symmetry vector \mathbf{R} defined in Eq. (3.12).

From a physical standpoint, the vector \mathbf{R} consists of a rotation around the nanotube axis by an angle ψ combined with a translation τ in the direction of \mathbf{T} , and reflects the basic space group symmetry operation of a chiral nanotube, denoted by $R = (\psi|\tau)$ and shown in Fig. 3.3. The physical significance of the vector \mathbf{R} is that the projection of \mathbf{R} on the chiral vector \mathbf{C}_h gives the angle ψ scaled by L/d_t [see Eq. (3.2)], while the projection of \mathbf{R} on \mathbf{T} gives the translation τ of the basic symmetry operation of the 1D space group of the carbon nanotube. The integers (p, q) denote the coordinates reached when the symmetry operation $(\psi|\tau)$ acts on an atom at $(0, 0)$, i.e., $(\psi|\tau)(0, 0) = (p, q)$. If $(\psi|\tau)$ is a symmetry operation for the nanotube, then $(\psi|\tau)^2, (\psi|\tau)^3, \dots, (\psi|\tau)^N$ are all distinct symmetry operations of an Abelian group denoted by C_N , where $(\psi|\tau)^N = E$ is the identity operation.

Taking the indicated vector products $\mathbf{R} \times \mathbf{C}_h$ and $\mathbf{R} \times \mathbf{T}$ and using Eqs. (3.2), (3.8), (3.9), and (3.12), we obtain the expressions for the length of τ and the rotation angle ψ , as follows:

$$\begin{aligned}\tau &= \frac{|\mathbf{R} \times \mathbf{C}_h|}{L} = \frac{(mp - nq)|\mathbf{a}_1 \times \mathbf{a}_2|}{L} = \frac{(mp - nq)T}{N} \\ \psi &= \frac{|\mathbf{T} \times \mathbf{R}|}{T} \frac{2\pi}{L} = \frac{d_R(t_1q - t_2p)}{\sqrt{3}L} \frac{\sqrt{3}a^2}{2} = \frac{2\pi}{N},\end{aligned}\tag{3.16}$$

and using these definitions, the rotation angle ψ becomes $2\pi/N$, where N is the number of hexagons in the 1D unit cell of the nanotube given by Eq. (3.9).

Referring to Fig. 3.3, the symmetry operator $(\psi|\tau)^N$ brings the lattice point O to an equivalent lattice point C as shown in Fig. 3.4, where

$$N\mathbf{R} = \mathbf{C}_h + M\mathbf{T},\tag{3.17}$$

and where

$$M \equiv mp - nq\tag{3.18}$$

is an integer which denotes the number of \mathbf{T} vectors that are necessary for reaching the distance from O to $N\mathbf{R}$.

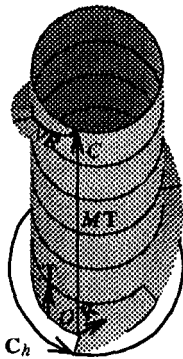


Fig. 3.4: The vector $NR = (\psi|\tau)^N$ is shown on the cylindrical surface. After rotating by 2π around the tube, the vector NR reaches a lattice point C equivalent to point O , but separated from O by the vector MT . In the figure we show the case $C_h = (4, 2)$ where $M = 6$.

Table 3.2: Values for characterization parameters^{a)} for selected carbon nanotubes labeled by the chiral vector $C_h = (n, m)$.

C_h	d	d_R	d_t (Å)	L/a	T	T/a	N	R	M
(4, 2)	2	2	4.15	$\sqrt{28}$	(4, -5)	$\sqrt{21}$	28	(1, -1)	6
(5, 5)	5	15	6.78	$\sqrt{75}$	(1, -1)	1	10	(1, 0)	5
(9, 0)	9	9	7.05	9	(1, -2)	$\sqrt{3}$	18	(1, -1)	9
(6, 5)	1	1	7.47	$\sqrt{91}$	(16, -17)	$\sqrt{273}$	182	(1, -1)	11
(7, 4)	1	3	7.55	$\sqrt{93}$	(5, -6)	$\sqrt{31}$	62	(1, -1)	11
(8, 3)	1	1	7.72	$\sqrt{97}$	(14, -19)	$\sqrt{291}$	194	(3, -4)	41
(10, 10)	10	30	13.56	$\sqrt{300}$	(1, -1)	1	20	(1, 0)	10
(n, n)	n	$3n$	$\sqrt{3na}/\pi$	$\sqrt{3}n$	(1, -1)	1	$2n$	(1, 0)	n
($n, 0$)	n	n	na/π	n	(1, -2)	$\sqrt{3}$	$2n$	(1, -1)	n

a) $C_h = (n, m)$ is given by Eq. (3.1). d is the greatest common divisor of n and m . d_t and $L = |C_h|$ are the diameter and equatorial length of a carbon nanotube, respectively, which are given by Eq. (3.2). The translational vector, $T = (t_1, t_2)$, is given by Eq. (3.5) whose length T is given by Eq. (3.8) in units of $a = \sqrt{3}a_{C-C}$ given by Eq. (2.22). N is the number of hexagons in the 1D unit cell of the carbon nanotube, which is given by Eq. (3.9). $R = (p, q)$ is the symmetry vector defined in Eq. (3.10). $M = mp - nq$ indicates how many T translations are necessary for going from O to NR in Fig. 3.4.

In Table 3.2 we list the characteristic parameters of carbon nanotubes specified by (n, m) , including d , the greatest common divisor of n and m , and the related quantity d_R which is given by Eq. (3.7). Also listed in Table 3.2 are the nanotube diameters d_t in units of Å, the lengths of the chiral vector L and of the translation repeat distance T of the 1D lattice (both in units of the lattice constant $a = \sqrt{3}a_{C-C}$ for a 2D graphene sheet), the number N of hexagons per unit cell of the 1D nanotube, the translation vector T , the symmetry vector R

and the integer M . The basic symmetry operation $R = (\psi|\tau)$ can be obtained from Table 3.2, Eq. (3.16) and values for $T = (t_1, t_2)$ and $R = (p, q)$.

To illustrate use of Table 3.2 we refer to the $C_h = (4, 2)$ nanotube shown in Fig. 3.2, which has $T = (4, -5)$, $\mathbf{R} = (1, -1)$, $N = 28$, $d = d_R = 2$, $T = \sqrt{21}a$, $L = \sqrt{28}a$, $\tau = 6T/28$ and $M = 6$ translations of the vector \mathbf{T} to reach the point C in Fig. 3.4. As a second example, we consider the case of the nanotube $C_h = (7, 4)$ which is a chiral nanotube for which $n - m = 3$ [49, 50]. For this nanotube, there are no common divisors, so $d = 1$, but since $n - m = 3$, we have $d_R = 3$. Thus we obtain $L = \sqrt{93}a$, $T = \sqrt{31}a$, $N = 62$, and $M = 11$ translations of the vector \mathbf{T} . For the armchair nanotube $(5, 5)$, which has half a C_{60} fullerene to form its end caps, the highest common divisor is 5, and since $n - m = 0$, we have $d_R = 3 \times 5 = 15$, yielding $N = 10$, $\psi = 2\pi/10$, $\tau = \mathbf{T}/2$, and $M = 5$. As a final example, we give the smallest observed zigzag nanotube $(9, 0)$ also having end caps consisting of C_{60} hemispheres, and for this nanotube, we have $d = d_R = 9$, $N = 18$, $\psi = 2\pi/18$, $\tau = \mathbf{T}/2$, and $M = 9$.

All parameters defined in this section are summarized in Table 3.3. The values of all the parameters listed here depend on the two integers, n and m , of the chiral vectors C_h . In Appendix we show programs which generate the parameters and the coordinates for given (n, m) values.

3.5 Unit Cells and Brillouin Zones

The unit cell for a carbon nanotube in real space is given by the rectangle generated by the chiral vector C_h and the translational vector \mathbf{T} , as is shown in $OAB'B$ in Fig. 3.2. Since there are $2N$ carbon atoms in this unit cell, we will have N pairs of bonding π and anti-bonding π^* electronic energy bands. Similarly the phonon dispersion relations will consist of $6N$ branches resulting from a vector displacement of each carbon atom in the unit cell.

Expressions for the reciprocal lattice vectors \mathbf{K}_2 along the nanotube axis and \mathbf{K}_1 in the circumferential direction* are obtained from the relation $\mathbf{R}_i \cdot \mathbf{K}_j = 2\pi\delta_{ij}$, where \mathbf{R}_i and \mathbf{K}_j are, respectively, the lattice vectors in real and reciprocal

*Since nanotubes are one-dimensional materials, only \mathbf{K}_2 is a reciprocal lattice vector. \mathbf{K}_1 gives discrete k values in the direction of C_h .

Table 3.3: Parameters for Carbon Nanotubes.^{a)}

symbol	name	formula	value
a	length of unit vector	$a = \sqrt{3}a_{\text{C-C}} = 2.49 \text{ \AA}$, $a_{\text{C-C}} = 1.44 \text{ \AA}$	
$\mathbf{a}_1, \mathbf{a}_2$	unit vectors	$\left(\frac{\sqrt{3}}{2}, \frac{1}{2}\right) a, \left(\frac{\sqrt{3}}{2}, -\frac{1}{2}\right) a$	x, y coordinate
$\mathbf{b}_1, \mathbf{b}_2$	reciprocal lattice vectors	$\left(\frac{1}{\sqrt{3}}, 1\right) \frac{2\pi}{a}, \left(\frac{1}{\sqrt{3}}, -1\right) \frac{2\pi}{a}$	x, y coordinate
\mathbf{C}_h	chiral vector	$\mathbf{C}_h = n\mathbf{a}_1 + m\mathbf{a}_2 \equiv (n, m)$, $(0 \leq m \leq n)$	
L	length of \mathbf{C}_h	$L = \mathbf{C}_h = a\sqrt{n^2 + m^2 + nm}$	
d_t	diameter	$d_t = L/\pi$	
θ	chiral angle	$\sin \theta = \frac{\sqrt{3}m}{2\sqrt{n^2 + m^2 + nm}}$ $\cos \theta = \frac{2n + m}{2\sqrt{n^2 + m^2 + nm}}$, $\tan \theta = \frac{\sqrt{3}m}{2n + m}$	$0 \leq \theta \leq \frac{\pi}{6}$
d	$\gcd(n, m)^b)$		
d_R	$\gcd(2n + m, 2m + n)^b)$	$d_R = \begin{cases} d & \text{if } (n - m) \text{ is multiple of } 3d \\ 3d & \text{if } (n - m) \text{ is not multiple of } 3d \end{cases}$	
\mathbf{T}	translational vector	$\mathbf{T} = t_1\mathbf{a}_1 + t_2\mathbf{a}_2 \equiv (t_1, t_2)$ $t_1 = \frac{2m + n}{d_R}, t_2 = -\frac{2n + m}{d_R}$	$\gcd(t_1, t_2) = 1^b)$
T	length of \mathbf{T}	$T = \mathbf{T} = \frac{\sqrt{3}L}{d_R}$	
N	Number of hexagons in the nanotube unit cell.	$N = \frac{2(n^2 + m^2 + nm)}{d_R}$	
\mathbf{R}	symmetry vector	$\mathbf{R} = p\mathbf{a}_1 + q\mathbf{a}_2 \equiv (p, q)$ $t_1q - t_2p = 1, (0 < mp - nq \leq N)$	$\gcd(p, q) = 1^b)$
τ	pitch of \mathbf{R}	$\tau = \frac{(mp - nq)T}{N} = \frac{MT}{N}$	
ψ	rotation angle of \mathbf{R}	$\psi = \frac{2\pi}{N}$	in radians
M	number of \mathbf{T} in $N\mathbf{R}$.	$N\mathbf{R} = \mathbf{C}_h + M\mathbf{T}$	

^{a)} In this table n, m, t_1, t_2, p, q are integers and d, d_R, N and M are integer functions of these integers.

^{b)} $\gcd(n, m)$ denotes the greatest common divisor of the two integers n and m .

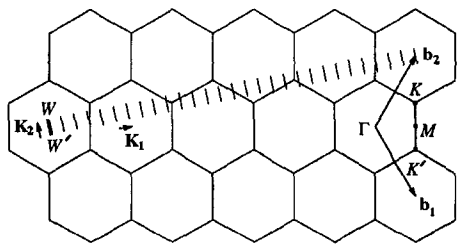


Fig. 3.5: The Brillouin zone of a carbon nanotube is represented by the line segment WW' which is parallel to \mathbf{K}_2 . The vectors \mathbf{K}_1 and \mathbf{K}_2 are reciprocal lattice vectors corresponding to \mathbf{C}_h and \mathbf{T} , respectively. The figure corresponds to $\mathbf{C}_h = (4, 2)$, $\mathbf{T} = (4, -5)$, $N = 28$, $\mathbf{K}_1 = (5\mathbf{b}_1 + 4\mathbf{b}_2)/28$, $\mathbf{K}_2 = (4\mathbf{b}_1 - 2\mathbf{b}_2)/28$.

space. Then, using Eqs. (3.6), (3.9), and the relations

$$\begin{aligned}\mathbf{C}_h \cdot \mathbf{K}_1 &= 2\pi, & \mathbf{T} \cdot \mathbf{K}_1 &= 0, \\ \mathbf{C}_h \cdot \mathbf{K}_2 &= 0, & \mathbf{T} \cdot \mathbf{K}_2 &= 2\pi,\end{aligned}\quad (3.19)$$

we get expressions for \mathbf{K}_1 and \mathbf{K}_2 :

$$\mathbf{K}_1 = \frac{1}{N}(-t_2\mathbf{b}_1 + t_1\mathbf{b}_2), \quad \mathbf{K}_2 = \frac{1}{N}(m\mathbf{b}_1 - n\mathbf{b}_2), \quad (3.20)$$

where \mathbf{b}_1 and \mathbf{b}_2 are the reciprocal lattice vectors of two-dimensional graphite given by Eq. (2.23). In Fig. 3.5, we show the reciprocal lattice vectors, \mathbf{K}_1 and \mathbf{K}_2 , for a $\mathbf{C}_h = (4, 2)$ chiral nanotube. The first Brillouin zone of this one-dimensional material is the line segment WW' . Since $N\mathbf{K}_1 = -t_2\mathbf{b}_1 + t_1\mathbf{b}_2$ corresponds to a reciprocal lattice vector of two-dimensional graphite, two wave vectors which differ by $N\mathbf{K}_1$ are equivalent. Since t_1 and t_2 do not have a common divisor except for unity (see Sect. 3.3), none of the $N - 1$ vectors $\mu\mathbf{K}_1$ (where $\mu = 1, \dots, N - 1$) are reciprocal lattice vectors of two-dimensional graphite. Thus the N wave vectors $\mu\mathbf{K}_1$ ($\mu = 0, \dots, N - 1$) give rise to N discrete k vectors, as indicated by the $N = 28$ parallel line segments in Fig. 3.5, which arise from the quantized wave vectors associated with the periodic boundary conditions on \mathbf{C}_h . The length of all the parallel lines in Fig. 3.5 is $2\pi/\mathbf{T}$ which is the length of the one-dimensional first Brillouin zone. For the N discrete values of the k vectors, N one-dimensional energy bands will appear (see Chapter 4). Because of the translational symmetry of \mathbf{T} , we have continuous wave vectors in the direction of \mathbf{K}_2 for a carbon nanotube of infinite length. However, for a nanotube of finite length L_t , the spacing between wave vectors is $2\pi/L_t$; this spacing between wave vectors has been observed experimentally [51].

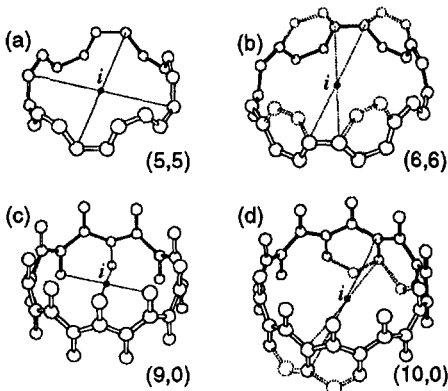


Fig. 3.6: Symmetry of armchair (a,b) and zigzag (c,d) nanotubes with odd (a,c) and even (b,d) numbers of unit cells around the circumferential direction: (a) (5,5) armchair, (b) (6,6) armchair (c) (9,0) zigzag and (d) (10,0) zigzag nanotubes. Here we show the inversion centers i . Dot circles show carbon atoms in part of the neighboring unit cell.

3.6 Group Theory of Carbon Nanotubes

Here we discuss of the symmetry of carbon nanotubes which are classified in Sect. 3.1. The symmetry of the carbon nanotubes is used in the interpretation of the Raman spectra in Chapter 10.* Here we only consider the point group of the unit cell and we do not discuss the space group of the lattice. Since many of the the physical properties of solids depend on the dispersion relations near $k = 0$, the symmetry of the unit cell gives sufficient information for the interpretation of many physical properties.

Hereafter we define the horizontal or vertical directions as those that are perpendicular or parallel to the nanotube axis, respectively. In the achiral nanotubes, armchair (n, n) and zigzag ($n, 0$) nanotubes (see Fig. 3.1 and Table 3.1) have (1) a vertical, n -fold rotational axis, C_n , and (2) n horizontal, 2-fold axes, nC_2 . Each horizontal C_2 axis intersects the center of a C–C bond or the center of a hexagon which are located at opposite sides of the nanotube from each other.[†] Thus the achiral nanotubes belong to the point group D_n . The D_n group has a different group structure, depending on whether n is even ($n = 2j$) or odd ($n = 2j + 1$), as can be seen in the character tables, shown in Tables 3.4 and 3.5, respectively. The horizontal nC_2 operations are either divided into the two

*The reader who is not familiar with group theory may skip this section, which is necessary, however, to understand the group theory for the Raman spectra observed in single-wall carbon nanotubes.

[†]Since we now have ‘up’ and ‘down’ directions in a nanotube, the center of the hexagon has only 2-fold symmetry.

classes for groups with $n = 2j$, or are in a single class in the case of $n = 2j + 1$. In the case of $n = 2j$, a C_2 operation in one class bisects the angle between two adjacent C_2 axes in the other class.

Table 3.4: Character Table for Group $D_{(2j)}$

\mathcal{R}	E	C_2	$2C_{\phi_j}^1$ ^{a)}	$2C_{\phi_j}^2$...	$2C_{\phi_j}^{j-1}$	jC_2^I	jC_2^{II}
A_1	1	1	1	1	...	1	1	1
A_2	1	1	1	1	...	1	-1	-1
B_1	1	-1	1	1	...	1	1	-1
B_2	1	-1	1	1	...	1	-1	1
E_1	2	-2	$2 \cos \phi_j$	$2 \cos 2\phi_j$...	$2 \cos(j-1)\phi_j$	0	0
E_2	2	2	$2 \cos 2\phi_j$	$2 \cos 4\phi_j$...	$2 \cos 2(j-1)\phi_j$	0	0
:	:	:	:	:	:	:	:	:
E_{j-1}	2	$(-1)^{j-1} 2$	$2 \cos(j-1)\phi_j$	$2 \cos 2(j-1)\phi_j$...	$2 \cos(j-1)^2 \phi_j$	0	0

a) Where $\phi_j = 2\pi/(2j)$.

Table 3.5: Character table for point group $D_{(2j+1)}$.

\mathcal{R}	E	$2C_{\phi_j}^1$ ^{a)}	$2C_{\phi_j}^2$...	$2C_{\phi_j}^j$	$(2j+1)C_2'$
A_1	1	1	1	...	1	1
A_2	1	1	1	...	1	-1
E_1	2	$2 \cos \phi_j$	$2 \cos 2\phi_j$...	$2 \cos j\phi_j$	0
E_2	2	$2 \cos 2\phi_j$	$2 \cos 4\phi_j$...	$2 \cos 2j\phi_j$	0
:	:	:	:	:	:	:
E_j	2	$2 \cos j\phi_j$	$2 \cos 2j\phi_j$...	$2 \cos j^2 \phi_j$	0

a) Where $\phi_j = 2\pi/(2j+1)$.

Further it is clear from Fig. 3.6 that for both zigzag and armchair nanotubes, there is an inversion center for both even and odd number n achiral nanotubes. In Fig. 3.6 (b) and (d) we show part of the nearest unit cell by dotted lines and circles. We can choose the unit cell so that the inversion operation transforms the carbon atoms in the unit cell to the other carbon atoms within the same unit cell.^t The total symmetry of an achiral nanotube is expressed by the direct product of the groups $D_n \otimes C_i$, where the group C_i consists of the identity and inversion operators, E and i . Group theory tells us that the direct product

^tIn the case of the (6,6) armchair nanotube, the corresponding unit cell is such that half of the carbon atoms lie on the boundary of the unit cell. For the boundary atoms, we consider the half balls for operations. In this case, a symmetry operation from an upper-half ball to a lower-half ball for the same atom is different from the identity operation.

$D_n \otimes C_i$ depends on whether n is an even or an odd number, as follows:

$$D_n \otimes C_i = \begin{cases} D_{nh} & \text{when } n = 2j \text{ (even)} \\ D_{nd} & \text{when } n = 2j + 1 \text{ (odd)} \end{cases}. \quad (3.21)$$

If n in D_n is even ($n = 2j$), there is a class of π ($C_{2m}^m = C_2$) rotations along the principal C_n axis. Since the product of the vertical C_{2m}^m rotation with the inversion operation gives a mirror operation on the ‘horizontal’ plane, which is perpendicular to the principal axis,

$$C_{2m}^m \times i = \sigma_h \quad (3.22)$$

we have an element of σ_h in the direct product of $D_n \otimes C_i$, which corresponds to D_{nh} . The product of a horizontal C_2 axis and the inversion center i gives a ‘vertical’ mirror plane $n\sigma_v$ which are the elements of D_{nh} . Here we take the horizontal C_2 axes to include the inversion center in the axes.

If n in D_n is odd ($n = 2j + 1$), there is no C_2 rotation along the principal C_n axis. Thus in the direct product of $D_{(2j+1)} \otimes C_i = D_{(2j+1)d}$, there is no σ_h operation but there is rather a ‘diagonal’ vertical mirror plane between two horizontal C_2 axes. The vertical mirror planes are given by the product of a horizontal C_2 rotation and the inversion center i . These symmetry issues are clarified in Fig. 3.6.

It is very confusing in the case of odd n numbers ($n = 2j + 1$) that we can visually see the mirror symmetry on a horizontal plane, through the horizontal C – C bonds of the armchair tubes or through the centers of the vertical C – C bonds of the zigzag tubes. However, there is no σ_h operation in the $D_{(2j+1)d}$ group. This might raise a question about whether there might be higher symmetry in achiral carbon nanotubes. The answer to this question is no, so far as we consider the symmetry of the unit cell, since the σ_h operation for ($n = 2j + 1$) is used only for the space group.[§]

Let us consider this question in the case of the armchair tube with $n = 5$, (5, 5). There is 20 atoms in the unit cell as shown in Fig. 3.6 (a). When

[§]The following is the reason why we need these statements in the text. All horizontal lines which intersect the nanotube axis and the center of C–C bond can be C_2 axes, thus giving rise to $2n$ C_2 axes in the unit cell for achiral (n, n) or ($n, 0$) nanotubes. We will select only n C_2 axes of the $2n$ C_2 axes which can be elements of the point group. The other n C_2 axes are operators for the space group of the lattice, because these other n C_2 axes require a translation along the nanotube axis.

we keep the chemical bonds between two carbon atoms rigid, we have only 20 inequivalent operations that do not change the unit cell. Ten of the 20 operations are operations which change the A atom to an equivalent A atom, and the other 10 are operations which change the A atom into a B atom. Here A and B atoms denote inequivalent carbon atoms of the hexagonal network as shown in Fig. 2.3. Furthermore, 5 of the 10 $A \rightarrow A$ operations are given by proper C_5 operations, and the other 5 require the inversion operation, which changes an A atom on one horizontal plane to an A atom on the other horizontal plane. When we consider the inversion center, as shown in Fig. 3.6 (a), the symmetry corresponds to the D_{5d} point group. In D_{5d} symmetry, we have 20 symmetry elements which are sufficient to describe 20 possible operations for the 20 atoms in the unit cell.

Table 3.6: Character table for D_{5d} ($\bar{5}m$).

D_{5d}	E	$2C_5$	$2C_5^2$	$5C'_2$	i	$2S_{10}^{-1}$	$2S_{10}$	$5\sigma_d$	($h = 20$)
A_{1g}	+1	+1	+1	+1	+1	+1	+1	+1	$(x^2 + y^2), z^2$
A_{2g}	+1	+1	+1	-1	+1	+1	+1	-1	R_z
E_{1g}	+2	$\tau - 1$	$-\tau$	0	+2	$\tau - 1$	$-\tau$	0	$z(x + iy, x - iy)$
E_{2g}	+2	$-\tau$	$\tau - 1$	0	+2	$-\tau$	$\tau - 1$	0	$[(x + iy)^2, (x - iy)^2]$
A_{1u}	+1	+1	+1	+1	-1	-1	-1	-1	
A_{2u}	+1	+1	+1	-1	-1	-1	-1	+1	z
E_{1u}	+2	$\tau - 1$	$-\tau$	0	-2	$1 - \tau$	$+\tau$	0	$(x + iy, x - iy)$
E_{2u}	+2	$-\tau$	$\tau - 1$	0	-2	$+\tau$	$1 - \tau$	0	

Note: $iC_5 = S_{10}^{-1}$ and $iC_5^2 = S_{10}$. Also $iC'_2 = \sigma_d$. $\alpha = 2\pi/5 = 72^\circ$, $\tau = (1 + \sqrt{5})/2$ so that $\tau = -2 \cos 2\alpha = -2 \cos 4\pi/5$ and $\tau - 1 = 2 \cos \alpha = 2 \cos 2\pi/5$.

Table 3.7: Character table for D_{5h} ($\bar{10}m2$).

D_{5h}	E	$2C_5$	$2C_5^2$	$5C'_2$	σ_h	$2S_5$	$2S_5^3$	$5\sigma_v$	($h = 20$)
A'_1	+1	+1	+1	+1	+1	+1	+1	+1	$x^2 + y^2, z^2$
A''_2	+1	+1	+1	-1	+1	+1	+1	-1	R_z
E'_1	+2	$\tau - 1$	$-\tau$	0	+2	$\tau - 1$	$-\tau$	0	$(x, y), (xz^2, yz^2)$
E''_2	+2	$-\tau$	$\tau - 1$	0	+2	$-\tau$	$\tau - 1$	0	$(x^2 - y^2, xy)$
A''_1	+1	+1	+1	+1	-1	-1	-1	-1	
A''_2	+1	+1	+1	-1	-1	-1	-1	+1	$z, z^3, z(x^2 + y^2)$
E''_1	+2	$\tau - 1$	$-\tau$	0	-2	$1 - \tau$	$+\tau$	0	$(R_x, R_y), (xz, yz)$
E''_2	+2	$-\tau$	$\tau - 1$	0	-2	$+\tau$	$1 - \tau$	0	$[xyz, z(x^2 - y^2)]$

Note that $\tau = (1 + \sqrt{5})/2$ so that $\tau = -2 \cos 2\alpha = -2 \cos 4\pi/5$ and $\tau - 1 = 2 \cos \alpha = 2 \cos 2\pi/5$.

Let us show that D_{5h} is not the proper point group symmetry of the $(5, 5)$ armchair nanotube. D_{5h} is given by direct product $D_5 \times C_h$, where C_h is the point group which has only the symmetry elements E and σ_h . In Tables 3.6

and 3.7, we show the character tables of D_{5d} and D_{5h} , both having the same structure, and thus both symmetries seem to be applicable. However, in the D_{5h} point group there is no operation which changes an A atom in one horizontal plane to an A atom in the other plane. Thus D_{5h} is not sufficient for describing the 20 distinct operations in the unit cell.

Achiral nanotubes are the only nanotube types that have the vertical (or horizontal) mirror operation. The chiral nanotube, which does not belong to either the armchair or zigzag nanotube categories, has no mirror plane. When n and m in a chiral vector (n, m) have no common divisor except for unity, $d = 1$, the lattice belongs to a non-symmorphic translational group which only has pure spiral symmetry operations, that are given by the symmetry vector \mathbf{R} and repeated operations of \mathbf{R} . As discussed in Sect. 3.4, we either go over all N A atoms or all N B atoms in the unit cell by operating with \mathbf{R}^i ($i = 1, \dots, N$) on a carbon atom. Thus the operations \mathbf{R}^i ($i = 1, \dots, N$) form an Abelian group. An Abelian group is a group in which all symmetry operations commute with each other.

Table 3.8: The character table for the Abelian group C_N for chiral nanotubes

C_N	E	C^1	C^2	...	C^ℓ	...	C^{N-1}
A	1	1	1	...	1	...	1
B	1	-1	1	...	$(-1)^\ell$...	-1
E_1	$\begin{cases} 1 \\ 1 \end{cases}$	$\begin{cases} \epsilon \\ \epsilon^* \end{cases}$	$\begin{cases} \epsilon^2 \\ \epsilon^{*2} \end{cases}$...	$\begin{cases} \epsilon^\ell \\ \epsilon^{*\ell} \end{cases}$...	$\begin{cases} \epsilon^{N-1} \\ \epsilon^{*(N-1)} \end{cases}$
E_2	$\begin{cases} 1 \\ 1 \end{cases}$	$\begin{cases} \epsilon^2 \\ \epsilon^{*2} \end{cases}$	$\begin{cases} \epsilon^4 \\ \epsilon^{*4} \end{cases}$...	$\begin{cases} \epsilon^{2\ell} \\ \epsilon^{*2\ell} \end{cases}$...	$\begin{cases} \epsilon^{2(N-1)} \\ \epsilon^{*2(N-1)} \end{cases}$
:	:	:	:	:	:	:	:
$E_{\frac{N}{2}-1}$	$\begin{cases} 1 \\ 1 \end{cases}$	$\begin{cases} \epsilon^{\frac{N}{2}-1} \\ \epsilon^{*\frac{N}{2}-1} \end{cases}$	$\begin{cases} \epsilon^{2(\frac{N}{2}-1)} \\ \epsilon^{*2(\frac{N}{2}-1)} \end{cases}$...	$\begin{cases} \epsilon^{\ell(\frac{N}{2}-1)} \\ \epsilon^{*\ell(\frac{N}{2}-1)} \end{cases}$...	$\begin{cases} \epsilon^{(N-1)(\frac{N}{2}-1)} \\ \epsilon^{*(N-1)(\frac{N}{2}-1)} \end{cases}$

^a The complex number ϵ is $e^{2\pi i/N}$.

When the common divisor of n and m , d is not unity, the nanotube is invariant under a pure rotation of C_d around the nanotube axis. In this case the symmetry group of such a chiral vector is the direct product of the two Abelian groups,

$$C_N = C_d \otimes C_{N/d} \quad (3.23)$$

where C_p ($p = N, d$, and N/d) denotes any one of the three Abelian groups in

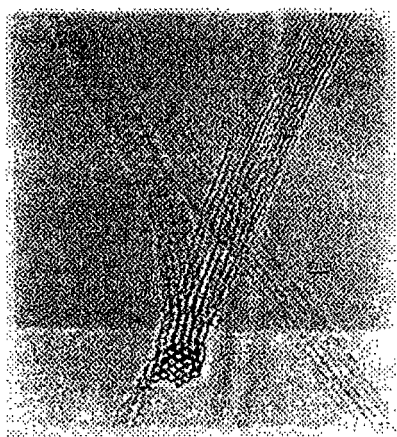


Fig. 3.7: High resolution TEM micrograph of the top view of one bundle of single-wall nanotubes from the collarette of the cathode of a carbon arc apparatus (see Sect. 5.3). The nanotube bundle is bent in such a way that it is seen edge-on in the image plane, showing single-wall carbon nanotubes in a triangular lattice, with a tube diameter of 1.4 nm and an average inter-tube distance of 1.7 nm. Each bundle in the micrograph consists of about 20 aligned single-wall nanotubes which are self-organized into a triangular lattice [52].

Eq. 3.23, each having p elements, $E, C, C^2, \dots, C^{p-1}$ and $C^p = E$. In Table 3.8 we show the character table for C_N for chiral nanotubes. All characters in this table are N th roots of unity. The irreducible representations are either two-dimensional E_n representations, whose characters for each operation are complex conjugates of each other, or one-dimensional A or B irreducible representations.

3.7 Experimental evidence for nanotube structure

The existence of single-wall carbon nanotubes has been confirmed experimentally through high resolution transmission electron microscopy (TEM) (see Fig. 3.7) and scanning tunneling microscopy (STM) (see Fig. 3.8). These techniques are especially useful for the structural characterization of the nanotubes. Because of the sensitivity of the electronic, vibrational, and other physical properties of carbon nanotubes to their geometrical structure, as described by the integers (n, m) or their characteristic parameters (d_t, θ) , the structural characterization of carbon nanotubes on which physical measurements are made is very important. Structural characterization measurements of d_t and θ are difficult to make because of the small physical size of the nanotubes, and the low atomic number Z of carbon which gives rise to low cross sections for x-rays and electrons, the two more commonly used conventional structural characterization probes.

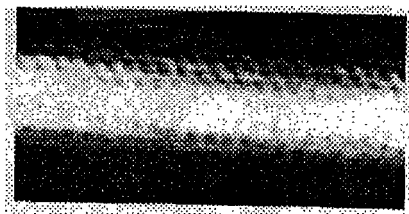


Fig. 3.8: Atomic resolution STM topographic image of a single-wall nanotube on an Au (111) substrate at 4.2 K. The dark spots indicate the hexagons which are spaced by 2.46 Å. The lattice sites show that this nanotube is not a zigzag nanotube, indicating that it could be either an armchair (chiral angle 30°) or a general chiral nanotube. Image size is $51 \times 26 \text{ \AA}^2$ [54].

In addition, there is considerable difficulty associated with the manipulation of individual single-wall nanotubes. Some progress has been made in developing sensitive tools for the structural characterization of nanotubes, particularly using the STM and TEM techniques, and progress has also been made with the manipulation of individual nanotubes [53].

The TEM micrograph of Fig. 3.7 shows the tendency for the single-wall nanotubes to grow in bundles containing 10–50 aligned nanotubes, held together by weak inter-tube interactions. The single-wall nanotubes shown in Fig. 3.7 were grown in an electric arc discharge apparatus using a 1 at% Y and 4.2 at% Ni catalyst contained in the anode, and the nanotubes were collected from a collarette located around the cathode electrode [52]. Since the bundles of nanotubes are frequently bent, so that some portions of the nanotubes are oriented parallel to the electron beam, the tube ends can be imaged in a transmission electron microscope, resulting in a cross-section-like view, showing individual single-wall nanotubes. The bundles typically are 5–20 nm in diameter and exhibit a triangular lattice with an inter-tube distance of ~ 1.7 nm [52, 55]. The periodic packing of these nanotubes is confirmed by electron diffraction patterns obtained from an assembly of such nanotube bundles. Similar arrays of nanotube bundles were first reported using the laser vaporization technique [55].

The very weak electron scattering from nm diameter carbon nanotubes (atomic number $Z = 6$) and their high susceptibility to damage by the 100–200 keV electron beam of the TEM instrument make it difficult to carry out electron diffraction studies. By taking precautions to use low electron beam currents, it has been possible to obtain good TEM measurements of lattice

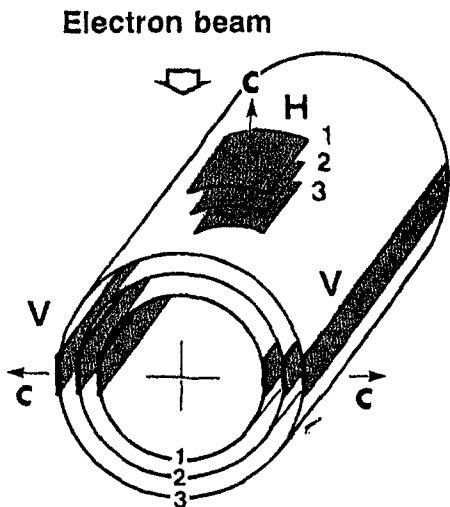


Fig. 3.9: This sketch indicates how the interference pattern for the electron beam that is incident radially on the planes with the *H* orientation is used to determine the chiral angle θ , which is the angle between the nanotube axis and the nearest zigzag axis. The interference pattern, obtained when the lattice planes are in the orientation *V* with respect to the electron beam and the nanotube shells, determines the inter-shell distances in the case of multi-wall carbon nanotubes [19].

fringe images and electron diffraction patterns on single-wall nanotubes [56] and multi-wall nanotubes [57]. However, TEM experiments on single-wall (and even double wall) nanotubes remain an experimental challenge. Nevertheless, TEM evidence has been presented to show that the walls of single-wall nanotubes have the local structure of a graphene sheet [58].

Referring to Fig. 3.9, we see, in principle, how the electron diffraction techniques can be used in the *H* geometry to measure the orientation (i.e., chiral angle of an individual nanotube) as is, for example, done with the LEED technique in surface science, while the *V* geometry can be used to determine the inter-tube spacing in the case of multi-wall nanotubes. Transmission electron microscopy has been widely used to characterize the many defect structures that have been observed in multi-wall nanotubes [57, 59–62]. Whereas nanotubes with diameters > 2 nm tend to show many structural defects, very small diameter nanotubes tend to be more perfect, with fewer structural defects.

The interpretation of TEM electron diffraction patterns on single-wall carbon nanotubes should be greatly aided by the use of computer simulations which give the diffraction pattern expected for an (n, m) nanotube [63]. These computer simulations are based on an analysis carried out by Cochran, Crick and Vand in 1952 [64] in connection with their elucidation of the structure of the

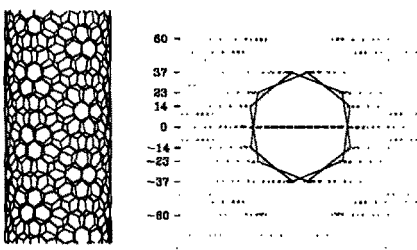


Fig. 3.10: Left: Atomic structure of the (17,3) carbon nanotube projected on a plane normal to the incident wave vector. Right: Corresponding electron-diffraction pattern in which the most intense features appear the darkest. The dimensions of the diffraction pattern scale linearly with $\sin\theta$, where 2θ is the scattering angle (see list of numbers) and $\theta = 0$ is at the center of the pattern. The vertical direction is parallel to the nanotube axis [63].

DNA molecule from X-ray diffraction experiments. By calculating the structure factor for all the atoms in the 1D unit cell of a general single-wall nanotube, the expected diffraction spots (and streaks) and their relative intensities are found [63], such as the diffraction pattern shown in Fig. 3.10 for a (17,3) single-wall carbon nanotube. At present, the experimentalist would have to compare the observed patterns to available simulations. At present, the computer simulation [63] is not yet able to carry out the inverse process of converting an observed diffraction pattern into a real space structure (n, m) for the atomic sites within the 1D unit cell.

Rather detailed information on the site location and the periodic arrangement of the carbon atoms within the nanotube is found from atomic resolution STM micrographs, and such experiments can be done successfully on single-wall nanotubes, especially at low temperature. An example of an STM topographic pattern of a single-wall carbon nanotube ~ 1 nm in diameter is shown in Fig. 3.8, which was made at 4.2 K [54]. Combined STM measurements to monitor d_t and θ and STS (scanning tunneling spectroscopy) to give the 1D density of states provides a powerful technique for studying the electronic structure of carbon nanotubes [65]. Measurements of the cross-sectional STM profile shows direct evidence for the curved surface of the nanotube [66].

The tube diameter is continuously measured by the STM technique in terms

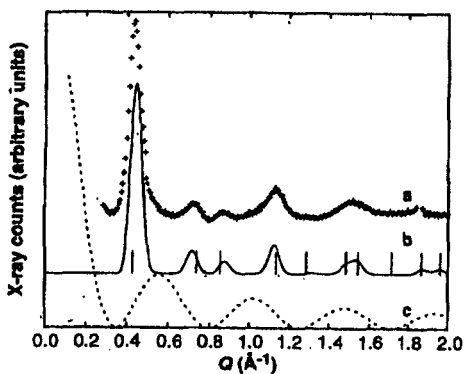


Fig. 3.11: XRD profile of SWNT material prepared by the laser vaporization method [55]. Data-fitted background (curve a) compared with a model profile (curve b) that assumes a 2D triangular lattice of uniformly charged cylinders, with a lattice constant of 16.95\AA , and a circle radius 6.9\AA . Vertical tick marks on curve b are the calculated Bragg positions. Curve c show analysis of the form factor used to obtain the lattice constant of the triangular lattice [55].

of the height difference between a substrate and the maximum height of the nanotube relative to the substrate, while the chiral angle determination can be made from the site positions of the carbon atoms relative to the nanotube axis (see Fig. 3.8). With the STM it is also been possible to measure the nearest neighbor carbon distance and to show that its value is essentially the same as that for graphite (1.42\AA) [66].

It is expected that improvements in the techniques for characterizing and manipulating carbon nanotubes will be forthcoming and that these techniques will enhance our general capabilities for the characterization of carbon nanotubes. It is further expected that carbon nanotubes will be widely used for the manipulation of nanostructures more generally because of their excellent mechanical properties (see Chapter 11).

The possibility of forming arrays of single-wall carbon nanotubes, weakly interacting through a van der Waals interaction, has been treated theoretically [67, 68]. These calculation considered the stabilization of a nanotube array of (6,6) nanotubes, and showed the most stable configuration to be that of a triangular lattice with the space group $P6/mcc$ where the nearest-neighbor carbon atoms on adjacent nanotubes are oriented in the ABAB stacking arrangement of 3D graphite [67, 68]. Recent experimental studies of the lattice structure of arrays of single-wall carbon nanotubes [55] using X-ray diffraction techniques

confirm that the 3D structure is that of a triangular lattice with a lattice constant of 17\AA for nanotubes of 1.38 ± 0.02 nm diameters and an inter-tube separation of 0.315 nm (see Fig. 3.11). Variation in the mean nanotube diameter and the diameter distribution can be achieved by using different catalysts and growth conditions (see Chapter 5). Many of the early quantitative experiments relevant to single-wall nanotubes have thus far been carried out on nanotube arrays that were prepared in the same way as the material yielding the diffraction pattern of Fig. 3.11.

CHAPTER 4.

Electronic Structure of Single-Wall Nanotubes

Using the definition of the structure of carbon nanotubes discussed in Chapter 3, the electronic structure of carbon nanotubes is derived by a simple tight-binding calculation for the π -electrons of carbon atoms. Of special interest is the prediction that the calculated electronic structure of a carbon nanotube can be either metallic or semiconducting, depending on its diameter and chirality. This one-dimensional metal is stable under the so-called Peierls instability. The energy gap for a semiconductor nanotube, which is inversely proportional to its diameters, is directly observed by scanning tunneling microscopy measurements.

4.1 One-electron dispersion relations

4.1.1 Zone-Folding of Energy Dispersion Relations

The electronic structure of a single-wall nanotube can be obtained simply from that of two-dimensional graphite. By using periodic boundary conditions in the circumferential direction denoted by the chiral vector \mathbf{C}_h , the wave vector associated with the \mathbf{C}_h direction becomes quantized, while the wave vector associated with the direction of the translational vector \mathbf{T} (or along the nanotube axis) remains continuous for a nanotube of infinite length.* Thus the energy bands consist of a set of one-dimensional energy dispersion relations which are cross sections of those for two-dimensional graphite (see Fig. 2.4).

When the energy dispersion relations of two-dimensional graphite, $E_{g2D}(\mathbf{k})$ [see Eqs. (2.27) and/or (2.29)] at line segments shifted from WW' by $\mu\mathbf{K}_1$ ($\mu =$

*For real carbon nanotubes, since the length of a nanotube (L_{CN}) is on the order of μm , discrete k vectors ($\Delta k = 2\pi/L_{CN}$) can be expected. In low temperature transport experiments [51], this discreteness becomes important. See further details in Sect. 8.2.

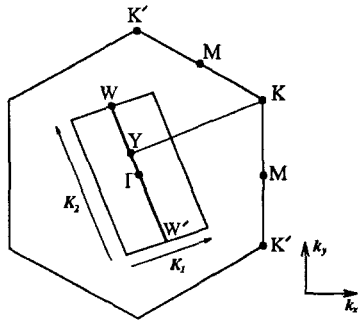


Fig. 4.1: The condition for metallic energy bands: if the ratio of the length of the vector \overrightarrow{YK} to that of \mathbf{K}_1 is an integer, metallic energy bands are obtained.

$0, \dots, N - 1$) are folded so that the wave vectors parallel to \mathbf{K}_2 coincide with WW' as shown in Fig. 3.5, N pairs of 1D energy dispersion relations $E_\mu(k)$ are obtained, where N is given by Eq. (3.9). These 1D energy dispersion relations are given by

$$E_\mu(k) = E_{g2D} \left(k \frac{\mathbf{K}_2}{|\mathbf{K}_2|} + \mu \mathbf{K}_1 \right), \quad (\mu = 0, \dots, N - 1, \text{ and } -\frac{\pi}{T} < k < \frac{\pi}{T}), \quad (4.1)$$

corresponding to the energy dispersion relations of a single-wall carbon nanotube. The N pairs of energy dispersion curves given by Eq. (4.1) correspond to the cross sections of the two-dimensional energy dispersion surface shown in Fig. 2.4, where cuts are made on the lines of $k\mathbf{K}_2/|\mathbf{K}_2| + \mu\mathbf{K}_1$. If for a particular (n, m) nanotube, the cutting line passes through a K point of the 2D Brillouin zone (Fig. 2.3), where the π and π^* energy bands of two-dimensional graphite are degenerate by symmetry, the one-dimensional energy bands have a zero energy gap. Further, as will be shown in Sect. 4.2, the density of states at the Fermi level has a finite value for these carbon nanotubes, and they therefore are metallic. If, however, the cutting line does not pass through a K point, then the carbon nanotube is expected to show semiconducting behavior, with a finite energy gap between the valence and conduction bands.

The condition for obtaining a metallic energy band is that the ratio of the length of the vector \overrightarrow{YK} to that of \mathbf{K}_1 in Fig. 4.1 is an integer.[†] Since the vector

[†]There are two inequivalent K and K' points in the Brillouin zone of graphite as is shown in Fig. 4.1 and thus the metallic condition can also be obtained in terms of K' . However, the results in that case are identical to the case specified by YK .

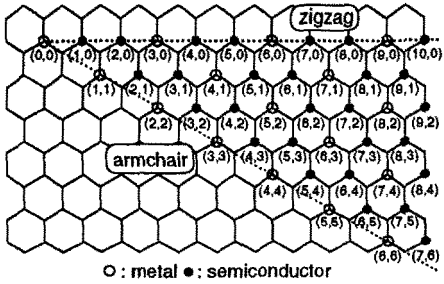


Fig. 4.2: The carbon nanotubes (n, m) that are metallic and semiconducting, respectively, are denoted by open and solid circles on the map of chiral vectors (n, m) .

\overrightarrow{YK} is given by

$$\overrightarrow{YK} = \frac{2n+m}{3} \mathbf{K}_1, \quad (4.2)$$

the condition for metallic nanotubes is that $(2n+m)$ or equivalently $(n-m)$ is a multiple of 3.^t In particular, the armchair nanotubes denoted by (n, n) are always metallic, and the zigzag nanotubes $(n, 0)$ are only metallic when n is a multiple of 3.

In Fig. 4.2, we show which carbon nanotubes are metallic and which are semiconducting, denoted by open and solid circles, respectively. From Fig. 4.2, it follows that approximately one third of the carbon nanotubes are metallic and the other two thirds are semiconducting.

4.1.2 Energy Dispersion of Armchair and Zigzag Nanotubes

To obtain explicit expressions for the dispersion relations, the simplest cases to consider are the nanotubes having the highest symmetry. Referring to Fig. 4.3, we see the unit cells and Brillouin zones for the highly symmetric (achiral) nanotubes, namely for (a) an armchair nanotube and (b) a zigzag nanotube.

The appropriate periodic boundary conditions used to obtain the energy eigenvalues for the (n, n) armchair nanotube define the small number of allowed wave vectors $k_{x,q}$ in the circumferential direction

$$n\sqrt{3}k_{x,q}a = 2\pi q, \quad (q = 1, \dots, 2n). \quad (4.3)$$

Substitution of the discrete allowed values for $k_{x,q}$ given by Eq. (4.3) into

^tSince $3n$ is a multiple of 3, the remainders of $(2n+m)/3$ and $(n-m)/3$ are identical.

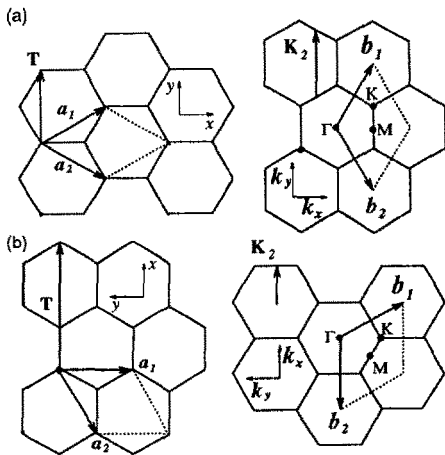


Fig. 4.3: Part of the unit cell and extended Brillouin zone of (a) armchair and (b) zigzag carbon nanotubes. \mathbf{a}_i and \mathbf{b}_i are unit vectors and reciprocal lattice vectors of two-dimensional graphite [see Eqs. (2.22) and (2.23) and Fig. 2.3], respectively. In the figure, the translational vector \mathbf{T} [Eq. (3.5)] and the corresponding reciprocal lattice vector \mathbf{K}_2 [Eq. (3.20)] of the nanotube are shown.

Eq. (2.29) yields the energy dispersion relations $E_q^a(k)$ for the armchair nanotube, $C_h = (n, n)$ [69],

$$E_q^a(k) = \pm t \left\{ 1 \pm 4 \cos\left(\frac{q\pi}{n}\right) \cos\left(\frac{ka}{2}\right) + 4 \cos^2\left(\frac{ka}{2}\right) \right\}^{1/2}, \quad (-\pi < ka < \pi), \quad (q = 1, \dots, 2n) \quad (4.4)$$

in which the superscript a refers to armchair and k is a one-dimensional vector in the direction of the vector $\mathbf{K}_2 = (\mathbf{b}_1 - \mathbf{b}_2)/2$. This direction corresponds to the Γ to K point vector in the two-dimensional Brillouin zone of graphite* (see the top of Fig. 4.3). The resulting calculated 1D dispersion relations $E_q^a(k)$ for the $(5, 5)$ armchair nanotube are shown in Fig. 4.4(a), where we see six dispersion relations for the conduction bands† and an equal number for the valence bands. In each case, two bands are nondegenerate labeled by “ a ” and the four labeled by “ e ” are doubly degenerate, leading to 10 levels in each case, consistent with the 10 hexagons around the circumference of the $(5, 5)$ nanotube. For all armchair nanotubes, the energy bands show a large degeneracy at the zone boundary, where $ka = \pi$, so that Eq. (2.29) becomes

$$E_{g_{2D}}(k_x, q, \pi/a) = \pm t \quad (4.5)$$

*Note that \mathbf{K}_2 vector is not a reciprocal lattice vector of 2D graphite.

†The Fermi energy corresponds to $E/t = 0$. The upper half of Fig. 4.4 corresponds to the unoccupied conduction bands.

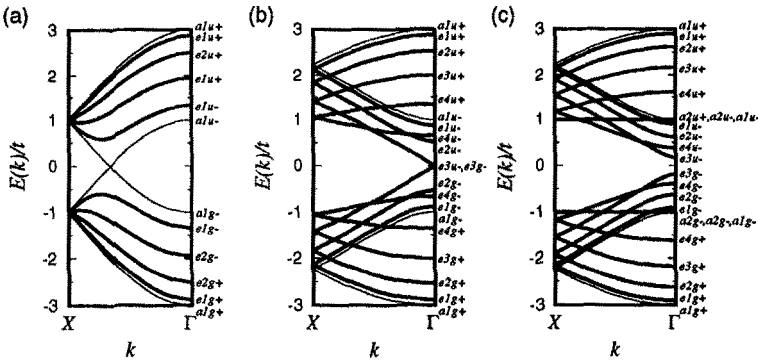


Fig. 4.4: One-dimensional energy dispersion relations for (a) armchair (5,5), (b) zigzag (9,0), and (c) zigzag (10,0) carbon nanotubes labeled by the irreducible representations of the point group D_{nd} or D_{nh} , depending on whether there are even or odd numbers of bands n at the Γ point ($k = 0$). The a -bands are nondegenerate and the e -bands are doubly degenerate at a general k -point [70]. X points for armchair and zigzag nanotubes correspond to $k = \pm\pi/a$ and $k = \pm\pi/\sqrt{3}a$, respectively. (See Eqs. (4.4) and (4.7).)

for the 2D graphene sheet, independent of zone folding and independent of n .[†] Although there are four carbon atoms in the unit cell of Fig. 4.3(a) for the real space lattice, the two carbon atoms on the same sublattice of a graphene sheet are symmetrically equivalent, which causes a degeneracy of the energy bands at the boundary of the Brillouin zone. The valence and conduction bands in Fig. 4.4(a) for the armchair nanotube cross at a k point that is two thirds of the distance from $k = 0$ to the zone boundary at $k = \pi/a$. The crossing takes place at the Fermi level and the energy bands are symmetric for $\pm k$ values.

Because of the degeneracy point between the valence and conduction bands

[†]The large degeneracy comes from the equi-energy lines of the energy bands of 2D graphite which connect the two nearest M points (See Fig. 2.4). When K_2 is perpendicular to the equi-energy line, a large degeneracy of Eq. (4.5) occurs. When K_2 is parallel to the equi-energy line, we have dispersionless energy bands with an energy of $\pm t$. The latter case corresponds to zigzag nanotubes ($n, 0$) with an even number of n .

at the band crossing, the (5, 5) armchair nanotube is thus a zero-gap semiconductor which will exhibit metallic conduction at finite temperatures, because only infinitesimal excitations are needed to excite carriers into the conduction band.

Similar calculations, as given by Eqs. (2.29), (4.3), and (4.4), show that all (n, n) armchair nanotubes yield $4n$ energy subbands analogous to Eq. (4.4) with $2n$ conduction and $2n$ valence bands, and of these $2n$ bands, two are nondegenerate and $(n - 1)$ are doubly degenerate. The symbols u and g in Fig. 4.4(a) indicate the even and odd behavior of these states regarding inversion symmetry, the \pm signs refer to the corresponding signs in Eq. (4.4) and the integers $(1, 2, \dots)$ are used to distinguish energy bands with the same symmetry from one another. All (n, n) armchair nanotubes have a band degeneracy between the highest valence band and the lowest conduction band at $k = \pm 2\pi/(3a)$, where the bands cross the Fermi level. Thus, all armchair nanotubes are expected to exhibit metallic conduction, similar to the behavior of 2D graphene sheets [69, 71–76].

The energy bands for the $C_h = (n, 0)$ zigzag nanotube $E_q^z(k)$ can be obtained likewise from Eq. (2.29) by writing the periodic boundary condition on k_y as:

$$nk_{y,q}a = 2\pi q, \quad (q = 1, \dots, 2n), \quad (4.6)$$

to yield the 1D dispersion relations for the $4n$ states for the $(n, 0)$ zigzag nanotube (denoted by the superscript z)

$$E_q^z(k) = \pm t \left\{ 1 \pm 4 \cos \left(\frac{\sqrt{3}ka}{2} \right) \cos \left(\frac{q\pi}{n} \right) + 4 \cos^2 \left(\frac{q\pi}{n} \right) \right\}^{1/2}, \quad (4.7)$$

$$\left(-\frac{\pi}{\sqrt{3}} < ka < \frac{\pi}{\sqrt{3}} \right), \quad (q = 1, \dots, 2n).$$

The resulting calculated 1D dispersion relations $E_q^z(k)$ for the $(9, 0)$ and $(10, 0)$ zigzag nanotubes are shown in Figs. 4.4(b) and (c), respectively. There is no energy gap for the $(9, 0)$ nanotube at $k = 0$, whereas the $(10, 0)$ nanotube indeed shows an energy gap. Especially in the case of the $(10, 0)$ nanotube, there is a dispersionless energy band at $E/t = \pm 1$, which gives a singular density of states at that energy. Dispersionless energy bands occur at $q/n = 1/2$ in Eq. (4.4), which gives $E(\pi/a) = \pm t$. For a general $(n, 0)$ zigzag nanotube, when n is a multiple of 3, the energy gap at $k = 0$ becomes zero; however, when n is not

a multiple of 3, an energy gap opens at $k = 0$. Further, when n is an even number, dispersionless energy bands appear, but not in the case when n is an odd number. As is pointed out in Sect. 3.6, different symmetries, D_{nd} and D_{nh} , occur for odd and even numbers of n , respectively.

4.1.3 Dispersion of chiral nanotubes

It should be noted that the k values for the band degeneracies for metallic nanotubes are $k = \pm 2\pi/3T$ or $k = 0$ for armchair or zigzag nanotubes, respectively, and that these k -values are also the locations of the band gaps for the semiconducting zigzag nanotubes. The same k values also denote the positions of the energy gaps (including zero energy gaps) for the general case of chiral tubes. In Figs. 4.5 and 4.6, we show dispersion relations for the (9, 6) and (7, 4) chiral nanotubes, respectively. Since $n - m$ is a multiple of 3 in the both cases, these two chiral nanotubes are metallic. Further, the k values at the Fermi level band crossings are at $k = 0$ and $\pm 2\pi/3T$ for Figs. 4.5 and 4.6, respectively. Since the highest degeneracy of irreducible representations of the group of the wave vector at $k = 0$ is two, the crossing of the four energy bands at $k = 0$ in the case of the (9,6) nanotube in Fig. 4.5 is an accidental degeneracy.

A more detailed analysis of the $E(k)$ relations for chiral nanotubes which is generally given by Eq. (4.1) shows that the nanotubes can be classified into three general categories [77, 78], depending on: (1) whether or not $n - m$ is a multiple of 3, and (2) whether or not $n - m$ is multiple of $3d$, whenever $n - m$ is a multiple of 3. Here d is the highest common divisor of n and m in $\mathbf{C}_h = (n, m)$. The three cases are summarized in Table 4.1. The classification in this table can be understood in terms of the length ΓY shown in Fig. 4.1, which is given by

$$\Gamma Y = \frac{m}{d_R} |\mathbf{K}_2|, \quad (4.8)$$

where $|\mathbf{K}_2|$ is along the nanotube axis, d_R is given by Eq. (3.7) and m is one of the integers of the chiral vector, $\mathbf{C}_h = (n, m)$. Since the metallic condition Eq. (4.2) is satisfied in these cases, the point K in Fig. 4.1 is folded into the Y point. Further when m/d_R is an integer, the Y point becomes the Γ point since the \mathbf{K}_2 vector becomes a reciprocal lattice vector in this case. The situation of metal-1 in Table 4.1 corresponds to this case, since $d_R = d$, and d is the highest common divisor of n and m . In this case, the band degeneracy at the Fermi level

Table 4.1: Classification of solid state properties of nanotubes, $\mathbf{C}_h = (n, m)$

Properties	$gcd(n - m, 3)^{(a)}$	$d_R^{(b)}$	Degeneracy ^(c)
Semiconductor	1	d	0 (Energy gap $\propto 1/d_t$).
Metal-1	3	d	4 at $k = 0$. ^(d)
Metal-2	3	$3d$	2 at $k = \pm 2\pi/3T$.

^(a) gcd denotes the greatest common divisor.

^(b) d_R is given by Eq. (3.7).

^(c) Degeneracy at the Fermi energy. When the spin of the electron is included, the effect of spin-orbit interaction in carbon [79, 80] must be considered for the case of orbitally degenerate bands.

^(d) Since group theory allows only one and two-dimensional irreducible representations, the four-fold degeneracy is accidental.

occurs at $k = 0$ and involves a 4-fold accidental band degeneracy, as discussed above. When $d_R = 3d$, then m/d_R is not an integer, but rather $m/d_R = \nu \pm 1/3$, (ν is an integer). This corresponds to the case of metal-2 and the degeneracy occurs at $k = \pm 2\pi/3T$. Since the inequivalent K and K' points are folded into different points in the Brillouin zone, the \pm signs occur in both cases for the dispersion relations near $k = \pm 2\pi/3T$. Metallic zigzag nanotubes, denoted by $(3q, 0)$, always fall into the category of metal-1. Armchair nanotubes (n, n) are in the category metal-2.

4.2 Density of States, Energy gap

For all metallic nanotubes, independent of their diameter and chirality, it follows that the density of states per unit length along the nanotube axis is a constant given by

$$N(E_F) = \frac{8}{\sqrt{3\pi a|t|}} \quad (4.9)$$

where a is the lattice constant of the graphene layer and $|t|$ is the nearest-neighbor C–C tight binding overlap energy usually denoted by γ_0 in the graphite literature [78].*

*While the value of γ_0 for 3D graphite is 3.13 eV, a value of $|t| = 2.5$ eV is obtained for this overlap energy in the 2D case when the asymmetry in the bonding and antibonding states is averaged out, and this 2D value has been found to yield good agreement with first principles calculations [81]. Experimentally the value $|t| = 2.7$ eV has been estimated by the Delft group

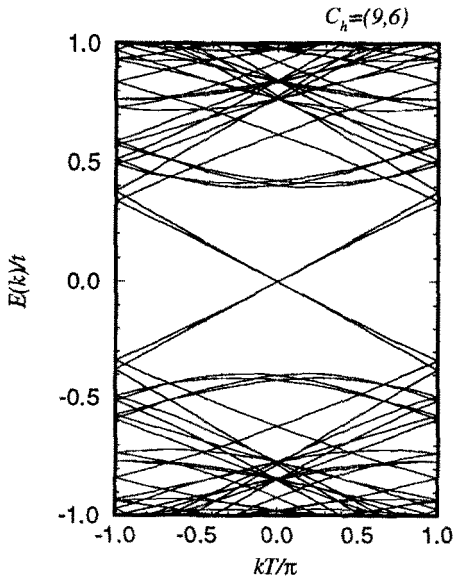


Fig. 4.5: Plot of the energy bands $E(k)$ for the metallic 1D nanotube $(n, m) = (9, 6)$ for values of the energy between $-t$ and t , in dimensionless units $E(k)/|t|$. The Fermi level is at $E = 0$. The largest common divisor of $(9, 6)$ is $d = 3$, and the value of d_R is $d_R = 3$. The general behavior of the four energy bands intersecting at $k = 0$ is typical of the case where $d_R = d$ (Metal 1) [77].

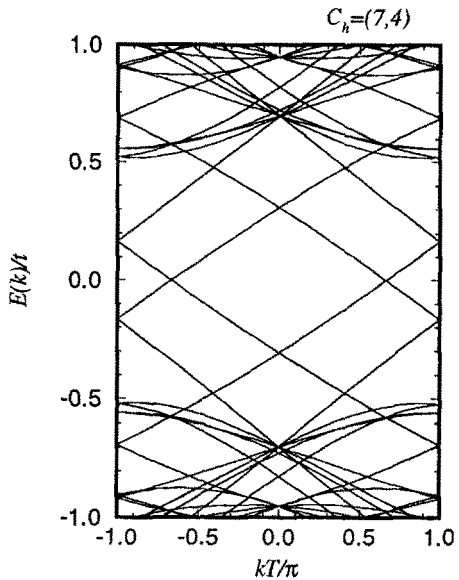


Fig. 4.6: Plot of the tight binding energy bands $E(k)$ for the metallic 1D chiral nanotube $(n, m) = (7, 4)$ for values of the energy between $-t$ and t in dimensionless units $E(k)/|t|$. The values of d and d_R are $d = 1$ and $d_R = 3$, respectively. The general behavior of the two band degeneracies at $k = \pm(2/3)(\pi/T)$ is typical of the case where $d_R = 3d$ (Metal 2)[77].

[82] in fitting STM density of states data. This STM value may be about the best experimental

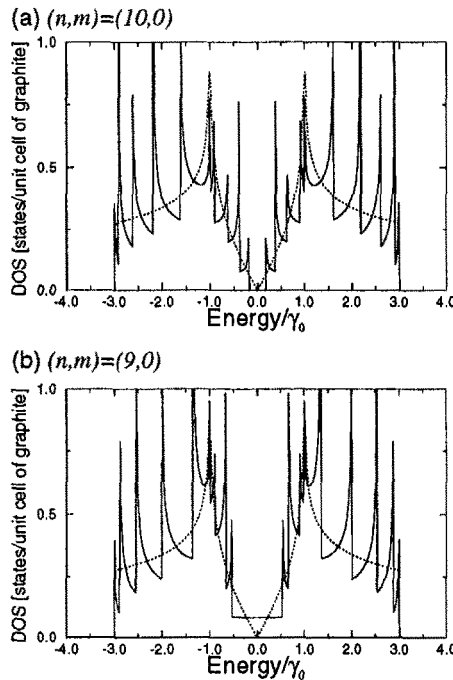


Fig. 4.7: Electronic 1D density of states per unit cell of a 2D graphene sheet for two $(n, 0)$ zigzag nanotubes: (a) the $(9, 0)$ nanotube which has metallic behavior, (b) the $(10, 0)$ nanotube which has semiconducting behavior. Also shown in the figure is the density of states for the 2D graphene sheet [76].

Of particular interest has been the energy dependence of the nanotube density of states, as shown in Fig. 4.7 which compares the density of states for metallic $(9,0)$ and semiconducting $(10,0)$ zigzag nanotubes. Of particular interest is the density of states near the Fermi level E_F located at $E = 0$. This density of states has a value of zero for semiconducting nanotubes, but is non-zero (and small) for metallic nanotubes. Of equal interest are the singularities in the 1D density of states corresponding to extrema in the $E(k)$ relations. The comparison between the 1D density of states for the nanotubes and the 2D density of states for a graphene layer is included in the figure. We also show in Fig. 4.8 the 1D density of states for a $(10,10)$ nanotube; these data have been extensively used for the analysis of various experimental data.

Another important result, pertaining to semiconducting nanotubes, shows

value we have for $|t|$ so far, which is within 15% of the 3D value.

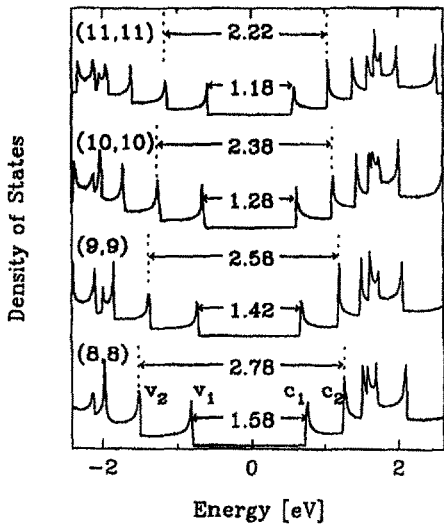


Fig. 4.8: Electronic density of states (DOS) calculated in a tight binding model for (8,8), (9,9), (10,10) and (11,11) armchair nanotubes. Wavevector conserving optical transitions can occur between mirror image spikes, i.e., $v_1 \rightarrow c_1$ and $v_2 \rightarrow c_2$ as indicated for the case of the (8,8) nanotube. The energies (in eV) for various optical transitions are indicated on the figure [83].

that their energy gap depends upon the reciprocal nanotube diameter d_t ,

$$E_g = \frac{|t|a_{C-C}}{d_t}, \quad (4.10)$$

independent of the chiral angle of the semiconducting nanotube, where $a_{C-C} = a/\sqrt{3}$ is the nearest-neighbor C-C distance on a graphene sheet. A plot of E_g vs. $1/d_t$ is shown in Fig. 4.9 for the graphite overlap integral taken as $|t| = 3.13$ eV. The results in Fig. 4.9 are important for testing the 1D model for the electronic structure of carbon nanotubes, because this result allows measurements to be made on individual semiconducting nanotubes, which are characterized only with regard to nanotube diameter without regard to their chiral angles. Using a value of $|t| = 2.5$ eV, as given by the local density functional calculation [81], Eq. (4.10) suggests that the band gap exceeds thermal energy at room temperature for nanotube diameters $d_t \leq 140$ Å. Furthermore, since about one third of the cylinders of a multi-wall nanotube are conducting, certain electronic properties, such as the electrical conductivity of nanotubes, will be dominated by the contributions from the conducting constituents, and the non-conducting constituents will play almost no role.

Density of states measurements by scanning tunneling spectroscopy (STS) provide a powerful tool for probing the electronic structure of carbon nanotubes

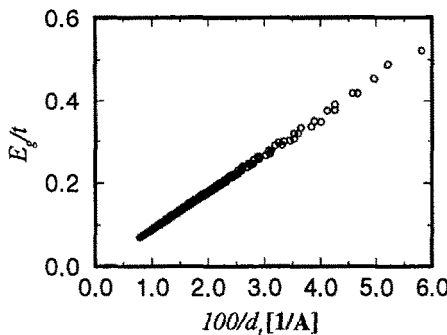


Fig. 4.9: The energy gap E_g scaled by $|t|$ for a semiconducting, chiral carbon nanotube as a function of $100 \text{ \AA}/d_t$, where d_t is the nanotube diameter in \AA and a value of $|t| = 2.5 \text{ eV}$ is taken for the transfer integral. It is noted that the relationship becomes linear for large values of d_t [77].

[65, 82]. Such measurements confirm that some nanotubes (about 1/3) are conducting, and some (about 2/3) are semiconducting (see Fig. 4.2). Measurements on semiconducting nanotubes confirm that the band gap is proportional to $1/d_t$ (see Fig. 4.9) [65, 82]. Resonances in the density of states (see Fig. 4.7) have been observed on metallic and semiconducting nanotubes whose diameters and chiral angles were determined by operating the instrument in the scanning tunneling microscopy (STM) mode [82]. The STS results confirm the theoretical model that the energy between the lowest-lying resonance in the conduction band and the highest-lying resonance in the valence band is smaller for semiconducting nanotubes and larger for metallic nanotubes, and that the density of states at the Fermi level is non-zero for metallic nanotubes, but zero for semiconducting nanotubes [82]. Thus the main 1D quantum features predicted theoretically for carbon nanotubes have now been observed experimentally.

4.3 Effects of Peierls distortion and nanotube curvature

Metallic 1D energy bands are generally unstable under a Peierls distortion. However, the Peierls energy gap obtained for the metallic nanotubes is found to be greatly suppressed by increasing the nanotube diameter, so that the Peierls gap quickly approaches the zero-energy gap of 2D graphite [69, 71]. Thus if we consider finite temperatures or fluctuation effects, it is believed that such a small Peierls gap can be neglected. Detailed discussion is presented in Sect.11.3.

As the nanotube diameter increases, more wave vectors become allowed for the circumferential direction, the nanotubes become more two-dimensional, and

as illustrated in Fig. 4.9, the semiconducting band gap decreases. From the figure we clearly see that the energy gap is inversely proportional to the diameter. The dependence of E_g on d_t^{-1} is obtained analytically from $k \cdot p$ theory near the K point [84].

The effect of curvature of the carbon nanotubes has been considered within the tight binding approximation [81]. The inclusion of curvature effects complicates the calculation considerably, by introducing four tight binding parameters, with values given by $V_{pp\pi} = -2.77$ eV, $V_{ss\sigma} = -4.76$ eV, $V_{sp\sigma} = 4.33$ eV, and $V_{pp\sigma} = 4.37$ eV [85, 86], instead of the single tight binding parameter $V_{pp\pi} = -2.5$ eV, which has been used to describe carbon nanotubes when their curvature is neglected. It should be mentioned that for both the armchair and zigzag nanotubes, the band crossings at E_F are between energy bands of different symmetry. (Even when nanotube curvature is considered the bands that cross will have different symmetries.) Thus no interaction or band splitting would be expected at E_F . Some first principles calculations for the electronic structure have been carried out for carbon nanotubes [72, 81, 87–89], yielding results in substantial agreement with the simple tight binding results which are described in this section.

Tight-binding calculations which consider $2s$ electrons [73] and other local density approximation (LDA) calculations [87, 90] show that the large curvature of small single-wall carbon nanotubes leads to a hybridization of σ^* and π^* orbitals, resulting in a small energy gap (on the order of meV) for nanotubes with small diameters, except for armchair nanotubes.* The effect of this hybridization is large for nanotubes of diameter less than that of C_{60} but is not so great for nanotubes in the range ($d_t > 0.7$ nm), the range that has been observed experimentally. The simple tight binding result for single-wall nanotubes which considers only π orbitals, that one third of the nanotubes are metallic and two thirds are semiconducting, has a symmetry basis which is discussed in

*When we see unfolded energy bands of carbon nanotubes in the two-dimensional Brillouin zone of graphite, the degenerate point at the K point moves away from the K point by taking account of the hybridization effect. However, the degeneracy of the conduction and valence bands is not affected by the hybridization. This degeneracy comes from the symmetry that A and B atoms are equivalent to each other in the unit cell of graphite. Thus, since the hybridization effect does not change the equivalence between the A and B atoms, this symmetry holds. In armchair nanotubes, since the shift of the k vector at the Fermi energy by the curvature effect is along the one-dimensional Brillouin zone, we get a metallic condition for armchair nanotubes even when curvature effects are taken into account.

Sect. 4.1.1. There are several physical processes that tend to modify these simple considerations. A first principles LDA calculation [90] has determined that for very small-diameter nanotubes the curvature of the graphene sheet results in band shifts which move their band edges into the semiconducting energy gap, hence suggesting that all very small-diameter nanotubes should be metallic. A contrary conclusion could be reached if a Peierls distortion of the 1D conductor produced an energy gap at the Fermi level.

LDA-based calculations have also been carried out for BN nanotubes, and the results suggest that BN nanotubes should be stable and should have a band gap of ~ 5.5 eV, independent of diameter [90, 91], and the band gap of crystalline BN is of about the same magnitude throughout the Brillouin zone. Thus no quantum effects as are observed in carbon nanotubes are expected for BN nanotubes. However, a relatively large energy gap is expected, compared with carbon nanotubes, so that BN nanotubes on either the inside or outside of carbon nanotubes can be used to provide insulation to carbon nanotubes. These calculations for the electronic structure of BN nanotubes stimulated experimental work, leading to the successful synthesis of pure BN multi-wall nanotubes [92], with inner diameters of 1–3 nm and lengths up to 200 nm. The BN nanotubes are produced in a carbon-free plasma discharge between a BN-packed tungsten rod and a cooled copper electrode. Electron energy loss spectroscopy studies on individual nanotubes confirmed the BN stoichiometry [92, 93].

CHAPTER 5. Synthesis of Carbon Nanotubes

This chapter describes synthesis methods for carbon nanotubes, with primary emphasis on single-wall nanotubes. Two relatively efficient methods to synthesize single-wall carbon nanotubes have been identified: laser vaporization and carbon arc synthesis, and both methods depend on the use of catalysts. Other techniques such as vapor growth are also reviewed. Also discussed in this chapter are the synthesis of multi-wall carbon nanotubes, the purification of carbon nanotubes, the insertion of metals into the hollow core of carbon nanotubes, and the doping of carbon nanotubes with alkali metals.

5.1 Single-Wall Nanotube Synthesis

The first experimental identification in 1991 of carbon nanotubes was on multi-wall nanotubes[19]. This report stimulated a large number of theoretical works on the structure and properties of the simpler and more fundamental single-wall carbon nanotubes, one atomic layer in thickness in the radial direction (see Fig. 3.1). The experimental discovery of single-wall carbon nanotubes in 1993[58, 94] further stimulated work in the field, though, at first, only small quantities of single-wall nanotubes were available experimentally for systematic studies. These single-wall nanotubes were generally found along with very much larger concentrations of amorphous carbon, carbon nanoparticles and other carbon-based materials, and the single-wall constituents contained a distribution of diameters and chiral angles, as explained below. For these reasons most of the experimental studies continued to be done on multi-wall nanotubes.

The recent discovery in 1996 of a much more efficient synthesis route, involving laser vaporization of graphite [55] to prepare arrays or “ropes” of ordered single-wall nanotubes, offered major new opportunities for quantitative experi-

mental studies of carbon nanotubes. By making the single-wall nanotubes available to many research groups worldwide, progress was made for the first time in quantitative measurements of the physical properties of single-wall carbon nanotubes.

The detailed mechanisms responsible for the growth of these nanotubes are not yet well understood. Therefore we can expect extensive research to be carried out on the growth mechanism and on the development of new growth techniques that provide more controlled growth of nanotubes. Whereas multi-wall nanotubes require no catalyst for their growth, catalyst species are necessary for the growth of the single-wall nanotubes, and more than one catalytic species seem to be necessary to grow ropes of single-wall nanotubes.

Soon after the publication of the laser vaporization method for the synthesis of single-wall carbon nanotube ropes, another synthesis route was found for the synthesis of gram quantities of single-wall carbon nanotubes, using the carbon arc method [52]. Because of the potential interest of carbon nanotubes for practical applications, there is also interest in developing continuous synthesis methods more appropriate for scale-up and low cost, and this may perhaps be accomplished by vapor growth methods discussed in Sect. 5.4. The remaining sections of the chapter briefly deal with the purification of nanotube samples (Sect. 5.5), nanotube opening, wetting, filling and alignment (Sect. 5.6), nanotube doping (Sect. 5.7), temperature regimes for carbonization and graphitization (Sect. 5.8), and growth mechanics (Sect. 5.9).

5.2 Laser Vaporization Synthesis Method

An efficient route for the synthesis of bundles of single-wall carbon nanotubes with a narrow diameter distribution employs the laser vaporization of a graphite target.

In the early reports of the laser synthesis technique [55], high yields with >70%–90% conversion of graphite to single-wall nanotubes were reported in the condensing vapor of the heated flow tube (operating at 1200°C). A Co–Ni/graphite composite laser vaporization target was used, consisting of 1.2 atom % Co–Ni alloy with equal amounts of Co and Ni added to the graphite (98.8 atom %) [55]. Two sequenced laser pulses were used to evaporate a target containing carbon mixed with a small amount of transition metal from the target (see

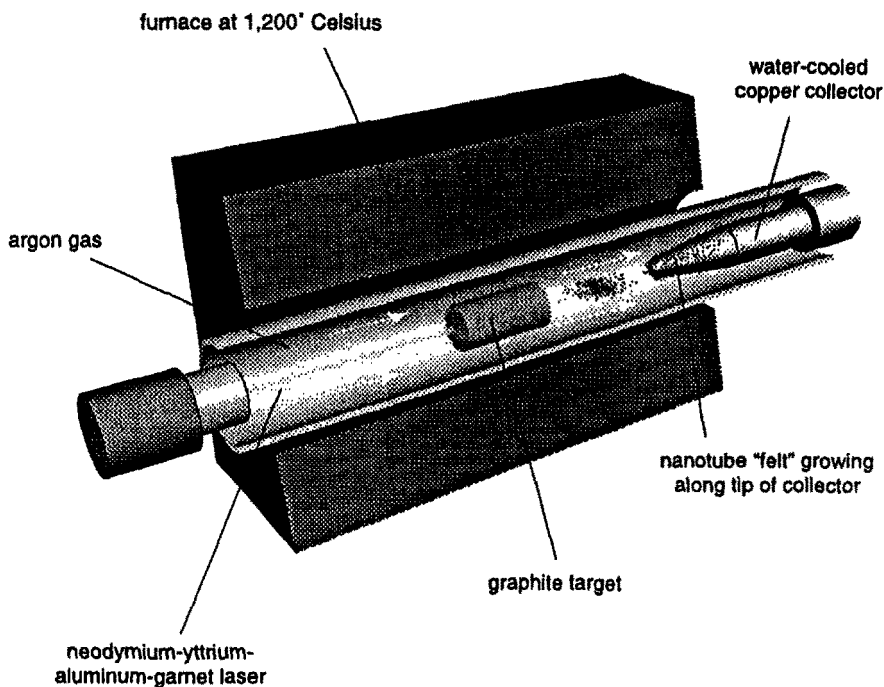


Fig. 5.1: Single-walled nanotubes produced in a quartz tube heated to 1200°C by the laser vaporization method, using a graphite target and a cooled collector for nanotubes [95].

Fig. 5.1). Flowing argon gas sweeps the entrained nanotubes from the high temperature zone to the water-cooled Cu collector downstream, just outside the furnace [55, 96].

The material thus produced appears in a scanning electron microscope (SEM) image as a mat of “ropes” 10–20 nm in diameter and up to 100 μm or more in length [see Fig. 5.2(a)]. Under transmission electron microscope (TEM) examination [see Fig. 5.2(b)], each rope is found to consist primarily of a bundle of single-wall carbon nanotubes aligned along a common axis. X-ray diffraction (which views many ropes at once) and transmission electron microscopy experiments (which view a single rope) show [55] that the diameters of the single-wall nanotubes have a strongly peaked distribution at 1.38 ± 0.02 nm, very close to

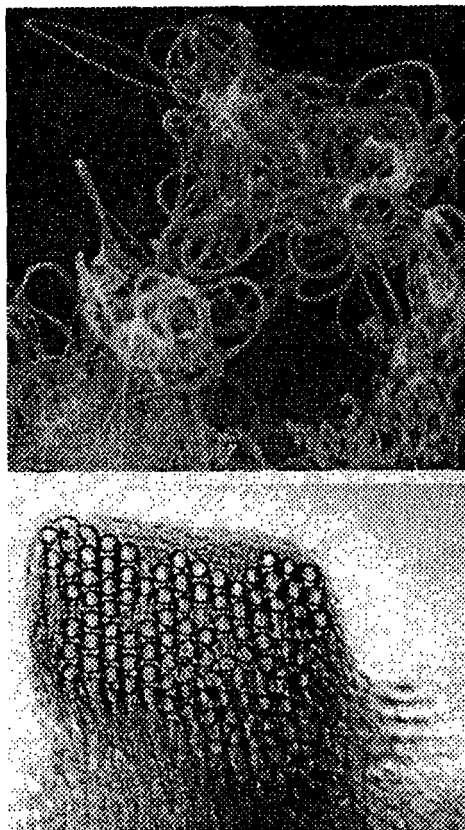


Fig. 5.2: (a) Ropes of single-wall carbon nanotubes observed by scanning electron microscopy (SEM). The ropes are 10–20 nm thick and ~100 μm long. (b) At higher magnification, the TEM image shows that each rope contains a bundle of single-wall nanotubes with diameters of ~1.4 nm, arranged in a triangular lattice (with lattice constant 1.7 nm). Such an image is seen when the rope bends through the image plane of the microscope [55].

the diameter of an ideal (10,10) nanotube which is defined in Eq. 3.2. A detailed transmission electron microscopy study of carbon nanotubes prepared by the laser vaporization method [55] has shown that the carbon nanotube chiral indices (n, m) are mainly (10,10) (~44%), (9,9) (~20%), and some (12,8) [97], while others, presumably using different growth conditions, have reported chiral angles in the range $\Delta\theta = 7.3^\circ$ [56, 98]. Thus for nanotube diameters ranging from that for the (8,8) to (11,11) armchair nanotubes, there are only 17 possible nanotubes [97]. The single-wall nanotubes are held together by weak van der Waals inter-nanotube bonds to form a two-dimensional triangular lattice with a lattice constant of 1.7 nm, and an inter-tube separation of 0.315 nm at closest approach within a rope [55]. By varying the growth temperature, the catalyst

composition and other growth parameters, the average nanotube diameter and diameter distribution can be varied [99]. It is found that the spread in nanotube diameters within a single rope is smaller than between ropes grown at the same time and under the same nominal growth conditions.

5.3 Arc Method of Synthesizing Carbon Nanotubes

The carbon arc provides a simple and traditional tool for generating the high temperatures needed for the vaporization of carbon atoms into a plasma ($>3000^{\circ}\text{C}$) [100–102]. This technique has been used for the synthesis of single-wall and multi-wall carbon nanotubes, and ropes of single-wall nanotubes [52].

Typical conditions for operating a carbon arc for the synthesis of carbon nanotubes include the use of carbon rod electrodes of 5–20 mm diameter separated by \sim 1 mm with a voltage of 20–25 V across the electrodes and a dc electric current of 50–120 A flowing between the electrodes. The arc is typically operated in \sim 500 torr He with a flow rate of 5–15 ml/s for cooling purposes. As the carbon nanotubes form, the length of the positive electrode (anode) decreases (see Fig. 5.3).

Once the arc is in operation, a carbon deposit forms on the negative electrode. For the multi-wall carbon nanotube synthesis, no catalyst need be used and the nanotubes are found in bundles in the inner region of the cathode deposit where the temperature is a maximum (2500 – 3000°C). The nanotube bundles are roughly aligned in the direction of the electric current flow (see Fig. 5.3) [101, 104]. Surrounding the nanotubes is a hard grey shell consisting of nanoparticles, fullerenes and amorphous carbon [105–107].* Adequate cooling of the growth chamber is necessary to maximize the nanotube yield in the arc growth process. The growth of carbon nanotubes appears to be unfavorable under the conditions that are optimized to synthesize fullerene molecules.

Catalysts used to prepare isolated single-wall carbon nanotubes include transition metals such as Co, Ni, Fe and rare earths such as Y and Gd, while mixed catalysts such as Fe/Ni, Co/Ni and Co/Pt have been used to synthesize ropes of single-wall nanotubes. Although the details of the diameter (and chirality) distribution of the single-wall carbon nanotubes depend on the synthesis conditions,

*During arc synthesis fullerenes are predominantly found in the soot produced by the arc and removed by the helium gas flow, while the nanotubes are contained in a deposit on the cathode.

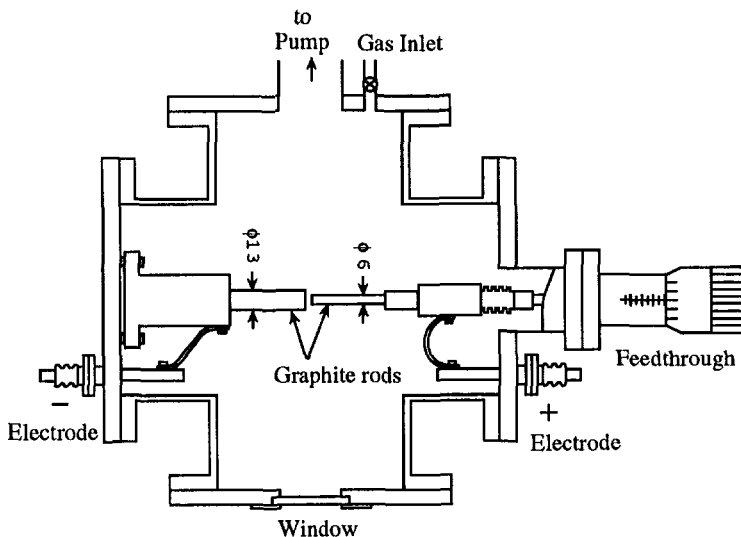


Fig. 5.3: Cross-sectional view of a carbon arc generator that can be used to synthesize carbon nanotubes [103].

temperature of the arc and the catalyst that is used, the average nanotube diameter is usually small (≤ 1.5 nm) and the diameter distribution is usually narrow, as illustrated in Fig. 5.4. It is interesting to note that the minimum nanotube diameter that has been observed for single-wall carbon nanotubes is ~ 0.7 nm, corresponding to the diameter of C_{60} , the smallest fullerene to obey the isolated pentagon rule [108].

An efficient method for the synthesis of gram quantities of bundles of single-wall carbon nanotubes using the carbon arc technique has been achieved [52]. The greatest mass of single-wall carbon nanotubes is found in a collarette around the cathode, with $\sim 20\%$ of the consumed carbon being converted into single-wall carbon nanotubes in the collarette.

Since the length of a carbon nanotube is typically on the order of $1 \mu\text{m}$, and the growth rate of a $1 \mu\text{m}$ carbon nanotube is estimated to be less than 0.1 second, the time for the growth of a single circumferential carbon ring is $\sim 10^{-5}$ second. This time scale is much shorter than the time needed for the direct obser-

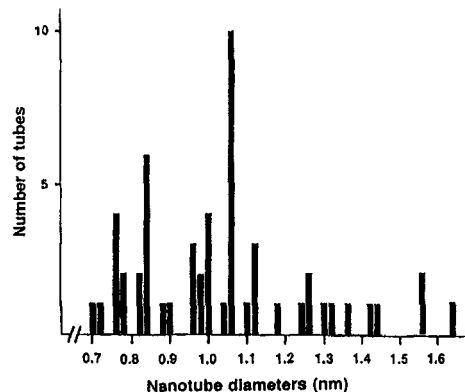


Fig. 5.4: Diameter distribution of isolated single-wall carbon nanotubes prepared by the arc method using a Fe catalyst [58].

vation of the carbon arc electrodes by transmission electron microscopy (TEM) but is much longer than the phonon frequency 10^{15} Hz. Thus the growth of carbon nanotubes occurs under stable conditions but over a limited range of He (or Ar) pressure, electric current and arc voltage. The iron or cobalt catalyst in the arc process forms both single-wall carbon nanotubes and nanometer-size carbide particles surrounded by graphene layers, as well as metal clusters encapsulated within graphene layers [58, 94]. Thus purification is necessary to separate out a pure single-wall nanotube sample.

When certain transition metals (Fe, Co, Ni, Pb, Mo, W, Cu, Au, ...), rare-earth metals (La-Nd, Gd-Tm, Lu), or their oxides are packed into a hole in the central region of the positive electrode, carbon nano-capsules are often obtained in the deposit on the negative electrode [109].[†] Carbon nano-capsules consist of multi-wall polyhedra of graphene sheets with interlayer separations of 0.34 nm inside which are contained metals (Fe, Co, Ni, Cu and Au) or metal carbides M_xC (M = transition metal such as La_2C (La = rare earth metal)).

5.4 Vapor Growth and Other Synthesis Methods

Fe, Co, and Ni particles are known to be catalysts for vapor grown carbon fiber synthesis [9, 17, 44], in which hydrocarbons (e.g., CH_4 , C_6H_6) and H_2 gases are reacted in the presence of Fe, Co, or Ni particles in a reaction tube at $1100^\circ C$.

[†]In the case of Fe, Co, and Ni, catalysts, single-wall nanotubes are observed at the surface of the deposit and nano-capsules are observed in other regions.

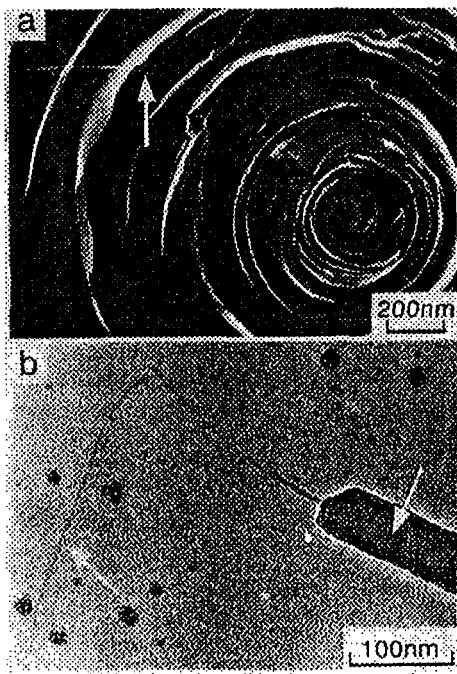


Fig. 5.5: Carbon nanotubes appear after breakage of the vapor-grown carbon fiber. (a) An SEM image of a broken vapor-grown carbon fiber, cut in liquid nitrogen and showing (white arrow) a carbon nanotube emerging from the center of the fiber. (b) HRTEM image showing the broken part of a very thin vapor-grown carbon fiber. The nanotube is clearly observed, indicating that thin vapor-grown carbon fibers grow from a nanotube core by thickening [59].

The innermost tubes of vapor-grown carbon fibers are considered to be carbon nanotubes, as shown in Fig. 5.5. Growth of carbon nanotubes from the vapor phase has also been demonstrated [59].

5.4.1 Vapor Growth Method

The synthesis of carbon nanotubes from the vapor phase utilizes equipment similar to that used for the preparation of vapor-grown carbon fibers [17, 44], with the furnace temperature held at 1100°C and using Fe catalyst particles, but using a low benzene gas pressure [59, 110]. A variety of other hydrocarbons, catalysts and catalyst supports have been used successfully by various groups worldwide to synthesize carbon nanotubes. One big advantage of the vapor growth approach is that carbon nanotubes can be made continuously and thus if the optimum conditions for growing pure carbon nanotubes could be found, this could be a very good way to synthesize large quantities of carbon nanotubes under relatively controlled conditions. Thus the vapor growth method

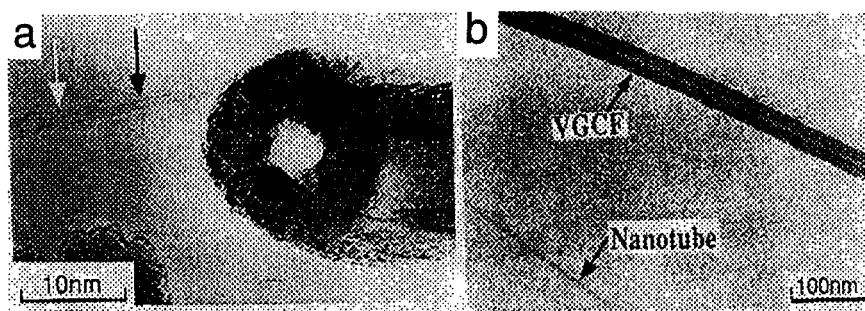


Fig. 5.6: Two kinds of vapor-grown carbon fibers (VGCF) observed in an as-grown sample: (a) a thick hollow fiber formed by a catalytic metal particle, (b) an exposed nanotube and a nanotube that had been pyrolytically coated, thereby increasing the nanotube diameter.

has some advantage for scale-up and commercial production. Many presently identified applications of carbon nanotubes can be met with vapor grown carbon nanotubes.

Carbon nanotubes can grow at the same time as conventional vapor-grown carbon fibers, as is seen in Fig. 5.6. Most of these nanotubes are multi-wall, but some single-wall nanotubes can also be present.

Vapor-grown carbon nanotubes have been studied by high-resolution TEM in both their as-grown form and after heat treatment. The as-grown nanotubes generally show poor crystallinity. The crystallinity, however, is much improved after heat treatment to 2500–3000°C in argon, as seen in high-resolution TEM studies [110]. Fracture of a thin vapor grown carbon fiber shows the presence of a nanotube at the fiber core, as shown in Fig. 5.5.

Referring to the bamboo structure seen on the inside of vapor grown carbon nanotubes (see Fig. 5.7), Endo [110] argues that the capping of an inner layer terminates its growth, so that the exposed cap layer provides growth along the length and the epitaxial layers follow this growth while at the same time adding to the nanotube diameter. The frequently-observed bending of the growth axis of the nanotubes is related to the introduction of a heptagonal defect at the bend location.

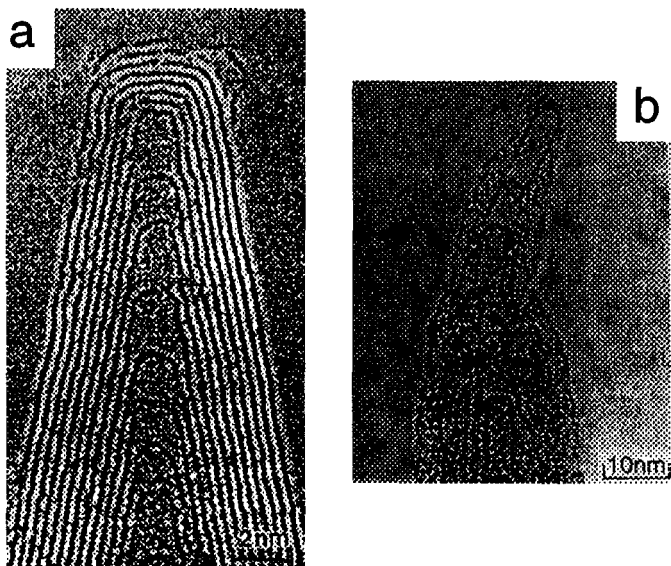


Fig. 5.7: (a) Transmission electron micrograph of a cone containing only single conical shells. The nearly periodic structures of the conical shells appear inside the cone tips [see (a)], which are attributed to overshooting growth on the basis of the open tube growth model [107]. (b) Commonly observed nanotube structure for the cap region of vapor-grown carbon nanotubes heat treated at 2800°C in Ar. Here a number of bamboo-like structures are observed in the core region near the cap [110].

5.4.2 Other Synthesis Methods

Another method of nanotube synthesis relates to the use of carbon ion bombardment to make carbon whiskers [111, 112]. Carbon whiskers are known as a graphite material with high crystallinity [4] whose diameter is $\sim 0.1\text{-}1 \mu\text{m}$ and several mm in length. In the ion bombardment growth method, carbon is vaporized in vacuum through ion or electron irradiation [113], and the resulting deposit containing carbon nanotubes, along with other structures is collected on a cold surface. Little is known about the optimization of the ion bombardment technique in relation to the preparation of nanotubes.

The use of solar energy for the synthesis of single-wall carbon nanotubes has

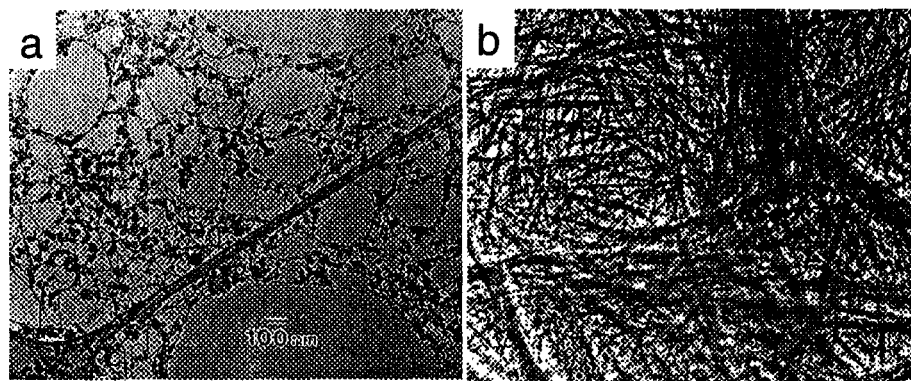


Fig. 5.8: (a) Transmission electron micrograph of a web of single-shell nanotubes formed in the catalytic carbon arc method. (b) TEM picture of gas phase purified nanotubes [116].

been reported [114, 115], using an experimental chamber where solar energy is focussed on the crucible to achieve a temperature of 3000 K on a clear day. A mixture of Ni and Y catalysts is used in an argon atmosphere (pressure of \sim 450 mbar). Further research is needed to optimize and control the synthesis process, increase the yield of ropes of single-wall nanotubes, minimize the concentration of carbon nanoparticles and amorphous carbon produced, and to characterize the carbon nanotubes that are produced.

5.5 Purification

In many of the synthesis methods that have been reported, carbon nanotubes are found along with other materials, such as amorphous carbon and carbon nanoparticles (see Fig. 5.8). Purification generally refers to the isolation of carbon nanotubes from other entities. The separation of nanotubes according to diameter (and chirality) is not considered under the topic of purification, and is not thought to be practical at this time.

Three basic methods have been used with limited success for the purification of the nanotubes: gas phase, liquid phase, and intercalation methods [116]. The classical chemical techniques for purification (such as filtering, chromatography, and centrifugation) have been tried, but not found to be effective in removing the

carbon nanoparticles, amorphous carbon and other unwanted species shown in Fig. 5.8 [116]. Heating preferentially decreases the amount of disordered carbon relative to carbon nanotubes. Heating could thus be useful for purification, except that it results in an increase in nanotube diameter due to the accretion of epitaxial carbon layers from the carbon in the vapor phase resulting from heating.

The gas phase method removes nanoparticles and amorphous carbon in the presence of nanotubes by an oxidation or oxygen-burning process [104, 117, 118]. Much slower layer-by-layer removal of the cylindrical layers of multi-wall nanotubes occurs because of the greater stability of a perfect graphene layer to oxygen than disordered or amorphous carbon or material with pentagonal defects [117, 118]. This method was in fact first used to synthesize a single-wall carbon nanotube. The oxidation reaction for carbon nanotubes is thermally activated with an energy barrier of 225 kJ/mol in air [118]. The gas phase purification process also tends to burn off many of the nanotubes. The carbon nanotubes obtained by gas phase purification are generally multi-wall nanotubes with diameters in the range 20–200 Å and 10 nm–1 μm in length [104], since the smaller diameter tubes tend to be oxidized with the nanoparticles.

Liquid phase removal of nanoparticles and other unwanted carbons has been carried out with some success using a potassium permanganate KMnO_4 treatment method which tends to give higher yields than the gas phase method, but results in nanotubes of shorter length [116, 119]. Finally, the intercalation of unpurified nanotube samples with $\text{CuCl}_2\text{--KCl}$ results in intercalation of the nanoparticles and other carbon species, but not the nanotubes which have closed cage structures. Thus subsequent chemical removal of the intercalated species can be carried out [120].

A method for the purification of samples containing single-wall nanotube ropes in the presence of carbon nanoparticles, fullerenes and other contaminants has also been reported [83, 121–123].

5.6 Nanotube Opening, Wetting, Filling and Alignment

5.6.1 *Nanotube Opening*

Experimental studies show that the cap of a nanotube is more reactive than the cylindrical part because of the presence of pentagons and hence the greater

curvature and reactivity of the caps. Thus in a vapor phase oxidation process, the cap region is burned off first, thereby providing one method for tube opening. The presence of the pentagons in the cap region also promote tube opening by various chemical reactions, such as with HNO_3 [116, 124]. Tube opening can occur at quite low temperatures ($\sim 400^\circ\text{C}$), using, for example, a lead metal catalyst in air [125]. The material that is sucked up the nanotube, however, is an oxide of lead [104].

5.6.2 Nanotube Wetting

A number of liquids have been found to wet the hollow core of carbon nanotubes and others do not show wetting behavior [126]. On the basis of classical theories for wetting, the hollow core of the nanotube will be wet by a fluid if

$$\cos \Theta = (\gamma_{sv} - \gamma_{sl}) / \gamma_{lv} \quad (5.1)$$

where Θ is the contact angle of a liquid on a surface, γ_{sv} , γ_{sl} and γ_{lv} are, respectively, the solid-vapor, solid-liquid, and liquid-vapor interfacial surface tensions. Wetting occurs when $\Theta > \pi/2$ or $\gamma_{sv} > \gamma_{sl}$. Examples of liquids which wet carbon nanotubes are HNO_3 , S, Cs, Rb, Se, water, various organic solvents and various oxides such as Pb and Bi_2O_2 [124, 126].

5.6.3 Nanotube Filling

Three methods have been used to fill the hollow core of carbon nanotubes: capillarity, pressure, and solvent carrier methods [126]. The capillarity method exploits removal of the cap (or the opening of the tube) followed by wetting, where the contact angle Θ exceeds $\pi/2$, as discussed in Sect. 5.6.2. In many cases only partial filling of a nanotube compartment has been achieved, though in some cases whole compartments have been filled [124], with some reports of long continuous nano-wires [127, 128]. In this work sulfur was shown to catalyze nanotube filling with many metal species. If a liquid does not wet the nanotube, then pressures exceeding $2\gamma/r$ are needed for tube filling, where r is the inner radius of the nanotube. Another method that has been successful for introducing high surface tension materials such as Co, Ni, Fe is the use of a solution using HNO_3 that performs both wetting and tube opening, and at the same time

contains a solute which is to be deposited within the nanotube. Subsequent chemistry is used to remove the carrier solvent [129].

5.6.4 Alignment of Nanotubes

For a variety of experiments and applications it is desirable to align the carbon nanotubes parallel to each other. If a sample contains an assembly of randomly oriented nanotubes, alignment can be achieved by rubbing in one direction or by cutting a material such as paraffin which contains embedded nanotubes. Nevertheless, the most common source for the alignment of nanotubes is by a self-alignment growth process. Self-aligned bundles of multi-wall and single-wall carbon nanotubes are found on the copper collector in the laser vaporization method, on the cathode deposit, and in the collarette for the case of growth by the arc method.

5.7 Nanotube Doping, Intercalation, and BN/C Composites

The substitutional doping of carbon nanotubes with B and N dopants to make the nanotubes *p*-type and *n*-type has been discussed [130]. Although some experimental work has been done on the substitutional doping of carbon nanotubes with B and N, most of the experimental activity on the doping of nanotubes has been with the alkali metals [131, 132], which do not act as substitutional dopants, but are predicted to lead to enhanced metallic conductivity [133]. Alkali metals readily intercalate into graphite as sheets of alkali metal which are located between graphene sheets in the crystal lattice. These alkali metal layers donate electrons to the graphite layers, thus greatly increasing the electrical conductivity, while at the same time greatly expanding the sample size along the direction normal to the lattice planes. Because of the closed cylindrical structure of carbon nanotubes, the relatively large alkali metal ions cannot find easy entry into perfect nanotubes, nor is there enough space for these ions between adjacent shells of a multi-wall nanotube. Therefore the alkali metal ions enter into the carbon nanotubes near structural defects. Once the ions penetrate the outer surface of the nanotube, their large size rips open the nanotube wall. This effect can be seen by microscopic probe studies on carbon nanotubes that have been attacked by alkali metals [131, 132].

For the intercalation of alkali metals and halogens into ropes of single wall carbon nanotubes, a two-zone furnace was utilized similar to that previously used for similar intercalations into crystalline graphite [134]. Typical temperatures that were used in the two-zone furnace for the alkali metals were $\sim 120^\circ\text{C}$ for the nanotubes were $\sim 160^\circ\text{C}$. The large uptake of the alkali metals Rb and K is consistent with a decoration of the carbon atoms on the nanotube surface by a (2×2) superlattice of alkali metal species, as well as uptake of alkali metal in the interstitial spaces between the nanotubes in the triangular lattice [135, 136]. The A_g vibrational mode at 1593 cm^{-1} in the undoped nanotubes are down shifted by Rb and K intercalation, consistent with electrons donated by the alkali metals to the nanotubes, while the Br_2 intercalation leads to an upshifted mode frequency, consistent with the transfer to electrons from the nanotubes to the halogen [135]. Transport measurements confirm that the intercalant uptake by the nanotube results in a dramatic increase in the electrical conductivity both for the case of Br_2 and K [136].

A composite multi-wall nanotube 12 nm in diameter, with 3 carbon shells at the interior followed by 6 BN shells in the central region, and 5 carbon shells on the outside, has been synthesized by the arc discharge method using an HfB_2 electrode and a carbon electrode in a N_2 atmosphere [137]. The structure and composition was obtained by a scanning EELS probe across the diameter of the nanotube. BN nanotubes have also been prepared by packing a tungsten rod with BN [87].

5.8 Temperature Regimes for Carbonization and Graphitization

Because of the importance of temperature as a growth parameter for carbon nanotubes, we summarize in the following some of the important temperature regimes for carbon materials. In addition to the melting ($\sim 4450\text{ K}$) and vaporization ($\sim 4700\text{ K}$) temperatures for carbon, two other temperatures are of importance: the carbonization temperature ($\sim 650\text{--}750^\circ\text{C}$) and the graphitization temperature ($\sim 2300\text{ K}$). The carbonization temperature is the temperature at which the volatile species are driven off from precursors for carbon materials, leaving behind the basic structural units on the order 1 nm in thickness, as shown in Fig. 5.9. The graphitization temperature ($\sim 2300^\circ\text{C}$) is the temperature at which interplanar site correlation is established and the ABAB stacking

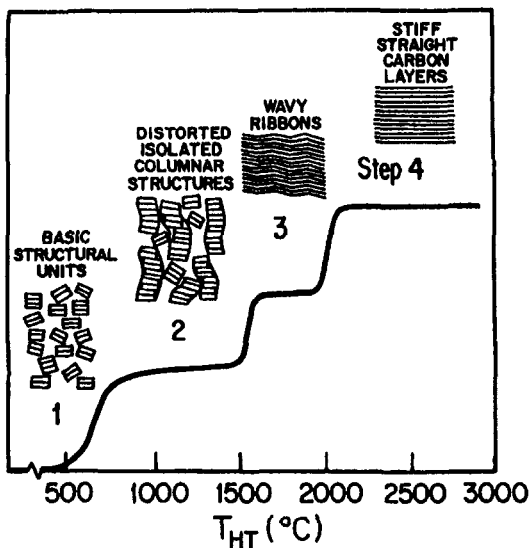


Fig. 5.9: Various steps of the graphitization process as a function of heat treatment temperature T_{HT} [138].

arrangement of the 3D graphite structure is formed. The melting and vaporization temperatures for carbon are both extremal values for the condensed phases of matter, with only a small stability region for the liquid phase of carbon.

Below the carbonization temperature, carbon cannot change its sp^2 covalent bonding configuration. Thus if the solid state is formed by a rapid quenching process to amorphous carbon, the state of amorphous carbon is metastable below the carbonization temperature. If the solid state is single crystal graphite, this phase is always the most stable state.

Between the carbonization and graphitization temperatures, carbon can transform from an amorphous carbon to a stable graphite planar structure at ambient pressure by cutting and reconnecting sp^2 covalent bonds. The carbonization temperature is closely related to the desorption temperature of oxygen or hydrogen that is chemically bonded at the edge of graphitic nanocrystals. Oxygen or hydrogen atoms are removed above about 700°C in the form of H_2O , CO , CO_2 , and CH_x molecules by cutting carbon-carbon bonds. Chemical reactions also occur in the presence of O_2 , H_2O , CO_2 at temperatures in the 800°C–1200°C range where the oxidation process occurs. Dangling carbon bonds, which are related to C–H, C–O, and C–N, etc. bonds, are broken in the

carbonization process, and C–C bonds are reformed at somewhat higher temperatures. The purification temperature for carbon nanotubes corresponds to the temperature for CO and CO₂ formation.

The various steps leading to graphitization have been studied by heating amorphous carbons to various temperature T_{HT} (see Fig. 5.9) and then observing the TEM micrographs [139, 140]. For $T_{HT} \leq 800^\circ\text{C}$, the basic structural units, consisting of a short length ($\approx 10\text{\AA}$) of about three parallel layers, start to pile up and form distorted columnar structures, as impurity atoms are released, mostly in gaseous form. For $800 \leq T_{HT} \leq 1500^\circ\text{C}$, the columnar structures increase in length with a lesser degree of misorientation of the basic structural units as shown in Fig. 5.9. In this step, individual misoriented basic structural units become aligned and the crystallite size along the *c*-axis L_c increases gradually. For $1500 \leq T_{HT} \leq 1900^\circ\text{C}$, the columnar structure disappears as wavy ribbons or wrinkled layers are formed by hooking the adjacent columns together, and in this range of T_{HT} , both the in-plane and *c*-axis crystallite sizes L_a and L_c increase rapidly. By $T_{HT} \sim 1700^\circ\text{C}$, the wavy planar structure begins to disappear and a turbostratic planar stacking arrangement starts to appear, with L_a values higher than 200 Å at $T_{HT} \sim 2000^\circ\text{C}$. By 2100°C , most of the in-plane structural defects have been eliminated so that a rapid increase in L_a can occur due to the disappearance of tilt and twist boundaries. As the graphitic structure develops further with increasing T_{HT} , the interlayer distance decreases. At higher T_{HT} , interlayer site correlation between layers starts to develop. Although the graphitization temperature is usually given as 2300°C , much higher T_{HT} values (2800 – 3000°C) are generally used to obtain 3D graphite crystals by the heat treatment approach.

5.9 Growth Mechanisms

The growth mechanism for cylindrical fullerene nanotubes is especially interesting and has been hotly debated. One school of thought [141, 142] assumes that the nanotubes are always capped and that the growth mechanism involves a C₂ absorption process that is assisted by the pentagonal defects on the caps. The second school [107, 108, 143] assumes that the nanotubes are open during the growth process and that carbon atoms are added at the open ends of the nanotubes. Since the experimental conditions for forming carbon nanotubes vary

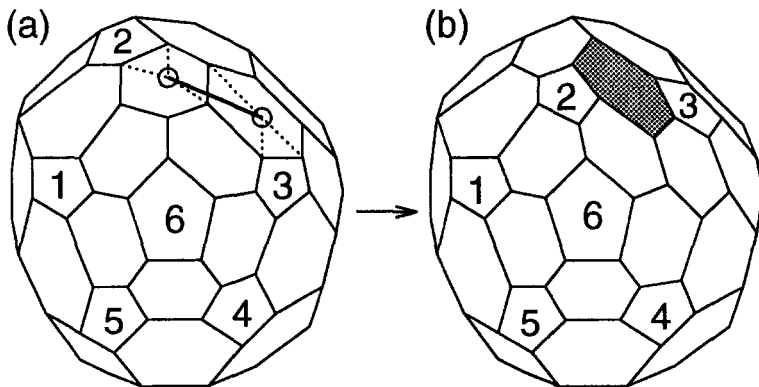


Fig. 5.10: C_2 addition to a cap of $(6,5)$ nanotube. (a) Numbers from 1 to 6 indicate the position of the six pentagons on the hemispherical cap. If we add one C_2 molecule, indicated by open circles between 2 and 3, and if the new bonds denoted by dotted lines form, we get a new hexagon denoted in (b) by dark shading. (b) Through rotation by 72° , it is seen that the shape of the cap is the same for (a) and (b).[144]

significantly according to growth method, more than one mechanism may be operative in producing carbon nanotube growth.

The first school of thought focuses on nanotube growth at relatively low temperatures ($\sim 1100^\circ\text{C}$) and assumes that growth is nucleated at active sites of a vapor-grown carbon fiber of about 1000 \AA diameter. Although the parent vapor-grown carbon fiber is itself nucleated by a catalytic transition metal particle [44], the growth of the carbon nanotube is thought to be associated with the absorption of a C_2 dimer near a pentagon in the cap of the nanotube. Referring to the basic model for C_2 absorption in Figs. 5.10 and 5.11, we see that sequential addition of C_2 dimers results in the addition of a row of hexagons to the carbon nanotube. To apply the C_2 absorption mechanism, it is usually necessary to use the Stone-Wales mechanism to bring the pentagons into their canonical positions, as necessary for the execution of each C_2 absorption, in accordance with Fig. 5.10. In Fig. 5.10(a) we show a hemisphere cap of $(6,5)$ nanotube which have six pentagons denoted by numbers from 1 to 6. When we introduce

C_2 molecule between the pentagons 2 and 3, we get a new hexagon denoted by dark shading in Fig. 5.10(b). In Fig. 5.10(a) we consider new chemical bonds denoted by dotted lines. When we rotate Fig. 5.10(b) by 72° , we see that the shape of the cap is the same for Fig. 5.10(a) and (b).[110, 144] Repeating this process five times, we return to Fig. 5.10(a) but with the addition of one more ring of carbon hexagons around the nanotube.

For the growth of carbon nanotubes by the arc discharge method, it has been proposed that the nanotubes grow at their open ends[143, 145]. If the nanotube has chirality (see Fig. 5.11), it is easily seen that the absorption of a single C_2 dimer at the active dangling bond edge site will add one hexagon to the open end. Thus the sequential addition of C_2 dimers will result in continuous growth of the chiral nanotube. If carbon atoms should be added out of sequence, then addition of a C_2 dimer would result in the addition of a pentagon, which could lead to capping of the nanotube, while the addition of a C_3 trimer out of sequence merely adds a hexagon. In the case of an armchair edge, here again a single C_2 dimer will add a hexagon. Multiple additions of C_2 dimers lead to multiple additions of hexagons to the armchair edge. For the case of a zigzag edge, initiation of growth requires one trimer C_3 (see Fig. 5.11), which then provides the necessary edge site to complete one row of growth for the nanotube through the addition of C_2 dimers, except for the last hexagon in the row, which requires only a C_1 monomer. If, however, a C_2 dimer is initially bonded at a zigzag edge, it will form a pentagon. Because of the curvature that is introduced by the pentagon, the open end of the nanotube will likely form a cap, and growth of the nanotube by the open end process will be terminated.

A schematic diagram for the open tube growth method is shown in Fig. 5.12 [107]. While the tubes grow along the length, they also grow in diameter by an epitaxial growth process, as shown in Fig. 5.12. The large aspect ratio of the nanotubes implies that growth along the tube axis is more likely than growth along the nanotube diameter. Referring to Fig. 5.7, Iijima argues that the inner tubes are capped first with the capping providing a method for relieving strain in the cap region. The introduction of pentagons leads to positive curvature, while capping with heptagons lead to changes in nanotube size [see Fig. 5.7(b)] and orientation. The introduction of heptagon–pentagon pairs can produce a variety of nanotube shapes.

At present the growth model for carbon nanotubes remains incomplete with

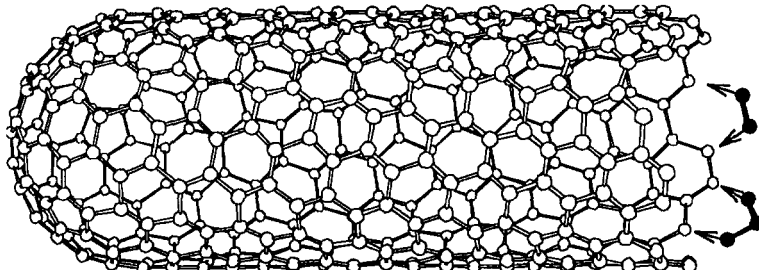


Fig. 5.11: Proposed growth mechanism of carbon nanotubes at an open end by the absorption of C_2 (dimers) and C_3 (trimers). Absorption of a C_3 trimer at the open end of a zigzag carbon nanotube and subsequent C_2 dimer absorption.

regard to the role of temperature and helium gas. Since the vapor phase growth occurs at only 1100°C , any dangling bonds that might participate in the open nanotube growth mechanism would be unstable, so that the closed tube approach would be favored. In this lower temperature regime, the growth of the nanotube core and the thickening process occur separately. In contrast, for the arc discharge synthesis method, the temperature where nanotube growth occurs has been estimated to be about 3400°C [146]. At these high temperatures, nanotube growth and the graphitization of the thickening deposits occur simultaneously, so that all the coaxial nanotubes grow at once at these elevated temperatures [141], and the open nanotube growth may be favored.

One interesting growth feature, reported by several groups [106, 107, 147], is the containment of a small-diameter carbon nanotube inside a larger-diameter nanotube, where the inner nanotube has no access to a carbon source. Such a feature seems to require growth by an open tube mechanism.

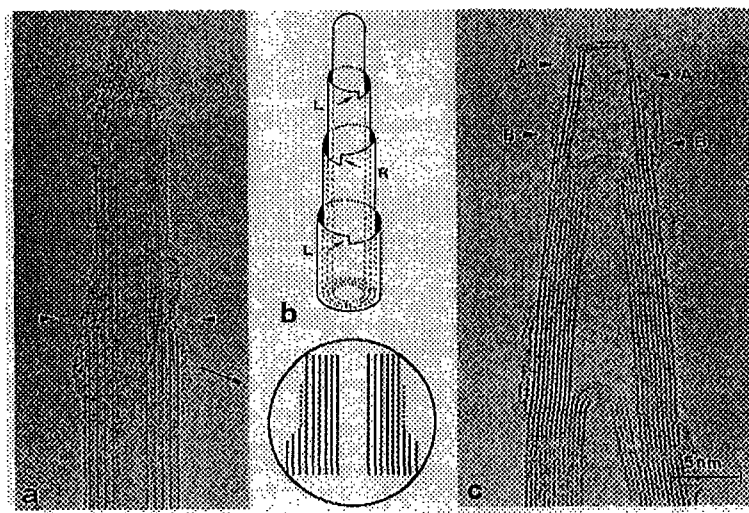


Fig. 5.12: Schematic diagram for open tube growth of nanotubes from a carbon supply. The figure shows the addition of carbon atoms to the open ends, the capping of the longest open end, and the initiation of new nanotubes. (a) Some shells are terminated at the positions indicated by arrowheads as illustrated in the circle. (b) Terminated shells carry left-handed or right-handed kink sites, owing to the helical tube structure. (c) Similar termination of the shells near the top of the tip, forming steps, one atom in height, as indicated by the arrowheads [107].

CHAPTER 6.

Landau Energy Bands of Carbon Nanotubes

Itinerant electrons in a magnetic field give rise to Landau quantization of the energy bands. In this chapter we show how to calculate the Landau energy bands of carbon nanotubes using the tight-binding method. Quantum confinement of electrons in one-dimensional carbon nanotubes and confinement through application of a magnetic field show interesting phenomena as a function of the chirality of the carbon nanotubes and of the direction and strength of the magnetic field.

6.1 Free Electron in a Magnetic Field

In a uniform static magnetic field,* \mathbf{B} , an electron with velocity \mathbf{v} experiences a Lorentz force $e\mathbf{v} \times \mathbf{B}$, which is perpendicular to both \mathbf{B} and \mathbf{v} . By solving the equations of motion, we obtain the so-called cyclotron motion of the electron in a magnetic field with a cyclotron frequency

$$\omega_c = \frac{eB}{m} \quad (6.1)$$

and a cyclotron radius of $r_c = v/\omega_c$.

In quantum mechanics, the motion of an electron is described by the transformation \mathbf{p} to $\mathbf{p} - e\mathbf{A}$ in the Hamiltonian,[†] where \mathbf{A} is the vector potential ($\nabla \times \mathbf{A} = \mathbf{B}$). A gauge for \mathbf{A} , such as the Landau gauge, is used to relate \mathbf{A}

*We here simply call the magnetic field, $\mathbf{B} = \mu_0 \mathbf{H}$, where μ_0 is the permeability of free space and \mathbf{H} is the magnetic field in free space. Strictly \mathbf{B} should be called the density of magnetic flux on a unit surface.

[†]We use MKS (SI) units here. In CGS units, we simply replace e by e/c , so that the transformation of $\mathbf{p} - e\mathbf{A}$ becomes $\mathbf{p} - e\mathbf{A}/c$ in CGS units. This is, however, not the case for the Hall coefficient, R_H , for which SI units give $R_H = -1/ne$, but $R_H = -1/nec$, in CGS units.

explicitly to the magnetic field $\mathbf{B} = (0, 0, B)$,

$$\mathbf{A} = (0, Bx, 0). \quad (6.2)$$

The Hamiltonian for a free electron ($V = 0$) in the Landau gauge becomes

$$\mathcal{H} = -\frac{\hbar^2}{2m} \left\{ \frac{\partial^2}{\partial x^2} - \left(-i\frac{\partial}{\partial y} - \frac{eBx}{\hbar} \right)^2 + \frac{\partial^2}{\partial z^2} \right\}. \quad (6.3)$$

Since the Hamiltonian does not depend on y and z , ($\partial\mathcal{H}/\partial y = 0$, and $\partial\mathcal{H}/\partial z = 0$), we can assume that the wavefunction, $\Phi(x, y, z)$, has the form

$$\Phi(x, y, z) = e^{i(k_y y + k_z z)} \varphi(x), \quad (6.4)$$

in which $\varphi(x)$ satisfies the harmonic oscillator Hamiltonian,

$$\left\{ -\frac{\hbar^2}{2m} \frac{\partial^2}{\partial x^2} + \frac{m\omega_c^2}{2}(x - X)^2 \right\} \varphi(x) = \left\{ E - \frac{\hbar^2 k_z^2}{2m} \right\} \varphi(x) \quad (6.5)$$

and $X = \hbar k_y/eB$. When we use the solution to Schrödinger's equation for a one-dimensional harmonic oscillator Hamiltonian, the energy levels E_N are given by

$$E_N(k_z) = \hbar\omega_c(N + \frac{1}{2}) + \frac{\hbar^2 k_z^2}{2m}, \quad (N = 0, 1, 2, \dots). \quad (6.6)$$

Thus the two-dimensional (x, y) motion of the free electron is quantized by the Landau index N , and the three-dimensional energy bands in zero magnetic field are divided into one-dimensional energy bands labeled by N as in Eq. (6.6). Further, the Hamiltonian and the operator X commute, so that the quantum number associated with X is a good quantum number[†] describing the wavefunction and its degeneracy. The corresponding wave function $\varphi(x)$ in Eq. (6.4) for the N th magnetic energy subband and harmonic oscillator center X is,

$$\varphi_{NX}(x) = \frac{1}{\sqrt{\sqrt{\pi} 2^N N! \ell}} H_N\left(\frac{x - X}{\ell}\right) \exp\left[-\frac{(x - X)^2}{2\ell^2}\right], \quad (6.7)$$

[†]For a crystalline solid, the center of the harmonic motion, $X = \hbar k_y/eB$, is not a constant but is an operator which does not commute with the position y . Thus a general uncertainty relation applies to the two operators X and Y for the centers of the harmonic motion in a magnetic field, $[X, Y] = i\hbar/eB$, and this commutator relation does not depend on the gauge.

where H_N is the N th Hermite polynomial[§] defined here as

$$H_N(\xi) = (-1)^N e^{\xi^2} \frac{d^N}{d\xi^N} e^{-\xi^2} \quad (6.8)$$

and ℓ is the Landau radius defined by

$$\ell = \sqrt{\frac{\hbar}{eB}}. \quad (6.9)$$

The Landau radius represents the size of the wavefunction in a magnetic field and depends on the strength of the magnetic field. When $B = 1\text{T}$, then $\ell = 25.66\text{ nm}$. The Landau radius is thus a quantum variable which is clearly different from the classical, cyclotron radius of $r_c = v/\omega_c$.

Using a periodic boundary condition in the direction of y with period, $L_y a$, and a lattice constant a , the wave number k_y is quantized as $k_y = 2\pi M_y/L_y a$, ($M_y = 0, 1, 2, \dots, L_y - 1$) and thus $X = \hbar k_y/eB = 2\pi\ell^2 M_y/L_y a$ is quantized, too. We then have $L_x L_y a^2/2\pi\ell^2$ degenerate states[¶] in the area $L_x a \times L_y a$. Thus when we consider a two-dimensional electron system, we have one degenerate state (Landau level) per area $2\pi\ell^2$ for a given Landau index, N .

When we consider Landau quantization of the π -energy bands, we should consider the periodicity of the unit cell due to the crystal potential. Thus, the ratio of $2\pi\ell^2$ to the area of the unit cell is an important factor for describing the energy bands in a magnetic field. The overall picture for the energy bands in a magnetic field can be obtained using the tight binding approximation, which we will discuss in the following section. Even in this case it is found that most energy bands show Landau quantization in a uniform magnetic field. However, in the case of carbon nanotubes, since the magnetic field that is applied to the curved surface of a carbon nanotube is not uniform, and since the net magnetic flux penetrating the surface is always zero, a special situation occurs, in which the energy bands do not show explicit Landau levels, but they do instead have energy dispersion for all values of the magnetic field. The energy band width in this case shows new oscillations with a period that is scaled by the cross section

[§]Different definitions of the Hermite polynomials may give rise to confusion. The $H_n(\xi)$ used here has the explicit expressions for $n = 0, 1, 2$ given by $H_0(\xi) = 1$, $H_1(\xi) = 2\xi$, and $H_2(\xi) = 4\xi^2 - 2$.

[¶]Orthogonality between two harmonic oscillator wavefunctions comes from the orthogonality of the plane waves in the y direction.

of the unit cell of the nanotube, which in turn is specified by the symmetry of the nanotube (see Sect. 3.3).

An interesting feature of the electronic structure of carbon nanotubes in a magnetic field is the dependence of the solid state properties on the chiral vector of the nanotube. As is discussed in Sect. 4.1, the electronic structure is especially unusual in the sense that carbon nanotubes can be either metallic or semiconducting, depending only on the symmetry of the tube, as specified by its chiral vector, \tilde{C}_h , in Fig. 3.2 [69, 71, 73, 75, 148, 149]. The magnetic response of the electronic structure for such one-dimensional materials, which have a two-dimensional surface, is especially interesting, and is relevant to recent magnetoresistance [150] and magnetic susceptibility [151, 152] experiments on carbon nanotubes.

6.2 Tight Binding Approximation in a Static Magnetic Field

Here we explain a formalism for the tight binding approximation in a static magnetic field. A simple result of this formalism shows that in describing the magnetic field dependence of the wave function, we need only consider a phase factor, depending on the vector potential. This phase factor corresponds to the continuous modulation of the periodic boundary condition for the wave function in a periodic system. Because of the breakdown of the Bloch condition in the wavefunction, the size of the unit cell changes as a function of magnetic field.

Within the tight binding scheme, the Bloch functions in a static magnetic field can be expressed as

$$\Phi(\mathbf{k}, \mathbf{r}) = \frac{1}{\sqrt{N}} \sum_{\mathbf{R}} \exp(i\mathbf{k} \cdot \mathbf{R} + i\frac{e}{\hbar} G_{\mathbf{R}}) \varphi(\mathbf{r} - \mathbf{R}), \quad (6.10)$$

where \mathbf{R} is a lattice vector and $G_{\mathbf{R}}$ is the phase factor associated with the magnetic field and is expressed by [153]

$$G_{\mathbf{R}} = \int_{\mathbf{R}}^{\mathbf{r}} \mathbf{A}(\xi) \cdot d\xi = \int_0^1 (\mathbf{r} - \mathbf{R}) \cdot \mathbf{A}(\mathbf{R} + \lambda[\mathbf{r} - \mathbf{R}]) d\lambda, \quad (6.11)$$

where it is noted that $G_{\mathbf{R}}$ is a function of \mathbf{r} and the integration in Eq. (6.11) is taken along the line from \mathbf{R} to \mathbf{r} as shown in Fig. 6.1. When the Hamiltonian \mathcal{H} for an electron in a crystal potential $V(r)$ and in a magnetic field,

$$\mathcal{H} = \frac{1}{2m} (\mathbf{p} - e\mathbf{A})^2 + V, \quad (6.12)$$

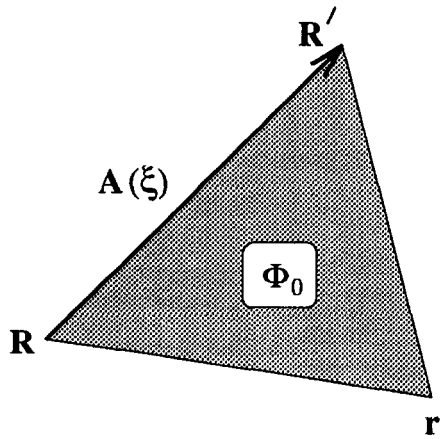


Fig. 6.1: The vector \mathbf{RR}' shows the integration path of $A(\xi)$ in calculating $G_{\mathbf{R}} - G_{\mathbf{R}'}$ in Eq. (6.14). $\Phi_0(r)$ is the flux that penetrates the triangle defined by the three points, \mathbf{R} , \mathbf{R}' and \mathbf{r} .

operates on $\Psi(\mathbf{k}, \mathbf{r})$, we obtain

$$\begin{aligned}
 & \mathcal{H}\Psi(\mathbf{k}, \mathbf{r}) \\
 &= \frac{1}{\sqrt{N}} \sum_{\mathbf{R}} \exp(i\mathbf{k} \cdot \mathbf{R}) \left[\frac{1}{2m} (\mathbf{p} - e\mathbf{A})^2 + V \right] \exp(i\frac{e}{\hbar}G_{\mathbf{R}}) \varphi(\mathbf{r} - \mathbf{R}) \\
 &= \frac{1}{\sqrt{N}} \sum_{\mathbf{R}} \exp(i\mathbf{k} \cdot \mathbf{R} + i\frac{e}{\hbar}G_{\mathbf{R}}) \left[\frac{1}{2m} (\mathbf{p} - e(\mathbf{A} - \nabla G_{\mathbf{R}}))^2 + V \right] \varphi(\mathbf{r} - \mathbf{R}) \\
 &= \frac{1}{\sqrt{N}} \sum_{\mathbf{R}} \exp(i\mathbf{k} \cdot \mathbf{R} + i\frac{e}{\hbar}G_{\mathbf{R}}) \left[\frac{\mathbf{p}^2}{2m} + V \right] \varphi(\mathbf{r} - \mathbf{R}).
 \end{aligned} \tag{6.13}$$

It is important to note that in the last line of Eq. (6.13) the operator which acts on the wavefunction is the Hamiltonian in zero magnetic field. Thus the Hamiltonian matrix element in a magnetic field can be obtained through multiplication of the Hamiltonian matrix element in zero field by a phase factor. In obtaining the last line of Eq. (6.13), we use the fact that: (1) the magnetic field is slowly changing with distance r compared with the spatial change of $\varphi(\mathbf{r} - \mathbf{R})$, and (2) $\varphi(\mathbf{r} - \mathbf{R})$ is localized at $\mathbf{r} = \mathbf{R}$. Except for the phase factor, Eq. (6.13) is independent of the value of the magnetic field B and the functional form of \mathbf{A} [153].

Using Eq. (6.13), we can calculate the matrix elements of \mathcal{H} between two Bloch functions and solve the matrix Hamiltonian to obtain the eigenvalues. It is noted here that we will have a term in $\exp((ie/\hbar)(G_{\mathbf{R}} - G_{\mathbf{R}'}))$ in the matrix

elements, which is explicitly dependent on \mathbf{r} as

$$G_{\mathbf{R}} - G_{\mathbf{R}'} = \int_{\mathbf{R}}^{\mathbf{R}'} \mathbf{A}(\xi) d\xi + \Phi_0(\mathbf{r}), \quad (6.14)$$

where $\Phi_0(\mathbf{r})$ is the flux that penetrates the triangle defined by the three points, \mathbf{R} , \mathbf{R}' and \mathbf{r} as shown in Fig. 6.1. For simplicity we neglect the phase factor coming from $\Phi_0(\mathbf{r})$ in the integrals over the atomic matrix element. This approximation is valid when the magnetic field changes slowly as a function of the lattice constant. This approximation is consistent with the assumptions that we made above [154]. Thus the integration on \mathbf{r} of the Hamiltonian matrix element gives the zero field matrix element multiplied by the phase factor, $\exp[(ie/\hbar)(G_{\mathbf{R}} - G_{\mathbf{R}'}))]$.

6.3 Two-Dimensional Cosine Band in a Magnetic Field

A simple example of a two-dimensional electron system is a square lattice, whose energy dispersion is known to be that of a two-dimensional cosine band.* In a two-dimensional cosine band with lattice constant a , a fractal behavior has been found theoretically in the energy band spectra in a magnetic field of magnitude B , depending on whether Ba^2/ϕ_0 is a rational or irrational number, where ϕ_0 is the flux quantum† defined by,

$$\phi_0 = \frac{\hbar}{e} = 4.1356 \times 10^{-15} [\text{T}/\text{m}^2] \quad (6.15)$$

and a is the lattice constant of a graphene sheet [155]. All of the energy dispersion relations are periodic functions of integer values of Ba^2/ϕ_0 . However, the magnetic field necessary to observe this fractal behavior explicitly is too large ($\sim 10^5 \text{T}$) for presently available laboratory magnetic fields. In relatively weak fields ($\sim 10^2 \text{T}$), we only observe Landau levels, except for the Landau subbands near $E = 0$ in the case of a 2D cosine band, since the wave functions near $E = 0$ are for extended orbits [156].

Let us start from the simple case of a two-dimensional square lattice in a magnetic field, \mathbf{B} , which is perpendicular to the two-dimensional surface. The

*We hereafter neglect the effect of the magnetic field on the overlap integral matrix, S . Thus the matrix S is always taken to be the unit matrix.

†The flux quantum in a superconductor is half of this definition, $\hbar/2e$. The difference between the two definitions comes from the different charge of a carrier compared to a Cooper pair.

vector potential \mathbf{A} in the Landau gauge is given by

$$\mathbf{A} = (0, Bx). \quad (6.16)$$

Using a Bloch wave function in a magnetic field, the matrix element of the Hamiltonian in Eq. (6.12) between states \mathbf{k} and \mathbf{k}' is given by

$$\mathcal{H}_{\mathbf{k}\mathbf{k}'} = \langle \Phi_{\mathbf{k}} | \mathcal{H} | \Phi_{\mathbf{k}'} \rangle = \frac{1}{N} \sum_{\mathbf{R}, \mathbf{R}'} e^{-i(\mathbf{k} \cdot \mathbf{R} - \mathbf{k}' \cdot \mathbf{R}') - (ie/\hbar)(G_{\mathbf{R}} - G_{\mathbf{R}'})} \mathcal{H}_{\mathbf{R}\mathbf{R}'} \quad (6.17)$$

in which \mathbf{R} and \mathbf{R}' are taken as lattice vectors to nearest-neighbor sites. From Eq. (6.13), we can define $\mathcal{H}_{\mathbf{R}\mathbf{R}'}$ as the following Hamiltonian matrix element in zero magnetic field,

$$\mathcal{H}_{\mathbf{R}\mathbf{R}'} = \left\langle \varphi(\mathbf{r} - \mathbf{R}) \left| \frac{\mathbf{p}^2}{2m} + V \right| \varphi(\mathbf{r} - \mathbf{R}') \right\rangle. \quad (6.18)$$

The phase factor difference $G_{\mathbf{R}} - G_{\mathbf{R}'}$ is calculated by using Eqs. (6.11) and (6.16),

$$G_{\mathbf{R}} - G_{\mathbf{R}'} = \int_0^1 (\mathbf{R}' - \mathbf{R}) \cdot \mathbf{A}(\mathbf{R} - \lambda[\mathbf{R}' - \mathbf{R}]) d\lambda. \quad (6.19)$$

In the inner product between $\mathbf{R}' - \mathbf{R}$ and \mathbf{A} , only the two cases of $(\mathbf{R}' - \mathbf{R}) = (0, \pm a)$ among the four nearest neighbor sites have non-zero values, because the vector potential \mathbf{A} in Eq. (6.16) has only y components. Further, since the integration path in the case of $(\mathbf{R}' - \mathbf{R}) = (0, \pm a)$ is in the y direction, the vector potential \mathbf{A} , which is only a function of x , has the same value of $\mathbf{A}(\mathbf{R} - \lambda[\mathbf{R}' - \mathbf{R}]) = (0, Bx)$ along the entire integration path from \mathbf{R} to \mathbf{R}' , where x is the x component of \mathbf{R} (or \mathbf{R}'). Thus Eq. (6.19) gives

$$G_{\mathbf{R}} - G_{\mathbf{R}'} = \int_0^1 (\pm a) Bx d\lambda = \pm Bax. \quad (6.20)$$

Using $\mathbf{k} \cdot \mathbf{R} - \mathbf{k}' \cdot \mathbf{R}' = \mathbf{R} \cdot (\mathbf{k} - \mathbf{k}') + \mathbf{k}' \cdot (\mathbf{R} - \mathbf{R}')$ and the fact that we can sum Eq. (6.17) over \mathbf{R}' , then $\mathcal{H}_{\mathbf{k}\mathbf{k}'}$ is given by

$$\mathcal{H}_{\mathbf{k}\mathbf{k}'} = t \sum_{\mathbf{R}} e^{i\mathbf{R} \cdot (\mathbf{k} - \mathbf{k}')} \left(e^{ik_x a} + e^{-ik_x a} + e^{2\pi i Bax/\phi_0 - ik_y a} + e^{-2\pi i Bax/\phi_0 + ik_y a} \right) \quad (6.21)$$

where t is the transfer integral, and $\mathbf{R} = (x, y)$. Here we consider periodic boundary conditions for the area of a square $La \times La$ in real space. Then the lattice vector \mathbf{R} and the wave vector \mathbf{k} are quantized as follows:

$$\mathbf{R} = (x, y) = (na, ma), \quad \mathbf{k} = \left(\frac{2\pi}{La} p, \frac{2\pi}{La} q \right) \quad (6.22)$$

where $1 \leq n, m, p, q \leq L$ are integers. Then we can carry out the summation on \mathbf{R} of Eq. (6.21) as follows

$$\begin{aligned} \mathcal{H}_{\mathbf{kk}'} &= t \{ e^{ik_x a} + e^{-ik_x a} \} \delta_{\mathbf{kk}'} \\ &\quad + t \left\{ e^{-ik_y a} \sum_n e^{2\pi i(p-p'+rL')n/L} + e^{ik_y a} \sum_n e^{2\pi i(p-p'-rL')n/L} \right\} \delta_{k_y k'_y} \\ &= t \{ e^{ik_x a} + e^{-ik_x a} \} \delta_{\mathbf{kk}'} + t \{ e^{-ik_y a} \delta_{k'_x, k_x + \Delta k} + e^{ik_y a} \delta_{k'_x, k_x - \Delta k} \} \delta_{k_y k'_y} \end{aligned} \quad (6.23)$$

where we have used

$$e^{i\mathbf{R} \cdot (\mathbf{k} - \mathbf{k}') } = 2\pi i \{ (p - p')n + (q - q')m \} \quad (6.24)$$

and

$$\frac{Bax}{\phi_0} = \frac{Ba^2}{\phi_0} n \equiv \mathcal{B}n = \frac{r}{s}n, \quad (6.25)$$

in which $\mathcal{B} = Ba^2/\phi_0$ is the magnetic field per the unit cell measured in units of flux quanta. Here we consider only the case where \mathcal{B} is a rational number, i.e., $\mathcal{B} = r/s$, (where r, s are integers whose largest common denominator is unity). From Eq. (6.23), we can see that k_x in a magnetic field is no longer a good quantum number and k_x couples with other k'_x separated by

$$\Delta k = \frac{2\pi}{La} r L' = \frac{2\pi r}{a s}, \quad (6.26)$$

where $L' = L/s$. Thus, the states with $k_x, k_x + \Delta k, k_x + 2\Delta k, \dots$ interact with each other. Since $s\Delta k$ corresponds to the reciprocal lattice vector of the two-dimensional square lattice, the number of k_x values which interact with each other becomes a finite number (s) whenever \mathcal{B} has a rational value. Thus to obtain the energy dispersion relations, we solve the $s \times s$ Hamiltonian matrix of Eq. (6.23), with B as a rational value.

Since the wavevector k_y is still a good quantum number even in the presence of magnetic field, we can solve the Hamiltonian matrix for given k_y values to

obtain s energy bands. It is convenient to express the k_x and k_y values as

$$\begin{aligned} k_x &= \frac{2\pi}{La} p, \quad (p = 1, \dots, L'), \\ k_y &= \frac{2\pi}{La} q, \quad (q = 1, \dots, L). \end{aligned} \tag{6.27}$$

Since we will solve the Hamiltonian matrix for given k_x , too, we will have to diagonalize the $s \times s$ Hamiltonian matrix $L \times L'$ times. It is important to note that the calculated energy dispersion relations in a magnetic field are two-dimensional and are a function of both k_x and k_y . Furthermore, we note that the Brillouin zone is folded s times in the direction of k_x to k_x/s . It is useful to show the energy dispersion for different k_x values simultaneously as a function of k_y . An explicit form of the Hamiltonian matrix is given by,

$$\mathcal{H} = \begin{pmatrix} 2t \cos k_x a & te^{-ik_y a} & 0 & \dots & 0 \\ te^{ik_y a} & 2t \cos(k_x + \Delta k)a & te^{-ik_y a} & \dots & \vdots \\ 0 & te^{ik_y a} & \ddots & \ddots & \\ \vdots & & \ddots & \ddots & te^{-ik_y a} \\ 0 & \dots & & te^{ik_y a} & 2t \cos(k_x + (s-1)\Delta k)a \end{pmatrix}, \tag{6.28}$$

where a is the lattice constant of the 2D square lattice.

In Fig. 6.2, the calculated Landau energy levels of the two-dimensional (2D) cosine energy band are shown for a magnetic field value for which the ratio of the unit cell to the area per quantum flux is $1/60$. Along the horizontal axis, the k values in the k_y direction are plotted using the Landau gauge given by Eq. (6.2). In this case, since $r = 1$ and $s = 60$, the unit cell in the magnetic field becomes a rectangle in the x, y coordinate system with area $sa \times a$. The corresponding Brillouin zone consequently becomes a rectangle in reciprocal space with area $2\pi/a \times 2\pi/sa$. Thus we consider the Landau energy levels for only the value $k_y = 0$ and the energy dispersion is given as a function of k_x . The above discussion makes explicit use of the gauge of the vector potential. However, the calculated energy states should not depend on the gauge. In fact, we can see from Fig. 6.2 that most of the energy bands are dispersionless, as is also observed in the case of the Landau quantization of the 2D free electron gas. Near the $E = 0$ region, some oscillations in the energy bands can be seen, and these oscillations may reflect the delocalized nature of the wave functions.

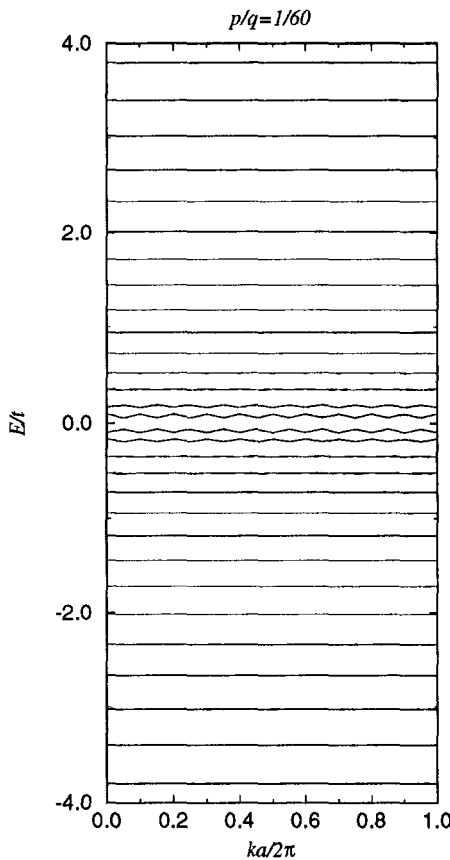


Fig. 6.2: Landau energy bands for a two-dimensional cosine band in a magnetic field perpendicular to the two-dimensional plane. Here the ratio of the area of the unit cell to the area per quantum flux is 1/60. The energy is normalized to the nearest neighbor overlap energy t and the horizontal axis plots k values in the direction of y in dimensionless units, using the Landau gauge of Eq. (6.2).

6.4 Landau Energy Bands of Graphite

Next we consider the Landau energy bands for two-dimensional graphite, and we will use the formulation discussed in the previous section. The two differences from the previous section are that for the case of a 2D graphene sheet: (1) there are two atomic sites, A and B , in the unit cell as discussed in Sect. 2.3, and (2) the directions of the nearest neighbors is not always parallel to the x or y axes.

The Hamiltonian matrix between A and B sites is given by,

$$\langle \Phi_{\mathbf{k}'}^B | \mathcal{H} | \Phi_{\mathbf{k}}^A \rangle = \frac{t}{N} \sum_{\mathbf{R}, \mathbf{R}'} e^{i(\mathbf{k} \cdot \mathbf{R} - \mathbf{k}' \cdot \mathbf{R}') + (ie/\hbar)(G_{\mathbf{R}} - G_{\mathbf{R}'})} \quad (6.29)$$

where t is the transfer integral between nearest-neighbor sites in zero magnetic field, which is defined in Eq. (2.18).

Using the same magnetic field derived from Eq. (6.16) and the nearest neighbor direction $\mathbf{R} - \mathbf{R}' = \mathbf{R}_j$, ($j = 1, 2, 3$) of Eq. (2.24), we can calculate $\Delta G \equiv G_{\mathbf{R}} - G_{\mathbf{R}'}$ as follows:

$$\begin{aligned}\mathbf{R}_1 &= \left(\frac{a}{\sqrt{3}}, 0 \right); & \Delta G &= 0 \\ \mathbf{R}_2 &= \left(-\frac{a}{2\sqrt{3}}, \frac{a}{2} \right); & \Delta G &= \int_0^1 \left(\frac{a}{2} \right) B \left(x - \frac{\lambda a}{2\sqrt{3}} \right) d\lambda = \frac{Bax}{2} - \frac{Ba^2}{8\sqrt{3}} \\ \mathbf{R}_3 &= \left(-\frac{a}{2\sqrt{3}}, -\frac{a}{2} \right); & \Delta G &= \int_0^1 \left(-\frac{a}{2} \right) B \left(x - \frac{\lambda a}{2\sqrt{3}} \right) d\lambda = -\frac{Bax}{2} + \frac{Ba^2}{8\sqrt{3}}\end{aligned}\quad (6.30)$$

Expressing \mathbf{R} in unit vectors of \mathbf{a}_1 and \mathbf{a}_2 , and \mathbf{k} in units of the reciprocal lattice vectors \mathbf{b}_1 and \mathbf{b}_2 , we have discrete values of \mathbf{R} and \mathbf{k} as follows:

$$\mathbf{R} \equiv (x, y) = m\mathbf{a}_1 + n\mathbf{a}_2 = \left(-\frac{\sqrt{3}}{2}m, n + \frac{m}{2} \right), \quad \mathbf{k} = (p\mathbf{b}_1 + q\mathbf{b}_2)/L \quad (6.31)$$

where m, n, p, q are integers between 1 and L , $1 \leq m, n, p, q \leq L$. Then we transform the phase factor in Eq. (6.29) to $i(\mathbf{k} \cdot \mathbf{R} - \mathbf{k} \cdot \mathbf{R}') = i\mathbf{R} \cdot (\mathbf{k} - \mathbf{k}') - ik' \cdot (\mathbf{R}' - \mathbf{R})$, and the first term becomes $i\mathbf{R} \cdot (\mathbf{k} - \mathbf{k}') = 2\pi i[n(p-p') + m(q-q')]/L$, using Eq. (6.31). Further, the magnetic phase factor appearing in Eq. (6.29) can be expressed as:

$$\frac{ie}{\hbar} \frac{Bax}{2} = -2\pi i \left(\frac{B}{\phi_0} \frac{\sqrt{3}a^2}{4} \right) m \equiv -2\pi i \mathcal{B}m, \quad (6.32)$$

where \mathcal{B} is the number of magnetic flux quanta within a hexagon of the honeycomb lattice. Here we again assume, as in the previous section, that \mathcal{B} is a rational number which can be expressed by the ratio of two integers, r, s which have no common divisor except for unity, $\mathcal{B} = r/s$. Finally, we obtain the

following result for a matrix element of Eq. (6.29):

$$\begin{aligned} \langle \Phi_{\mathbf{k}'}^B | \mathcal{H} | \Phi_{\mathbf{k}}^A \rangle &= \frac{t}{N} \sum_{n,m} e^{2\pi i(n(p-p')+m(q-q'))/L} \left\{ e^{ik'_x a/\sqrt{3}} \right. \\ &\quad + e^{ik'_x a/2\sqrt{3}} e^{-ik'_y a/2} e^{-2\pi imr/s} e^{-2\pi ir/6s} \\ &\quad \left. + e^{ik'_x a/2\sqrt{3}} e^{ik'_y a/2} e^{2\pi imr/s} e^{2\pi ir/6s} \right\} \\ &= t\delta_{pp'} \left\{ \delta_{qq'} e^{-ik'_x a/\sqrt{3}} \right. \\ &\quad + \delta_{q,q'+L'r} e^{-2\pi ir/6s} e^{ik'_x a/2\sqrt{3}} e^{-ik'_y a/2} \\ &\quad \left. + \delta_{q,q'-L'r} e^{2\pi ir/6s} e^{ik'_x a/2\sqrt{3}} e^{ik'_y a/2} \right\}. \end{aligned} \quad (6.33)$$

The matrix element $\langle \Phi_{\mathbf{k}'}^A | \mathcal{H} | \Phi_{\mathbf{k}}^B \rangle$ is calculated in a similar way. We can then solve the $2s \times 2s$ matrix Hamiltonian as a function of k_x and k_y . In Fig. 6.3 we show the Landau energy bands of two-dimensional graphite in a magnetic field perpendicular to the two-dimensional plane. Here the ratio of the area of the unit cell to the area per quantum flux unit is $1/60$ and the energy is plotted in units of the nearest neighbor overlap energy t . Along the horizontal axis, $k_y a/4\pi$ values are plotted using the Landau gauge of Eq. (6.2). Again we can see dispersionless energy bands, except that the Landau levels near $E = 0$ have some dispersion. Comparing Fig. 6.3 with Fig. 6.2, we see that the level spacing between two dispersionless energy bands at $k = 0$ near $E = 0$ is not uniform in the case of two-dimensional graphite, in contrast to the uniform level spacing observed for the two-dimensional cosine bands.

These results are identical with the original Landau level calculation of two-dimensional graphite by McClure [9, 157] using $k \cdot p$ perturbation theory near the Fermi energy $E = 0$. When we use the approximation of linear energy dispersion near $E = 0$, the density of states is proportional to E and thus the Landau quantization occurs at $E_n = \pm C\sqrt{n}$, where C is a constant and $n = 0, 1, 2, \dots$. In this case it is interesting that we always have the $n = 0$ Landau level at $E = 0$, with a density of states that increases with increasing magnetic field, causing an increase of the free energy. This is why we calculate a large diamagnetism for graphite, in agreement with experiment. The $n = 0$ Landau level at $E = 0$ arises from a wavefunction consisting of contributions from both the bonding π and antibonding π^* bands. The equivalence between the A and B sites in the unit cell, which is discussed in Sect. 2.3 in connection with the energy dispersion relations of two-dimensional graphite, results in a band degeneracy at $E = 0$, so

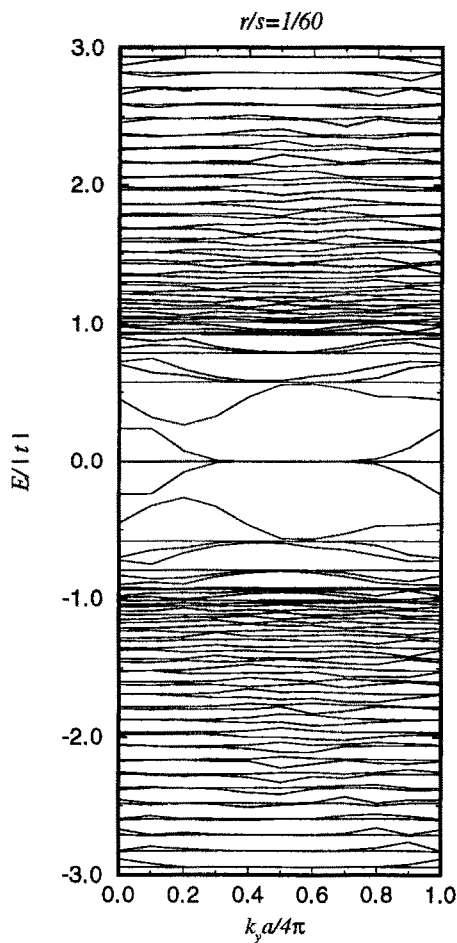


Fig. 6.3: Landau energy bands for two-dimensional graphite in a magnetic field perpendicular to the two-dimensional plane. Here the ratio of the area of the unit cell to the area per magnetic quantum flux is $1/60$. The vertical axis expresses the energy in units of the nearest neighbor overlap energy and the horizontal axis plots the k values in the y direction using the Landau gauge of Eq. (6.2).

that the π and π^* bands are not split, even in the presence of interband coupling.

In a real system, the deviation from the linear k dispersion is important for understanding the level spacing between the Landau energy bands. For example, the density of states diverges logarithmically at $E/t = \pm 1$ giving rise to a high density of energy bands. If we have dense energy bands folding into the first Brillouin zone in a weak magnetic field, we can expect the energy dispersion to become flat and the predicted \sqrt{n} level spacing to be clearly seen. Figure 6.3, however, corresponds to a very large magnetic field, for which there

is a quantum flux unit per 60 hexagons or $B \sim 10^3 \text{ T}$. In this case the number of Bloch wavefunctions that are coupled to each other ($s = 60$) is not large enough to make completely flat bands. Such a situation will occur for the case of a carbon nanotube for which the number of Bloch wavefunctions is limited not by the magnetic field, but rather by the periodic boundary conditions along the chiral vector.

6.5 Magnetic Energy Bands of Carbon Nanotubes for $\mathbf{B} \parallel z$: Aharonov–Bohm Effect

Using the method discussed in Sect. 6.3, we now consider the electronic structure of carbon nanotubes in a uniform external magnetic field. There are two high symmetry cases for the direction of the magnetic field: one with the magnetic field parallel to the nanotube axis ($\mathbf{B} \parallel z$) and the other with the magnetic field perpendicular to the nanotube axis, ($\mathbf{B} \perp z$). Hereafter the nanotube axis is taken along the z -axis. In this section we consider the case of $\mathbf{B} \parallel z$.

When the magnetic field is parallel to the nanotube axis, electrons moving within the nanotube surface will feel a force perpendicular to the surface. As far as we consider only the transfer integral between two atoms within the nanotube surface, the electronic structure would appear to be unaffected by the magnetic field. This, however, is *not* correct. The wavefunction will change its phase factor and thus its momentum, k , will shift depending on the magnetic flux penetrating the cross section of the carbon nanotube. This phenomenon is generally known as the Aharonov–Bohm effect, discussed often in the case of cylindrical geometry. Since the carbon nanotube can be a metal or a semiconductor, depending on whether there is an allowed wavevector k in the circumferential direction that has the value of the K point in the two-dimensional Brillouin zone (see Fig. 3.5), this Aharonov–Bohm effect will modify the energy gap of a carbon nanotube as a function of magnetic field [84].

Here we use the two-dimensional Cartesian coordinates (x, y) in the directions of \mathbf{C}_h and \mathbf{T} in the honeycomb lattice of Fig. 3.2 [158, 159], respectively.*

*When we roll the honeycomb lattice into a cylinder, the two-dimensional coordinate $x = r\varphi$ (where r, φ are cylindrical coordinates) becomes a curvilinear coordinate in three dimensions. We now take special care on making a rotation of the vector potential. However, as far as we use two-dimensional coordinates (x, y) on a cylindrical surface in three-dimensional space by adding a coordinate in the radial direction, r , instead of using cylindrical coordinates, (r, φ, z) ,

The vector potential \mathbf{A} for \mathbf{B}_\parallel in this coordinate system is given by,

$$\mathbf{A} = \left(\frac{\phi}{L}, 0 \right) \quad (6.34)$$

where ϕ is the magnetic flux penetrating the cross section of a carbon nanotube, and $L = |\mathbf{C}_h|$.[†] The magnetic phase factor $G_{\mathbf{R}}$ of Eq. (6.11) is given by

$$G_{\mathbf{R}} = \int_0^1 (\mathbf{r} - \mathbf{R}) \cdot \left(\frac{\phi}{L}, 0 \right) d\xi = (x - X) \frac{\phi}{L}, \quad (6.35)$$

so that the phase factor difference, $\Delta G_{\mathbf{R}\mathbf{R}'} = G_{\mathbf{R}} - G_{\mathbf{R}'}$ becomes

$$\Delta G_{\mathbf{R}\mathbf{R}'} = i \frac{X - X'}{L} \phi. \quad (6.36)$$

Thus if we shift k_x by $\phi/(L\phi_0)$, that is

$$k_x \rightarrow k_x + \frac{\phi}{L\phi_0} \quad (6.37)$$

in the magnetic Hamiltonian, the phase factor of the Bloch matrix element of Eq. (6.17) becomes,

$$\left(k_x + \frac{\phi}{L\phi_0} \right) X - \left(k'_x + \frac{\phi}{L\phi_0} \right) X' = (k_x X - k'_x X') - (X - X') \frac{\phi}{L\phi_0} \quad (6.38)$$

The second term of Eq. (6.38) cancels with the term $iG_{\mathbf{R}\mathbf{R}'}/\phi_0$ of Eq. (6.36) upon substitution into Eq. (6.17). Using this fact, we can obtain the energy bands of a carbon nanotube in a magnetic field, $\mathbf{B} \parallel z$, by shifting the one-dimensional energy bands in the direction of k_x (or \mathbf{K}_1 in Fig. 3.5) in the two-dimensional reciprocal lattice of two-dimensional graphite.

Since the presence of an energy gap in a carbon nanotube is determined by whether or not the one-dimensional energy bands cross or do not cross at the K

no complicated situations occur due to curvilinear coordinates. In fact, the coefficients often used in vector analysis becomes unity; $h_1 = h_2 = h_3 = 1$.

[†]An integration of the vector potential \mathbf{A} in Eq. (6.34) on a circumferential loop, c , satisfies

$$\phi = \oint_c \mathbf{A} \cdot d\mathbf{r} = \int_S \nabla \times \mathbf{A} \cdot d\mathbf{S} = \int_S \mathbf{B} \cdot d\mathbf{S},$$

which is consistent with the fact that the magnetic flux, ϕ , penetrates the cross section S in accordance with Stokes' theorem.

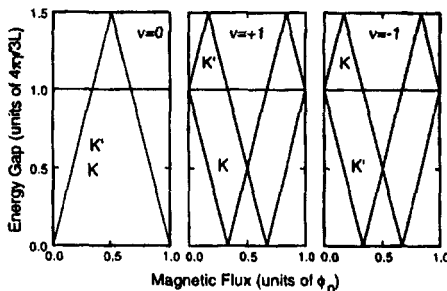


Fig. 6.4: The energy gap in units of $4\pi|\gamma|/3L$ ($\gamma \equiv |t|$) at the K and K' points of the Brillouin zone are plotted as a function of magnetic field in units of ϕ_0 for metallic ($\nu = 0$) and semiconducting ($\nu = \pm 1$) nanotubes [160]. Here ν is the residue of $(n - m)$ divided by 3.

or K' points at the corners of the 2D Brillouin zone, a semiconducting carbon nanotube can become metallic in a parallel magnetic field at certain values of the phase shift, and conversely a metallic nanotube can become semiconducting in a parallel magnetic field. The energy gap thus oscillates like a triangular chopped wave as shown in Fig. 6.4 [160], where the energy gap is plotted in units of $4\pi|t|/3L$ ($\equiv 4\pi|\gamma|/3L$ in the figure) at the K and K' points of the Brillouin zone as a function of magnetic field in units of ϕ_0 for metallic ($\nu = 0$) and semiconducting ($\nu = \pm 1$) nanotubes. Here ν is the residue of $(n - m)$ divided by 3. The energy gap is found to oscillate with a period of ϕ_0 . In the semiconducting nanotubes, the oscillations of the energy gap at the K and K' points have different phases with respect to each other, while the oscillations have the same phase in metallic nanotubes. This can be explained by a shift in the k vector in the direction of \mathbf{K}_1 .

This phenomenon corresponds to the Aharonov–Bohm (AB) effect for a carbon nanotube. The significance of the AB effect in a carbon nanotube is that the semiconducting or metallic nature of the nanotube can be altered only by applying a magnetic field parallel to the nanotube axis. This is because the distinction between a semiconducting and a metallic carbon nanotube arises from a quantum effect in which discrete wave numbers in the circumferential direction distinguish between metallic and semiconducting properties. It is noted that the one-dimensional energy dispersion relations for carbon nanotubes at the top of the valence band and the bottom of the conduction band follow a linear k relation only when the carbon nanotube is metallic. When the carbon nanotube has a semiconducting energy gap, the energy dispersion is quadratic at the top of the valence band and at the bottom of the conduction band. Thus the effective mass

of an electron contributing to the transport properties of a carbon nanotube is a function of magnetic field.

The period of the oscillatory behavior associated with the AB effect is ϕ_0 for the cross section of a given carbon nanotube. Thus the AB effect is expected to have periodicity involving a lower magnetic field for larger diameter nanotubes. In fact, the magnetic field corresponding to ϕ_0 is 1400 T for a circumference of 60 Å, but only ~ 8 T for a circumference of 800 Å.

6.6 Magnetic Energy Bands of Carbon Nanotubes for $B \perp z$: Quantum-Oscillations

Next we consider the magnetic energy bands for a magnetic field perpendicular to the nanotube axis: $B \perp z$. The two-dimensional vector potential \mathbf{A} for the nanotube surface is then given by

$$\mathbf{A} = \left(0, \frac{LB}{2\pi} \sin \frac{2\pi}{L} x \right), \quad (6.39)$$

where L is the length of the chiral vector, \mathbf{C}_h , ($L = |\mathbf{C}_h|$), and the coordinates x and y are taken along the circumferential and nanotube axis directions, respectively, in analogy to those defined in Eq. (6.34) (see Fig. 3.2).

Since all the magnetic flux which comes in at one side of a nanotube goes out from the other side, the net magnetic flux penetrating the nanotube surface is always zero. Thus when we consider the phase factor due to the magnetic field, the phase factor will always be zero (a rational number) for the original unit cell of the carbon nanotube in zero magnetic field. For a chiral vector, $\mathbf{C}_h = n\mathbf{a}_1 + m\mathbf{a}_2 = (n, m)$, (n, m : integers; $\mathbf{a}_1, \mathbf{a}_2$: unit vectors), the unit cell of the nanotube is a rectangle specified by \mathbf{C}_h and a translational vector \mathbf{T} as shown in Fig. 3.2,

$$\begin{aligned} 0 < x < L; \quad & L = a\sqrt{n^2 + m^2 + nm} \\ 0 < y < T; \quad & T = |\mathbf{T}| = \frac{\sqrt{3}L}{d_R}, \end{aligned} \quad (6.40)$$

where a is the lattice constant of the honeycomb lattice ($a = \sqrt{3}a_{C-C}$), and the integer d_R is the highest common divisor of $(2n + m, 2m + n)$ [see Eq. (3.7)].

Using the vector potential Eq. (6.39), ΔG defined by Eq. (6.19) is given by

$$\begin{aligned}\Delta G &= G_{\mathbf{R}} - G_{\mathbf{R}'} \\ &= \int_0^1 d\lambda \Delta Y \frac{LB}{2\pi} \sin \frac{2\pi}{L}(X + \lambda \Delta X) \\ &= \begin{cases} \left(\frac{L}{2\pi}\right)^2 B \frac{\Delta Y}{\Delta X} \left[\cos \frac{2\pi}{L}X - \cos \frac{2\pi}{L}(X + \Delta X) \right] & (\Delta X \neq 0) \\ \left(\frac{L}{2\pi}\right) B \Delta Y \sin \frac{2\pi}{L}X & (\Delta X = 0), \end{cases}\end{aligned}\quad (6.41)$$

where $\mathbf{R} = (X, Y)$ and $\Delta \mathbf{R} = \mathbf{R}' - \mathbf{R} = (\Delta X, \Delta Y)$. Since a carbon atom at an *A* (or *B*) site will have three nearest neighbors, we have three possible values of $(\Delta X, \Delta Y)$. Since all carbon atoms belong to either *A* sites or *B* sites, the values of $(\Delta X, \Delta Y)$ are the same for *A* sites or *B* sites. Further, the *x* coordinate of \mathbf{R} , is *X* given by the definition of the symmetry vector defined in Eq. (3.12),

$$\frac{2\pi}{L}X = \frac{2\pi}{L} \frac{N}{N}r = \frac{2\pi}{N}r, \quad (r = 1, \dots, N). \quad (6.42)$$

Since ΔG depends only on *X*, we can immediately carry out the summation on *Y* in Eq. (6.29), and thus the wavevector k_y in the *y* direction remains a quantum number of translation even in the presence of a magnetic field, $(-\pi < k_y T \leq \pi)$. This reflects the invariance of the unit cell with respect to the magnetic field. The wavevectors k_x in the *x* direction mix with each other in the presence of a magnetic field in accordance with Eq. (6.39). The total number of wavevectors in the *x* direction is *N* where

$$k_x^p = \frac{2\pi}{L}p, \quad (p = 0, \dots, N-1) \quad (6.43)$$

and *N* is the number of hexagons in the nanotube unit cell given by Eq. (3.9). Since we have two inequivalent carbon sites, *A* and *B*, in the graphene unit cell, we must solve a $2N \times 2N$ matrix to find the energy eigenvalues for a given k_y wave vector. In Fig. 6.5 we show the calculated energy dispersion relations in a transverse magnetic field for a $C_h = (10, 0)$ zigzag carbon nanotube as a function of the dimensionless wave vector $\eta = k_y T / 2\pi$ for several values of the dimensionless inverse magnetic length $L/2\pi\ell$: (a) 0.0, (b) 1.0 (c) 2.0 (d) 3.0 for the magnetic field *B* perpendicular to nanotube axis. In Fig. 6.5 we see that the energy dispersion relations for the sub-bands of the 1D carbon nanotubes become less dispersive with increasing magnetic field. Because of the

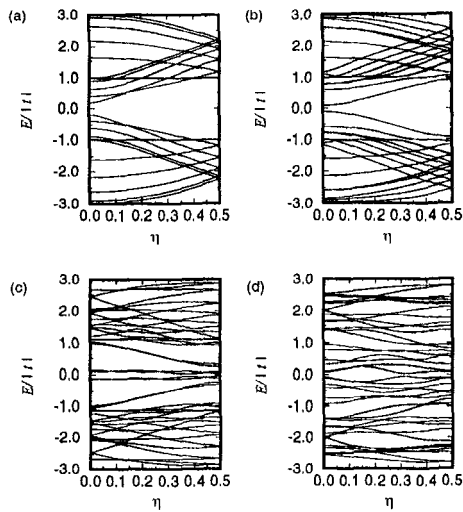


Fig. 6.5: Energy dispersion relations of a $C_h = (10,0)$ zigzag carbon nanotube as a function of the dimensionless wave vector $\eta = k_y T / 2\pi$ for several values of the dimensionless inverse magnetic length $L/2\pi\ell$: (a) 0.0, (b) 1.0 (c) 2.0 (d) 3.0, where $\ell = \sqrt{\hbar/eB}$. The magnetic field B is perpendicular to the nanotube axis, and the energy is plotted in units of $|t|$, the magnitude of the transfer integral.

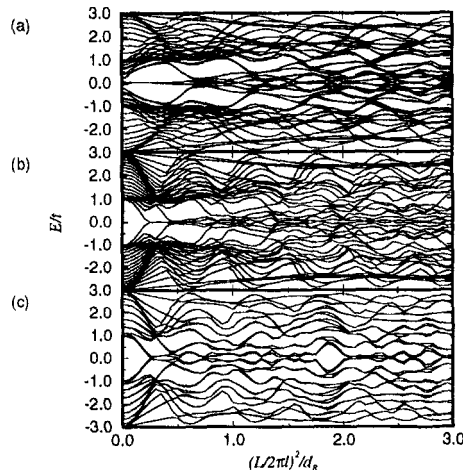


Fig. 6.6: The energy at $k_y = 0$ as a function of the dimensionless magnetic field $(L/2\pi\ell)^2/d_R$ for a zigzag nanotube (a) $(n, m) = (20, 0)$, and two armchair nanotubes of different diameters: (b) $(n, m) = (20, 20)$ (b), and $(9, 9)$ (c).

finite number (20) of wave vectors k_x along the circumference of the carbon nanotube $(n, m) = (10, 0)$, a large magnetic field (3.86×10^4 T) is required to reach $L/2\pi\ell = 3.0$. When the diameter (or L) increases, the magnetic field required to form Landau subbands becomes smaller, and the calculated dispersion relations approach those of $\vec{k} \cdot \vec{p}$ perturbation theory near the Γ point.

In Fig. 6.6 the energy at $k_y = 0$ as a function of the dimensionless magnetic

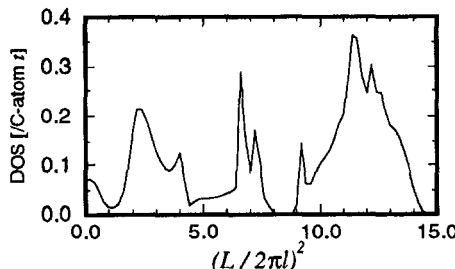


Fig. 6.7: Density of states per carbon atom at the Fermi energy for a $C_h = (9, 0)$ zigzag nanotube as a function of the dimensionless magnetic field $(L/2\pi\ell)^2$.

field, $(L/2\pi\ell)^2/d_R$, is shown for a zigzag nanotube $(n, m) = (20, 0)$ [Fig. 6.6(a)], and for two armchair nanotubes of different diameters $(n, m) = (20, 20)$ [Fig. 6.6(b)] and $(9, 9)$ [Fig. 6.6(c)]. The mixing of Bloch orbitals with different k_x values oscillates periodically as a function of magnetic field, which can be scaled by the dimensionless magnetic field.

The energy dispersion near the Fermi energy is especially important. In Fig. 6.7 the density of states at the Fermi energy is plotted for a $C_h = (9, 0)$ zigzag nanotube as a function of the dimensionless magnetic field $\nu^2 = (L/2\pi\ell)^2$. Figure 6.7 shows that when the magnetic field increases, a metallic Fermi surface appears and disappears in an irregular manner. This phenomena can be identified with the Aharonov–Bohm effect, in analogy to the case of $B_{||}$ discussed in Sect. 6.5. The irregular oscillation in Fig. 6.7 might be related to the oscillation of the electronic conductance of a multi-layer carbon nanotube as a function of magnetic field at low temperature.

CHAPTER 7. Connecting Carbon Nanotubes

Connecting two single-wall carbon nanotubes is an interesting problem, since a semiconductor-metal junction is realized by connecting a semiconductor and a metal carbon nanotube. In this chapter we first show how to connect two carbon nanotubes and then we calculate the electrical conductance of such a junction.

7.1 Net Diagrams of a Junction

There are many illustrations such as Fig. 7.1 in the literature showing the junction between two carbon nanotubes with different diameters using high resolution transmission microscopy [107]. In this figure the larger diameter multi-wall carbon nanotube AB is joined to a smaller diameter multi-wall nanotube CD through a junction section BC containing a single pentagon B and a single heptagon C . In this chapter the general framework for joining two single-wall nanotubes of different diameters and chiralities is presented in Sect.7.1, Sect.7.2 and Sect.7.3, while in Sect.7.4 the transport properties of such nanotube junctions are discussed. Coiled carbon nanotubes are reviewed in Sect.7.5.

As discussed in Fig. 3.2, a net diagram of a carbon nanotube, as it relates to rolling up a graphene honeycomb sheet of width L equal to the magnitude of the chiral vector, provides a useful description for considering the three dimensional structure of a single carbon nanotube. In this section we use a net diagram to describe a junction which connects two carbon nanotubes of different geometries [i.e., described by different chiral vectors (n, m)]. In Sect.7.2 we show that two arbitrary nanotubes can be joined in a unique way by introducing a single pentagon and heptagon pair, and by demonstrating the resulting junction explicitly.

In Fig. 7.2, we show examples of (a) $(12,0)-(9,0)$ and (b) $(12,0)-(8,0)$ zigzag

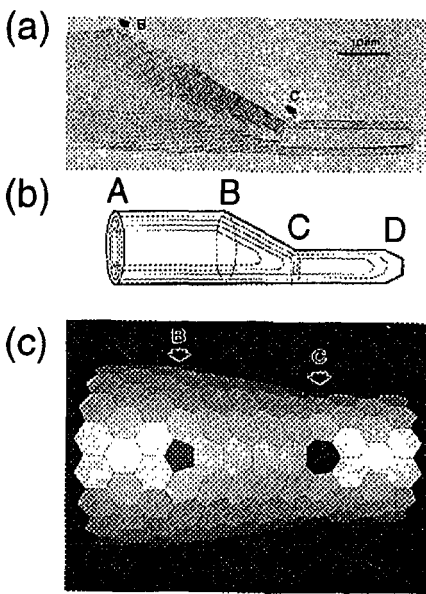


Fig. 7.1: (a) A high resolution TEM image of the junction between two multi-wall carbon nanotubes. (b) A schematic representation of (a). (c) A schematic illustration of the transition region between nanotubes of different diameters, showing a pentagon and heptagon at *B* and *C*, respectively [107].

nanotube junctions, in which the carbon atoms of the pentagon and the heptagon rings are indicated by filled circles. All the other polygons in the nanotube junction region are hexagons. All carbon atoms in the junction have three σ sp^2 covalent bonds, and there are no sp^3 covalent bonds in the junction.* Thus we can say that the pentagon and heptagon defects are topological point defects, associated with the joining of the two nanotubes. The positive curvature of the pentagonal ring, as is generally seen in fullerenes, makes the diameter of the carbon nanotube decrease in going from left to right in Fig. 7.2, and the negative curvature of the heptagonal ring prevents further decrease in the nanotube diameter. Thus, when the difference between the diameters of the

*Here we neglect the small sp^3 component in the σ bonds due to the curvature of the tube and the junction.

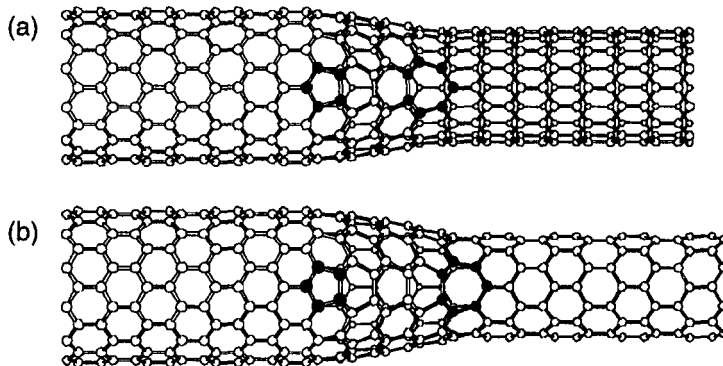


Fig. 7.2: (a) (12,0)–(9,0) and (b) (12,0)–(8,0) zigzag nanotubes are shown in which the carbon atoms of the pentagon and the heptagon are indicated by filled circles. For each nanotube, eight circumferential zigzag chains are shown.

two carbon nanotubes becomes large, the distance between the pentagon and heptagon also becomes large.

In Fig. 7.3 we show a net diagram of two carbon nanotubes which are given by the rectangles $TABU$ and $RCDS$. The smaller tube $TABU$ and the larger tube $RCDS$, are uniquely determined by the chiral vectors, \overrightarrow{AB} and \overrightarrow{CD} , respectively. Here a pentagon exists at the site C (or D) and a heptagon exists at A (or B).[†] Since the solid angles of a pentagon and a heptagon in the fullerene are $2\pi - \pi/3$ and $2\pi + \pi/3$, respectively, the sum of the angles on the net diagram around the pentagon and the heptagon, indicated by shaded hexagons, should correspond to these angles. This fact gives the angle relations:

$$\angle ACR + \angle BDS = \frac{5\pi}{3}, \quad \text{and} \quad \angle CAT + \angle DBU = \frac{7\pi}{3}. \quad (7.1)$$

The three-dimensional structure is obtained by connecting AT to BU , AC to BD , and CR to DS through cylindrical surfaces. When we roll up the net diagram to make a tube, the chiral vectors \overrightarrow{AB} and \overrightarrow{CD} correspond to the

[†]This situation can be easily understood when the reader copies Fig. 7.3 and makes a junction by cutting and connecting the edges.

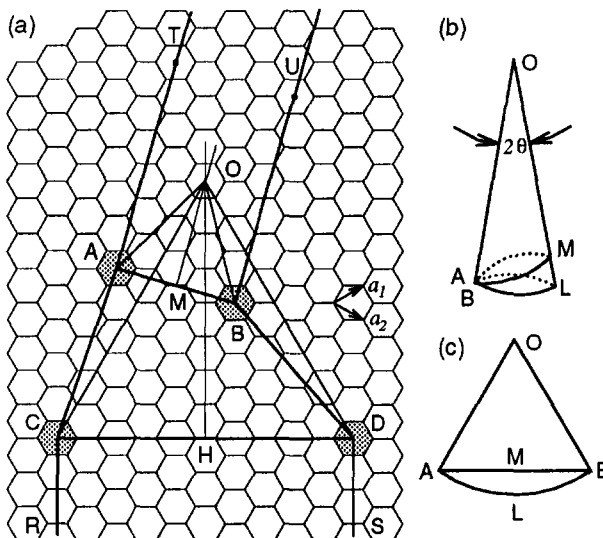


Fig. 7.3: (a) Net Diagram for the joint between two nanotubes. The chiral vectors for the two nanotubes are shown by \vec{AB} and \vec{CD} . The three-dimensional structure is obtained by connecting AT to BU , AC to BD , and CR to DS through cylindrical surfaces. At the shaded hexagons in the figure, a pentagon exists at the site C (or D) and a heptagon exists at A (or B). The joint region is uniquely expressed by a vector, \vec{CA} , which is given by Eq. (7.5). (b) The cone of $OALB$ and (c) its projection are shown for understanding that the line AMB is a line of minimum length for going around the surface of the cone. The relation $OM \perp AMB$ satisfies both (b) and (c).

circumferential directions of the tubes while the translational vectors \vec{AT} and \vec{CR} which are perpendicular to \vec{AB} and \vec{CD} , respectively, correspond to the directions of the nanotube axes in three dimensions.

7.2 The Rule for Connecting Two Nanotubes

From Eq. (7.1) and using the fact that we connect AC to BD in Fig. 7.3, we get

$$\angle ACD + \angle BDC = \frac{2\pi}{3} \quad \text{and} \quad AC = BD. \quad (7.2)$$

Then \overrightarrow{BD} is given by (1) rotating \overrightarrow{AC} around C by $\pi/3$ and then (2) translating by \overrightarrow{CD} . The conditions in Eq. (7.2) give the rule for connecting two nanotubes as discussed below.

First we will give a formula for rotating a vector $\vec{v}_{n,m} = n\vec{a}_1 + m\vec{a}_2 \equiv (n, m)$ by $\pi/3$ on a honeycomb lattice. Denoting a $\pi/3$ rotation by \mathcal{R} , we get

$$\mathcal{R}\vec{a}_1 = \vec{a}_1 - \vec{a}_2, \quad \mathcal{R}\vec{a}_2 = \vec{a}_1. \quad (7.3)$$

Thus $\mathcal{R}\vec{v}_{n,m}$ is given by

$$\mathcal{R}\vec{v}_{n,m} = n(\vec{a}_1 - \vec{a}_2) + m\vec{a}_1 = \vec{v}_{n+m, -n}. \quad (7.4)$$

This formula of Eq. (7.4) for $\mathcal{R}\vec{v}_{n,m}$ will be used frequently in the following discussion.

Hereafter we denote \overrightarrow{CD} , \overrightarrow{AB} , and \overrightarrow{CA} as $\overrightarrow{CD} = \vec{C}_5 = (n_5, m_5)$, $\overrightarrow{AB} = \vec{C}_7 = (n_7, m_7)$,* and $\overrightarrow{CA} = \vec{j} = (j_1, j_2)$, respectively, where n_5, m_5, n_7, m_7, j_1 , and j_2 are integers. Then the condition for j_1 and j_2 for given \vec{C}_5 and \vec{C}_7 vectors is,

$$\overrightarrow{DC} + \overrightarrow{CA} + \overrightarrow{AB} = -\vec{C}_5 + \vec{j} + \vec{C}_7 = \mathcal{R}\vec{j} = \overrightarrow{DB}. \quad (7.5)$$

Using Eq. (7.4), we obtain the components of the joint vector \vec{j}

$$(j_1, j_2) = (n_5 + m_5 - n_7 - m_7, n_7 - n_5). \quad (7.6)$$

Thus the joint vector, \vec{j} , is uniquely determined, once the two chiral vectors, \vec{C}_5 and \vec{C}_7 are given. Figure 7.3 is drawn for $\vec{C}_5 = (5, 5)$, and $\vec{C}_7 = (1, 3)$, which gives $\vec{j} = (6, -4)$, and $\mathcal{R}\vec{j} = (2, -6)$.

*Here 5 and 7 in \vec{C}_5 and \vec{C}_7 mean that the chiral vectors C_5 and C_7 exist on the pentagon and heptagon sides of the junction, respectively.

7.3 Shape of a Junction

The polygon, $ACDB$, in the net diagram of Fig. 7.3(a) denotes the joint which connects the two nanotubes. The shape of the joint determines the shape and axis of the cone as shown in Figs. 7.3(b) and (c). $ACDB$ is part of a cone whose vertex is denoted by O in Fig. 7.3(a), while the cone and its projection, respectively, are shown in Figs. 7.3(b) and (c). For the cone, $OALB$, the line AMB is a line of minimum length for going around the surface of the cone, in which $OM \perp AMB$ satisfies both Figs. 7.3(b) and (c). We assume here that the lines AMB and CHD in Fig. 7.3(a) correspond to the minimum lines of the cone surface. This idea is valid, too, for the two tubes, $TABU$ and $RCDS$, where the lines AMB and CHD are minimum in length for going around the nanotube surface. Thus this assumption regarding minimum length lines seems to be reasonable. It should be mentioned here that the path AMB is an ellipse on the cone surface in three dimensions [see Fig. 7.3(b)], while the path AMB is a circle on the nanotube surface. Thus we always expect some distortion arising from the elliptical shape of the cone section relative to the circle shape of the nanotube surface. However, this fact does not affect the angle on the tube or cone surface, since the distortion is perpendicular to the surface.

Within this assumption, the vertex of the cone, O , is defined as the crossing of the two lines OM and OH such that OM and OH are perpendicular bisectors of AB and CD , respectively. Since $OA = OB$, $OC = OD$, and $AC = BD$, the two triangles, $\triangle OAC \equiv \triangle OBD$, are identical to each other. Thus $\angle ACO = \angle BDO$, which gives $\angle ACD + \angle BDC = \angle OCD + \angle ODC = \pi/3$. Thus we conclude that $\triangle OCD$ is a regular triangle. Similarly, since $\angle AOC = \angle BOD$, we have $\angle AOB = \angle COD = \pi/3$. Thus $\triangle OAB$ is a regular triangle, too. The position of O is given by rotating \vec{CD} or \vec{AB} by $\pi/3$,

$$\begin{aligned}\vec{CO} &= \mathcal{R} \vec{CD} = (n_5 + m_5, -n_5), \\ \vec{AO} &= \mathcal{R} \vec{AB} = (n_7 + m_7, -n_7).\end{aligned}\tag{7.7}$$

We can easily check from Eqs. (7.6) and (7.7) that $\vec{CO} - \vec{AO} = \vec{j}$.

When we define the angle of the vertex of the cone in three dimensions as 2θ , as is shown in Fig. 7.3(b), θ is given by

$$\theta = \sin^{-1} \frac{1}{6} \simeq 9.594^\circ.\tag{7.8}$$

The angle θ is the angle between the axis of the tube and the axis of the cone in three dimensions. If the points O , B , and D in Fig. 7.3(a) lie on a line, the angle between the two axes of the tubes becomes zero, but when the pentagon and the heptagon are on opposite sides of the cone surface, then the angle between the two axes of the tubes becomes $2\theta = 19.19^\circ$.

When the pentagon and heptagon are neither along the same line nor on opposite sides of the cones, the two nanotube axes do not intersect with each other. In this case, we can define a dihedral angle, φ , between two planes as shown in Fig. 7.4. The two planes are defined by (1) the cone axis OF and an axis of the tube at the pentagon side FE , and (2) the cone axis OF and an axis of the tube at the heptagon side GK . The dihedral angle, φ , is defined by the rotation angle around the cone axis between $\triangle OFD$ and $\triangle OFN$, as shown in Figs. 7.4(a) and (b).

The dihedral angle φ is relevant to the angle $\angle BOD = \Phi$ shown in the projection map of Fig. 7.3(a) as follows,*

$$\varphi = 2\pi \times \frac{\Phi}{\pi/3} = 6\Phi \quad (7.9)$$

where Φ is given by

$$\cos \Phi = \frac{|\vec{C}_5|^2 + |\vec{C}_7|^2 - |\vec{j}|^2}{2\vec{C}_5 \cdot \vec{C}_7}. \quad (7.10)$$

Using Eq. (7.6), we can write the angles, Φ and φ , as a function of n_5 , m_5 , n_7 and m_7 .

The dihedral angle is useful for understanding the three-dimensional structure of the two nanotube axes and the single cone axis joining the two carbon nanotubes. The thick line $EFGK$ provides a wire frame model for representing the axes for the nanotubes and the cone. The definition of the dihedral angle provides a good analogy to chemistry, since the dihedral angle of a three-dimensional molecule is defined by three chemical bonds.

When the dihedral angle φ is π , the positions of the pentagon and the heptagon (D and B in Fig. 7.4, respectively) are opposite each other. In this case the bending angle of the nanotube axes in the net diagram, which corresponds

*To obtain Eq. (7.9), we use the following facts [see Fig. 7.4(b)]: $DN = OD \cdot \Phi = FN \cdot \varphi$ and $OD : FN = 2\pi : \pi/3$.

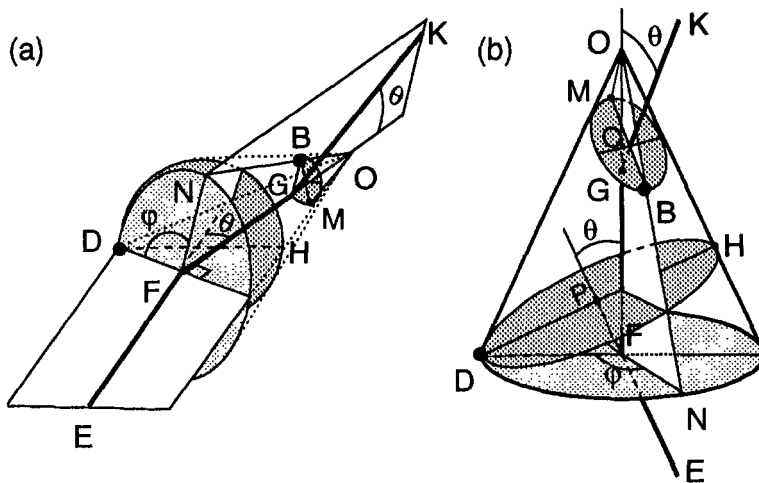


Fig. 7.4: (a) The dihedral angle, $\angle NFD = \varphi$ is defined between the two planes $\triangle OFD$ and $\triangle OFN$. Here the axis of the cone, OF , is on both planes. FE and GK are the axes of the two nanotubes. It is noted that points O, F, D and E are in a plane and that G, F, K and N are in another single plane. The thick line $EFGK$ corresponds to a wire frame model for reproducing the axes for the nanotubes and the cone. D and B are the positions of the pentagon and the heptagon, respectively, in the joint region (see Fig. 7.3). The light shaded circle is the bottom surface of the cone and two dark shaded ellipses are the cross sections between the cone and each nanotube. The crossing points of the cone axis with the nanotube axes, F and G , are not located on these ellipses. The bond angles, $\angle GFE$ and $\angle FGK$, sum to $\pi - \theta$. (b) Another view of the dihedral angle, φ , shown on the cone. Here $DH \perp OH$ and $OM \perp MB$. Points P and Q are both centers of ellipses.

to Φ in Eq. (7.9), becomes $\pi/6$ (or 30°), which corresponds to the case discussed by Dunlap [161, 162].

The points P and Q are both centers of the dark shaded ellipses in Fig. 7.4(b), and both P and Q are on the nanotube axes. The ellipses are defined by rolling

up AMB and CHD in Fig. 7.3 so that $DH \perp OH$ and $OM \perp MB$ in Figs. 7.3 and 7.4. It is clearly seen from Fig. 7.4(b) that P and Q are not crossing points of the nanotube axes with the cone axis, FG . Thus the nanotube axis length on the pentagon side becomes shorter by PF in the wire frame model and the nanotube axis length on the heptagon side becomes longer by GQ , where PF and GQ are given by

$$PF = |\vec{C}_5| \sin^2 \theta, \quad GQ = |\vec{C}_7| \sin^2 \theta. \quad (7.11)$$

The length of the cone axis FG is given by

$$FG = OF - OG = (|\vec{C}_5| - |\vec{C}_7|) \cos \theta, \quad (7.12)$$

using the fact that $OG \perp GB$.

Finally we discuss the shape of the dark shaded ellipses shown in Fig. 7.4(b). The bond angles, $\angle GFE$ and $\angle FGK$, sum to $\pi - \theta$, and the two dark shaded ellipses have the same eccentricity but have different sizes. When we denote the longer and the shorter axes of the ellipses as a and b , the ratio of b to a is given as a function of θ . After some calculation, b/a is given by

$$\frac{b}{a} = \left(1 + \frac{4}{3} \sin^2 \theta - \frac{2\sqrt{3}}{3} \tan \theta \right)^{1/2} \sim 0.918 \quad (7.13)$$

where we make use of Eq. (7.8). Thus the cross section of the circle at the end of the nanotube is distorted by $1 - 0.918 = 0.082 = 8.2\%$ distortion at the junction. Using all the formulae given here, the skeleton of the wire frame in three dimensions is well defined by only the four integers of the two chiral vectors, n_5 , m_5 , n_7 and m_7 . It is important to point out that there is no ambiguity in the structure of the junction if we specify the two chiral vectors of the nanotubes. Thus the geometrically optimized structure or electronic structure of the connected nanotubes is uniquely described by the chiral vectors of the two nanotubes. In the next section, we consider some specific cases and their electronic structure.

7.4 Tunneling Conductance of a Junction

To discuss the electronic structure and the tunneling conductance of a junction connecting two carbon nanotubes, we consider a system that includes the

(n_5, m_5) nanotube, the (n_7, m_7) nanotube, and the junction region between them. Since we consider carbon nanotubes of finite length, all electronic states are given by discrete electronic levels, and Gaussian broadening is used for calculating the density of states and for calculating the conductance.

The structure of the junctions that we use for illustrative purposes is the junction between two zigzag nanotubes [69]. A zigzag nanotube defined by $(n, 0)$, where n is an integer, has one of the smallest unit cells among carbon nanotubes, and the electronic structure of a zigzag nanotube is either metallic or semiconducting, depending on whether or not n is a multiple of 3, respectively, as discussed in Fig. 4.2. An armchair nanotube, (n, n) , also has a small unit cell, but all armchair nanotubes are known to be metallic. Thus zigzag nanotubes are suitable for considering a metal-semiconductor junction and armchair nanotubes are not. In Fig. 7.2 we show the top view of the junction of two zig-zag nanotubes for the cases: (a) $(12,0)-(9,0)$ and (b) $(12,0)-(8,0)$ zigzag nanotubes, which are used here as examples of a metal-metal junction and a metal-semiconductor junction, respectively. Carbon atoms for the pentagon and heptagon rings are indicated in Fig. 7.2 by filled circles. The corresponding junction vectors, (j_1, j_2) , are given by $(3, -3)$ and $(4, -4)$, respectively, and the dihedral angle φ is always zero for zigzag-zigzag carbon nanotube junctions. The three-dimensional lattice structure is represented by formulae given in Sect. 7.3. In the calculation, the lengths of the carbon nanotubes at both ends are taken as 16 unit cells, though only 8 unit cells are shown in Fig. 7.2. Here the unit vector of each zigzag nanotube is \vec{a}_2 if \vec{a}_1 is selected in the circumferential direction, and the unit cells of each carbon nanotube start from the carbon atoms of the pentagon or the heptagon that is connected to each nanotube. The total numbers of carbon atoms in the calculations are thus 735 and 720 for the $(12,0)-(9,0)$ and $(12,0)-(8,0)$ zigzag nanotubes, respectively.

The electronic structure is calculated by a simple tight-binding method in which only the nearest-neighbor transfer energy, t , for π orbitals is considered, and the small hybridization due to the curvature of the nanotube or junction is neglected. All the calculated energies are in units of t , whose magnitude is known to be between 2.5 eV and 3.13 eV [69]. At the ends of the carbon nanotube, the dangling covalent π bonds give rise to edge states, with eigenvalues $E = 0$ and eigenfunctions localized in a region about $6a$ ($a = |\vec{a}_1|$) from the nanotube end. Since only the amplitude of the wavefunction in the junction is included

in the conductance calculation, the effect of these edge states is automatically excluded.

The calculated results show that the eigenfunctions of the energy levels consist of contributions from: (1) the delocalized wavefunction for the whole system, (2) the delocalized wavefunctions for each of the carbon nanotubes, and (3) edge states localized at the both ends. Since translational symmetry is broken at the junction, the Bloch wavefunctions of each carbon nanotube are scattered by the pentagon, the heptagon and the junction region of the nanotubes. If the energies of the wavefunctions in the two carbon nanotubes are equal to each other, a delocalized wavefunction for the whole system is formed. Otherwise, a delocalized wavefunction is formed only in each nanotube region. This situation is easily explained by the fact that the plane wave of an electron is reflected or transmitted at a positive square potential, which gives rise to a tunneling probability as a function of electron energy. There are, however, no localized states in the junction region, because the junction does not correspond to an attractive potential.

In Fig. 7.5, the density of states for the junction of the (a) (12,0)–(9,0) and (b) (12,0)–(8,0) zigzag nanotubes is plotted per carbon atom per energy t , as a function of energy in units of $|t|$. The energies of all eigenstates are within $|E/t| \leq 3$, which is consistent with three carbon bonds associated with each carbon atom. Here again all $E = 0$ states (see Fig. 7.5) correspond to edge states whose wavefunctions are localized not in the junction region but rather at both ends of the nanotubes. Thus these states do not contribute to the conductance, though their energy is at the Fermi energy $E = 0$. The density of states of these connected two-nanotube systems can be understood primarily as the sum of the density of states of the two constituent carbon nanotubes. We can see in the plot of the density of states (Fig. 7.5) that not only the two-dimensional van Hove singularities of graphite at $E/t = \pm 1$ but also many one-dimensional $1/\sqrt{E}$ singularities due to the one-dimensional energy bands are quantized in the circumferential direction [69]. Even when we remove the contribution of the localized states to the density of states, the resulting density of states is finite near the Fermi energy $E/t = 0$ which indicates that one-dimensional metallic energy bands exist for both the (12,0) and (9,0) nanotubes.

In the case of the metal-semiconductor (12,0)–(8,0) zigzag nanotubes, the density of states near the Fermi energy is smaller than that of the (12,0)–(9,0)

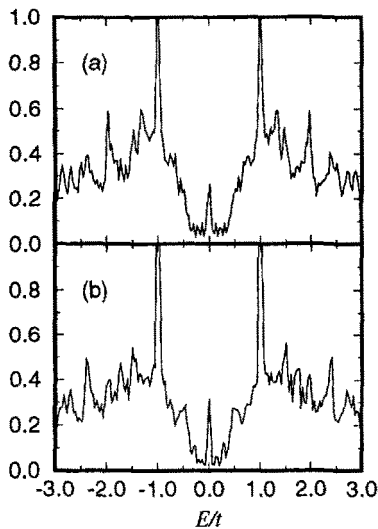


Fig. 7.5: The density of states of junctions for (a) (12,0)–(9,0) and (b) (12,0)–(8,0) zigzag nanotubes plotted in units per single carbon atom per energy t , where the structures are shown in Fig. 7.4. All $E = 0$ states correspond to edge states whose wavefunctions are localized not in the junction region but rather at either end of the nanotubes.

system because of the absence of a finite density of states for the (8,0) carbon nanotube near the Fermi energy. It might be difficult to see the differences between Fig. 7.5(a) and (b). However when we look carefully at the almost constant density of states region around $E = 0$, Fig. 7.5(a) shows a larger value of the density of states than Fig. 7.5(b), and also the energy width for the constant region is the larger in the case of Fig. 7.5(a). These differences can be explained as follows. By calculating the energy levels of a (8,0) nanotube with the same length, we get an energy gap of $E_g/|t| = 0.62$. Because of the Gaussian broadening that is used, $\Delta E/|t| = 0.033$, the energy gap is reduced to $E_g/|t| = 0.55$. In this case the wavefunctions are only delocalized in the (12,0) nanotube region near the Fermi energy, and not in the (8,0) nanotube.

Using the eigenfunctions for the electrons in the nanotube junction structures shown in Fig. 7.4, the conductance can be determined by calculating the current density. When a voltage V is applied to this system, the tunneling electric current, I , is given by [163]

$$I = 2\pi e\hbar \int dE \{f(E) - f(E + eV)\} \times \sum_{ii'jj'} G_{ii'}(E) J_{ij} G_{jj'}(E + eV) J_{i'j'}. \quad (7.14)$$

Here G is the imaginary part of the resolvent given by

$$G_{ii}(E) = \sum_{\mu} C_{i\mu}^* C_{i\mu} \delta(E - E_{\mu}), \quad (7.15)$$

where E_{μ} and $C_{i\mu}$ are the μ -th eigenvalue and i -th component of the μ -th eigenfunction, respectively, which are obtained by solving the tight-binding Hamiltonian for the junction structure, such as shown in Fig. 7.4. Returning to Eq. (7.14), J_{ij} is the current operator for atomic orbitals at sites i and j given by

$$J_{ij} = \frac{\hbar}{2m} \int_{S_0} dS \{ \varphi_i \nabla \varphi_j^* - \varphi_j^* \nabla \varphi_i \} \quad (7.16)$$

where φ_i is i -th atomic orbital, and the integration is taken at the same surface S_0 as was used for calculating the current density. By converting Eq. (7.16) from a surface integral to a volume integral [163], we see that J_{ij} is non-vanishing only for i and j at nearest neighbor sites, and in regions where the voltage changes significantly between sites i and j . Here we assume that it is only in the junction region that we expect a voltage drop. Since this nanotube junction system is so small, we consider the carbon network to be in the mesoscopic regime, in which electrons are not scattered in the periodic region but only in the junction region. Tunneling current appears when the energy of the wavefunction to the left of the junction coincides with the energy plus eV of that to the right. This formulation may be valid even for delocalized wavefunctions over the whole region. When the voltage matches the tunneling condition for connecting delocalized wavefunctions over the whole region, the wavefunction that is then obtained should be approximated by a delocalized wavefunction at $V = 0$.

In Fig. 7.6, we show the calculated conductance I/V for the carbon nanotube junctions of Fig. 7.4 (a) (12,0)–(9,0) and (b) (12,0)–(8,0) zigzag carbon nanotubes. The plots in Fig. 7.6 are made as a function of applied voltage $-0.5 < V/t < 0.5$, for two different Gaussian broadening values, $\Delta E/t = 0.33$ (solid line) and $\Delta E/t = 0.50$ (dotted line), used above for calculating G_{ii} , etc. In the case of (a) for metallic-metallic nanotube junctions, the conductance increases with increasing applied voltage. The oscillations in the conductance show resonances in the tunneling probability between the two nanotubes, and these oscillations are closely related to the universal conductance fluctuations [164] recently reported in carbon nanotubes [165]. The increase of the conductance with increasing V comes from the fact that (1) the resonance tunneling probability is

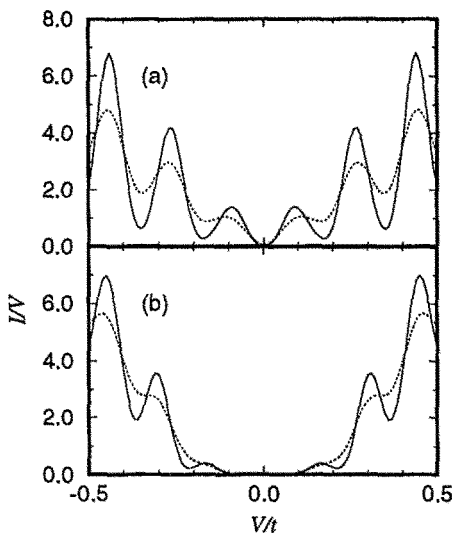


Fig. 7.6: Calculated conductance I/V for (a) $(12,0)-(9,0)$ and (b) $(12,0)-(8,0)$ zigzag carbon nanotube junction (see Fig. 7.4 for their structures), as a function of voltage V in units of $|t|$, using two different Gaussian broadening values, $\Delta E/|t| = 0.33$ (solid line) and $\Delta E/|t| = 0.50$ (dotted line). The estimated energy gap for the $(8,0)$ semiconductor nanotube is $0.55|t|$.

proportional to V , if the density of states is constant near the Fermi energy, and that (2) the current operator, J_{ij} , is proportional to V . Again it is noted that there is no contribution to the conductance from the edge states, which can be automatically excluded because their wavefunctions have no amplitude in the junction region.

On the other hand, in the case of Fig. 7.6(b) for a metal-semiconductor nanotube junction, there is no conductance in the energy gap region for the semiconducting $(8,0)$ nanotube though there is a finite density of states near the Fermi level. The results clearly show that a delocalized wavefunction is present near the Fermi level only in the metallic $(12,0)$ nanotube region. Thus it is concluded that a semiconductor-metal junction is well established even in a nano-scale, mesoscopic structure.

When the length of the nanotube increases, there are more states near the Fermi level. Thus the amplitude of the oscillations will decrease relative to the absolute value of the tunneling conductance and the average level spacings will decrease as energy bands are formed. The calculated results with larger energy broadening ΔE (dotted line in Fig. 7.6) are closer to this case compared to the plot for smaller ΔE . However, if there is a structural defect in the nanotube, weak localization will make it possible to have a finite level spacing near the

junction region which gives rise to conductance fluctuations. This might be a possible reason for the observation of universal conductance fluctuations in carbon nanotube systems in which the region of the voltage drop corresponds to a disordered region [164].

In the above discussion we have assumed a voltage drop in the junction. The reason for this assumption is that we obtain three kinds of wavefunctions in the above calculation and that two of the three are localized in the constituent nanotubes. However, if there is no voltage drop at the junction nor over the nanotubes, we can treat the conductivity by the linear-response theory known as Landauer's formula [166, 167] (see Sect. 8.1.1). Especially when we consider a metal-metal junction system connecting two semi-infinite metallic nanotubes, the energy subbands at the Fermi energy can be well defined over the junction and thus this assumption may be applied.

In Landauer's formula, the conductance G is given by

$$G = \frac{e^2}{\pi \hbar} \sum_{m,n} |t_{mn}|^2, \quad (7.17)$$

where t_{mn} is the transmission coefficient between the incident channel n on the left side and the outgoing channel m in the right side. As for the channels, we consider only energy subbands which cross the Fermi energy. We have shown in the Chapter 4 that there are two metallic channels whose wave vector corresponds to the K and K' points of the two-dimensional Brillouin zone. Thus, we have four contributions of channels $\{m, n\} = \{K, K\}, \{K, K'\}, \{K', K\},$ and $\{K', K'\}$ [168, 169]. The transmission probability t_{mn} is calculated by the recursive Green's function technique [170] in which the S matrix is calculated by a tight-binding calculation [169] or by a $k \cdot p$ method in a magnetic field [168]. An interesting result is a scaling law for the radii of the constituent nanotubes, R_2/R_1 , expressed by a dimensionless scaling function f ,

$$\sigma = \frac{e^2}{\pi \hbar} f\left(\frac{R_2}{R_1}\right). \quad (7.18)$$

When $R_2/R_1 \gg 2$, numerical calculations show that $f(R_2/R_1) \propto (R_2/R_1)^3$ [169]. This result clearly gives the power dependence of the amplitude of the wavefunctions in the junction region.

The conductance of a junction in a magnetic field is an important tool for monitoring the phase change of the scattered wavefunction at the junction. The

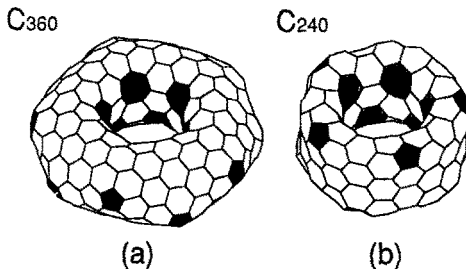


Fig. 7.7: Optimized toroidal structures: (a) torus C_{360} and (b) torus C_{240} : Pentagons and heptagons are shaded. The diameters of the central toroidal hole are the same for (a) and (b), 7.8 Å, which is close to the diameter of the C_{60} molecule [171].

mixing of the wavefunctions between the K and K' wave vectors occurs at a pair of pentagonal and heptagonal defects, which are known as inter-valley scattering centers. We also have intra-valley scattering centers where the wavefunction is scattered by defects without experiencing any change of wave vector. Numerical calculations show that the ratio of the intra- and inter-valley scattering processes can be modified by a magnetic field [168]. These phenomena can be applied to enhance the capabilities of nano-scale magnetic devices.

7.5 Coiled Carbon Nanotubes

In this section, we show much more complicated cage structures which have many pentagon-heptagon pairs. These complicated cage structures were first discussed in detail mainly by Ihara and his coworkers [171]. One possible shape for a nanotube is a toroidal (or donut) shape, and the other shape is a helically coiled shape, as shown in Figs. 7.7 and 7.8, respectively.

Several observations of semi-toroidal structures are described in the literature for single-wall nanotubes [54], and for multi-wall nanotubes, including both arc discharge grown nanotubes [107] and carbon nanotubes prepared from pyrolytic carbon and heat treated to 2800°C [59]. Figure 7.9(b) shows a typical toroidal structure, which can be readily understood using the schematic diagram in Fig. 7.9(a) in terms of a sock turned inside out.

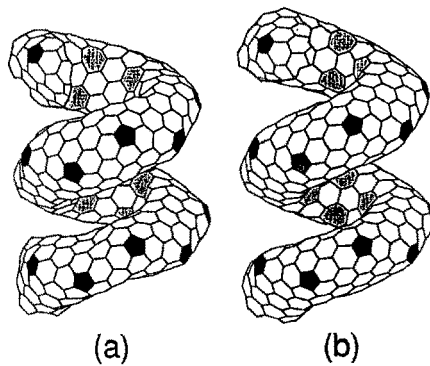


Fig. 7.8: Helically coiled nanotubes: in both cases, one pitch contains a torus C_{360} . (a) coil length = 12.9 Å and (b) coil length = 13.23 Å. The tiling pattern of heptagons in the inner ridge line is changed upon changing the coil length, though the pattern of pentagons in the outer ridge is fixed.

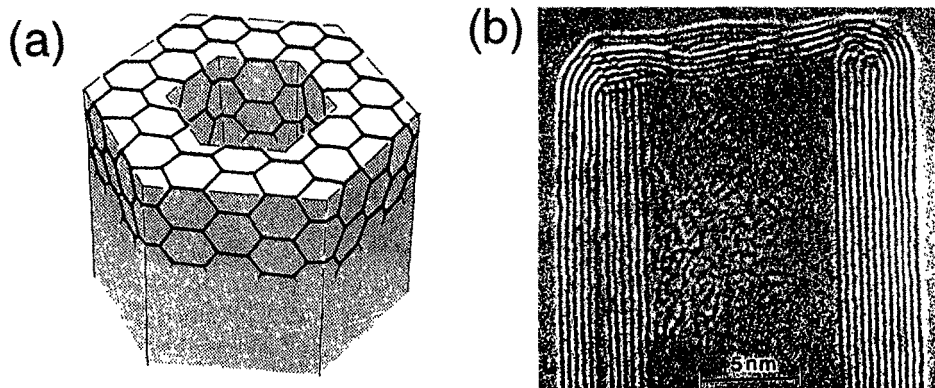


Fig. 7.9: (a) Illustration of a semi-toroidal termination of a nanotube which is caused by six pairs of pentagonal and heptagonal rings in a hexagon network. (b) A TEM micrograph of a semi-toroidal termination of a nanotube which consists of six graphene shells [107].

Helically-coiled carbon nanotubes which are obtained by using a cobalt cat-

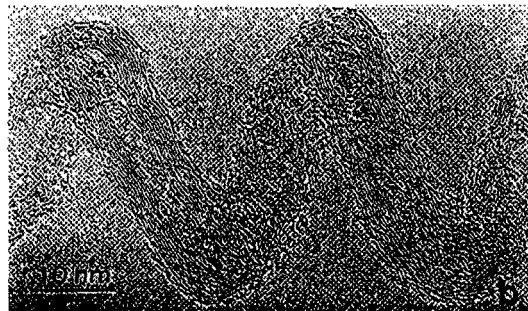


Fig. 7.10: A high resolution TEM image of a helix-shaped structure with a radius of about 18 nm, and a pitch of about 30 nm. This multi-wall coiled carbon nanotube contains about 10 wall layers [173].

alyst on a silica surface, have also been observed by high resolution TEM with inner and outer diameters in the range 3–7 nm and 15–20 nm, respectively, and up to 30 μm in length, as shown in Fig. 7.10. This helical structure is well known in carbon fiber growth patterns [172], in which two growth points can occur at a single nanotube cap, and these two growth points provide the mechanism for twist growth which characterizes helical carbon nanotubes. The multi-wall twisted helical carbon nanotube obtained in Fig. 7.10 for the catalytic pyrolysis of acetylene might be considered to follow the same basic crystal growth mechanism.

Another category of torus that has been observed experimentally is formed from a long single-wall nanotube by joining the two ends in a seamless way and thus has a very large outer diameter compared to the tube diameter. This self-assembled torus has been called a “crop circle” [174]. It is estimated from TEM observations that 0.01–1% of certain nanotube samples are crop circle tori.

Experimental observations of toroidal structures [173] have also inspired theoretical investigation of such structures [81]. The number of pentagons and heptagons, f_5 and f_7 , in the toroidal structures is given by the Euler theorem for polyhedra as

$$f_5 - f_7 = 12(1 - g) \quad (7.19)$$

in which the *genus* g is the number of topological holes. Since a torus (or a donut) has a single hole at the center, (that is $g = 1$), the number of pentagons



Fig. 7.11: A superlattice structure consisting of the periodic joining of the two armchair sections; (8,8)–(5,5) [175].

and heptagons are equal; $f_5 = f_7$. An infinite length of carbon nanotube can be considered as a torus with an infinite toroidal radius, and thus $f_5 = f_7$ here also. When $f_5 = f_7 = 0$, we get a single-wall carbon nanotube defined by a single chiral vector. When the structure is periodic and $f_5 = f_7 = n$ (for $n = 1, 2, 3, \dots$) per the unit cell, we generally get helical coiled carbon nanotubes, which can be specified by $n + 1$ sets of chiral vectors. Thus a general coiled-shape nanotube can be considered to connect many joints, each with a pentagon-heptagon pair.

If the helical coiled carbon nanotube does not have any helical pitch, and if some joint conditions concerning the twisting of the nanotube are satisfied at the ends, a toroidal carbon nanotube is formed, as in Fig. 7.10. Further, when the dihedral angle defined in Eq. (7.9) becomes zero, a one-dimensional superlattice is obtained, as shown in Fig. 7.11.

When we consider the caps at the both ends of a nanotube, we can no longer image a loop, so that g becomes zero, giving $f_5 - f_7 = 12$. When we do not consider any heptagons at the caps, the number of pentagons f_5 becomes twelve for the two caps. This case corresponds to all fullerenes, in which case we have twelve pentagons per fullerene.

In the case of a toroidal shape structure, pentagons and heptagons appear in both the outside and inside of the main ring of the torus. Thus the angle φ defined by Fig. 7.4 is about π , and the angle 2θ defined by Eq. (7.8) is close to 20° . If a torus consists of such a joint with a bend angle of 20° , eighteen pentagon-heptagon pairs are necessary to make 360° . On the other hand, if the

hole of the torus is missing at the center, then twelve pentagons are sufficient to form a fullerene. Since a solid angle of $\pi/6$ is missing at a pentagon defect, we can imagine a cone shape around a pentagon. The apex angle of the cone made by a pentagon is $2\arcsin(5/6) = 113^\circ$.^{*} That means that if adjacent pentagons are close to one another or are arranged in three dimensions, the effective curvature becomes large compared with an isolated pentagon-heptagon pair. In fact, the most geometrically optimized calculation shows that from ten to fourteen pentagons are necessary for constructing the outer side of a torus.

The actual number of pentagon-heptagon pairs in the optimized structure calculated by Ihara et al., using a Stillinger–Weber model potential [171], is fourteen for C_{240} and twelve for C_{360} as shown in Fig. 7.7, which is consistent with the above discussion. Ihara et al. have also calculated the cohesive energy per carbon atom of $(C_n)_m$ by changing the order m of the rotational symmetry for a given unit of C_n . The optimized m depends on the shape of the torus and the value of n , and the optimized cohesive energy lies between that of C_60 (-7.29 eV) and that of graphite (-7.44 eV)[171].

Helically-coiled carbon nanotubes such as in Fig. 7.10 should be defined by two chiral vectors and the length of the pitch per unit of the two nanotubes. The inner and outer radii, tubular radius, as well as the pitch and twist values of the helical structure may be obtained from the chiral vectors, which are obtained numerically by an optimization of the calculated structure.

The electronic structure of coiled carbon nanotubes was discussed by Akagi et al. [176]. Their calculated results for the π orbitals within the tight binding approximation show that helical nanotubes can be either (1) a metal, (2) a semiconductor, or (3) a semi-metal, depending on the position of the pentagon and the heptagon, after folding the energy bands of the constituent carbon nanotube shells in accordance with the superstructure of the coiled carbon nanotubes. The semi-metallic electronic structure, with overlapping valence and conduction bands, comes from the fact that a coiled carbon nanotube consists of at least two different constituent carbon nanotube shells. Thus the lowest conduction bands and the highest valence bands do not always come from the same constituent shells. As a result, a small charge transfer occurs between these two bands, giving rise to semi-metallic behavior. Since each carbon atom has three σ bonds,

^{*}The corresponding angle for corannulene is 130.9° and that for a regular truncated icosahedron is 117.4° .

the number of carbon atoms and thus the number of π electrons in the unit cell is always an even number.[†] Therefore, the crossing of two energy bands at the Fermi level is sufficient for semi-metallic behavior, which however never occurs for a single-wall carbon nanotube without a pentagon or heptagon, because the π electrons show electron-hole symmetry around the Fermi energy.[‡]

[†]This fact clearly follows from Euler's theorem. If we denote the number of carbon atoms and σ bonds by N_c and N_σ , respectively, then $3N_c = 2N_\sigma$ holds if there are no dangling bonds. The equation $3N_c = 2N_\sigma$ implies that N_c is an even number.

[‡]The symmetry breaking between electrons and holes in tight binding results from the inclusion of the overlap matrix elements S_{AB} in the matrix Hamiltonian. If these matrix elements are neglected, the band widths of the conduction and valence bands are identical, which means there is electron-hole symmetry. In the $\vec{k} \cdot \vec{p}$ approximation, the electron-hole symmetry also holds.

CHAPTER 8.

Transport Properties of Carbon Nanotubes

At low temperature a single-wall carbon nanotube is a quantum wire in which the electrons in the wire move without being scattered by scattering centers. We review the difference between classical and quantum transport very briefly in Section 8.1. Then some results on transport experiments in carbon nanotubes are summarized in Section 8.2. Conductance fluctuations as a function of the magnetic field, known as universal conductance fluctuations, are found in carbon nanotubes, and are discussed both experimentally and theoretically.

8.1 Quantum transport in a one-dimensional wire

In considering an electric current in a square wire with a width (and a depth), W , and a length L , the resistance $R[\Omega]$ is given by Ohm's law,

$$R = \rho \frac{L}{W^2}, \quad (8.1)$$

where $\rho [\Omega\text{m}]$ is the resistivity. The inverse of R in Eq. (8.1) is the conductance $G[\text{S}]$ which is related to the conductivity $\sigma \equiv 1/\rho[\Omega\text{m}^{-1}]$ by

$$G = \sigma \frac{W^2}{L}. \quad (8.2)$$

In a macroscopic conductor, the resistivity ρ and the conductivity σ are physical properties which do not generally depend on either the length of the wire L or the applied voltage to the sample but only on the material. However, when the size of the wire becomes small compared with the characteristic lengths for the motion of electrons, then ρ and σ will both depend on the length L through quantum effects. In the quantum regime, the electrons act like waves that show

interference effects, depending on the boundary conditions and the impurities and defects that are present in the nanotube.

In mesoscopic systems* we consider three kinds of characteristic lengths: (1) the momentum relaxation length (or simply, mean free path) L_m , (2) the Fermi wavelength λ_F and (3) the phase-relaxation length L_φ [177]. The mean free path L_m is the average length that an electron travels before it is scattered by a scattering center. The Fermi wavelength $\lambda_F = 2\pi/k_F$ is the de Broglie wavelength ($\lambda_B \equiv h/mv$) for electrons at the Fermi energy. The phase-relaxation length L_φ is the length over which an electron retains its coherence as a wave. This infers that the phase of the electron is well defined along the propagating path of the wave. Thus the electron waves can interfere not only with other electron waves, but also with themselves within the coherence or phase relaxation length L_φ . If the scattering of an electron is elastic,[†] a phase shift of the wavefunction can be expected after the elastic scattering event, and thus the wave remains coherent. Thus elastic scattering does not contribute to L_φ but only to L_m . If the scattered wave loses energy by either exciting core electrons, spins associated with magnetic impurities or phonons, such inelastic scattering events contribute both to L_φ and L_m . It is useful to note that the effect of spin excitation can be suppressed by applying a magnetic field.

Electron-electron scattering between two valence electrons does not contribute to L_m but only to L_φ . After two electrons are scattered by their mutual Coulomb potential that is dynamic, the phase information of the wavefunction as a function of the position r is lost. Thus the electron-electron interaction decreases L_φ . However, when we consider N electrons on the Fermi sphere, where electrons occupy states from the bottom of the valence band to the Fermi energy in accordance with the Pauli exclusion principle, electron-electron interaction between any two of the N electrons does not change the electronic state under interchange of the two electrons with each other.[‡] In this sense there

*A mesoscopic system is a solid of small enough size, so that the interference of electron wavefunctions can be observed. A typical size of a mesoscopic system is around 1 – 100 nm which is larger than the microscopic or atomic size of around 1 – 10 Å and smaller than the macroscopic size which is more than 1 μm.

[†]In an elastic scattering process an electron does not change its energy as a result of the scattering event. The scattering by a static potential is known to be elastic. Here 'static' means that the potential has no freedom to promote the electron to an excited state.

[‡]Strictly speaking, the ground state of the N electrons is no longer the Fermi sphere in the presence of electron-electron interactions. When we take into account electron-electron in-

is no change in the Fermi sphere before and after electron-electron scattering. Here we do not consider the excitation of the two electrons out from the Fermi sphere, since such an excitation process requires energy which could be supplied by phonons. In accordance with the Pauli exclusion principle, we cannot distinguish any two electrons in the N -electron state, and therefore we cannot say that the electron state is changed upon electron-electron scattering. In this sense we conclude that electron-electron scattering in the valence band does not contribute to L_m .

In transport experiments, only electrons near the Fermi energy contribute, so that the lengths L_m and L_φ are scaled by the Fermi velocity v_F as

$$L_m = v_F t_m, \quad \text{and} \quad L_\varphi = v_F t_\varphi, \quad (8.3)$$

where t_m and t_φ are called the momentum relaxation time and the phase relaxation time, respectively. These times are compared with the transit time t_t during which an electron transverses the sample length L . However, t_m and t_φ do not imply the time of a single scattering event by the relevant scattering mechanism, but rather correspond to an average time for the many collisions which result in significant changes of momentum and phase, respectively. Here a significant change means, for example, that the sum of the changes in momentum and phase over the times t_m and t_φ reach $\hbar k_F$ and π , respectively.

In Table 8.1 we show the parameters which are used in the present chapter. In Table 8.1 we do not define yet M , L_c , L_T , D , R_0 and G_0 which will be introduced later in this chapter. The table will be useful for finding the parameters in this chapter. The relationship between these characteristic lengths determines the three transport regimes: ballistic, diffusive, and classic transport. Ballistic transport consists of single electron conduction with no phase and momentum relaxation. In a ballistic conductor, the wavefunction of an electron is determined over the sample by solution of Schrödinger's equation. On the other hand, in diffusive motion, many elastic scattering events occur. However, the phase relaxation length is much longer than the mean free path in diffusive motion, which brings about the localization of the wavefunction. Classical conductance is the conductance which satisfies the Ohm's law. In classical

teractions, the excited states of the N electrons are added to the variational function of N electrons which is expressed by a sum of the linear combination of the Slater determinants, and is known as the configuration interaction.

Table 8.1: Parameters in transport phenomena

Symbol	Name	Definition
M	Number of Channels [States]	A channel is the electronic states which propagate an electron in a coherent way.(See Eq. (8.4))
L	Sample length	Length of sample in the direction of the current.
λ_F	Fermi wavelength ^{a)}	Wavelength of an electron at the Fermi energy $2\pi/k_F$
L_m	momentum relaxation length ^{b)}	Length over which an electron changes most of its original momentum.
L_φ	phase relaxation length ^{a)}	Length over which an electron changes most of its original phase.
L_c	localization length	Length over which an electron wavefunction is extended. $L_c = ML_m$ (See Eq. (8.18)).
L_T	Thermal diffusion length	$L_T^2 = \frac{D\hbar}{k_B T}$ (See Eq. (8.28))
t_t	transit time	Time for an electron to go a distance L .
t_m	momentum relaxation time ^{a)}	$t_m = L_m/v_F$
t_φ	phase relaxation time ^{a)}	$t_\varphi = L_\varphi/v_F$
D	diffusion constants	$D = L_\varphi^2/t_\varphi$ (see Eq. (8.28))
R_0	quantized resistance	$R_0 = \frac{\hbar}{2e^2} = 12.9064\text{k}\Omega$ (see Eq. (8.6))
G_0	quantized conductance	$G_0 = \frac{2e^2}{h} = 77.4809 \times 10^{-6}\text{S}$ (see Eq. (8.7))

^{a)} Here v_F is the Fermi velocity and k_F is the Fermi wave vector.

^{b)} We simply call L_m the mean free path (see further discussion in the text).

Table 8.2: Dependence of characteristic lengths on scattering mechanism

Length	Scattering mechanism		
	magnetic elastic ^{a)}	impurity ^{b)}	Phonons
N_i		N_s, B	T
L_m	Dec.	Dec.	Dec.
L_φ	No	Dec.	Dec.

No: no effect, Dec.: Decreases

^{a)} Elastic means no freedom for carrier excitation by the scattering potential.

^{b)} The freedom for excitation of a spin can be suppressed by applying a magnetic field.

^{c)} Only electron-electron interaction in the valence band is considered.

conductance, both momentum and phase relaxation occur frequently and thus an electron can be considered as a particle. These conductance regimes will be introduced in the following subsections.

In Table 8.2 we list the relationship between the characteristic lengths and the scattering mechanisms. In the table we list, too, how a given scattering mechanism changes the characteristic lengths. In elastic and magnetic scattering, the concentration of ionic and magnetic impurities, N_i and N_s , are parameters which can vary from sample and sample. The magnetic scattering can be suppressed by a magnetic field. The excitation of phonons is suppressed at low temperature but the relaxation of an electron by emitting a phonon is determined by the electron-phonon interaction. The electron-electron interaction is determined by the carrier concentration N_c and the band width W of the valence band. The energy band width W can be changed by pressure and by some special geometry of the crystal such as the presence of superlattices. The frequency of all scattering processes can be changed (not independently) by changing the Fermi velocity, which is implemented by applying a gate voltage to the semiconductor-metal junction. Thus we can prepare materials for transport experiments by making the desired relationship between these parameters and the various scattering mechanisms.

In the following subsections we review the characteristics of various transport regimes: ballistic transport (Sect. 8.1.1), classical transport (Sect. 8.1.2), local-

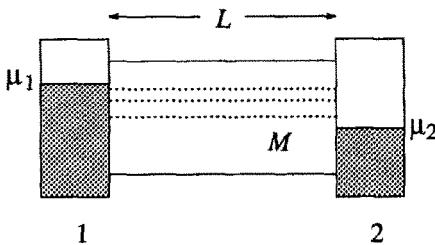


Fig. 8.1: A ballistic conductor with length L is connected to two electrodes 1 and 2 whose chemical potentials are μ_1 and μ_2 , respectively. M is the number of channels for electrons with wave vectors $k > 0$ to propagating from 1 to 2.

ization phenomena (Sect. 8.1.3), universal conductance fluctuations (Sect. 8.1.4), and negative magnetoresistance (Sect. 8.1.5), all of which pertain to transport in carbon nanotubes under appropriate conditions.

8.1.1 A ballistic conductor ($L \ll L_m, L_\varphi$)

For ballistic transport we consider an ideal case where we have no electron scattering on a wire of length L connected to two electrodes, 1 and 2 (see Fig. 8.1). Since the two electrodes have a large electron capacity, the electron chemical potentials for electrodes 1 and 2 are constants denoted by μ_1 and μ_2 , ($\mu_1 > \mu_2$), respectively. If there are no reflections of electrons at the electrodes, only those electrons having wave vectors $k > 0$ (in going from the left to the right in Fig. 8.1) and having energies in the range $\mu_2 < E < \mu_1$ contribute to the net current. Electrons going to electrode 2 are assumed to have an initial energy E at the point contact of electrode 1. In this case a voltage drop occurs at the contacts with the electrodes. The pseudo-Fermi energies* for the wire should be μ_1 and μ_2 for the $k > 0$ and $k < 0$ electrons, respectively.

Because of the quantization of electronic states in the direction perpendicular to the current, there are several energy subbands $E_j(k)$ which have the same k value. Thus the total current I is given by the sum of the microscopic currents for the $k > 0$ states of all the subbands $E_j(k)$ which have an energy $\mu_2 < E_j(k) < \mu_1$. Hereafter the subbands which have k states in the energy range $\mu_2 < E < \mu_1$ are called channels. The number of channels is a function of energy E , which is denoted by $M(E)$ [states]. An electron which has a velocity

*The pseudo-Fermi energies are defined here by the highest occupied energy for $k > 0$ and $k < 0$ electrons. If there is a thermal equilibrium state, there is a single Fermi energy for electrons. However, since there is no scattering between $k > 0$ and $k < 0$ electrons, we can treat $k > 0$ and $k < 0$ electrons as independent electrons.

$v = \hbar^{-1}(\partial E/\partial k) > 0$ in an unoccupied state for $\mu_2 < E < \mu_1$ contributes to the microscopic current $I = e/t_t$, in which t_t is the carrier transit time $t_t = L/v$ (See Table. 8.1). Then the total current I is given by

$$\begin{aligned} I &= \frac{e}{L} \cdot \frac{2L}{2\pi} \sum_j \int_{k>0} \frac{1}{\hbar} \frac{\partial E_j(k)}{\partial k} [f(E_j - \mu_1) - f(E_j - \mu_2)] dk \\ &= \frac{2e}{\hbar} \int [f(E - \mu_1) - f(E - \mu_2)] M(E) dE \\ &= \frac{2e^2}{h} M \frac{(\mu_1 - \mu_2)}{e}, \end{aligned} \quad (8.4)$$

where the sum on k is converted to the integral with a spin degeneracy of 2 and the inverse of the level spacing $L/2\pi$. $2e/h$ in Eq. (8.4) is the quantized current per subband per unit energy [A/J]. $f(E - \mu_i)$ ($i = 1, 2$) is the Fermi distribution function with the Fermi energy denoted by μ_i . When we assume that the total number of conduction channels $M(E)$ is constant M over $\mu_2 < E < \mu_1$, we obtain the last line of Eq. (8.4). It is important to note that $M(E)$ is not a density of states. In fact the dimension of $M(E)$ and M is not [states/J], but is rather [states]. If the width of a wire W is very small (less than 1 nm), $M = 1$ even for $\mu_1 - \mu_2 = 1$ eV. On the other hand, if the width of a wire is on the order of 1 μ m, and the Fermi energy is about 1 eV, M becomes very large ($\sim 10^6$) for $\mu_1 - \mu_2 = 1$ eV. It should be noted that we have many k states even when $M = 1$. All the k states are integrated in Eq. (8.4). Thus we should not count the number of k states in the direction parallel to the current to M .

Since $V = (\mu_1 - \mu_2)/e$ is the voltage between the electrodes, the resistance of the ballistic conductor is given by

$$R_c = \frac{(\mu_1 - \mu_2)/e}{I} = \frac{\hbar}{2e^2} \cdot \frac{1}{M}, \quad (8.5)$$

where R_c is called the contact resistance and $\hbar/2e^2$ is the quantized resistance R_0 ,

$$R_0 = \frac{\hbar}{2e^2} = 12.9064 k\Omega. \quad (8.6)$$

The inverse of Eq. (8.5) gives the contact conductance G_c which is related to the quantized conductance G_0 by

$$G_c = G_0 M, \quad G_0 = \frac{2e^2}{h} = 77.4809 \times 10^{-6} \text{U}. \quad (8.7)$$

Thus in a wire with no scattering the conductance is proportional to M . The quantized resistance and conductance can be observed in clean semiconductors at very low temperature on samples which have a small M [178].

When we consider the range of values of M for a metal nanotube of finite length L , we expect to find two energy bands ($M = 2$) for $k > 0$ (see Figs. 4.4, 4.5 and 4.6). Thus in the ballistic limit, the conductance of metallic nanotubes is $2G_0$ [179]. When the length of a nanotube L is finite, we expect to find discrete k values spaced by $2\pi/L$. Even if the k states are discrete but still numerous, the relation $v = \partial E_j(k)/\partial k$ in Eq. (8.4) is applicable as a first approximation.

When we consider static scattering, that is, scattering by a potential in one dimension, the wavefunction is solved by a one-dimensional Schrödinger equation. Since the phase and amplitude of the wavefunction at electrode 2 can be obtained from those at electrode 1, a similar discussion for the contact conductance can be applied. The conductance G and the resistance R are thus given by

$$G = \frac{2e^2}{h} MT \equiv \frac{2e^2}{h} \sum_{ij}^M |t_{ij}|^2, \quad R = \frac{h}{2e^2} \cdot \frac{1}{MT}, \quad (8.8)$$

where T is the transmission probability for a channel to go from electrode 1 to electrode 2, which is given by the sum of transmission probability from i th to j th channel, $|t_{ij}|^2$. Here we assume again that T is constant near the Fermi energy. Equation (8.8) is known as the Landauer formula. The Landauer formula applies only if the wavefunction can spread over the whole sample.

The resistance of a mesoscopic wire R_w for a single channel is given in terms of the transmission probability T as

$$R_w = R - R_c = R_0 \frac{1 - T}{T} \equiv R_0 \frac{\mathcal{R}}{T}, \quad (8.9)$$

since the reflected wavefunction, which is proportional to $\mathcal{R} = 1 - T$, causes a voltage drop in the wire.

8.1.2 Classic transport, $L_\varphi \ll L_m \ll L$

In a macroscopic metal, phase recombination processes are expected. Thus we cannot solve the Schrödinger equation over the entire sample since the electron wavefunction cannot be described by a single phase. When we neglect the effect of interference during a scattering event, the total transfer probability is given by

summing over each transmission T_i probability and of each reflection $\mathcal{R}_i = 1 - T_i$, ($i = 1, \dots, N$). When we consider multiple reflections between $i = 1$ and $i = 2$, the overall transmission probability T_{12} between electrodes 1 and 2, is given by

$$\begin{aligned} T_{12} &= T_1 T_2 (1 + \mathcal{R}_1 \mathcal{R}_2 + \mathcal{R}_1^2 \mathcal{R}_2^2 + \dots) \\ &= \frac{T_1 T_2}{1 - \mathcal{R}_1 \mathcal{R}_2}. \end{aligned} \quad (8.10)$$

We can rewrite Eq. (8.10) by using

$$\frac{1 - T_{12}}{T_{12}} = \frac{1 - T_1}{T_1} + \frac{1 - T_2}{T_2}. \quad (8.11)$$

Using the formula for the resistance given by Eq. (8.9), and Eq. (8.11) we see that the resistance of the wires is additive, $R_{12} = R_1 + R_2$. We then apply this result to the N scatterers and we get

$$R - R_c = R_0 \sum_i^N \frac{1 - T_i}{T_i} \sim N R_0 \frac{1 - T}{T} \quad (8.12)$$

where N is the number of scattering events and T is an average transmission probability for an individual scattering event over a mean free path L_m . Thus the total resistance is given by a series connection of microscopic resistances [see Eq. (8.9)] for every momentum relaxation length L_m . This is nothing but Ohm's law [see Eq. (8.1)] in which the macroscopic resistance is proportional to L .

8.1.3 Localization, ($L_m \ll L_\varphi \ll L$)

When we consider the phase shift at each scattering event, the wavefunctions which are reflected many times between 1 and 2 are added along with their phases and the sum is then squared to obtain the transmission probability. When we consider the transmission coefficient t_{12} for a wavefunction between electrodes 1 and 2, then t_{12} is given by an equation similar to Eq. (8.10),

$$t_{12} = \frac{t_1 t_2}{1 - r_1 r_2 e^{i\theta}}, \quad (8.13)$$

where t_1 , t_2 , r_1 and r_2 is the transmission and reflection amplitudes of a wavefunction, called the S -matrix. The phase shift θ corresponds to a round trip

between electrodes 1 and 2. From Eq. (8.13) we obtain the probability for the transfer of an electron from electrode 1 to electrode 2

$$T_{12}^c = |t_{12}|^2 = \frac{T_1 T_2}{1 - 2\sqrt{\mathcal{R}_1 \mathcal{R}_2} \cos \theta + \mathcal{R}_1 \mathcal{R}_2}, \quad (8.14)$$

where $T_i = |t_i|^2$, and $\mathcal{R}_i = |r_i|^2$. It might seem that Eq. (8.14) should be compared to the case of the incoherent limit given by Eq. (8.10). However the two equations (8.14) and (8.10) are not analytically connected to each other, since the assumptions for the two equations are different as follows. In the incoherent limit of Eq. (8.10), we consider that the reflected wave is incoherent to the original wave. Thus we add the probability of multiple reflections in Eq. (8.10). On the other hand, in the coherent case, we consider many reflections of a coherent wave in Eq. (8.13) where we add the amplitude of multiple reflections. Thus the calculated T_{12} 's in Eqs.(8.14) and (8.10) are generally independent.

The resistance R_{12} is obtained by taking an average over θ such that $\langle \cos \theta \rangle = 0$, to obtain

$$R_{12} = R_0 \left\langle \frac{1 - T_{12}^c}{T_{12}^c} \right\rangle = R_0 \frac{1 + \mathcal{R}_1 \mathcal{R}_2 - T_1 T_2}{T_1 T_2} = R_1 + R_2 + 2R_1 R_2 / R_0, \quad (8.15)$$

where R_1 and R_2 are given by Eq. (8.9). In Eq. (8.15), R_{12} is not additive (that is $R_{12} \neq R_1 + R_2$) and thus Ohm's law is not expected to be valid. The non-additive term in Eq. (8.15) that involves $2R_1 R_2$ causes an exponential divergence for R as a function of L , when $R(L)$ is defined by a step of $L_c \sim L_m$. Then Eq. (8.15) gives the differential equation,*

$$\frac{dR}{dL} = \frac{R(L + L_c) - R(L)}{L_c} = \frac{R_0 + 2R}{L_c}. \quad (8.16)$$

The solution of Eq. (8.16) is

$$R(L) = \frac{R_0}{2} \left\{ e^{2L/L_c} - 1 \right\} \rightarrow \infty, \quad (L \rightarrow \infty). \quad (8.17)$$

Thus the resistance becomes very large in the limit of large L so that the material becomes an insulator. This means that the wavefunction near the Fermi energy becomes localized so that the transmission probability from one electrode to the

*Here we assume the following: $R_{12} = R(L + L_m)$, $R_1 = R(L)$, and $R_2 = R(\Delta L) = R(L_m) \sim R_0$.

Table 8.3: Transport regimes of a conductor

Regime	Relationship	Coherence length
Classical	$L_\varphi < L_m \ll L$	$\sim L_m$
Localized	$L_m \ll L_\varphi < L$	many L_m 's
weak	$L_\varphi < L_c$	L_φ
strong	$L_\varphi > L_c$	L_c
Ballistic	$L_m > L_\varphi > L$	L

other is almost zero. This is known as the localization phenomenon.[†] Localization can occur even when M is large. In the case of large M , we can redefine the localization length L_c by[180]

$$L_c = M L_m. \quad (8.18)$$

When L_φ is much larger than L_c , then the strong localization effect of Eq. (8.17) occurs. In the strongly localized regime, the conductance arises from the thermal hopping from one localized site to another. On the other hand, when L_c is larger than L_φ , then L in Eq. (8.17) should be terminated at $L = L_\varphi$. In this case, the conductor is said to be in the weakly localized regime. For both strong and weak localization, the phase relaxation length L_φ is required to be much larger than the mean free path L_m .

The localization becomes strong for large L_φ , for small M , and for small L_m which makes L_c smaller. Most low-dimensional metals, such as thin metallic wires or carbon fibers with high T_{HT} , are known to be in the weakly localized regime and heavily-doped semiconductors and intercalated graphite with a large fluorine uptake are known to be in the strongly localized regime [181, 182].

In Table 8.3 we summarize the conditions pertinent to the various transport regimes by listing the pertinent relations between the characteristic lengths and the coherence length of an electron. The coherence length of an electron infers the existence of an upper limit for the length over which we can solve the Schrödinger equation for an electron with a single phase. When the coherence

[†]There are two kinds of localization. The localization described by Eq. (8.17) is the effect of a random potential on the one-electron wavefunction and this is called Anderson localization. When the electron-electron repulsion is large compared with the average level spacing, the electron cannot move, just like cars on a highway not being able to move above a critical density. This second type of localization is called Mott localization.

length or inelastic scattering length ($\sim L_\varphi$) is smaller than the elastic scattering length (L_m), classical transport occurs, in which the resistance is an additive property. When the coherence length contains many elastic scattering lengths ($L_m \ll L_\varphi$), quantum interference occurs within the lengths of L_φ or L_c for the weak or strong localization regimes, respectively. When the sample is large and thick, the interference effect can be observed as a microscopic scattering process, but its contribution to the resistance becomes small compared with the classical resistance. On the other hand, if the coherence length is close to the sample size, the conductance is described by a wavefunction that is defined over the entire sample. Furthermore, in a ballistic conductor, the conductance is given by the Landauer formula [Eq. (8.8)] in which the number of propagating states and their probability for transmission determines the conductance.

In the weak localization regime ($L_m \ll L_\varphi < L_c$), we can observe two interesting quantum interference effects: universal conductance fluctuations (UCF) and negative magnetoresistance (NM), as discussed in Sect. 8.1.4 and Sect. 8.1.5, respectively.

8.1.4 Universal Conductance Fluctuations

When the phase delocalization length L_φ is close to the sample size L , interference effects associated with the wavefunction become important [164, 183]. If we prepare many samples of the same size, the conductance will fluctuate from sample to sample because of differences in the inhomogeneous distribution of scattering centers. Let us consider M paths of conducting current for each sample. For each path, we have many scattering centers and thus many scattering processes because of the multiple scattering events for the many centers. When $M = 1$, the conductance fluctuation, $\sqrt{\langle \delta G^2 \rangle}$ is $2e^2/h$ since the transmission probability may be distributed homogeneously from 0 to 1. Here the $\langle \delta G^2 \rangle$ is defined by

$$\langle \delta G^2 \rangle = \langle G^2 \rangle - \langle G \rangle^2, \quad (8.19)$$

where $\langle X \rangle$ denotes the ensemble average of X for the sample. An ensemble average means an average for many samples with different impurity distributions.

Here we show that the fluctuations do not depend on M unless $L_\varphi \sim L$.*

*If M paths were independent, the fluctuation $\sqrt{\langle \delta G^2 \rangle}/\langle G \rangle$ for M paths would be proportional to $\sim 1/\sqrt{M}$. The fact that the fluctuation does not depend on M is an interference effect which

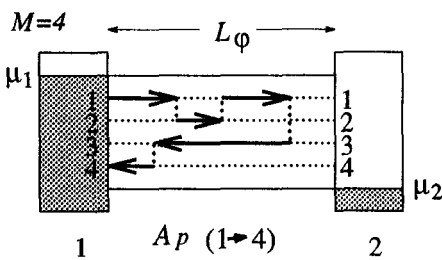


Fig. 8.2: A scattering process of the reflected wavefunction for the path entering 1 and exiting 4 in electrode 1 ($A_p(1 \rightarrow 4)$). Here we consider 4 channels ($M=4$). Within the phase coherence length L_φ , the amplitude of the scattering wavefunction is given by Eq. (8.23).

We start from the Landauer formula Eq. (8.8) for the conductance normalized by $2e^2/h$,

$$g \equiv \frac{G}{2e^2/h} = M\bar{T} = M - M\bar{\mathcal{R}}, \quad (8.20)$$

where \bar{T} , $\bar{\mathcal{R}}$ denote the average on M possible paths of $T(m \rightarrow n)$ and $\mathcal{R}(m \rightarrow n)$, ($1 \leq n \leq M$) for given m , where m and n denote specific channels. In Fig. 8.2 we show a scattering process of $\mathcal{R}(1 \rightarrow 4)$. There are many scattering processes in $\mathcal{R}(1 \rightarrow 4)$ as shown below. When we have M channels, the conductance is generally proportional to M as shown in Eq. (8.20). Since $\langle g \rangle = M\langle \bar{T} \rangle = M - M\langle \bar{\mathcal{R}} \rangle$ and $\langle g^2 \rangle = M^2\langle \bar{T}^2 \rangle = M^2 - 2M^2\langle \bar{\mathcal{R}} \rangle + \langle \bar{\mathcal{R}} \rangle^2$, the conductance fluctuations can be derived from either the fluctuation of $\langle \delta \bar{\mathcal{R}}^2 \rangle$ or of $\langle \delta \bar{T}^2 \rangle$,

$$\langle \delta g^2 \rangle = M^2 \langle \delta \bar{T}^2 \rangle = M^2 \langle \delta \bar{\mathcal{R}}^2 \rangle. \quad (8.21)$$

Here we consider the fluctuations of the reflectivity, which are known to be relevant for the following discussion. The reflected wave function $\Psi(n \rightarrow m)$, for the path entering n and exiting to m in electrode 1 (see Fig. 8.2), is given by the summation of the wavefunction $A_p(m \rightarrow n)$ for the p th multiple scattering processes,

$$\Psi(n \rightarrow m) = \sum_p A_p(m \rightarrow n), \quad (8.22)$$

where a scattering process of the reflected wave, $A_p(m \rightarrow n)$ can be expressed, for example, by

$$A_p(m \rightarrow n) = t(m \rightarrow m_1) \exp\{ik_{m_1}L_{m_1}\} r(m_1 \rightarrow m_2) \exp\{ik_{m_2}L_{m_2}\} \cdots t(m_q \rightarrow n) \exp\{ik_nL_n\}. \quad (8.23)$$

can be seen universally. Note that the fluctuations become small for samples large compared with L_φ .

When we assume that the overall phase of $A_p (m \rightarrow n)$ is random in $\Psi(n \rightarrow m)$, the ensemble average of the reflection probability $\mathcal{R}(m \rightarrow n)$ is given by

$$\langle \mathcal{R}(m \rightarrow n) \rangle = |\Psi(n \rightarrow m)|^2 = \left\langle \sum_p |A_p|^2 + \sum_{p \neq p'} A_p A_{p'}^* \right\rangle = \left\langle \sum_p |A_p|^2 \right\rangle, \quad (8.24)$$

where we use the fact that the ensemble average of the sum of $A_p A_{p'}^*$, for $p \neq p'$ gives zero because of the assumption of a random phase. In order to discuss the fluctuations we define the following quantity

$$\begin{aligned} \langle \mathcal{R}(m \rightarrow n)^2 \rangle &= \sum_{p,p',p'',p'''} \langle A_p A_{p'} A_{p''} A_{p'''} \rangle \\ &= \sum_{p,p',p'',p'''} \langle |A_p|^2 |A_{p'}|^2 [\delta_{p,p''} \delta_{p',p'''} + \delta_{p,p'''} \delta_{p',p''}] \rangle \\ &= 2 \langle \mathcal{R}(m \rightarrow n) \rangle^2 \end{aligned} \quad (8.25)$$

Thus the fluctuations of the reflectivity are given by

$$\langle \delta \mathcal{R}(m \rightarrow n)^2 \rangle \equiv \langle \mathcal{R}(m \rightarrow n)^2 \rangle - \langle \mathcal{R}(m \rightarrow n) \rangle^2 = \langle \mathcal{R}(m \rightarrow n) \rangle^2. \quad (8.26)$$

Since $\langle \mathcal{R}(m \rightarrow n) \rangle \sim 1/M^\dagger$ we get from Eq. (8.21),

$$\langle \delta g^2 \rangle \sim 1. \quad (8.27)$$

Thus the fluctuations in g are on the order of the quantum of conductance $2e^2/h$ which does not depend on M (or on a particular choice of material). We cannot avoid this fluctuation from sample to sample with the same impurity concentration. This fluctuation can be seen by changing the length of the sample provided that the sample size is smaller than the phase relaxation length ($L < L_\varphi$). The effective distribution of impurities can be changed by applying a magnetic field since the phase of each process [see Eq. (8.23)] is changed by the vector potential eA .

When the phase delocalization length L_φ becomes smaller than L , the fluctuations can be smoothed out. When we consider $N = L/L_\varphi$ quantum fluctuating conductors in series, the fluctuation of the conductance become $1/N^{3/2} \sim L^{-3/2}$ smaller than for a single conductor. This power dependence can be seen by changing L .

[†]The probability of choosing channel n from M channels is on the order of $1/M$. Here we assume that \mathcal{R} and \mathcal{T} are in order of 1. Note that the conductance G is $\sim MG_0$.

When we fix the sample length L , the energy \hbar/t_φ can be considered as an energy width for phase-coherent motion. This means that within a lifetime t_φ , an electron can vary its energy by \hbar/t_φ from the uncertainty relation. At high temperatures such that $k_B T$ is larger than \hbar/t_φ and L_φ is larger than L , then $N = k_B T / (\hbar/t_\varphi)$ independent channels are open incoherently. When we define the thermal diffusion length L_T for a given diffusion constant D , the Einstein relation says that

$$L_T^2 = \frac{D\hbar}{k_B T} \quad \text{and} \quad L_\varphi^2 = D t_\varphi \quad (8.28)$$

so that

$$N = \frac{k_B T}{\hbar/t_\varphi} = \left(\frac{L_\varphi}{L_T} \right)^2. \quad (8.29)$$

Thus the universal conductance fluctuations show a temperature dependence given by

$$\sqrt{\langle \delta g^2 \rangle} = \begin{cases} \text{constant} & T < \frac{\hbar}{t_\varphi k_B} \\ G_0 \left(\frac{\hbar/t_\varphi}{k_B} \right)^{1/2} T^{-1/2} & T > \frac{\hbar}{t_\varphi k_B} \end{cases} \quad (8.30)$$

8.1.5 Negative Magnetoresistance

An another interesting phenomena observed in the weak localization regime is negative magnetoresistance, which refers to a decrease in the resistance with increasing magnetic field. Here we show the basic idea behind the negative magnetoresistance.

Consider the special case for A_p [see Eq. (8.23)] in which the starting and ending sites are identical, that is $\mathcal{R}(m \rightarrow m)$. Consider a process $A_p : m \rightarrow m_1 \rightarrow m_1 \rightarrow \dots \rightarrow m_q \rightarrow m$, and the time-reversed processes $A_p^\mathcal{R} : m \rightarrow m_q \dots \rightarrow m_2 \rightarrow m_1 \rightarrow m$, so that the overall phases are identical. Thus when we consider the reflection probability of Eq. (8.24) for $\mathcal{R}(m \rightarrow m)$, we expect a coherence between A_p and $A_p^\mathcal{R}$,

$$\mathcal{R}(m \rightarrow m) = |(A_1 + A_2 + \dots) + (A_1^\mathcal{R} + A_2^\mathcal{R} + \dots)|^2 \equiv |A + A^\mathcal{R}|^2 = 4|A|^2. \quad (8.31)$$

If there is no phase correlation between A and $A^\mathcal{R}$, $\mathcal{R}(m \rightarrow m)$ would give $2|A|^2$. Actually there is no time reversal symmetry in $\mathcal{R}(m \rightarrow n)$ for $n \neq m$, since $\mathcal{R}(m \rightarrow n)$ and $\mathcal{R}(n \rightarrow m)$ are different paths from each other, so that the

reflection probability becomes $2|A|^2$. The coherence associated with Eq. (8.31) is known as enhanced backward scattering, and can be applied to radar systems for searching a cloud which can be treated as a random material.

When a magnetic field is applied, the phases of A and A^R become different from one another. The phase difference is proportional to the magnetic flux penetrating through a loop made from a set of A_p and A_p^R . However, since the lengths of the loops are different for different A_p 's, thus we can no longer expect any enhanced backward scattering, thus decreasing the reflection probability. This is an explanation of the origin of negative magnetoresistance under weak localization conditions.

8.2 Transport experiments on carbon nanotubes

In this section we discuss quantum transport in carbon nanotubes. Whereas Sect. 8.1, considers quantum transport in general, we start this section with a few comments about quantum transport in carbon nanotubes generally and then proceed to discuss specific experiments. Since the Fermi surface of a 1D nanotube consists of the two points $\pm k_F$, scattering processes involve taking an electron from $+k_F$ to $-k_F$ or visa versa. For an armchair nanotube this would involve a phonon of $4\pi/3T$ where T is the length of the 1D translation vector, whereas for zigzag nanotubes, phonon with wave vectors $2\pi/T$ are effective. Transverse acoustic (out-of-plane) phonons are most effective in this scattering process through the electron-phonon interaction [78].

Transport measurements of nanotubes show different aspects depending on the sample type, such as a single-wall nanotube (SWNT), a single rope (SWNT bundle), a single multi-wall nanotube (MWNT) and a single MWNT bundle. The most difficult experimental problem for the transport experiments on carbon nanotubes is the attachment of electrodes to the extremely thin nanotubes, and this is discussed in Sect. 8.2.1. In the initial transport experiments on an individual carbon nanotube [184], rather large diameter (~ 20 nm) multi-wall nanotubes were used. Subsequently, single wall nanotubes became more available and the focus of research on the transport properties of carbon nanotubes shifted emphasis to the single-wall nanotubes, since single-wall nanotubes represent a model system for studies of quantum transport, as discussed in Sect. 8.2.2, where transport properties for an isolated single-wall nanotube are presented.

This is followed by a report in Sect. 8.2.3 on transport in a single rope of single-wall carbon nanotubes where inter-tube interactions play a role. Phenomena associated with weak localization and universal conductance phenomena are observed in multi-wall nanotubes and are discussed in Sect. 8.2.4.

8.2.1 Attaching Contacts

We summarize here some of the techniques that have been used for attaching contacts to carbon nanotubes for carrying out transport experiments [185]. One method for attaching contacts to an nanotube is to place a liquid drop, containing suspended nanotubes, on a substrate on which electrodes were previously deposited. For those nanotubes which connect two electrodes, transport measurements can be carried out [150, 151]. In another version of this method, a single contact is made with this technique and a scanning tunneling probe is used to make the second contact as this probe moves along the wire, continuously measuring the resistance as a function of nanotube length [186]. A third method involves the use of sophisticated semiconductor Si technology to attach 4 tungsten leads by a focused ion beam deposition technique, as seen in Fig. 8.3 for four contacts attached to a multi-wall nanotube in the 5–10 nm diameter range on an oxidized silicon surface [185]. The 80 nm wide tungsten wire contacts are deposited by focused-ion-beam induced deposition using a $\text{W}(\text{CO})_6$ carrier gas. The nanotube is visualized by the focused-ion-beam with a low beam current (4 pA) for imaging the nanotube. The deposition of the contacts is performed under computer control without any visualization. The distance between the probing leads on the sample is in the 0.3–1.0 μm range. The four leads are connected to a gold pad and the currents and voltages are observed by a four-point contact measurement. The advantages of this method is that 4 contacts can be placed reliable on the single nanotube. The effect of strain introduced by lead attachment process is not understood.

Another approach for making electrical contact, that utilizes so of the techniques mentioned above, is seen in Fig. 8.4 where the carbon nanotube is placed on top of a Si/SiO₂ substrate on which two Pt electrodes had previously been deposited. This method has the advantage of perturbing the nanotube only weakly, but has the disadvantage of a high contact resistance and of not providing four contacts

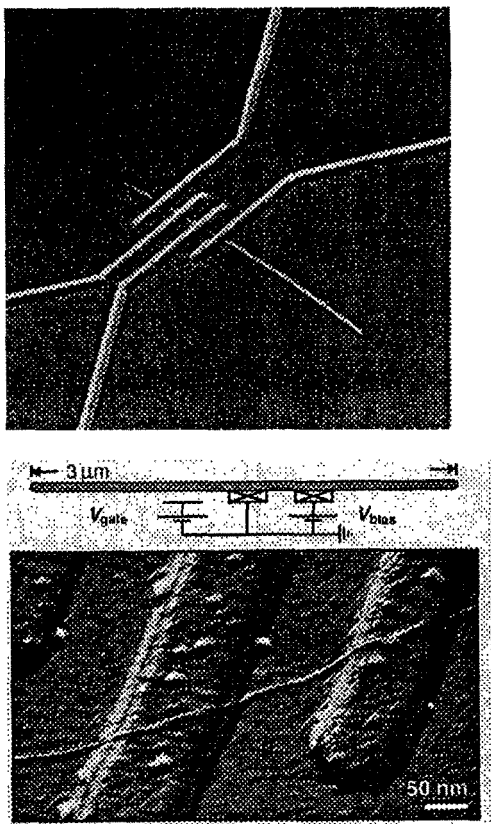


Fig. 8.3: An individual multi-wall carbon nanotube connected to four 80 nm wide tungsten wires by focused-ion-beam-induced deposition [185].

Fig. 8.4: AFM tapping-mode image of a carbon nanotube on top of a Si/SiO₂ substrate with two 15 nm-thick and 140 nm wide Pt electrodes. A schematic circuit diagram is presented at the top of this figure and is relevant to the transport experiments shown in Fig. 8.5 [51].

8.2.2 An Individual Single-Wall Nanotube

We now discuss experimental results from the first transport experiment on an individual isolated single-wall carbon nanotube [51]. In this experiment a single wall nanotube (the very thin wire in Fig. 8.4) is placed on top of a Si/SiO₂ substrate with two 15 nm-thick and 140 nm wide Pt electrodes as shown in Fig. 8.4 [51] and the bias voltage V_{bias} is measured between the two electrodes. A gate voltage V_{gate} , applied to the third electrode in the upper-left hand corner of Fig. 8.4 is used to change the electrostatic potential seen by the nanotube. The bias voltage V_{bias} changes the chemical potentials of the two electrodes, μ_1 and μ_2 (see Fig. 8.1), while the gate voltage V_{gate} changes the position of the energy levels of nanotube relative to the chemical potentials, μ_1 and μ_2 . Because

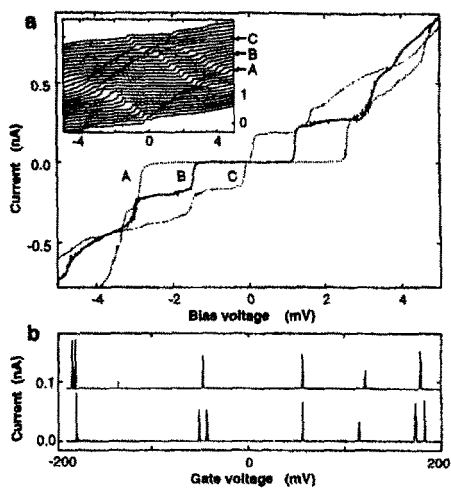


Fig. 8.5: a. Current-voltage curves of a carbon nanotube at a gate voltage of 88.2 mV (curve A), 104.1 mV (curve B) and 120.0 mV (curve C). In the inset, more $I - V_{\text{bias}}$ curves are shown with V_{gate} ranging from 50 mV (bottom curve) to 136 mV (top curve). b. Current versus gate voltage at $V_{\text{bias}} = 30 \mu\text{V}$. The two traces were performed under the same conditions and represent a bistability (see text) [51].

of the finite length of the nanotube ($L = 3 \mu\text{m}$), the one-dimensional energy band is split into energy levels whose spacing $\Delta E = \hbar v_F / 2L$ is estimated to be $\Delta E \sim 0.6 \text{ meV}$, where we use an estimate for the Fermi velocity of $v_F = 8.1 \times 10^5 \text{ m/s}$. The two-point resistance at room-temperature of such a single wall nanotube is $\sim 1 \text{ M}\Omega$. The estimated contact resistance, obtained from a similar nanotube on which a four-point contact geometry was used, is $300 \text{k}\Omega$ at room temperature and $1 \text{M}\Omega$ at 4 K.

In Fig. 8.5a, we show the $I - V_{\text{bias}}$ curves at a gate voltage of 88.2 mV (curve A), 104.1 mV (curve B) and 120.0 mV (curve C) at 5 mK. The plateaus of non-zero current clearly show ballistic transport when a conducting channel is in the range of $V_{\text{bias}} = (\mu_1 - \mu_2)/e$. The position of the steps in the $I - V_{\text{bias}}$ curves is changed by increasing the gate voltage. However, we must consider not only the level shift effect but also the Coulomb charging effect of the nanotube, whereby, the nanotube is considered as a capacitor with a capacitance C . At very low temperature, such that the thermal energy $k_B T$ is smaller than the charging energy E_c of an electron $k_B T < E_c = e^2/2C$, the current flow can be blocked by this energy shift when the charge from the current flow itself shifts the levels out of the bias window between μ_1 and μ_2 . Thus, current flow in Fig. 8.5b appears only when $V_{\text{bias}} > E_c$. Since the energy of the levels in a nanotube can be modified by V_{gate} , the step positions shown in the inset of Fig. 8.5a are

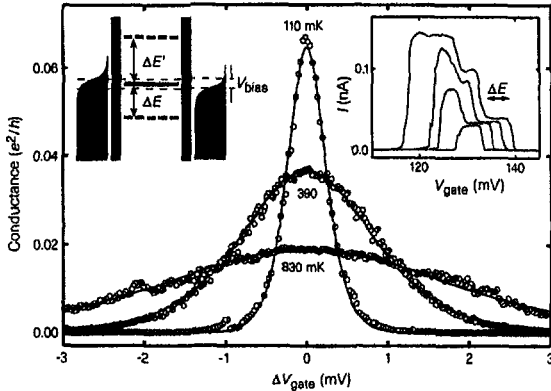


Fig. 8.6: Conductance $G = I/V_{\text{bias}}$ vs ΔV_{gate} at the bias voltage V_{bias} for three different temperatures with the bias window $V_{\text{bias}} = 10 \mu\text{V}$. The solid lines represent fits to the function $G \propto \cosh^{-2}(e\Delta V_{\text{gate}}/\alpha 2k_B T)$. Left inset shows a model for explaining the temperature dependence of G . Right inset shows the current vs gate voltage for $V_{\text{bias}} = 0.4, 0.8, 1.2$ and 1.6 mV , showing the contribution from the lower-lying levels within the bias window [51].

smoothly changed by changing V_{gate} .

When the bias window denoted by V_{bias} is very narrow ($30 \mu\text{V}$), the current flow appears like a delta function of V_{gate} , only when the energy levels are in the bias window between μ_1 and μ_2 , as shown in Fig. 8.5b. Some double δ -functions are also observed in the two traces in Fig. 8.5b, which are taken under the same experimental conditions. This bistability may be explained as the result of switching offset charges that shift the energy levels of the 1D carbon nanotube.

Figure 8.6 shows the temperature dependence of the spectra of a sharp peak that is observed in Fig. 8.5b, as a function of the gate voltage shift ΔV_{gate} from the peak conductance point, with the minimum bias window $V_{\text{bias}} = 10 \mu\text{V}$. A decrease in intensity and a broadening of the conductance peak with increasing temperature shows the relaxation of the phase and amplitude of the resonance tunneling by phonon scattering events. Solid lines in Fig. 8.6 are fitted to the function $G \propto \cosh^{-2}(e\Delta V_{\text{gate}}/2\alpha k_B T)$, where the factor $\alpha = 16$ obtained from Fig. 8.6 is the ratio of ΔV_{gate} to the shift of the energy levels. This ratio corre-

sponds to the ratio of the capacitance of the gate to that of the nanotube. The temperatures in Fig. 8.6 (110, 390, and 830 mK) are the fitted temperatures for the plotted curves, while the measured temperatures are 5, 240, and 600 mK, respectively. The discrepancy between the fitted and the observed temperatures is due to the finite bias voltage ($10\mu\text{V} = 116 \text{ K}$) and the residual noise in the measurement system. Although the absolute value of conductance is $\sim 0.03(2e^2/h)$, the quantum conductance $2e^2/h$ could be obtained at a smaller bias voltage. If the conductance is observed with a smaller bias voltage and a larger α value, the conductance of Fig. 8.6 will show saturation at $2e^2/h$, thus providing clear evidence for quantum conductance.

When the gate voltage increases (see the right inset of Fig. 8.6), step structures are observed. For curves at high gate voltages (about 140mV) plateaus can be seen for different values of V_{bias} . The plateaus correspond to the entry of a state at the Fermi level (denoted by the solid line in the left inset of Fig. 8.6) into the bias window. When we further decrease V_{gate} , the next plateau appears and is attributed to conduction processes associated with the lower level below $\Delta E \sim 0.4 \text{ meV}$ (see the left inset of Fig. 8.6), which is consistent with the estimated level spacing of $\Delta E \sim 0.6 \text{ meV}$ for a $L = 3\mu\text{m}$ nanotube. A value of $\alpha=12$ is estimated for the data in Fig. 8.6 from the ratio of ΔV_{gate} to ΔE . This value of $\alpha=12$ is in satisfactory agreement with the previous value of $\alpha=16$ in the first approximation. The further decrease of V_{gate} brings the system back to a no current situation, since the state at the Fermi level is now located outside of the bias window. These results are consistent with the fact that the curves in Fig. 8.6 with a larger bias window V_{bias} show a signal within a larger range of V_{gate} .

The experiments, described in Figs. 8.4, 8.5 and 8.6, clearly show ballistic transport effects associated with the discrete levels imposed by the finite length of the one-dimensional nanotube conductor. The observed phenomena can be understood by steps in the quantum conductance, and charging effects associated with the micro capacitances of the nanotube and the gate.

The resistance measurements for various nanotube samples show that there are metallic and semiconducting nanotubes, which was first predicted theoretically, as discussed in Sect. 4.1. The resistivity is about $10^{-4}\text{--}10^{-3} \Omega\text{cm}$ for the metallic nanotubes, while the room temperature resistivity is about $10^1 \Omega\text{cm}$ in semiconducting nanotubes. The semiconducting nanotubes exhibit a slope

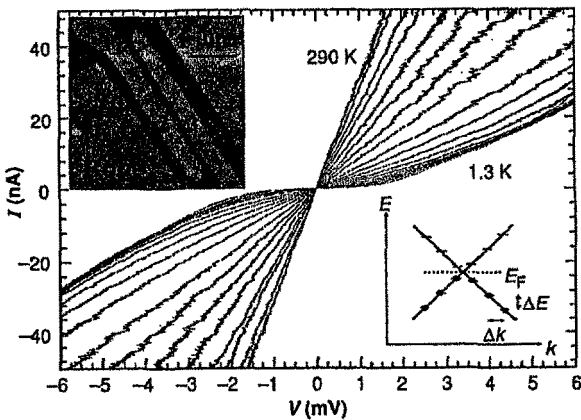


Fig. 8.7: $I - V$ characteristics of a single 12-nm-diameter rope made up about 60 1.4nm-diameter nanotubes at different temperatures for the rope segment between contacts between 2 and 3 (Left inset). In the right inset shows schematic energy levels near Fermi energy which are quantized because of the finite length of tube. [187]

in a plot of $\log R$ versus $1/T$, thereby indicating an energy gap in the range 0.1–0.3 eV, which is consistent with the theoretical values of the energy gap for the corresponding nanotube diameters. On the other hand, for the metallic nanotubes, large variations from sample to sample are observed in the absolute values of the resistance and in its temperature dependence from 4 K to 300 K. This variation has been attributed to the presence of many defects in multi-wall carbon nanotubes. Since the nanotube sample shows a slight positive magnetoresistance, the sample may contain a large number of defects, which seriously affect the measured conductance.

8.2.3 An Individual Rope of Single-Wall Nanotubes

Next we show transport results from a single 12-nm-diameter rope containing about 60 SWNTs of 1.4 nm-diameter [187]. In Fig. 8.7, the current-voltage characteristics are shown for the rope segment between contacts between 2 and 3 (Left inset). At room temperature, the $I - V$ characteristics gives Ohmic behavior, while the conductance is suppressed near $V = 0$ for $T < 10$ K. A similar

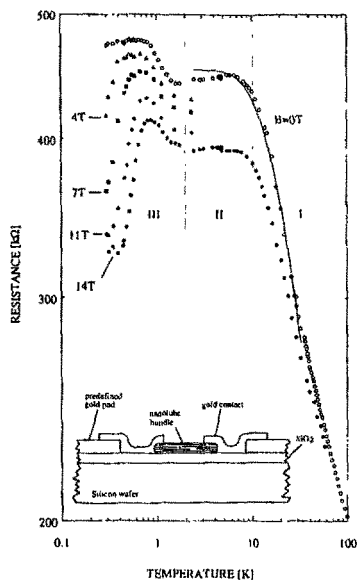


Fig. 8.8: Resistance $R(T)$ of a bundle of multi-wall nanotubes as a function of temperature at the indicated magnetic field values. The temperature-dependent resistance $R(T)$ shows three kinds of temperature regimes (see text [150]).

gap is obtained by other single ropes with different diameters and lengths [187]. From Fig. 8.7, we see that the resistivity decreases with increasing temperature, and this is not typical metallic behavior.

In another experiment on a single rope, about a 10% increase of the resistivity was reported from 50 K to 280 K [188], while a decrease in the resistivity with increasing T was found below 50 K. A negative $d\rho/dT$ with a dependence of $\rho(T) \sim T^{-0.397}$ was even found in the higher temperature region when a single rope has a disordered nanotube alignment. The reasons for these temperature-dependent trends are not explained. It is believed that the transport between single-wall nanotubes in a rope makes an essential contribution to the current at low temperatures.

8.2.4 Magneto-Transport in Multi-Wall Nanotubes

One of the early transport experiments on multi-wall nanotube bundles with 50 nm diameter showed a negative magnetoresistance. In Fig. 8.8 we show the resistance of a bundle of multi-wall nanotubes as a function of temperature at several values of the magnetic field (4 T, 7 T, 11 T, and 14 T) [150]. From

the figure we can see three kinds of temperature regimes denoted I, II, and III. In the higher temperature regime I, the resistance continuously increases with decreasing temperature. These phenomena were accounted for using a simple two-band semimetal model [189] for the electron and hole concentrations n and p as a function of temperature T , and a value of 3.7 meV for the band overlap, which is much smaller than $\Delta \approx 40$ meV in 3D graphite [190]. Since the interlayer interaction in the multi-wall nanotube is incommensurate, as discussed in Section 11.4, the band overlap can be expected to be much smaller, which is consistent with the smaller value of Δ in the small diameter nanotubes. In the temperature regime II, the resistance is almost independent of temperature and has a value of 10^{-2} to 10^{-3} $\Omega\text{-cm}$, thereby suggesting a conducting nature of carbon nanotube bundles. In the temperature regime III, a peak in the resistance is observed whose origin may relate to possible ordered states induced by lowering the symmetry. By lowering the temperature, the resistance quickly decreases.

In the low temperature regime below 77 K, a relatively small negative magnetoresistance $\Delta R/R = [R(H) - R(0)]/R(0) < 0.1$ is observed with \vec{H} normal to the tube axis. There are at least two possible reasons for the observed negative magnetoresistance. One explanation is the effect of weak localization, as discussed in the previous section. However, weak localization effects are expected to occur at much lower temperatures. The other possible reason is associated with Landau level formation at the Fermi level. As shown in Chapter 6, the $n = 0$ th Landau level in two dimensional graphite always appears at the Fermi energy, and the density of states increases with increasing magnetic field, reflecting the degeneracy of the Landau orbits. This enhancement of the density of states at the Fermi Level contributes to an increase in the current path and thus is expected to give rise to a negative magnetoresistance. Thus the negative magnetoresistance above 4 K may be associated with a Landau-level effect (called the Bright model [191]).

In the very low temperature region below 1 K, the negative magnetoresistance shows relatively large values of $\Delta R/R$ as shown in Fig. 8.9 [150]. In the figure, the magnetoresistance shows the same magnetic field dependence at 2.3 K and 1.13 K. However below 1 K, the magnetoresistance becomes quite large (up to $\Delta R/R = 0.3$), which is a typical value for the magnetoresistance in the weakly-localized regime [192]. The phase delocalization length L_φ increases

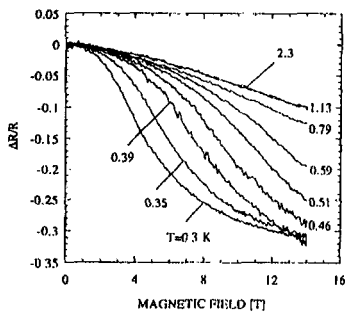


Fig. 8.9: Magnetoresistance $\Delta R/R$ as a function of magnetic field at low temperatures below 1 K. The data are taken on the same multi-wall carbon nanotube as in Fig. 8.8 [150].

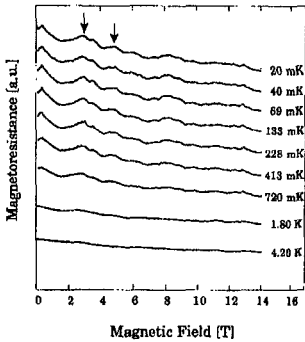


Fig. 8.10: Magnetic field dependence of the magnetoresistance of a 20 nm multi-wall carbon nanotube at the indicated temperatures. The fluctuations in resistance that are observed at the same values of magnetic field at different temperatures are known as universal conductance fluctuations [184].

with decreasing temperature so that the loop of phase difference discussed in the previous section becomes large even for small magnetic fields. Thus a negative magnetoresistance effect is observed in carbon nanotubes at lower magnetic fields than is usually found in graphite. At the lowest temperature of 0.3 K in Fig. 8.9 a saturation of $\Delta R/R$ is observed at large magnetic fields. These data show a complete quenching of the enhanced backscattering. It is interesting that the negative magnetoresistance phenomena occur below that temperature.

In Fig. 8.10 the magnetoresistance for a 20 nm multi-wall nanotube at very low temperature is presented as a function of the magnetic field. Clearly the magnetoresistance is seen to fluctuate randomly by varying the magnetic field. However the peaks in the magnetoresistance for different temperatures appear at the same value of the magnetic field. Thus the fluctuations in the magnetoresistance are not associated with noise but rather are due to a quantum interference effect known as universal conductance fluctuations, which is discussed in Sect. 8.1.4. By applying an external magnetic field, the carrier scattering

processes are changed, thus having the same effect on the magnetoresistance as is observed in Fig 8.10. The effect of variation of the magnetic field is the same as the fluctuations in the conductance that would be observed from sample to sample. The amplitudes of the two indicated fluctuations in Fig 8.10 are constant in magnitude below ~ 0.4 K, $\Delta G = 0.1G_0$, where $G_0 = 2e^2/h$ is the quantum conductance [see Eq. (8.7)], showing that the multi-wall carbon nanotube consists of $N \sim 5$ serial quantum wires of length L_φ . The amplitude of the fluctuation is constant below 0.4 K and decreases as $T^{1/2}$ above 0.4 K, consistent with Eq. (8.30), from which we can estimate $t_\varphi = 2 \times 10^{-11}$ sec.

CHAPTER 9. Phonon Modes of Carbon Nanotubes

The phonon dispersion relations of carbon nanotubes can be understood by zone folding the phonon dispersion curves for a single 2D graphene sheet. In Sec. 9.1 and Sec. 9.2, we first explain how to calculate phonon dispersion relations in two-dimensional graphite. Then we discuss phonon dispersion relations for carbon nanotubes in Sec. 9.3. The zone-folding technique is the same as that used in treating the electronic structure of carbon nanotubes, which is discussed in Sec. 4.1.1. We also consider the three-dimensional dynamical matrix, taking the curvature of the nanotubes into account, and obtain results for the phonon dispersion relations.

9.1 Dynamical matrix for phonon dispersion relations

We start with an approach for calculating the phonon dispersion relations within a force constant model, in which inter-atomic forces are represented by spring constants. Although the model is simple, we can reproduce the experimental results as closely as possible by increasing the number of the force constants.

In general, the equation of motion for the displacement of the i^{th} coordinate, $\mathbf{u}_i = (x_i, y_i, z_i)$ for N atoms in the unit cell is given by

$$M_i \ddot{\mathbf{u}}_i = \sum_j K^{(ij)} (\mathbf{u}_j - \mathbf{u}_i), \quad (i = 1, \dots, N), \quad (9.1)$$

where M_i is the mass of the i^{th} atom and $K^{(ij)}$ represents the 3×3 force constant tensor* between the i^{th} and the j^{th} atoms. The sum over j in Eq. (9.1),

*A second rank tensor is defined by a 3×3 matrix whose elements ($K_{xx}, K_{xy}, \dots, K_{zz}$) can be transformed as $U^{-1} K U$, where U is a unitary matrix which transforms the x, y, z coordinates into another orthogonal x', y', z' coordinate system.

is normally taken over only a few neighbor distances relative to the i^{th} site, which for a 2D graphene sheet has been carried out up to 4th nearest-neighbor interactions [193]. In a periodic system we can perform a Fourier transform of the displacement of the i^{th} atom with the wave number, \mathbf{k}' , to obtain the normal mode displacements $\mathbf{u}_{\mathbf{k}}^{(i)}$

$$\mathbf{u}_i = \frac{1}{\sqrt{N_{\Omega}}} \sum_{\mathbf{k}'} e^{-i(\mathbf{k}' \cdot \mathbf{R}_i - \omega t)} \mathbf{u}_{\mathbf{k}'}^{(i)}, \quad \text{or} \quad \mathbf{u}_{\mathbf{k}}^{(i)} = \frac{1}{\sqrt{N_{\Omega}}} \sum_{\mathbf{R}_i} e^{i(\mathbf{k} \cdot \mathbf{R}_i - \omega t)} \mathbf{u}_i, \quad (9.2)$$

where the sum is taken over all (N_{Ω}) the wave vectors \mathbf{k}' in the first Brillouin zone[†] and \mathbf{R}_i denotes the original position of the i^{th} atom. When we assume the same eigenfrequencies ω for all \mathbf{u}_i , that is $\ddot{\mathbf{u}}_i = -\omega^2 \mathbf{u}_i$, then Eq. (9.1) becomes

$$\left(\sum_j K^{(ij)} - M_i \omega^2 \right) \sum_{\mathbf{k}'} e^{-i\mathbf{k}' \cdot \mathbf{R}_i} \mathbf{u}_{\mathbf{k}'}^{(i)} = \sum_j K^{(ij)} \sum_{\mathbf{k}'} e^{-i\mathbf{k}' \cdot \mathbf{R}_j} \mathbf{u}_{\mathbf{k}'}^{(j)}. \quad (9.3)$$

Upon multiplying both sides of Eq. (9.3) by $e^{i\mathbf{k} \cdot \mathbf{R}_i}$, taking a summation on \mathbf{R}_i , and using the following orthogonality condition in the continuum \mathbf{k} space,[‡]

$$\sum_{\mathbf{R}_i} e^{i(\mathbf{k} - \mathbf{k}') \cdot \mathbf{R}_i} = N_{\Omega} \delta_{\mathbf{k}, \mathbf{k}'} \quad (9.4)$$

we get

$$\left(\sum_j K^{(ij)} - M_i \omega^2(\mathbf{k}) I \right) \mathbf{u}_{\mathbf{k}}^{(i)} - \sum_j K^{(ij)} e^{i\mathbf{k} \cdot \Delta \mathbf{R}_{ij}} \mathbf{u}_{\mathbf{k}}^{(j)} = 0, \quad (i = 1, \dots, N), \quad (9.5)$$

where I is a 3×3 unit matrix and $\Delta \mathbf{R}_{ij} = \mathbf{R}_i - \mathbf{R}_j$ is the relative coordinate of the i^{th} atom with respect to the j^{th} atom. The vibration of the i^{th} atom is coupled to that of the j^{th} atom through the $K^{(ij)}$ force constant tensor.

We note that j in Eq. (9.1) can be a site in the neighboring unit cell when the i^{th} atom is near the unit cell boundary. Here we show that all j in Eq. (9.5) can be shifted to a site in the original unit cell. When the j and j' sites are equivalent to each other (i.e., \mathbf{R}_j and $\mathbf{R}_{j'}$ differ by a lattice vector), then by

[†] N_{Ω} is the number of unit cells in the solid and thus $N_{\Omega} \sim 10^{23}$.

[‡] $\delta_{\mathbf{k}, \mathbf{k}'}$ is a delta function which vanishes unless $\mathbf{k} = \mathbf{k}'$, in which case $\delta_{\mathbf{k}, \mathbf{k}'}$ has the value of unity.

considering $\mathbf{R}_j - \mathbf{R}_{j'}$, we can show that $\mathbf{u}_k^{(j)} = \mathbf{u}_k^{(j')}$ using the definition of $\mathbf{u}_k^{(j)}$ in Eq. (9.2). Thus Eq. (9.5) contains the variables $\mathbf{u}_k^{(j)}$ within the original unit cell. The contributions of $K^{(ij')}$ in which the j' sites are equivalent to the j sites, are added to $K^{(ij)}$ with a phase factor $e^{i\mathbf{k} \cdot \Delta\mathbf{R}_{ij'}}$. Thus we obtain simultaneous equations in Eq. (9.5) for $3N$ unknown variables $\mathbf{u}_k \equiv {}^t(\mathbf{u}_k^{(1)}, \mathbf{u}_k^{(2)}, \dots, \mathbf{u}_k^{(N)})$, for a given \mathbf{k} vector, in which the superscript t denotes the transpose of a row vector into a column vector, and vice versa. Then Eq. (9.5) can be formally written as follows by defining a $3N \times 3N$ dynamical matrix $\mathcal{D}(\mathbf{k})$

$$\mathcal{D}(\mathbf{k})\mathbf{u}_k = 0. \quad (9.6)$$

To obtain the eigenvalues $\omega^2(\mathbf{k})$ for $\mathcal{D}(\mathbf{k})$ and non-trivial eigenvectors $\mathbf{u}_k \neq 0$, we solve the secular equation $\det\mathcal{D}(\mathbf{k}) = 0$ for a given \mathbf{k} vector. It is convenient to divide the dynamical matrix $\mathcal{D}(\mathbf{k})$ into small 3×3 matrices $\mathcal{D}^{(ij)}(\mathbf{k})$, ($i, j = 1, \dots, N$), where we denote $\mathcal{D}(\mathbf{k})$ by $\{\mathcal{D}^{(ij)}(\mathbf{k})\}$, and from Eq. (9.5) it follows that $\mathcal{D}^{(ij)}(\mathbf{k})$ is expressed as

$$\mathcal{D}^{(ij)}(\mathbf{k}) = \left(\sum_{j''} K^{(ij'')} - M_i \omega^2(\mathbf{k}) I \right) \delta_{ij} - \sum_{j'} K^{(ij')} e^{i\mathbf{k} \cdot \Delta\mathbf{R}_{ij'}}, \quad (9.7)$$

where the sum over j'' is taken for all neighbor sites from the i^{th} atom with $K^{(ij'')} \neq 0$, and the sum over j' is taken for the equivalent sites to the j^{th} atom. The first two terms[§] of Eq. (9.7) have non-vanishing values only when $i = j$, and the last term appears only when the j^{th} atom is coupled to the i^{th} atom through $K^{(ij)} \neq 0$.

In a periodic system, the dynamical matrix elements are given by the product of the force constant tensor $K^{(ij)}$ and the phase difference factor $e^{i\mathbf{k} \cdot \Delta\mathbf{R}_{ij}}$. This situation is similar to the case of the tight binding calculation for the electronic structure where the matrix element is given by the product of the atomic matrix element and the phase difference factor (see Sec. 2.1).

9.2 Phonon dispersion relations for two-dimensional graphite

[§]This corresponds to the diagonal block of the dynamical matrix. The last term in Eq. 9.7 is in the off-diagonal (ij) block of the dynamical matrix. When the i^{th} atom has equivalent neighbor atoms in the adjacent unit cells, the last term can appear in the diagonal block of the dynamical matrix.

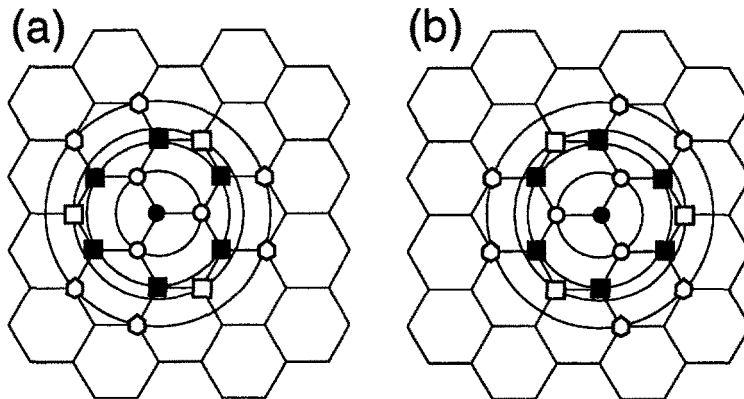


Fig. 9.1: Neighbor atoms of a graphitic plane up to 4th nearest neighbors for (a) an A atom and (b) a B atom at the center denoted by solid circles. From the 1st to the 4th neighbor atoms, we plot open circles (1st neighbor), solid squares (2nd), open squares (3rd), and open hexagons (4th), respectively. Circles connecting the same neighbor atoms are for guides to the eye.

The phonon dispersion relations for a single graphite plane (or a two-dimensional graphene sheet) are calculated by following the procedure used in Sec. 4.1.1 for the electronic energy bands for the σ and π electrons of graphite.*

In two-dimensional graphite, since there are two carbon atoms, A and B , in the unit cell, (see Fig. 2.3), we must consider six coordinates $u_{\mathbf{k}}$ (or 6 degrees of freedom) in Eq. (9.6). The secular equation to be solved is thus a 6×6 dynamical matrix \mathcal{D} . The dynamical matrix \mathcal{D} for two-dimensional graphite is written in terms of the 3×3 matrices D^{AA} , D^{AB} , D^{BA} , and D^{BB} for the A and B atoms within the unit cell, and the coupling between them

$$\mathcal{D} = \begin{pmatrix} D^{AA} & D^{AB} \\ D^{BA} & D^{BB} \end{pmatrix}. \quad (9.8)$$

When we consider an A atom, the three nearest-neighbor atoms (see Figs. 9.1 and 9.2) are $B1$, $B2$, and $B3$ whose contributions to \mathcal{D} are contained in D^{AB} ,

*From a symmetry standpoint, only the electronic bands related to the carbon p electrons have a direct correspondence to the phonon dispersion curves.

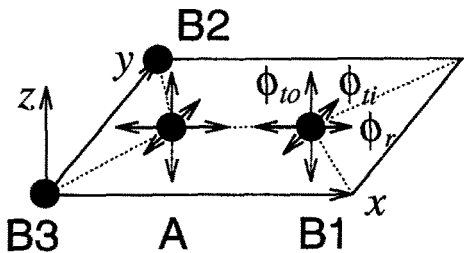


Fig. 9.2: Force constants between the A and B1 atoms on a graphene sheet. Here ϕ_r , ϕ_{ti} , and ϕ_{to} represent forces for the nearest-neighbor atoms in the radial (bond-stretching), in-plane and out-of-plane tangential (bond-bending) directions, respectively. B2 and B3 are nearest neighbors equivalent to B1, whose force constant tensors are obtained by appropriately rotating the tensor for A and B1.

while the six next-nearest-neighbor atoms denoted by solid squares in Fig. 9.1(a) are all A atoms, with contributions to \mathcal{D} that are contained in D^{AA} and so on. In Fig. 9.1 (a) and (b), we show neighbor atoms up to 4th nearest neighbors for the A and B atoms, respectively. It is important to note that the A and B sites do not always appear alternately for the nth neighbors. In fact the third and the fourth neighbor atoms belong to equivalent atoms.

The remaining problem is how to construct the force constant tensor $K^{(ij)}$. Here we show a simple way to obtain $K^{(ij)}$.[†] First we consider the force constant between an A atom and a nearest-neighbor B1 atom on the x axis as shown in Fig. 9.2 [see also Fig. 2.3 (a)]. The force constant tensor is given by

$$K^{(A,B1)} = \begin{pmatrix} \phi_r^{(1)} & 0 & 0 \\ 0 & \phi_{ti}^{(1)} & 0 \\ 0 & 0 & \phi_{to}^{(1)} \end{pmatrix}, \quad (9.9)$$

where $\phi_r^{(n)}$, $\phi_{ti}^{(n)}$, and $\phi_{to}^{(n)}$ represent the force constant parameters in the radial (bond-stretching), in-plane and out-of-plane tangential (bond-bending) direc-

[†]Since the determinant of the dynamical matrix is a scalar variable, the determinant should be invariant under any operation of the point group for the unit cell. Thus the proper combination of terms in the product of the force constant tensor $K^{(ij)}$ and the phase difference factor $e^{i\mathbf{k}\cdot\Delta\mathbf{R}_{ij}}$ is determined by group theory, which gives block-diagonalization in accordance with the irreducible representations of the symmetry group of periodic structures. Further details are given in the references: G. Dresselhaus and M. S. Dresselhaus, Int. J. Quantum Chem., Vol II s, 333 (1968) for silicon and germanium, and L. G. Johnson and G. Dresselhaus, Phys. Rev. B7, 2275 (1973) for graphite.

tions of the n^{th} nearest neighbors, respectively. Here the graphene plane is the xy plane, the radial direction (x in the case of Fig. 9.2) corresponds to the direction of the σ bonds (dotted lines), and the two tangential directions (y and z) are taken to be perpendicular to the radial direction. Since graphite is an anisotropic material, we introduce two parameters to describe the in-plane (y) and out-of-plane (z) tangential modes, and the corresponding phase factor, $e^{ik \cdot \Delta \mathbf{R}_{ij}}$, becomes $\exp(-ik_x a/\sqrt{3})$ for the $B1$ atom at $(a/\sqrt{3}, 0, 0)$.

The force constant matrices for the two other nearest-neighbor atoms, $B2$ and $B3$ are obtained by rotating the matrix in Eq. (9.9) according to the rules for a second-rank tensor:

$$K^{(A, Bm)} = U_m^{-1} K^{(A, B1)} U_m, \quad (m = 2, 3) \quad (9.10)$$

where the unitary matrix U_m is here defined by a rotation matrix around the z axis in Fig. 9.2, taking the $B1$ atom into the Bm atom,[†]

$$U_m = \begin{pmatrix} \cos \theta_m & \sin \theta_m & 0 \\ -\sin \theta_m & \cos \theta_m & 0 \\ 0 & 0 & 1 \end{pmatrix}. \quad (9.11)$$

To make the method explicit, we show next the force constant matrix for the $B2$ atom at $[-a/(2\sqrt{3}), a/2, 0]$, and U_2 is evaluated assuming $\theta_2 = 2\pi/3$,

$$K^{(A, B2)} = \frac{1}{4} \begin{pmatrix} \phi_r^{(1)} + 3\phi_{ti}^{(1)} & \sqrt{3}(\phi_{ti}^{(1)} - \phi_r^{(1)}) & 0 \\ \sqrt{3}(\phi_{ti}^{(1)} - \phi_r^{(1)}) & 3\phi_r^{(1)} + \phi_{ti}^{(1)} & 0 \\ 0 & 0 & \phi_{to}^{(1)} \end{pmatrix}, \quad (9.12)$$

and the corresponding phase factor is given by $\exp[-ik_x a/(2\sqrt{3}) + ik_y a/2]$.

In the case of the phonon dispersion relations calculation for 2D graphite, the interaction between two nearest-neighbor atoms is not sufficient to reproduce the experimental results, and we generally need to consider contributions from long-distance forces, such as from the n^{th} neighbor atoms, ($n = 1, 2, 3, 4, \dots$).[‡] To

[†]The formulation should be in terms of the rotation of the axes connecting an atom A to its various equivalent neighbors. However, for easy understanding, we present in Eq. (9.10) the rotation of atoms. The matrix for the rotation of the axes is the transpose matrix of the matrix for the rotation of atoms.

[‡]When we consider the force constant matrix of the n^{th} neighbor atoms, these atoms are not always located on the x (or y) axis. In that case it does not seem that we can build an initial force constant matrix as given by Eq. (9.9). This happens at 4th neighbor atoms in graphite. However, if we consider a virtual atom on the x axis, and if we then rotate the matrix, we can get the force constant matrix without any difficulty.

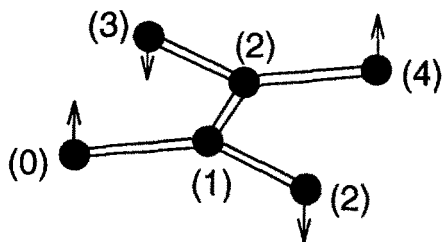


Fig. 9.3: In order to describe the twisted motion of four atoms, it is necessary to consider up to at least fourth-nearest-neighbor interactions. The numbers shown in the figure denote the n^{th} nearest-neighbor atoms from the leftmost 0^{th} atom.

describe the twisted motion of four atoms, in which the outer two atoms vibrate around the bond of the two inner atoms as shown in Fig. 9.3, contributions up to at least the fourth nearest-neighbor interactions are necessary [194]. Values for the force constants [193] (see Table 9.1) are obtained by fitting the 2D phonon dispersion relations over the Brillouin zone as determined experimentally, as for example from inelastic neutron scattering or electron energy loss spectroscopy measurements along the Γ M direction [194, 195].

Table 9.1: Force constant parameters for 2D graphite in units of 10^4dyn/cm [193]. Here the subscripts r , ti , and to refer to radial, transverse in-plane and transverse out-of-plane, respectively. See Figs. 9.1 and 9.2.

Radial		Tangential		
$\phi_r^{(1)}$ =	36.50	$\phi_{ti}^{(1)}$ =	24.50	$\phi_{to}^{(1)}$ = 9.82
$\phi_r^{(2)}$ =	8.80	$\phi_{ti}^{(2)}$ =	-3.23	$\phi_{to}^{(2)}$ = -0.40
$\phi_r^{(3)}$ =	3.00	$\phi_{ti}^{(3)}$ =	-5.25	$\phi_{to}^{(3)}$ = 0.15
$\phi_r^{(4)}$ =	-1.92	$\phi_{ti}^{(4)}$ =	2.29	$\phi_{to}^{(4)}$ = -0.58

In Fig. 9.4(a) the phonon dispersion curves of a two-dimensional graphene sheet, denoted by solid lines, are shown using the set of force constants in Table 9.1. In Fig. 9.4(b) the corresponding density of states is plotted per C atom per cm^{-1} , where the energy is in units of cm^{-1} . The calculated phonon dispersion curves of Fig. 9.4(a) reproduce the experimental points obtained by electron energy loss spectroscopy very well [194, 195]. Thus the inclusion of fourth-neighbor interactions is sufficient for reproducing the phonon dispersion relations of 2D graphite.

The three phonon dispersion curves (or branches), which originate from the

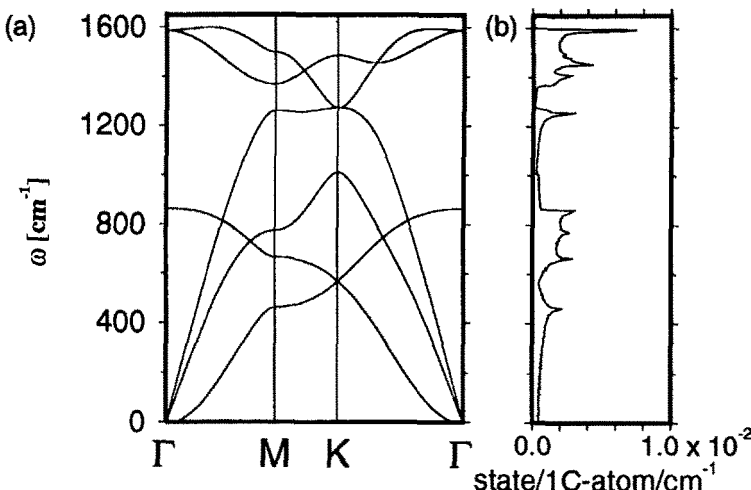


Fig. 9.4: (a) The phonon dispersion curves, plotted along high symmetry directions, for a 2D graphene sheet, using the set of force constants in Table 9.1 [193]. (b) The corresponding density of states vs phonon energy for phonon modes in units of states/ $1\text{C-atom}/\text{cm}^{-1} \times 10^{-2}$.

Γ point of the Brillouin zone [see Fig. 9.4(a)], correspond to acoustic modes: an out-of-plane mode, an in-plane tangential (bond-bending) mode and an in-plane radial (bond-stretching) mode, listed in order of increasing energy, respectively. The remaining three branches correspond to optical modes: one out-of-plane mode and two in-plane modes. It is noted that the out-of-plane (transverse) acoustic branch shows a k^2 energy dispersion relation around the Γ point, while the other two in-plane acoustic branches show a linear k dependence, as is normally seen for acoustic modes. One reason why we get a k^2 dependence for the out-of-plane mode is simply because this branch corresponds to a two-dimensional phonon mode and because graphite has three-fold rotational symmetry. It is clear in Eq. (9.10) that all rotations U are within the x, y plane in the case of two-dimensional graphite. Thus the force constant matrix can be decomposed into a 2×2 matrix of x, y components and a 1×1 matrix of z components. The 1×1 force constant tensor $K_{zz}^{(ij)}$ for the n^{th} neighbor atoms

does not depend on the coordinate, and $\omega(k)$ thus becomes an even function of k which is obtained from the sum of the differential phase factors $e^{ik \cdot \Delta \mathbf{R}_{ij}}$ given by Eq. (9.5).[¶] If we consider only the three nearest-neighbor atoms, the sum of the differential phase factors is nothing but $f(k)$ obtained in Eq. (2.25) when discussing the electronic structure. The energy dispersion relation thus obtained [see Eq. (2.28)] is an even function of k around the Γ point. The optical out-of-plane transverse branch ($\sim 865 \text{ cm}^{-1}$ at the Γ point) shows a k^2 dependence for the same reason. Thus there is neither a phase velocity nor a group velocity for the z component of the vibrations at the Γ point, and the phonon density of states shows a step function which is known as a two-dimensional van-Hove singularity [see Fig. 9.4(b)].

9.3 Phonon dispersion relations for nanotubes

9.3.1 Zone folding method

As a first approximation, the phonon dispersion relations for a single-wall carbon nanotube are determined by folding the phonon dispersion curves of a two-dimensional graphene layer, which was discussed in § 9.2. The method of folding the phonon dispersion curves for a given chiral vector $C_h \equiv (n, m)$ is the same as that for electrons, as discussed in § 4.1.1, except that the zone-folding is applied to the 2D *phonon* dispersion relations. Since there are $2N$ carbon atoms in the unit cell of a carbon nanotube, where $N = 2(n^2 + m^2 + nm)/d_R$ and d_R are defined in Eqs. (3.9) and (3.7), respectively (see also Table. 3.3), $6N$ phonon

[¶]In general, the phase factor $e^{ik \cdot \Delta \mathbf{R}_{ij}}$ goes into its complex conjugate if we change \mathbf{k} to $-\mathbf{k}$. Thus when we change \mathbf{k} to $-\mathbf{k}$, the dynamical matrix for the z components in a two-dimensional system becomes its complex conjugate. It is clear that $|D^*| = |D|$ for the Hermitian matrix D , and thus the eigenvalues are even functions of \mathbf{k} around $\mathbf{k} = 0$ (the Γ point). Even though $\omega(\mathbf{k})$ is an even function of \mathbf{k} , a term proportional to $|\mathbf{k}|$ might appear in $\omega(\mathbf{k})$. For example, for a one-dimensional spring constant model with the force constant, K , we get $\omega(k) = 2\sqrt{K/M} |\sin ka| \propto |k|$, ($k \sim 0$). The absence of a linear k term in the phonon dispersion relations along the z axis of graphite comes from the three-fold rotational axis, C_3 along the z direction. Because of this symmetry, the $\omega(k_x, k_y)$ should have three-fold rotational symmetry around the C_3 axis. However, no linear combination of k_x and k_y , such as $ak_x + bk_y$ (with constant values for a, b), can be invariant under a $2\pi/3$ rotation around the k_z axis. The simplest invariant form is a constant, and the quadratic form of $k_x^2 + k_y^2$ is also invariant. This is why we get a k^2 dependence for $\omega(k)$ for the out-of-plane branch. When the force constant matrix depends on the atom locations, such as for the in-plane modes, this invariant condition applies to the product of the force constant matrix and the phase difference factor, which generally has a linear k term in $\omega(k)$.

dispersion relations for the x , y , and z vibrations for each atom are folded into the one-dimensional Brillouin zone of a carbon nanotube along the \mathbf{K}_2 direction (Eq. (3.20)). The phonon dispersion relations of a carbon nanotube also depend on the chirality (n, m) and diameter of the carbon nanotube, d_t , since the phonon wave vector in the circumferential direction becomes discrete for every \mathbf{K}_1 vector [see Eqs. (3.20) and (4.1)], in accordance with the periodic boundary conditions of the chiral vector.

The corresponding one-dimensional phonon energy dispersion relation $\omega_{1D}^{m\mu}(k)$ for the nanotubes is given by,

$$\omega_{1D}^{m\mu}(k) = \omega_{2D}^m(k \frac{\mathbf{K}_2}{|\mathbf{K}_2|} + \mu \mathbf{K}_1), \quad \left(\begin{array}{l} m = 1, \dots, 6, \\ \mu = 0, \dots, N-1, \end{array} \text{ and } -\frac{\pi}{T} < k \leq \frac{\pi}{T} \right), \quad (9.13)$$

where $\omega_{2D}^m(k)$ denotes the two-dimensional energy dispersion relations for a graphene sheet, k is a one-dimensional wave vector, and T is the magnitude of the one-dimensional translation vector \mathbf{T} given in Eq. (3.8).

The idea of zone folding is applicable for almost all the phonon modes of a carbon nanotube. However, it has been pointed out [193] that zone-folding alone does not always give the correct dispersion relation for a carbon nanotube, especially in the low frequency region, and some additional physical concepts must be introduced. For example, the out-of-plane tangential acoustic (TA) modes of a graphene sheet shown in Fig. 9.5(a) on the left do not give zero energy at the Γ point when rolled into a nanotube as shown on the right. Here, at $\mathbf{k} = 0$, all the carbon atoms of the nanotube move radially in an out-of-plane radial acoustic vibration, which corresponds to a breathing mode with non-zero frequency [193] as shown in Fig. 9.5(a) on the right. In the breathing mode, only the in-plane force constants, ϕ_r and ϕ_{ti}^* in the circumferential direction of the tube are related to the vibration, and this results in a finite frequency at the Γ point.

On the other hand, when we consider the vibrations of a carbon nanotube in the context of three-dimensional space, we generally expect three acoustic modes which correspond to vibrational motions in the x, y, z directions. However, the two directions which are perpendicular to the nanotube axis do not correspond

*Since there is no vibration in the direction of the nanotube axis in the breathing mode, the bond angle of the hexagon network is modified. Thus the force constant ϕ_{ti} is necessary to describe the breathing mode.

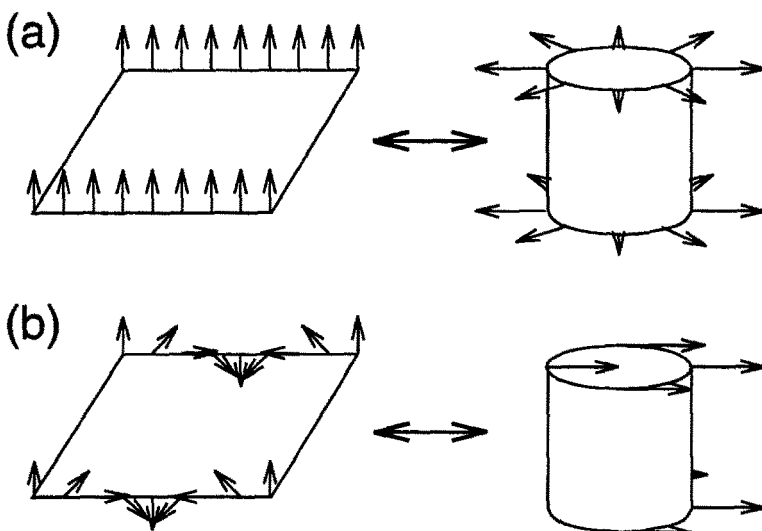


Fig. 9.5: (a) The out-of-plane tangential acoustic modes at $\mathbf{k} = 0$ (left) in a single layer of graphite give rise to a radial breathing mode in the carbon nanotube with non-zero frequency (right). (b) An acoustic mode of a carbon nanotube whose vibration is perpendicular to the nanotube axis (right) corresponds to a linear combination of both in-plane and out-of-plane graphite-derived modes (left). These modes do not couple in the case of a single graphite layer, but do couple for the nanotube because of the curvature that is introduced by rolling up the sheet.

to any two-dimensional graphite phonon modes. In a graphene sheet, the in-plane and out-of-plane modes are decoupled from each other. However, when the graphene strip is rolled up into a nanotube, the graphite-derived in-plane and out-of-plane modes do couple to each other, as shown on the left-hand side of Fig. 9.5(b), to form the acoustic mode of the nanotube shown on the right.

9.3.2 Force constant tensor of a carbon nanotube

In order to avoid these difficulties, we solve the three-dimensional carbon nanotube dynamical matrix problem directly using the force constant parameters

listed in Table 9.1. Since we have $2N$ carbon atoms, the dynamic matrix to be solved becomes a $6N \times 6N$ matrix. Here we denote the $2N$ atoms as Ai and Bj ($i, j = 1, \dots, N$), where the N Ai (or $N Bj$) atoms are geometrically equivalent to each other, as discussed in § 3.4. In fact, the position of each Ap (or Bp) atom can be obtained by operation of the symmetry vector \mathbf{R} defined in Eq.(3.10) $p - 1$ times on $A1$ (or $B1$):

$$A1 \xrightarrow{\mathbf{R}^{p-1}} Ap, \quad \text{and} \quad B1 \xrightarrow{\mathbf{R}^{p-1}} Bp, \quad (p = 1, \dots, N). \quad (9.14)$$

When we divide the big $6N \times 6N$ dynamical matrix into the 3×3 small matrices $\mathcal{D}^{(AiBj)}$ for a pair of Ai and Bj atoms, we then consider $(2N)^2 = 4N^2$ small matrices, $\mathcal{D}^{(AiAj)}$, $\mathcal{D}^{(AiBj)}$, $\mathcal{D}^{(BiAj)}$, and $\mathcal{D}^{(BiBj)}$, ($i, j = 1, \dots, N$). When a pair $(ApBq)$, (or $(ApAq)$, $(BpAq)$, $(BpBq)$) are within the 4th neighbor distance, we will consider $\mathcal{D}^{(ApBq)}$. The corresponding force constant tensor $K^{(ApBq)}$ is calculated using

$$K^{(ApBq)} = (U^{-1})^{p-1} K^{(A1Bq-p+1)} U^{p-1}, \quad (9.15)$$

where U is a unitary matrix for rotation by an angle $\Psi = 2\pi/N$ around the nanotube axis. Then U^{p-1} is defined in Eq. (3.16) as

$$U^{p-1} = \begin{pmatrix} \cos(p-1)\Psi & \sin(p-1)\Psi & 0 \\ -\sin(p-1)\Psi & \cos(p-1)\Psi & 0 \\ 0 & 0 & 1 \end{pmatrix}, \quad (9.16)$$

where the z axis is taken for the nanotube axis. When $(q - p + 1)$ is negative or zero in Eq. (9.15), we use $(N + q - p + 1)$ for $(q - p + 1)$. Thus we can generate all force constant tensors from the non-zero tensor related to $A1$ or $B1$.

When we consider $K^{(A1Bp)}$ or $K^{(B1Bp)}$, the effect of the curvature has been taken into account. For example, let us consider the case of $K^{(A1B1)}$ (see Fig. 9.6). When we put atom $A1$ on the x axis, $K^{(A1B1)}$ is obtained by: (a) rotating the tensor of Eq. (9.9) by $(\pi/6) - \theta$ around the x axis, then (b) rotating the tensor by an angle $\varphi/2$ around the z axis, and finally (c) rotating by Ψ around the z axis. Here the angles θ , φ and Ψ are, respectively, the chiral angle θ defined in Eq. (3.4), the angle φ between $A1$ and $B1$ around the z axis, and the angle Ψ between $A1$ and Ap around the z axis defined by $2(p-1)\pi/N$ in Eq. (3.4), as shown in Fig. 9.6 (a), (b) and (c), respectively.

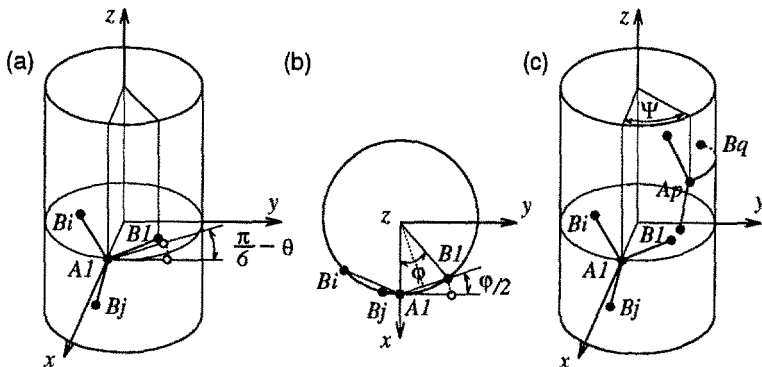


Fig. 9.6: The geometry of the A_1 atom and its nearest neighbor atoms, B_1 , B_i , B_j . The force constant tensor $K^{(A_1B_1)}$ is obtained by (a) rotating the tensor of Eq. (9.9) by $(\pi/6) - \theta$ around the x axis and by (b) rotating the force constant tensor by an angle $\varphi/2$ around the z axis. Here θ is the chiral angle defined in Eq. (3.4), and the angle φ is defined in this figure by the angle between A_1 and B_1 in the xy plane around the z axis. The upper open circle in (a) represents the projection of B_1 on the yz plane and the lower open circle represents its location after rotation by $\pi/6 - \theta$ on a 2D graphene plane. For $K^{(A_pB_q)}$, we further rotate in (c) the force constant tensor by Ψ around the z axis (see Eq. (9.16)).

Using the force constant tensor thus obtained and multiplying by $\exp ik\Delta z_{ij}$, where Δz_{ij} is the component of $\Delta \mathbf{R}_{ij}$ along the z or nanotube axis, the dynamical matrix for a k vector is obtained. The phonon energy dispersion relation is determined by solving the dynamical matrix for many k points in the one-dimensional Brillouin zone.

The results thus obtained for $\omega(k)$ for a (10,10) armchair carbon nanotube are given in Fig. 9.7(a), where T denotes the magnitude of the unit vector along the tube axis (see Eq. (3.5)). For the $2N = 40$ carbon atoms per circumferential strip for the (10,10) nanotube, we have 120 vibrational degrees of freedom, but because of mode degeneracies there are only 66 distinct phonon branches, of which 12 modes are non-degenerate and 54 are doubly degenerate. The number of distinct phonon branches can be obtained by point group theory for atoms

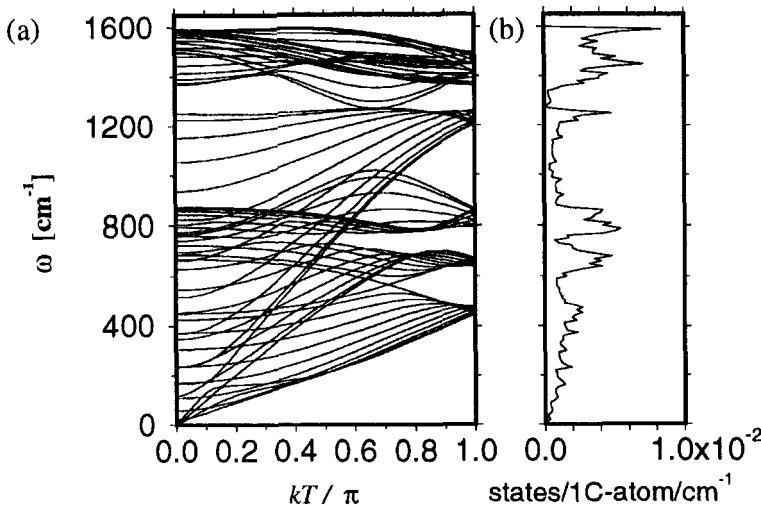


Fig. 9.7: (a) The calculated phonon dispersion relations of an armchair carbon nanotube with $C_h = (10, 10)$. The number of degrees of freedom is 120 and the number of distinct phonon branches is 66. (b) Phonon density of states of (10,10) nanotubes.

in the unit cell. In the case of the (10,10) armchair nanotube, D_{10h} is the point symmetry group, and the direct product of the reducible representation for the atomic sites* with the representations for x, y, z is decomposed into the irreducible representations for the phonon modes.

In Fig. 9.7(b) we show the phonon density of states for the (10,10) nanotube in units of states per C atom per cm^{-1} . When we integrate the phonon density of states with respect to the energy, we get 3 states/C-atom as the total number of states. Since we use the same units for the phonon density of states for 2D graphite [see Fig. 9.4(b)], we can directly compare the phonon density of states for the (10,10) nanotube and for 2D graphite. The phonon density of states for the (10,10) nanotube is close to that for 2D graphite [see Fig. 9.4(b)] since the phonon dispersion relations are, in principle, given by the zone-folding of

*The character of the atomic sites for an operation O of the point group is defined by the number of atoms which do not change their position when the operation O is carried out.

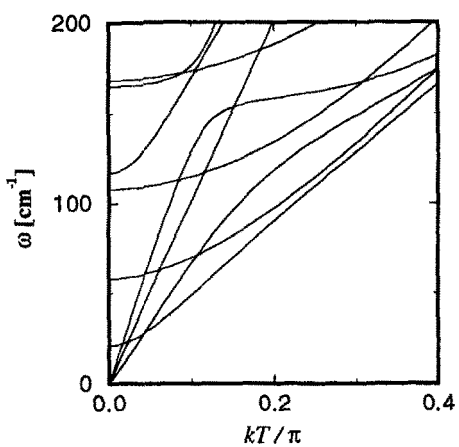


Fig. 9.8: Phonon dispersion relations of the (10,10) armchair carbon nanotube near the Γ point. The three lines near $\omega = 0$ which intersect at $k = 0$ correspond to the acoustic modes of a carbon nanotube. There are four acoustic modes in this cylindrical solid, including the lower energy x, y transverse acoustic modes (TA, doubly degenerate), the z longitudinal acoustic mode (LA), and the φ twisting mode (TW). The TW mode is related to the rotation of a nanotube along its axis.

those for 2D graphite. The difference in the phonon densities of states appear in the small peaks due to the one-dimensional van Hove singularities. It is noted that we integrated the phonon states within an accuracy of 10 cm^{-1} . Another difference between the (10,10) nanotube and graphite relates to the phonon density of states at $\omega = 0 \text{ cm}^{-1}$. Since there is k^2 dependence in the out-of-plane TA mode for 2D graphite, we get a finite density of states at $\omega = 0 \text{ cm}^{-1}$, which is known as the two-dimensional van Hove singularity at the band edge. However, since all acoustic modes of the (10,10) nanotube have a k dependence as shown below, we have no phonon density states at $\omega = 0$ as shown in Fig. 9.7(b).

Let us focus our attention on the acoustic modes of the (10,10) carbon nanotube. In Fig. 9.8, the phonon dispersion curves around the Γ point are shown on an expanded scale for the (10,10) carbon nanotube. The lowest energy modes are the transverse acoustic (TA) modes, which are doubly degenerate, and have x and y vibrations perpendicular to the nanotube (z) axis (see Fig. 9.5(b) right). The highest energy mode is the longitudinal acoustic (LA) mode in the direction of the nanotube axis. Since the displacements of all the acoustic modes are three dimensional, the frequencies of the phonon dispersion relations are proportional to k for all three phonon branches, as is commonly observed in the solid state. The corresponding phonon density of states is proportional to

the energy while the phonon density of states of 2D graphite is constant because of the k^2 dispersion relation for the out-of-plane TA graphite mode. The sound velocities of the TA and LA phonons for a (10,10) armchair carbon nanotube are estimated as 9.43 km/s and 20.35 km/s, respectively.[†] These results cannot be obtained by the zone-folding method discussed in the previous subsection, since the sound velocity for the zone-folded out-of-plane TA mode is zero because of the k^2 dependence as discussed above.

In addition, there is a fourth acoustic mode for the carbon nanotube, which is related to a rotation around the nanotube axis at $k = 0$. When we consider a single carbon nanotube as an infinite one-dimensional material, a rotation around the nanotube axis is possible [83, 196]. Since the driving force for this wave motion is a twisting motion of the nanotube, we call this mode a twisting mode (TW). The sound velocity of the TW mode is 15.00 km/s, which is the same as the calculated value of the in-plane TA mode for 2D graphite. The reason why the TW modes have the same velocity as the TA graphite mode is that the displacements associated with the TW mode are in the cylindrical plane and are perpendicular to the tubular axis.

It is noted that the sound velocities that we have calculated for 2D graphite are similar to those observed in 3D graphite [9], for which $v_{TA}^{G3D} = 12.3$ km/s and $v_{LA}^{G3D} = 21.0$ km/s. The difference of the sound velocity is due to the existence or absence of the interlayer interaction between graphene layers for 3D graphite and a 2D graphene sheet, respectively.

9.3.3 Force constant corrections due to curvature of 1D nanotubes

The three-dimensional phonon dispersion relations of a carbon nanotube can be obtained by the methods discussed in the previous subsection. However it should be mentioned that the force constant parameters of Table 9.1 are not well defined on the curved surface of the nanotube by merely considering the planar graphene force constants.

[†]The Young modulus, Y can be estimated by the LA velocity, $v = \sqrt{Y/\rho}$, in which ρ is the density of carbon atoms. When we assume the triangular lattice of the nanotubes (so called rope) with the lattice constants of $a = 16.95\text{\AA}$ and $c = 1.44 \times \sqrt{3}\text{\AA}$, the density ρ becomes $1.28 \times 10^3 \text{ kg/m}^3$ from which the Young modulus gives $Y = 532 \text{ GPa}$. This value is smaller than other calculated Y values. This small Y value arises from the small mass density of the rope. Details will be discussed in Chapter 11 on elastic constants.

For example, in Fig. 9.9, we show the effect of the rotational motion of the twisting mode with $k = 0$ on the cross section of the carbon nanotube in which all vectors of the motion should be parallel to the cylindrical surface and perpendicular to the nanotube axis. It is a physical requirement that we have a rotational mode with $\omega = 0$ at $k = 0$ in this system. However, the calculated result for the (10,10) carbon nanotube gives a finite value of $\omega = 4 \text{ cm}^{-1}$ at $k = 0$ for the twisting mode when we use the method of the previous subsection with the force constant parameters of Table 9.1. The other three acoustic modes correctly give $\omega = 0 \text{ cm}^{-1}$ at $k = 0$. When we denote a nearest-neighbor bond as the dotted line in Fig. 9.9, the two vectors \mathbf{u} and \mathbf{Gu} are not in the plane which is defined by the dotted line and tube axis. Thus, for this kind of rotational motion, the force associated with the tangential out-of-plane force constant, ϕ_{t0} , artificially introduces a force on the motion, which gives a non-zero value of ω at $k = 0$. Actually when we examine the eigenvectors of the motion, we can find a small radial component of the motion which is perpendicular to the cylindrical surface and is due to the effect of curvature on the force constant parameters. The ratio of the components of the motion in the radial direction to the cylindrical direction is on the order of 10^{-5} . The curvature effect will also apply to all of the other modes by an amount up to $\sim 10 \text{ cm}^{-1}$ even for the (5,5) armchair nanotube. Thus as a first approximation, this effect can be neglected compared with general nanotube phonon frequencies which are on the order of 10^3 cm^{-1} .

In order to treat the curvature effect correctly with the given force constant parameters of two-dimensional graphite, we could consider the dynamical matrix on a curved coordinate reflecting the cylindrical surface, which would mix the force constant parameters with each other depending on the curvature and the bond length. This phenomenon can be treated by elasticity theory for a thin film. However this treatment requires a different method from that used for a lattice of springs. When we consider a curved chemical bond, we find that the force constant parameters in Table 9.1 cannot be applicable to the curved coordinates. Actually the calculated results using the force constant parameters in Table 9.1 give less accurate values than the approach of the previous subsection. Sometimes the calculated results even give imaginary (i.e., negative ω^2) frequencies for the acoustic phonon modes. Thus we do not use the elasticity theory approach to the curved coordinates of carbon nanotubes.

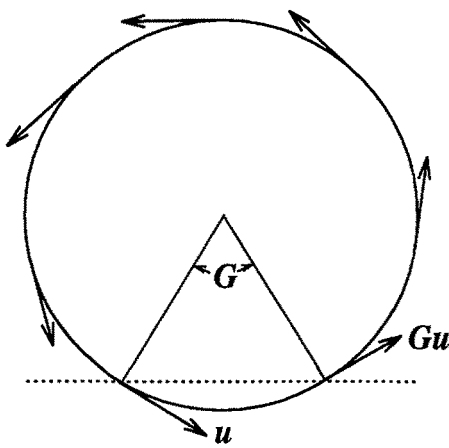


Fig. 9.9: The dependence of the twisting mode at $k = 0$ of a carbon nanotube on its cross section is shown. When we consider the interaction between the two atoms along the dotted line, the rotational motion appears to have a tangential out-of-plane motion in the plane defined by the dotted line and the nanotube axis.

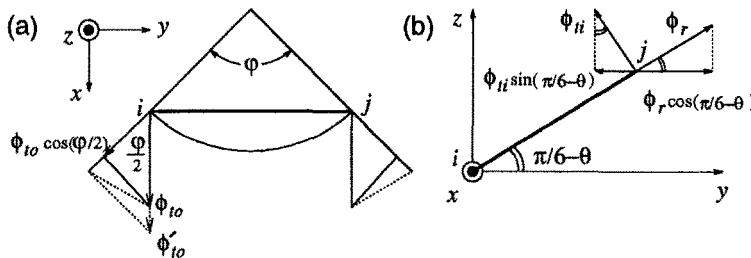


Fig. 9.10: (a) Correction of the force constant ϕ_{to} , which is given by Eq. (9.17) and (b) correction of the force constants of ϕ_r and ϕ_{ti} , which are given by Eqs. (9.18) and (9.19). Figure (a) illustrates the section of a plane perpendicular to the nanotube axis, and (b) illustrates a plane corresponding to an unrolled graphite sheet.

To avoid the difficulty of the curved coordinates, we have proposed the following approximation in which the force constants are scaled depending on their bond lengths. When we consider the tangential out-of-plane mode for the i^{th} site on the cylindrical surface as shown in Fig. 9.10 (a), the motion is in the direction perpendicular to the cylindrical surface. On the other hand, when we denote the bond ij by the thick line, whose subtended angle around the tube

axis is φ as shown in Fig. 9.10(a), the tangential out-of-plane direction for that bond is defined to be perpendicular to that bond. The difference between the two directions is the angle $\varphi/2$ which depends on the bond length. When the bond length is large, the correction for the force constant becomes large, but not so large as the original force constant. Here we scale the force constant ϕ_{to} by

$$\phi'_{to} = \phi_{to} + \phi_{to} \left(1 - \cos\left(\frac{\varphi}{2}\right)\right) \quad (9.17)$$

as an empirical correction for the force constant. A justification for the correction of Eq. (9.17) is as follows. When we calculate the motion using the tangential out-of-plane ϕ_{to} force constant for a given bond, the component of the force constant in the direction perpendicular to the cylindrical surface becomes $\phi_{to} \cos(\varphi/2)$. In order to obtain the same amplitude of the motion in this direction as is obtained in the case of two-dimensional graphite, we add $\phi_{to}(1 - \cos(\varphi/2))$ to ϕ_{to} .* The correction of Eq. (9.17) becomes relatively large with increasing bond length or increasing φ , which relates to the corresponding bond length becoming shorter than that in a two-dimensional graphite plane. Thus this bond length dependent correction is used to describe the vibrations perpendicular to the cylindrical surface.

Similarly, the force constants of ϕ_r , ϕ_{ti} are corrected by the following formulae, respectively,

$$\phi'_r = \phi_r + \phi_r \cos\left(\frac{\pi}{6} - \theta\right) \left(1 - \cos\left(\frac{\varphi}{2}\right)\right), \quad (9.18)$$

and

$$\phi'_{ti} = \phi_{ti} + \phi_{ti} \sin\left(\frac{\pi}{6} - \theta\right) \left(1 - \cos\left(\frac{\varphi}{2}\right)\right), \quad (9.19)$$

where $\pi/6 - \theta$ is the angle of the bond from the horizontal xy plane [see Figs. 9.10 (b) and 9.6 (a)]. Since we consider only the horizontal component of the force by a rotation of $\varphi/2$ around the z axis, we conclude that $\phi_r \cos(\pi/6 - \theta)$ and $\phi_{ti} \sin(\pi/6 - \theta)$ are the components to be corrected.

Using the scaled force constants, we calculate an improved version of the phonon dispersion relations for a (10,10) armchair carbon nanotube. In this case, the frequency of the twisting mode becomes very small ($|\omega| < 10^{-13} \text{ cm}^{-1}$)

*We could also consider other corrections of the force constant, such as $\phi_{to}/\cos(\varphi/2)$. For small φ , this correction gives the same effect as that of Eq. (9.17). However, this correction diverges at $\varphi = \pi$, and thus we do not adopt it.

at $k = 0$. As for the other modes, the corrections are generally small (less than 5 cm^{-1}). The only mode where the correction is significant is the E_{2g} mode which gives a large softening after this correction from 22 cm^{-1} to 17 cm^{-1} . It is interesting to note that the lowest phonon mode with non-zero energy at $k = 0$ is an E_{2g} mode in which the cross section of the carbon nanotube is vibrating with the symmetries corresponding to xy and $x^2 - y^2$. The calculated frequency of the E_{2g} mode for the (10,10) carbon nanotube is 17 cm^{-1} . Since this mode is a Raman-active mode and its frequency is sensitive to the radius of the carbon nanotube, the above arguments show the importance of investigating this mode experimentally. The observation of the Raman-active modes, are discussed in the following chapter.

Another important mode for experimental study is the Raman-active low frequency breathing mode (A_{1g} symmetry) shown in Fig. 9.5(a). The frequency of the breathing mode appears at 165 cm^{-1} for the (10,10) armchair nanotube. This mode frequency quickly decreases to 0 cm^{-1} with increasing radius.

CHAPTER 10.

Raman Spectra of Carbon Nanotubes

The Raman-active and infrared-active phonon modes of carbon nanotubes are described on the basis of group theoretical arguments in Sect. 10.1. A review is given in Sect. 10.2 of Raman scattering experiments on purified single-wall nanotubes and arrays of carbon nanotubes, called *ropes*. To analyze the unique Raman spectra that are observed, results from bond polarization theory are presented in Sect. 10.3. The dependence of the Raman mode frequencies on the nanotube diameter is discussed in Sect. 10.4 and the dependence of the Raman mode intensities on nanotube orientation is discussed in Sect. 10.5.

10.1 Raman or infrared active modes of carbon nanotubes

Among the $6N$ calculated phonon dispersion relations for carbon nanotubes whose unit cell contains $2N$ carbon atoms, only a few modes are Raman or infrared (IR) active, as specified by the symmetry of the phonon modes. Since only k vectors very close to $k = 0$ are coupled to the incident light because of the energy-momentum conservation requirements for the photons and phonons, we need only consider the symmetry of the nanotube zone-center vibrations at the Γ point ($k = 0$). Point group theory of the unit cell, as discussed in Sect. 3.6, predicts the number of Raman-active modes and IR-active modes.

As discussed in Chapter 9, there are four acoustic modes including the rotation around the nanotube axis (R_z) at the Γ point. Thus $6N - 4$ optical phonons are considered in this section. The Raman and infra-red(IR)-active modes correspond to modes whose irreducible representations transform as a quadratic form ($x^2 + y^2$, z^2 , $x^2 - y^2$, xy , yz and zx) for the Raman-active modes, or as a vector form (x , y , and z) for the infrared-active modes. The relationship between an

Table 10.1: Basis Functions for Point Groups D_{nd} and Numbers of Raman and IR Active modes.

Basis functions g	u	D_n	$C_{N/\Omega}$	Achiral ($2j, 2j$)	Chiral others	Chiral (n, m)
$(x^2 + y^2, z^2)^R$	z^{IR}, R_z	A_1 A_2	A_1 A_2	A	4 (0)	3 (1) (4)
$(xz, yz)^R$	$(x, y)^{IR}$ (R_x, R_y)	E_1	E_1	E_1	4(7)	6(5) 5(5)
$(x^2 - y^2, xy)^R$		E_2	E_2	E_2	8	6 6
Total			$6N - 4$	16(7)	16(6)	15(9)

Numbers without and with parentheses denote the numbers of Raman and IR active modes, respectively.

The superscripts R and IR , respectively, denote Raman-active and infrared-active modes.

irreducible representation and its basis function is given in the character tables. In Table 10.1 are listed the basis functions for the irreducible representations of the carbon nanotubes and the number of Raman-active modes for each irreducible representation. Each type of nanotube is classified by its symmetry. When we consider the nanotube axis to be in the z direction, the Raman modes whose vibrational amplitudes transform as z^2 or $x^2 + y^2$ are invariant under any operation of the group, and therefore have A_1 or A symmetry in the D_n or C_N groups, respectively (see Section 3.6). The other Raman-active modes belong to the E_1 and E_2 symmetry types, as shown in Table 10.1. In the case of the IR-active modes, the basis functions x and y are partners of a two-fold degenerate mode with E_1 (E) symmetry, and z transforms according to A_2 (A) symmetry. If we know the irreducible representation of the calculated eigenfunctions of the phonon modes, we can directly assign the symmetries of the Raman-active modes and IR-active modes among the $6N - 4$ phonon modes. An eigenfunction can be identified with an irreducible representation by applying a projection operator for the irreducible representation of the group to the phonon normal modes [197]. If the projected eigenfunction is not zero, the eigenfunction belongs to the corresponding irreducible representation.

The numbers of the Raman-active and IR-active modes for the solid can be predicted by group theory once the lattice structure and its symmetry are specified. The number of optically-active modes is calculated by the decomposition of the reducible representation of the vibration, Γ^{vib} , which is given by the direct

product of the two representations of the group as follows

$$\Gamma^{\text{vib}} = \Gamma_{\text{a.s.}} \otimes \Gamma_{x,y,z} \quad (10.1)$$

where $\Gamma_{\text{a.s.}}$ and $\Gamma_{x,y,z}$ are, respectively, the representations of the atomic sites for the equivalence transformation, and the irreducible representations which belong to the vector components x, y, z . The characters for $\Gamma_{\text{a.s.}}$ are given by the number of atoms in the unit cell that remain invariant under an operation of the group. The representations which correspond to x, y, z , are listed in Table 10.1 for the groups of nanotubes which are discussed in Section 3.6. When we decompose Γ^{vib} into the irreducible representations of the group, using the orthogonality relations between the characters of the irreducible representations, the number of times an irreducible representation is contained in Γ^{vib} is the number of phonon modes which belong to that irreducible representation. Since we know which irreducible representations correspond to the Raman-active and IR-active modes, we can easily find the number of Raman and IR modes. If the translational (E_{1u} : x, y , A_{2u} : z) and rotational (A_{2u} : R_z) motion belong to the symmetry types of the Raman (A_{1g}, E_{1g}, E_{2g}) and IR (A_{2u}, E_{1u}) modes, we subtract the number of those modes from the optically active modes in compiling Table 10.1.* The point group symmetries of armchair $C_h = (n, n)$ and zigzag $C_h = (n, 0)$ nanotubes are either D_{nd} or D_{nh} , respectively, depending on whether $n = \text{odd}$ or $n = \text{even}$, and the symmetry of chiral nanotubes is the non-symmorphic Abelian group C_N , which is discussed in Sect. 3.6. From the character Tables 3.4, 3.5 and 3.8, we get the decomposition of Γ^{vib} as follows [198]:

for armchair nanotubes (even $n = 2j$ with D_{nh} symmetry)[†]

$$\begin{aligned} \Gamma_{2j}^{\text{vib}} = & 4A_{1g} + 2A_{1u} + 4A_{2g} + 2A_{2u} + 2B_{1g} \\ & + 4B_{1u} + 2B_{2g} + 4B_{2u} + 4E_{1g} + 8E_{1u} + 8E_{2g} \\ & + 4E_{2u} + \cdots + 4E_{(j-1)g} + 8E_{(j-1)u} \end{aligned} \quad (10.2)$$

*The symmetries are for achiral nanotubes. For chiral nanotubes, the symbols are as follows: translational ($E + A$), rotational (A), Raman (A, E_1, E_2) and IR (A, E_1) modes.

[†]In Eq. (10.2) we assume that j is even. If j is odd [such as for $(n, m) = (6, 6)$], the 4 and 8 are interchanged in the last two terms in Eq. (10.2).

for zigzag nanotubes (even $n = 2j$ with D_{nh} symmetry):

$$\begin{aligned}\Gamma_{2j}^{\text{vib}} = & \ 3A_{1g} + 3A_{1u} + 3A_{2g} + 3A_{2u} \\ & + 3B_{1g} + 3B_{1u} + 3B_{2g} + 3B_{2u} \\ & + 6E_{1g} + 6E_{1u} + 6E_{2g} + 6E_{2u} \\ & + \cdots + 6E_{(j-1)g} + 6E_{(j-1)u}.\end{aligned}\tag{10.3}$$

For armchair and zigzag nanotubes (odd $n = 2j + 1$ with D_{nd} symmetry):

$$\begin{aligned}\Gamma_{2j+1}^{\text{vib}} = & \ 3A_{1g} + 3A_{1u} + 3A_{2g} + 3A_{2u} \\ & + 6E_{1g} + 6E_{1u} + 6E_{2g} + 6E_{2u} \\ & + \cdots + 6E_{jg} + 6E_{ju}.\end{aligned}\tag{10.4}$$

For chiral nanotubes:

$$\Gamma_N^{\text{vib}} = 6A + 6B + 6E_1 + 6E_2 + \cdots + 6E_{N/2-1}.\tag{10.5}$$

We list in Table 10.1 the numbers of Raman and IR active modes for achiral and chiral nanotubes in which the numbers without and with parentheses, respectively, refer to the numbers of Raman and IR-active modes. Among achiral nanotubes, only armchair nanotubes with even number indexes ($2j, 2j$) have a different numbers of Raman and IR modes from others such as armchair nanotubes with odd number indexes ($2j + 1, 2j + 1$) and zigzag nanotubes ($n, 0$). From Table 10.1 we see that the numbers of Raman and infrared-active modes for a carbon nanotube do not depend much on the nanotube diameter and chirality, though the total number of phonon modes $6N - 4$ is very different for different chiralities. Group theory selection rules indicate that there are 15 or 16 Raman-active modes and 6 to 9 IR-active modes for a single-wall carbon nanotube. The difference between D_{2j} and D_{2j+1} for armchair nanotubes comes from the different numbers of E_1 and E_2 modes in the decomposition of Γ^{vib} in Eqs. (10.2) and (10.4).

Since the basis functions of achiral nanotubes consist of even (g) and odd (u)[†] functions, because of the existence of an inversion center, Raman and IR active

[†]The g and u come from the traditional notation of the German words 'gerade' and 'ungerade', respectively.

modes can be found for several different irreducible representations. However for chiral nanotubes, modes with A and E_1 symmetry are both Raman and IR-active, because of the lack of an inversion center. A phonon mode can be Raman and IR active simultaneously in the lower symmetry chiral nanotubes. However, in these cases the intense Raman modes are generally weak IR modes and vice versa.

Even though group theory may indicate that a particular mode is Raman-active, this mode may nevertheless have a small Raman cross section. In fact, we have only six or seven intense Raman-active modes for any nanotube chirality, as shown in Sect. 10.3. Since similar eigenfunctions give similar Raman intensities for any kind of nanotube, the Raman spectra also have similar shapes, as shown by the calculations in Sect. 10.4.

10.2 Raman experiments on single-wall nanotubes

This section mainly describes Raman experiments on single-wall carbon nanotubes [52, 83, 99, 199]. Most of the Raman studies on single-wall carbon nanotubes were made on nanotubes synthesized by the laser vaporization method [55] with transition metal catalysts, though similar results were obtained on single-wall nanotubes synthesized by the carbon arc method [52]. In both of these synthesis methods, the single-wall carbon nanotubes grow in a triangular lattice to form a bundle or ‘rope’ containing 10–50 nanotubes (see Sect. 5.2) [55, 200]. Under some synthesis conditions, the (10,10) armchair nanotube is the dominant species in the rope. However, in general, the Raman samples have a narrow distribution of diameters and chiralities, which depend sensitively on the catalysts that are used in the synthesis and the growth conditions, especially the growth temperature. For example, when 1.2 weight % of Ni/Co catalyst is used in the sample synthesis at a temperature of 1150°C in 500 torr Ar, the diameter range is 1.0–1.4 nm, while thinner nanotubes with diameters of 0.8–1.0 nm are obtained in the case of a 2.4% Rh/Pd catalyst with growth at 1100°C [99]. Even when the same catalysts are used, a higher growth temperature gives a larger diameter. This situation may be explained by the probability for generating a pentagon. When the temperature is lowered, the probability of closing a carbon pentagonal ring increases, and thus the caps that are generated tend to be smaller. At a higher temperature, however, atomic vibrations prevent the for-

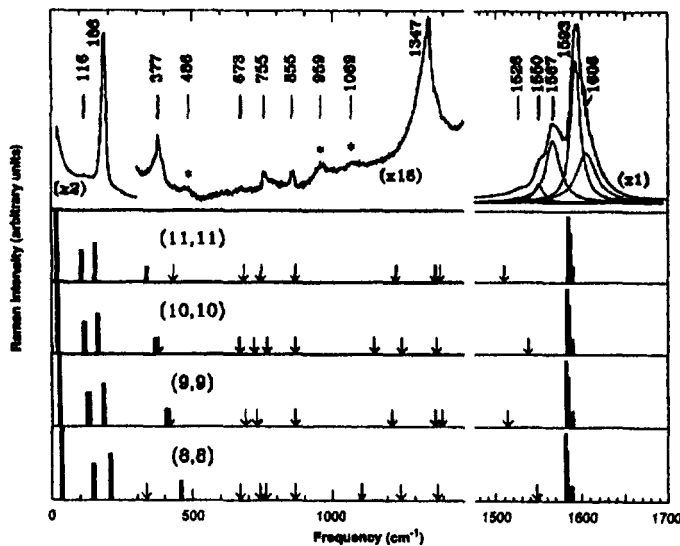


Fig. 10.1: Raman spectra (top) of the rope of single wall carbon nanotubes taken with 514.5 nm excitation at $\sim 2\text{ W/cm}^2$. The features in the spectrum denoted by the symbol “*” are assigned to second-order Raman scattering. The four bottom panels are the calculated Raman spectra for armchair (n,n) nanotubes, $n = 8$ to 11. The arrows in the panels indicate the positions of the remaining weak, Raman-active modes [83].

mation of relatively unstable pentagonal rings, compared with hexagonal rings, so the lower growth temperatures favor the growth of smaller diameter tubes.

Among the 15 or 16 Raman-allowed zone-center modes, the experiments show a few intense lines and several weaker lines, as illustrated in Fig. 10.1 [83]. The top panel of Fig. 10.1 shows Raman spectra for the single-wall nanotube rope using a laser excitation wavelength of 514.5 nm, and the lower panels show the calculated intensities for armchair nanotubes (n,n) , $n = 8$ to 11, respectively. Between 1550 and 1600 cm⁻¹, two strong features are observed at 1567 cm⁻¹ and 1593 cm⁻¹, which correspond to the graphite E_{2g} optic mode at 1582 cm⁻¹ which has been extensively studied in HOPG (highly oriented pyrolytic graphite) [9, 201]. The strong lines between 1550 and 1600 cm⁻¹ may be assigned to the

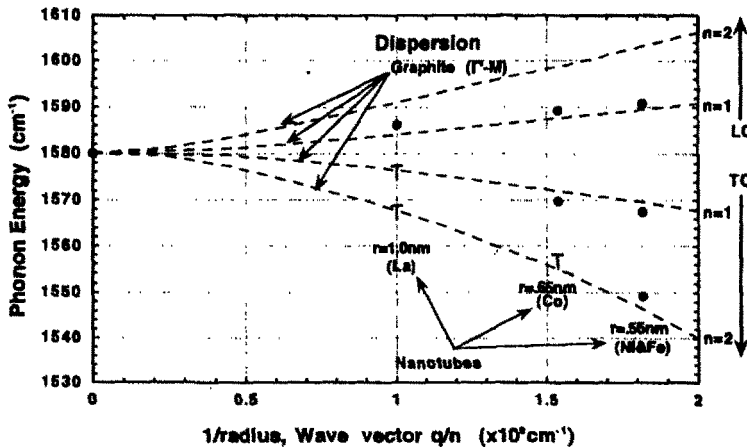


Fig. 10.2: Plot of the observed Raman frequencies for several different single-wall carbon nanotube samples, prepared with different catalysts under different growth conditions yielding different mean nanotube radii r : (a) Fe/Ni ($r = 0.55 \text{ nm}$), (b) Co ($r = 0.65 \text{ nm}$), and (c) La ($r = 1.0 \text{ nm}$). The dashed lines are theoretical LO and TO energy dispersion curves for graphite along Γ -M as a function of q and $q/2$ for $n = 1$ and $n = 2$ (first harmonic vibration), respectively. Solid dots and the symbol 'T' correspond to the observed frequencies of the peaks and shoulders in the Raman spectra, respectively [202].

E_{1g} , E_{2g} and A_{1g} modes in carbon nanotubes with different diameters. Rao et al. [83] assigned the two strong modes of 1567 cm^{-1} and 1593 cm^{-1} to the E_{2g} (8,8), and E_{1g} or A_{1g} (9,9) tubes, respectively. The Raman frequencies in this high frequency region do not vary much with carbon nanotube diameter, as shown in the lower panels of Fig. 10.1.

The Raman frequencies in the range $1550\text{--}1600 \text{ cm}^{-1}$ can be understood by zone-folding of the graphite phonon dispersion relations [202]. In Fig. 10.2, the observed Raman spectral frequencies are shown for three single-wall nanotube samples prepared with different catalysts and under different growth conditions yielding nanotubes with different mean diameters (radii) and different distribu-

tions of diameters (radii). Specifically the catalysts and resulting average radii are: (a) Fe/Ni ($r = 0.55$ nm), (b) Co ($r = 0.65$ nm), and (c) La ($r = 1.0$ nm). The dashed lines are theoretical LO and TO energy dispersion curves in graphite along Γ –M as a function of wavevector q and $q/2$ in units of 10^9 cm $^{-1}$ for $n = 1$ and $n = 2$ (first harmonic vibration), respectively. In armchair nanotubes, the Γ –M direction corresponds to the wave vector along the equator of the nanotubes. Thus LO ($n = 1$), TO ($n = 1$), and TO ($n = 2$) correspond to the A_{1g} , E_{1g} and E_{2g} Raman modes, which will be explained in the theoretical analysis in Sect. 10.4. Figure 10.2 shows a clear relationship between $1/r$ and q on the zone-folded phonon energy dispersion curves.

It is important to note that the Raman intensity for graphite in the 1300–1600 cm $^{-1}$ region is sensitive to sample quality. Generally the intensity of the E_{2g} modes of graphitic materials is sharp and strong when the sample is highly crystalline and defect free, while disordered graphites and carbons show a broad feature around 1350 cm $^{-1}$ [9, 201, 203, 204]. The 1347 cm $^{-1}$ signal seen in Fig. 10.1 may come from a symmetry-lowering effect, due to defects or nanotube caps, bending of the nanotube, and the presence of carbon nanoparticles and amorphous carbon.

At 186 cm $^{-1}$, a strong A_{1g} breathing mode is found in Fig. 10.1(a) [see Fig. 9.5(a) on the right]. Because of the strong dependence of the frequency of the A_{1g} breathing mode on nanotube diameter (see Sect. 10.3), the frequency of the A_{1g} breathing mode can be used as a marker for assigning the approximate diameter of the carbon nanotube. The radial breathing A_{1g} mode can also be clearly seen in fullerenes.* In the low frequency region, the calculations predict nanotube-specific E_{1g} and E_{2g} modes around 116 cm $^{-1}$ and 377 cm $^{-1}$, respectively, for (10,10) nanotubes, but their intensities are expected to be lower than that for the A_{1g} mode. However, these E_{1g} and E_{2g} modes are important since they also show a diameter dependence of their mode frequencies, as shown in the lower panels of Fig. 10.1. In the very low frequency region below 30 cm $^{-1}$, a strong low frequency Raman-active E_{2g} mode is expected. However, it is difficult to observe Raman lines in the very low frequency region, where the background Rayleigh scattering is very strong.

Even for a given sample, the Raman spectra may change if we change the frequency of the excitation laser. When the excitation energy is close to an energy

*For example, the A_{1g} of C₆₀ has a frequency of 497.5 cm $^{-1}$ [198].

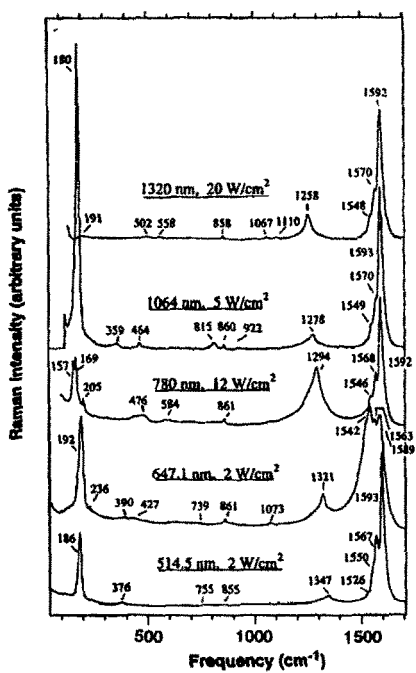


Fig. 10.3: Room temperature Raman spectra for purified single-wall carbon nanotubes excited at five different laser frequencies, showing the resonant enhancement of the Raman intensity associated with the van-Hove singularities in the nanotube density of states [83]. Each trace is labeled by the wavelength and power level of the laser light.

of high “optical” absorption, the Raman intensity is enhanced, and this effect is known as the resonant Raman effect. Under resonant conditions, more light can be absorbed, thereby enhancing the Raman signal through the electron-phonon coupling process. In Fig. 10.3 are shown Raman spectra obtained with different laser excitation frequencies. When the laser frequency increases, the Raman modes that are preferentially enhanced shift to higher frequencies, since the resonance effect is most pronounced when the joint density of states of the carbon π band is large, and the laser frequency matches a peak in the optical absorption. As discussed in the § 4.2, the density of states of the π band becomes singular by folding the two-dimensional energy bands of the graphene layer into the one-dimensional bands of the carbon nanotube, and these singularities are known as van-Hove singularities. For every one-dimensional band edge, as in a carbon nanotube, a $1/\sqrt{E}$ singularity is expected for the energy dependence of the one-dimensional density of states (see Fig. 4.7). The $1/\sqrt{E}$ singularities for the 1D density of states results in a much stronger resonant Raman effect than would be

observed for a 2D graphene sheet or for 3D crystalline graphite. Clearly the energy separation of these singularities in the 1D density of states increases as the number of energy bands decreases. When we consider only armchair nanotubes (n, n) , the energy separation between the van-Hove singularities becomes large with decreasing n . The Raman resonance condition thus selects the particular carbon nanotube (n, m) which has a singularity in its electronic density of states at the laser frequency. The observed phonon frequency of the low frequency A_{1g} mode provides the value of the nanotube diameter that is in resonance electronically, since the phonon frequencies for the low frequency normal modes increases with decreasing n . Thus the resonance effect is a quantum effect that can be understood in terms of both the electronic and phonon dispersion relations of the nanotubes. Since nominal single-wall carbon nanotube samples consist of nanotubes with different diameters and chiralities, the resonant Raman effect may be seen in different nanotubes for different laser excitation frequencies.

10.3 Bond Polarizability Theory of Raman Intensity for Carbon Nanotubes

In this section we discuss the non-resonant bond polarization theory for calculating the Raman intensity, which is also useful for the interpretation of the Raman spectra. The Raman intensity for \mathcal{N} atoms in the unit cell is calculated by the empirical bond polarizability model [205, 206];

$$I_{\eta' \eta}(\omega) \propto \omega_L \omega_S^3 \sum_{f=1}^{3\mathcal{N}} \frac{\langle n(\omega_f) \rangle + 1}{\omega_f} \left| \sum_{\alpha\beta} \eta'_\alpha \eta_\beta P_{\alpha\beta,f} \right|^2 \delta(\omega - \omega_f). \quad (10.6)$$

Here ω_L and ω_S are the incident and scattered light frequencies, η and η' are the corresponding unit vectors for the polarization of the light, respectively. ω_f is the frequency of the f -th normal phonon mode, while $\langle n(\omega_f) \rangle = 1/(\exp(\hbar\omega_f/k_B T) - 1)$ is the phonon occupation number at temperature T . The α and β subscripts in Eq. (10.6) denote Cartesian components of the vector or tensor, x, y, z , and $P_{\alpha\beta,f}$ is the derivative of the electronic polarization tensor for the f -th normal mode, which is given by [205],

$$P_{\alpha\beta,f} = \sum_{\ell\gamma} \left[\frac{\partial P_{\alpha\beta}}{\partial u_\gamma(\ell)} \right]_0 \chi_\gamma(\ell|f), \quad (\gamma = x, y, z, \ell = 1, \dots, \mathcal{N}, f = 1, \dots, 3\mathcal{N}) \quad (10.7)$$

where $P_{\alpha\beta}$ is the electronic polarization, and the derivative is performed with respect to the γ th Cartesian displacement, $u_\gamma(\ell)$, for the ℓ th atom. The term $\chi_\gamma(\ell|f)$ is the γ component of the unit vectors of the f th normal modes of the ℓ th atom. Both translational and rotational acoustic modes are included in f for simplicity. However, the acoustic modes do not contribute to the Raman intensity.

The term $P_{\alpha\beta}$ in Eq. (10.7) is approximated by a sum over the bond polarization contributions as follows

$$P_{\alpha\beta} = \frac{1}{2} \left[\sum_{\ell,B} \left\{ \frac{\alpha_{\parallel}(B) + 2\alpha_{\perp}(B)}{3} \right\} \delta_{\alpha\beta} + \{\alpha_{\parallel}(B) - \alpha_{\perp}(B)\} \left(\frac{R_\alpha(\ell, B) R_\beta(\ell, B)}{R(\ell, B)^2} - \frac{1}{3} \delta_{\alpha\beta} \right) \right], \quad (10.8)$$

where B denotes a bond which is connected to the ℓ -th atom in the unit cell, and $\mathbf{R}(\ell, B)$ is the corresponding vector from the ℓ -th atom to the neighbor atom ℓ' specified by B . The quantities $R_\alpha(\ell, B)$ and $R(\ell, B)$ are the α component and the length of $\mathbf{R}(\ell, B)$, respectively, and $\alpha_{\parallel}(B)$ and $\alpha_{\perp}(B)$ are the static molecular polarizabilities for the bond B in the directions parallel and perpendicular to the bond, respectively. Here we assumed that $\alpha_{\parallel}(B)$ and $\alpha_{\perp}(B)$ are functions of only the length $R(\ell, B)$.

When we denote the bond vector without the displacements of the two atoms of the bond as $\mathbf{R}_0(\ell, B)$, then $\mathbf{R}(\ell, B)$ can be defined by

$$\mathbf{R}(\ell, B) = \mathbf{R}_0(\ell, B) + \mathbf{u}(\ell') - \mathbf{u}(\ell), \quad (10.9)$$

while the derivative on u_γ in Eq. (10.7) is expressed by the derivative on $R(\ell, B)$ as follows:

$$\frac{\partial}{\partial u_\gamma(\ell)} = \sum_B \frac{\partial}{\partial R(\ell, B)} \frac{\partial R(\ell, B)}{\partial u_\gamma(\ell)} = - \sum_B \frac{\partial}{\partial R(\ell, B)} \frac{R_\gamma(\ell, B)}{R(\ell, B)}. \quad (10.10)$$

Here the summation is taken over the bonds connected to the ℓ -th atom and we use the following relations:

$$\frac{\partial R_\alpha(\ell, B)}{\partial u_\gamma(\ell)} = -\delta_{\alpha\gamma}, \quad (10.11)$$

and

$$\frac{\partial R(\ell, B)}{\partial u_\gamma(\ell)} = \sum_\alpha \frac{\partial R(\ell, B)}{\partial R_\alpha(\ell, B)} \frac{\partial R_\alpha(\ell, B)}{\partial u_\gamma(\ell)} = -\frac{\partial R(\ell, B)}{\partial R_\gamma(\ell, B)} = -\frac{R_\gamma(\ell, B)}{R(\ell, B)}. \quad (10.12)$$

When we calculate $P_{\alpha\beta,f}$ in Eq. (10.7), we have terms $\frac{\partial\alpha}{\partial u_\gamma}$, $\frac{\partial R_\alpha(\ell, B)}{\partial u_\gamma}$, and $\frac{\partial R(\ell, B)}{\partial u_\gamma}$ in $\frac{\partial P_{\alpha\beta}}{\partial u_\gamma(\ell)}$. After some calculation and making use of Eqs. (10.10), (10.11) and (10.12), we obtain an explicit form for $P_{\alpha\beta,f}$,

$$\begin{aligned} P_{\alpha\beta,f} = & - \sum_{\iota\beta} \left[\frac{\mathbf{R}_0(\ell, B) \cdot \vec{\chi}(\ell|f)}{R_0(\ell, B)} \times \left\{ \left(\frac{\alpha'_{||}(B) + 2\alpha'_\perp(B)}{3} \right) \delta_{\alpha\beta} \right. \right. \\ & + \left(\alpha'_{||}(B) - \alpha'_\perp(B) \right) \left(\frac{R_{0\alpha}(\ell, B)R_{0\beta}(\ell, B)}{R_0(\ell, B)^2} - \frac{1}{3}\delta_{\alpha\beta} \right) \Big\} \\ & + \left(\frac{\alpha_{||}(B) - \alpha_\perp(B)}{R_0(\ell, B)} \right) \left\{ \frac{R_{0\alpha}(\ell, B)\chi_\beta(\ell|f) - R_{0\beta}(\ell, B)\chi_\alpha(\ell|f)}{R_0(\ell, B)} \right. \\ & \left. \left. - \frac{\mathbf{R}_0(\ell, B) \cdot \vec{\chi}(\ell|f)}{R_0(\ell, B)} \times \frac{2R_{0\alpha}(\ell, B)R_{0\beta}(\ell, B)}{R_0(\ell, B)^2} \right\} \right], \end{aligned} \quad (10.13)$$

where $\alpha'_{||}(B)$ and $\alpha'_\perp(B)$ are the radial derivatives of $\alpha_{||}(B)$ and $\alpha_\perp(B)$, that is

$$\alpha'_{||}(B) \equiv \frac{\partial\alpha_{||}(B)}{\partial R(\ell, B)}, \quad \text{and} \quad \alpha'_\perp(B) \equiv \frac{\partial\alpha_\perp(B)}{\partial R(\ell, B)}, \quad (10.14)$$

respectively. The values of $\alpha_{||}(B)$, $\alpha_\perp(B)$, $\alpha'_{||}(B)$ and $\alpha'_\perp(B)$ are given empirically as a function of the bond length between two carbon atoms or between carbon-hydrogen atoms, and these values are listed for carbon nanotubes in Table 10.2. In order to obtain values for the parameters for carbon nanotubes, we start by interpolating between the values for the polarizability parameters for single (1.46 Å) and double (1.40 Å) carbon bonds in C₆₀ and related materials [205, 207]. Then we fit the values so as to reproduce the Raman signal for randomly oriented nanotubes. Although the calculated values are within a reasonable range for carbon materials, the values for the polarizability parameters listed in Table 10.2 do not converge well for carbon materials, because of the different results that have been reported by various groups.

Table 10.2: Bond lengths and Raman polarizability parameters for single-wall carbon nanotubes and for various carbon-related molecules.

Molecule	Bond Lengths [Å]	$\alpha_{\parallel} + 2\alpha_{\perp}$ [Å ³]	$\alpha_{\parallel} - \alpha_{\perp}$ [Å ³]	$\alpha'_{\parallel} + 2\alpha'_{\perp}$ [Å ²]	$\alpha'_{\parallel} - \alpha'_{\perp}$ [Å ²]
CH ₄ ^{a)}	C – H (1.09)	1.944			
C ₂ H ₆ ^{a)}	C – C (1.50)	2.016	1.28	3.13	2.31
C ₂ H ₄ ^{a)}	C = C (1.32)	4.890	1.65	6.50	2.60
C ₆₀ ^{b)}	C – C (1.46)		1.28	2.30 ± 0.01	2.30 ± 0.30
	C = C (1.40)		0.32 ± 0.09	7.55 ± 0.40	2.60 ± 0.36
C ₆₀ ^{a)}	C – C (1.46)		1.28 ± 0.20	1.28 ± 0.30	1.35 ± 0.20
	C = C (1.40)		0.00 ± 0.20	5.40 ± 0.70	4.50 ± 0.50
SWCN ^{c)}	C = C (1.42)		0.07	5.96	5.47
SWCN ^{d)}	C = C (1.42)		0.04	4.7	4.0

^{a)} S. Guha et al. [205].

^{b)} D. W. Snoke and M. Cardona [207].

^{c)} E. Richter et al. (unpublished data which is used in their work[83]).

^{d)} R. Saito et al. [208].

It is known, however, that the polarizability parameters of carbon are similar for a variety of carbon materials. Furthermore, the relative intensities for the Raman modes are not so sensitive to small changes in the values of the bond polarization parameters except for the lowest E_{2g} mode. The lowest E_{2g} mode is found to be most sensitive to the parameter $\alpha_{\parallel} - \alpha_{\perp}$. Thus the fitted values are used for calculating approximate Raman intensities. The Raman intensity is calculated using the eigenvectors for the vibrational modes, obtained by solving the dynamical matrix, and the polarization parameters are obtained using bond polarization theory [205].

10.4 Raman Spectra of Nanotubes with Random Orientations

The Raman intensities for the various Raman-active modes in carbon nanotubes are calculated at a phonon temperature of 300 K which appears in the formula of Eq. (10.6) for the Bose distribution function for phonons. The eigenfunctions for the various vibrational modes are calculated numerically at the Γ point ($k = 0$). Here we consider two possible geometries for the polarization of the light: the VV

and VH configurations. In the VV configuration, the incident and the scattered polarizations are parallel to each other, while they are perpendicular to each other in the VH direction. Generally the cross section for Raman scattering is a function of the scattered angle of the light. However, the formulae for the bond polarization theory consider only S -scattered waves [205], and thus the calculated results cannot distinguish between forward and backward scattering of the light.

In Fig. 10.4, we show the calculated Raman intensities for the $(10,10)$ armchair, $(17,0)$ zigzag and $(11,8)$ chiral nanotubes, whose radii are, respectively, 6.78\AA , 6.66\AA , and 6.47\AA and are close to one another. The Raman intensity is averaged over the sample orientation of the nanotube axis relative to the Poynting vector of the light, in which the average is calculated by summing over many (~ 50) directions, weighted by the solid angle for that direction. Thus Fig. 10.4 is the calculated result for randomly-oriented nanotubes. We divide the discussion into the following three frequency regions: the lower ($\omega \leq 500 \text{ cm}^{-1}$), higher ($\omega \geq 1500 \text{ cm}^{-1}$), and middle ($500 \text{ cm}^{-1} \leq \omega \leq 1500 \text{ cm}^{-1}$) frequency ranges. Then we discuss the phonon density of states for the Raman-active modes which depend strongly on the chirality.

Since we consider randomly-oriented nanotubes in this section, we do not need to mention the direction of the polarization vector for the VV and VH configurations. On the other hand, we need the directions of V and H for calculating the Raman intensity of a nanotube. We present the sample orientation dependence of the Raman spectra of a $(10,10)$ nanotube in the next section, in which we rotate the nanotube axis by fixing the polarization vectors.

10.4.1 Lower Frequency Raman Spectra

Here we discuss the Raman intensity for the lower frequency modes below 500 cm^{-1} . The Raman intensity is normalized for each nanotube to a maximum intensity (A_{1g} in the VV configuration) of unity. When we compare the VV with the VH polarizations (see Fig. 10.4), the Raman intensity shows anisotropy. Most importantly, the A_{1g} mode at 165 cm^{-1} is suppressed in the VH configuration, while the lower frequency E_{1g} and E_{2g} modes are not suppressed as much. This anisotropy is due to the low dimensionality of carbon nanotubes. The degenerate vibrations of the E modes, whose eigenfunctions

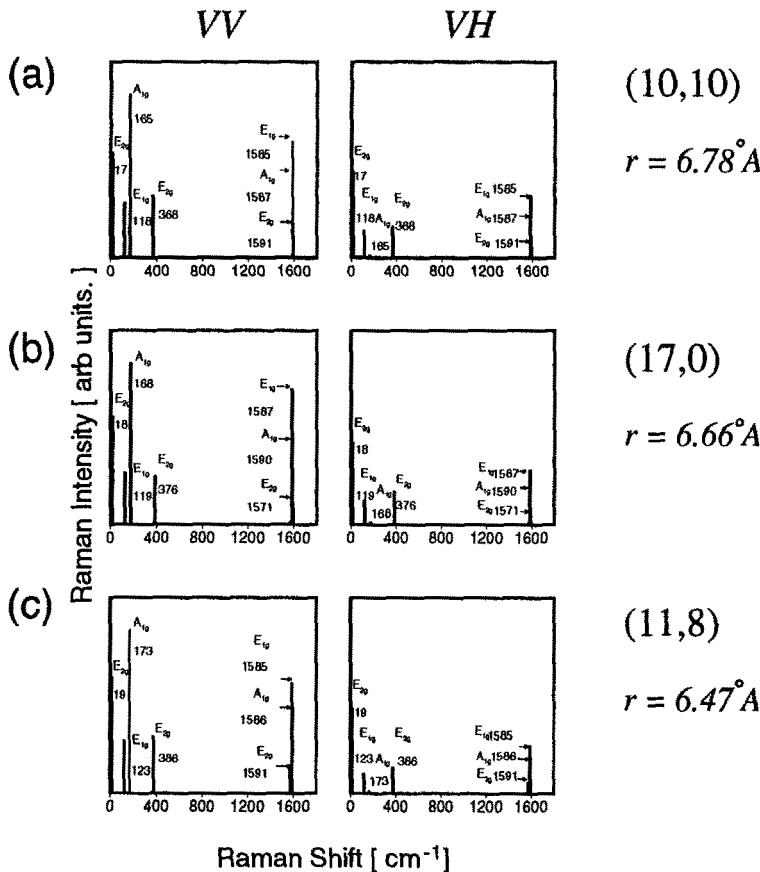


Fig. 10.4: The polarization dependence of the Raman scattering intensity for (a) (10,10) armchair, (b) (17,0) zigzag, and (c) (11,8) chiral nanotubes and the tube radius are given on the right. The left column is for the VV scattering configuration and the right column is for the VH configuration.

are orthogonal to each other, are relevant to VH signals. From the figure we see that the relative intensities for the same mode between the VV and VH polarizations are different but are on the same order for all the E modes.

When we compare the lower frequencies of these Raman modes for nan-

otubes, the frequency shifts systematically with increasing diameter. In Fig. 10.5 we give the calculated mode frequencies for the lower frequency Raman-active modes on a log-log plot as a function of the carbon nanotube radius r for (n, m) in the range ($8 \leq n \leq 10$, $0 \leq m \leq n$). Figure 10.5 clearly shows straight line dependences for all four Raman modes, thus indicating a power dependence of $\omega(r)$ on r . No chirality dependence is found for the mode frequencies for these modes, which is consistent with the fact that the energy gap of a semiconducting nanotube and the strain energy depend only on the nanotube radius and not on the chiral angle θ [81, 209]. From the slopes of $\omega(r)$ for this range of r , we conclude that, except for the lowest E_{2g} mode, the frequencies are inversely proportional to r making only a small deviation from the predictions of Fig. 10.5. This dependence is closely related to the circumferential length of the nanotube. As for the lowest E_{2g} mode, the frequency $\omega_{2g}(r)$ has a dependence of $r^{-1.95 \pm 0.03}$, which is approximately quadratic and may reflect the effect of curvature on the nanotube. The fitted power law for the A_{1g} mode that is valid in the region $3\text{\AA} \leq r \leq 7\text{\AA}$

$$\omega(r) = \omega_{(10,10)} \left(\frac{r_{(10,10)}}{r} \right)^{1.0017 \pm 0.0007}, \quad (10.15)$$

should be useful to experimentalists in interpreting their spectra. Here $\omega_{(10,10)}$ and $r_{(10,10)}$ are, respectively, the frequency and radius of the $(10,10)$ armchair nanotube, with values of $\omega_{(10,10)}=165 \text{ cm}^{-1}$ and $r_{(10,10)}=6.785\text{\AA}$, respectively.

It is noted that the E_{1g} and A_{1g} modes exist in a similar frequency region. However, since the intensity of the E_{1g} modes is not as strong as that for the A_{1g} mode, the experimental Raman spectra between 100 to 300 cm^{-1} are dominated by the A_{1g} mode as shown in Figs. 10.1 and 10.3. As for the higher frequency Raman modes, we do not see a strong dependence on r , since the frequencies of the higher frequency optical modes are more sensitively determined by the local movements of the atoms.

10.4.2 Higher Frequency Raman Modes

It is interesting that the higher frequency A_{1g} mode at 1587 cm^{-1} does not show a suppression between the VV and VH geometries, which is relevant to the Raman active E_{2g} mode of graphite. In the next section we will see that the A_{1g} modes depend on the orientation of the nanotube axis. This fact shows that

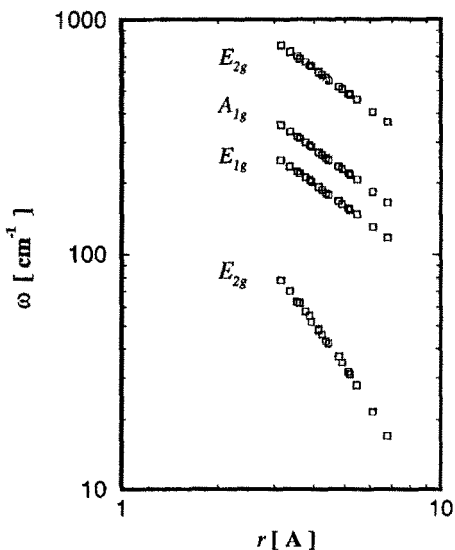


Fig. 10.5: Log-log plot of the lower Raman mode frequencies as a function of carbon nanotube radius.

a VH signal can be expected when the vibration of the A_{1g} mode is different from the polarization vector.

In the nanotube, the lattice can be split into two sublattices consisting A and B atoms. In the higher frequency A_{1g} mode, the A and B atom moves in opposite directions (out-of-phase) in the unit cell, while in the lower frequency A_{1g} mode the A and B atoms move in the same way (in-phase). In Fig. 10.6 we show the normal mode displacements for seven Raman modes for a (10,10) nanotube which have a relatively large intensity. It is clear from Fig. 10.6 (e) to (g), that the modes are out-of-phase between nearest neighbor carbon atoms, while the modes of Fig. 10.6 (a) to (d) show in-phase motion. The out-of-phase motions observed in Fig. 10.6 (e) to (g) are similar to the motion of the Raman-active E_{2g} mode of graphite at 1582 cm^{-1} , which corresponds to C=C bond stretching motions for one of the three nearest neighbor bonds in the unit cell. Thus this motion is an out-of-phase motion. It is reasonable that the out-of-phase motions of the higher frequency Raman modes of a nanotube have a large Raman intensity, because of the relation of these modes to the E_{2g} mode of graphite.

The motions shown in Fig. 10.6 are independent of the chirality. When we see the motion of the higher or the lower Raman-active modes of a nan-

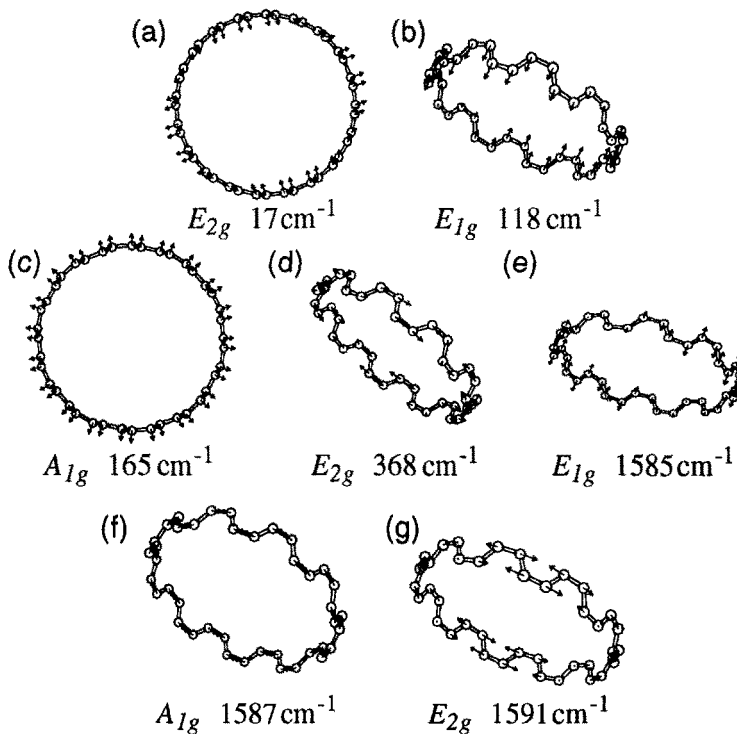


Fig. 10.6: The calculated Raman mode atomic displacements, frequencies, and symmetries for those (10,10) nanotube modes which show strong Raman intensity. The symmetry and the frequencies for these modes are almost independent of the chirality of the nanotube. We show the displacements for only one of the two modes in the doubly degenerate E_{1g} and E_{2g} modes.

otube, we can consider an envelope function for the amplitude of the vibration, multiplying it by the above-mentioned out-of-phase or in-phase motions, respectively. We can say that the envelope function should satisfy the symmetry for the Raman-active modes among the many phonon modes. For example, the envelope functions for the A_{1g} , E_{1g} and E_{2g} modes are functions with zero, two, and four nodes around the tube z -axis, respectively [see Fig. 10.6 (f), (e), and

(g) for out-of-phase motion, and (c), (b), and (a) for in-phase motion]. Thus the envelope functions with a given symmetry are similar to one another for nanotubes with any (n, m) values. This is the reason why we get similar Raman spectra for different chirality nanotubes. We can say within the discussion of the envelope function that we see a homogeneous elastic cylinder.

When we investigate the vibration of the higher frequency A_{1g} mode at 1587 cm^{-1} , the vibration corresponds to the folded vibration of one of the higher E_{2g} modes of graphite. Thus, in the cylindrical geometry, we may get a result that is not so polarization sensitive. On the other hand, in C_{60} , since all 60 atoms are equivalent, no carbon atom can move in an out-of-phase direction around the C_5 axes for either of the two A_{1g} modes, so that both modes show similar polarization behavior to each other [198]. However, the directions of the out-of-phase motions of the A_{1g} modes are different for armchair and zigzag nanotubes. In fact the C=C bond-stretching motions can be seen in the horizontally and the vertically vibrating C=C bonds for armchair and zigzag nanotube, respectively. Thus the curvature of the nanotube affects the frequency of these mode. When we focus our attention on armchair nanotubes, the higher Raman frequencies depend on the radius of the nanotube $1/r$ via the wave vector q around the equatorial direction [202], which is understood by the zone-folding method and is discussed in Sect. 10.2.

Although these higher frequency modes are difficult to distinguished from one another because of their similar frequencies, it will be possible to identify the different modes experimentally, once purified aligned samples become available, as shown in discussing the angular dependence of the Raman intensities, which is reviewed in Sect. 10.5.

10.4.3 Medium Frequency Raman Modes

It could be very interesting to discuss the Raman frequency in the intermediate frequency region where the frequency may be the most chirality dependent [210]. The calculated results, however, show almost no intensity for the intermediate Raman modes around $1200\text{-}1500\text{ cm}^{-1}$. The Raman experiments on single-wall nanotubes show weak features which have been assigned to armchair modes [83]. From the calculation we cannot explain why these low intensity peaks appears. The peaks might come from a lowering of the symmetry of the nanotube. In

fact, broad Raman peaks around the 1347 cm^{-1} are observed experimentally [83, 135]. These peaks are known to be associated with symmetry-lowering effects in disordered graphite [211] and carbon fibers [212] for which a broad peak is observed around 1350 cm^{-1} . The relative intensity of the broad peak around 1350 cm^{-1} to the strong E_{2g} mode at 1582 cm^{-1} is sensitive to the lowering of the crystal symmetry of graphite [211, 213], the amount of disorder in carbon fibers [212] and in graphite nano-clusters [214]. The amount of disorder in these systems can be controlled by the heat treatment temperature T_{HT} or by ion implantation [215]. The non-zone-center phonon mode at 1365 cm^{-1} has a flat energy dispersion around the M point in the Brillouin zone of graphite, which implies a high phonon density of states * [216]. Moreover, in small aromatic molecules, the frequency and the normal mode displacements are modified by the finite size effect, so that these M point phonon modes becomes Raman active [217] and have a large intensity [214, 218]. Thus some symmetry-lowering effects such as the effect of the end caps, bending of the nanotube and the other possible defects are likely to turn on the Raman intensity for this M -point mode. Note that if the nanotube is deformed to a 2×2 structure for any reason, the M point phonon can be folded to the Γ point and the folded modes becomes Raman-active A_g modes. However, since a Peierls instability is unlikely, as is discussed in Sect. 11.3, this situation may occur only in the case of intercalated nanotubes [135].

When we calculate the Raman intensity for a nanotube with open ends, the intermediate frequency Raman modes have a small intensity relative to the strong peaks in the higher and the lower frequency regions. The observed Raman signal in Fig. 10.1 in the intermediate frequency region can be relevant to the finite length of a nanotube.

As shown in Fig. 10.4, the chirality dependence of the Raman spectra is not clearly observed except for the frequency. However when we consider the absolute Raman intensity, it is important to consider also the effect of the phonon density of states. The three nanotubes in Fig. 10.4 have almost the same diameters. However the number of carbon atoms per 1D unit cell is very different. For example, the (10,10) and (17,0) nanotubes have 40 and 68 carbon atoms in their 1D unit cells, respectively. However, the (11,8) nanotube has 364 carbon atoms in its unit cell. Because of the large number of states for the (11,8) nanotube, it

*See Fig. 9.4 for 2D graphite. In this case we can see a flat band appearing below 1300 cm^{-1}

should be difficult to observe the singularities in the electronic density of states in a (11,8) nanotube within the resolution of the STM because the singularities occur so close to one another. Thus the resonant Raman effect for chiral nanotubes should also be relatively difficult to observe compared with the case of achiral nanotubes. It would be interesting to be able to assign the chirality of a nanotube from the Raman spectra by using many laser excitation frequencies.

10.5 Sample Orientation Dependence

In Sect. 10.4.2, we see that the high frequency Raman modes originate from the out-of-phase E_{2g} mode of graphite. As a result, the frequencies of the Raman modes in the high frequency region are close to one another. However since the symmetry of these modes are different, these mode can be separated from one another by exploiting special experimental geometry conditions.

In Fig. 10.7, we show the intensities of the various Raman-active modes for the (10,10) armchair nanotube as a function of sample orientation. Here we fix the polarization vectors to lie along the z and x axes, respectively for the V and H polarizations. Then we consider the effect of rotating the nanotube axis from the z axis. In this geometry, three rotations of the nanotube axis are possible for the VV and the VH configurations, and these three rotations are denoted by θ_i , ($i = 1, 2, 3$) as shown in Fig. 10.7. Here θ_1 , and θ_2 are the angles of the nanotube axis from the z axis to the x and y axes, respectively, while θ_3 is the angle of the nanotube axis around the z axis from the x to the y axis. Since we put the horizontal polarization vector along the x axis, θ_1 and θ_2 are different from each other for the VH configuration. Even for the VV configuration, the rotations by θ_1 and θ_2 are not equivalent to each other in the case of the (10,10) armchair nanotube, since the (10,10) armchair nanotube has a ten-fold symmetry axis (C_{10}) which is not compatible with the Cartesian axes. Here we define the x, y, z axes so that we put a carbon atom along the x axis when $\theta_3 = 0^\circ$. In Fig. 10.7, we show the relative Raman intensities for the (10,10) armchair nanotube for the VV and VH configurations for the various Raman modes of a (10,10) carbon nanotube as a function of θ_i , ($i = 1, 2, 3$).

In Fig. 10.7 we see that the Raman intensity for the A_{1g} mode at 1587 cm^{-1} as a function of θ_1 has a maximum at $\theta_1 = 0$, which corresponds to $\theta_2 = \theta_3 = 0$, for the VV configuration, while the E_{1g} mode at 1585 cm^{-1} has a maximum

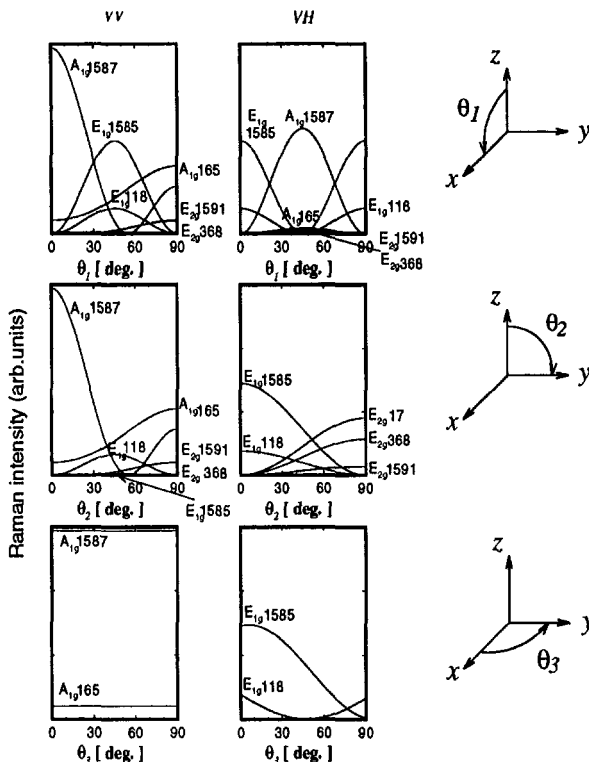


Fig. 10.7: The polarization dependence of the Raman intensities as a function of the orientation of the nanotube axis for a (10,10) armchair nanotube. θ_1 , and θ_2 are angles of the nanotube axis from the z axis toward the x and y axes, respectively. θ_3 is the corresponding angle around the z axis from the x to the y axes. The left and right hand figures correspond to the VV and VH polarizations, where V and H correspond to the light polarization in the direction of the z and x axes, respectively.

at $\theta_1 = 45^\circ$. When θ_1 increases to 45° , the relationship between the intensities of the A_{1g} mode at 1587 cm^{-1} and of the E_{2g} mode at 1591 cm^{-1} becomes reversed for the VV configuration relative to the VH configuration. Thus, we can distinguish these two close-lying modes from each other experimentally if we have an axially aligned sample. There is also an E_{2g} mode at 1591 cm^{-1}

which can be distinguished from the A_{1g} and E_{1g} modes, since the E_{2g} mode has a maximum intensity at $\theta_1 = 90^\circ$. As for the other Raman-active modes, we can also distinguish them by their frequencies. In Fig. 10.7, the two E_{2g} modes at 368 and 1591 cm^{-1} have almost the same intensity in the VV configuration. Thus we can see only a single line in the VV configuration of the figure. However in the θ_2 dependence of the VH configuration, we can see the difference between these E_{2g} modes.

Even the modes belonging to the same irreducible representation do not always have the same angular dependence with regard to the polarization of the light. For example, the intensity of the A_{1g} mode at 165 cm^{-1} has a different angular dependence from that of the A_{1g} mode at 1587 cm^{-1} , as shown in Fig. 10.7. Further, it is clear from the figure that the angular dependence with respect to θ_1 and θ_2 is different for the VH geometry since the horizontal polarization is taken in the x direction.

The symmetry analysis may be difficult even if we can get an aligned nanotube sample for which the direction of the carbon atoms is ordered, since the 10-fold symmetry of the (10,10) nanotube does not satisfy the symmetry of the triangular nanotube lattice. Thus an averaged angular dependence for θ_1 and θ_2 in the VV geometry is expected for a general aligned sample. Even in this case, since the A_{1g} mode at 1587 cm^{-1} is independent of θ_3 , the signal for this mode will be clearly seen. The (9,9) armchair nanotube is of special interest, since it is one of a few examples where the n -fold symmetry of the nanotube matches the triangular lattice; therefore, for (9,9) nanotubes in a triangular lattice, detailed angle-dependent selection rules can be expected.

In summary, the Raman intensity of armchair, zigzag, and chiral nanotubes is discussed in Sects. 10.4 and 10.5 as a function of their polarization geometry and sample orientation. No significant dependence on chiral angle is found for the Raman spectra. The Raman intensity is explained by the envelope function of the amplitude of the vibration, and this envelope function is sensitive only to the homogeneous elastic cylinder. However, we expect to see a large chiral dependence of the phonon density of states which is reflected in the absolute intensity. The sample orientation dependence of the Raman intensity shows that not only the symmetry but also the direction of the displacements give rise to their own angular dependence, and this angular dependence can be used for distinguishing between the symmetry assignments for the higher frequency Raman

modes. Such a symmetry analysis will also be useful for identifying the chirality of carbon nanotubes.

CHAPTER 11.

Elastic Properties of Carbon Nanotubes

Since the C=C bond in graphite is the strongest bond in nature, a carbon nanotube is widely regarded as the ultimate fiber with regard to its strength in the direction of the nanotube axis. Furthermore, single wall nanotubes are rather flexible in the direction normal to the nanotube surface. The static elastic properties of carbon nanotubes are discussed in Sect. 11.2. The unusual aspects of the Peierls instability, associated with the distortion which makes an energy gap at the Fermi energy, in carbon nanotubes are discussed in Sect. 11.3. Multi-wall carbon nanotubes have unique properties that do not appear in single wall nanotubes, and these are summarized in Sect. 11.4.

11.1 Overview of Elastic Properties of Carbon Nanotubes

In graphite and in carbon nanotubes, three kinds of forces between carbon atoms produce their characteristic elastic properties. The fundamental atomic forces consist of strong σ -bonding and π -bonding forces between intralayer C=C bonds and weak interlayer interactions. Although the three forces differ from one-another regarding their orders of magnitude, all three forces are essential for describing the elastic properties of carbon nanotubes, as shown in the following three sections, respectively. In each section we give an overview of the relationship between the properties and the force.

By rolling a graphene sheet to form a single wall carbon nanotube (SWCN), the total energy of the nanotube is increased by the strain energy associated with the curvature of the nanotube. The strain energy thus increases with decreasing nanotube diameter, so that a nanotube with a small diameter may be less stable than a nanotube with a larger diameter. In graphitic materials, sp^2 covalent

bonds mainly form the σ skeleton of the honeycomb lattice. Thus the strength in the direction of the nanotube axis may be considered as an elastic thin film for which classic elastic theories can be applied [219], as shown in Sect. 11.2. On the other hand, we expect a rather soft surface in SWCNs for a force applied perpendicular to the surface of a carbon nanotube, and this feature of SWCNs can also be explained by considering a tangential force on the σ -bond skeleton. Single wall carbon nanotubes have no interlayer interactions, since a hollow vacuum core exists inside each nanotube. In fact, a perpendicular deformation is not always stable and the cross section of carbon nanotubes is easily flattening by applying a force normal to the nanotube axis [220] and a large bending of single wall nanotubes is observed without breaking the σ skeleton [221]. Using elastic continuum theory to describe the elastic properties of nanotubes, we discuss in Sect. 11.2 the rigidity of carbon nanotubes and the weak chirality effects expected for their elastic properties.

Single-wall carbon nanotubes are believed to possess many of the desirable mechanical properties of carbon fibers, but, in addition, single-wall carbon nanotubes have a number of other desirable nanotube properties with regard to their flexibility, their ability to withstand cross-sectional and twisting distortions, their extensibility, and their ability to withstand compression without fracture. Just as for the carbon fibers that are produced commercially for aerospace applications, carbon nanotubes show excellent strength characteristics under extension, and molecular dynamics simulations [222] indicate that an increase in length (elongation) of several percent without fracture might be possible [95, 219]. In addition to these amazing predictions for their tensile properties, single-wall nanotubes show remarkable flexibility, and can be bent around small circles or about sharp bends without breaking [110]. Whereas carbon fibers fracture easily under compression, carbon nanotubes form kink-like ridges under compression, and these ridges can relax elastically when the stress is released. Computer simulations [222] further indicate that when the compressional or shear stress is released, the original circular cross-section of the nanotube can, in many cases, be restored [219]. It should be possible to utilize these excellent mechanical properties for applications directly, or in conjunction with their use for manipulating other nanostructures [53].

Although the π electron contribution to the elastic energy is relatively small compared with that from the σ electrons, the π contribution is nevertheless

important for obtaining the lattice distortion known as the Peierls distortion (see Sect. 11.3.2). Although one third of the possible carbon nanotubes that can be formed are one-dimensional metals, and it is well known that the Peierls instability is favored in low dimensional systems [223], the associated lattice distortion can be negligible in the case of carbon nanotubes because of the following physical situation. The Peierls instability is known to cause a metal-insulator transition, by opening an energy gap at the Fermi energy to benefit from the electronic energy gain which is introduced by the distortion of the lattice into a doubled unit cell. The values of the distortion are determined by minimizing the total energy as a function of the distortion, in which the energy gain associated with the electron-lattice interaction of the π electrons is balanced by the energy loss of the potential energy of the lattice. Starting from a general theory of the Peierls instability, we focus our attention on the reason why the Peierls distortion is suppressed in carbon nanotubes in Sect. 11.3.

Multi-wall carbon nanotubes have many interesting properties that are not observed or explained by the physics of single-wall nanotubes. In multi-wall nanotubes, the relatively weak interaction between two adjacent layers determines their relative stacking structure, which denotes the positions of the atom sites on the outer layer, relative to those on the inner layer of the nanotube. The lattice structure of the inner and the outer layers are generally incommensurate with each other, which describes the turbostratic structure of multi-wall carbon nanotubes. This turbostratic structure affects shear stress between the nanotube shells. However, in some cases, the interlayer stacking can become correlated, and experimental evidence has been found for faceting in some multi-layer nanotubes [224, 225].

Because of the weak and incommensurate electronic interaction between the two layers, the electronic structure between two adjacent carbon layers is considered in terms of a sum of the electronic structures of the constituent nanotubes. Furthermore, in discussing multi-layer nanotubes we require that in the limit of large nanotube diameter, all the nanotube properties should correspond to those of graphite. These topics are briefly summarized in Sect. 11.4.

11.2 Strain Energy of Carbon Nanotubes

When we consider a single-wall carbon nanotube as an elastic sheet, the strain energy E_σ is inversely proportional to the diameter of carbon nanotube, d_t : [12],

$$E_\sigma = \frac{\pi ET d_f^3}{6d_t}, \quad (11.1)$$

where E is the elastic modulus of the sheet, T is the length of the carbon nanotube per 1D unit cell in the direction of the nanotube axis [see Eq. (3.5)], and d_f is the thickness of the thin film, which can be considered as the interplanar distance between two turbostratic graphene layers (3.44 Å). Since the number of carbon atoms per unit cell $N = 2LT/\sqrt{3}a^2$ [see Eq. (3.9)] is also proportional to d_t (i.e., $L = 2\pi d_t$), the strain energy per carbon atom is inversely proportional to the square of the nanotube diameter:

$$\frac{E_\sigma}{N} = \frac{\sqrt{3}Ed_f^3a^2}{24d_t^2}. \quad (11.2)$$

This simple argument for a dependence of E_σ/N on d_t^{-2} is confirmed by a more detailed first principles calculation of the strain energies of many carbon nanotubes with different diameters and chiralities [209], as shown in Fig. 11.1. The solid curve in the figure depicts the $(1/d_t)^2$ dependence of E_σ given in Eq. (11.1), showing that we can understand the functional dependence of the strain energy of a carbon nanotube from the simple arguments given above for an elastic thin film. The small deviations of the strain energy as a function of nanotube diameter (or radius) suggests that the dependence of E_σ/N on chirality, is very weak, and this weak dependence may be due to: (1) chirality-dependent directions of the three equivalent σ bonds with respect to the nanotube axis, and (2) chirality-dependent contributions of the π bonds, depending on whether there is an energy gap or not in the dispersion relations.

Although the total energy depends on the nanotube chirality and thus should be related to the stability of the carbon nanotube, the abundance of a given diameter carbon nanotube should not depend on the chirality. This is because the abundance of nanotubes is determined by the initial formation of the end cap of the carbon nanotube. In fact, experimental results for the diameter distribution of single wall carbon nanotubes do not show the same diameter distribution for different catalysts [57]. Since the diameter and chirality cannot

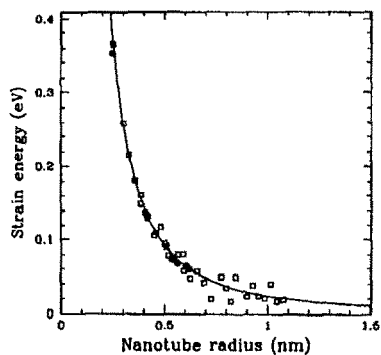


Fig. 11.1: Strain energy per carbon atom E_σ as a function of nanotube radius $r_t = d_t/2$ [81]. The solid curve depicts the $(1/d_t)^2$ dependence of E_σ given in Eq. (11.1).

be changed in a single-wall nanotube unless a defect exists, this result might show that the diameter and chirality that are obtained in the growth process depend mainly on the shape of the caps generated by the catalytic particle. The lower limit of the diameter of a single wall carbon nanotube seems to be the diameter of C_{60} . In fact there is no report of observation of a nanotube with a diameter smaller than that of C_{60} .

When a force acts perpendicular to the nanotube axis, the nanotube bends, as described by the Young's modulus Y [220]. When we consider a cantilever beam of length ℓ , the deflection d of the beam with a force f at its free end is given by [219]

$$d = \frac{f\ell^3}{3YI} \quad (11.3)$$

where I is the areal moment of inertia of the cross-section of the nanotube about its axis, $I = \pi(r_o^4 - r_i^4)/4$, in which r_o and r_i are the outer and inner radii of an elastic cylinder, respectively [220]. As a first approximation* we use $Y = C_{11}$ where the elastic modulus C_{11} for a carbon fiber for Y , $C_{11} = 1060$ GPa [9, 219, 226]. Overney et al. calculated the beam rigidity of a carbon nanotube in the same geometry, using the Keating potential whose parameters are given by the local density functional calculation [227]. Their calculated result shows that the beam rigidity is 200 times greater than a Pr bar of the same size. The

*The Young's modulus Y is given by $(S)_{11}^{-1}$, where S_{ij} denotes the compliance tensor. Since $C_{12} = 220$ GPa is not negligible in a carbon fiber, we expect Y for a carbon fiber (~ 800 GPa) to be somewhat smaller than C_{11} for graphite. However, since we expect C_{12} in a nanotube to be reduced relative to graphite, we may use the C_{11} values for graphite to obtain a value for Y for carbon nanotubes.

calculated Young's modulus for a carbon nanotube is about 1500 GPa. There are many calculations for the Young's modulus whose value varies from 500 to 1500 GPa, depending on the potential model and on the estimation for the cross section. When we consider a single wall nanotube, we may use Eq. (11.3) and we can consider the wall thickness to be 3.44 Å, which is the interlayer separation between turbostratically stacked graphene layers [9].

When the diameter of single wall nanotube increases, the nanotube is unstable in the direction perpendicular to the surface. The TEM observations show evidence for nanotubes collapsing into a flattened or bent nanotube without breaking the nanotube structure. TEM photos of a collapsed nanotube look similar to the bending of a rubber nanotube [228]. On a nanometer (nm) scale, the nanotube seems to be rather soft in the direction perpendicular to the nanotube axis.

The experimental observation of the Young's modulus of a single nanotube is difficult because of its small diameter. A novel method for measuring the Young's modulus of individual nanotubes has been developed, whereby the amplitude of a thermal vibration of the nanotube is observed as a function of temperature [229]. At a high temperature T where a classical Boltzmann distribution of probabilities, $P \propto \exp(-E/k_B T)$, can be used, the average of the vibrational energy, $\langle W_n \rangle$, for a vibrational mode, n , becomes $k_B T$, or $\langle W_n \rangle = k_B T$, where k_B is Boltzmann's constant. Since the averaged value of W_n is proportional to the square of the amplitude u_n^2 , we can write

$$\langle W_n \rangle = \frac{1}{2} c_n \langle u_n^2 \rangle = k_B T, \quad (11.4)$$

where c_n is a spring constant. The spring constant is estimated by directly observing the amplitude of the thermal vibration as a function of temperature within the standard deviation

$$\sigma^2 = k_B T \sum_n \frac{1}{c_n} \quad (11.5)$$

given by statistical physics. The relationship between c_n and the Young's modulus Y is given by use of elasticity theory for continuum media

$$c_n = \frac{\pi \beta_n^4 Y (r_o^4 - r_i^4)}{16 L_\ell^3}. \quad (11.6)$$

where the values β_n are solutions to the equation, $\cos \beta_n \cosh \beta_n + 1 = 0$. In their experiments the authors used a clamped hollow cylindrical cantilever of length L [229]. The leading numerical values for β_n , ($n = 0, 1, 2, 3, \dots$) are 1.8751, 4.6941, 7.8548 and 10.9955 and for larger β_n values, β_n can be found by the approximation $\beta_n \sim (n + 1/2)\pi$. By fitting a , b , and L to Eq. (11.6) for various nanotubes, the estimated results for Y are found to be in the range of ~ 1000 GPa, comparable to C_{11} for graphite.

11.3 The Peierls Instability of Nanotubes

11.3.1 Bond Alternation

Next we discuss the effect of π electrons on the elastic properties. When electrons occupy about half of the valence energy band of one-dimension materials, the energy bands are unstable to a distortion of the lattice into a doubled unit cell. For the doubled unit cell in real space, the corresponding unit cell in reciprocal space is reduced by a factor of 2. Therefore, the energy dispersion relations are folded in half and an energy gap is opened at the Fermi energy at the zone boundary of the folded Brillouin zone. This effect is known as the Peierls instability. For partially filled bands, such a distortion leads to a lowering of the energy of the system as the lower energy bands become occupied and the higher-lying energy bands remain empty. An example of the Peierls instability is the bond alternation or the Kekulé structure of neutral carbon nanotubes [230], which has been discussed [230–233] in terms of the Su–Schrieffer–Heeger (SSH) model, developed initially for polyacetylene $(CH)_x$ [234], and subsequently for C_60 and its ions [231–233].

In the SSH model, a tight-binding Hamiltonian describing bond-alternation is solved in a large unit cell in which the transfer integral between the n th and m th atoms, t_{nm} , is defined by

$$t_{nm} = t_{nm}^0 + \alpha(x_n - x_m), \quad (11.7)$$

and t_{nm} becomes a function of the distortions of atoms from their original positions, x_n and x_m . In Eq. (11.7), t_{nm}^0 is the transfer integral without bond alternation ($-2.5 \sim -3.2$ eV) and α denotes the electron-phonon coupling constant (~ 5.0 eV/Å). When the two atoms are close to each other, the absolute value

of the transfer integral* becomes large. In the case of polyacetylene (CH_x), the bond alternation problem can be solved by using a doubled unit cell with a distortion $x_n = (-1)^n x_0$ leading to two transfer integrals t_1 and t_2 , ($t_1 = t_0 - 2\alpha x_0$ and $t_2 = t_0 + 2\alpha x_0$, with $|t_1| < |t_2|$).

When we neglect the overlap integral, $s = 0$ in Eq. (2.20) for simplicity, \mathcal{H}_{AB} of Eq. (2.17) becomes

$$\mathcal{H}_{AB} = t_1 e^{ika/2} + t_2 e^{-ika/2}, \quad (11.8)$$

and the secular equation is given by

$$\begin{aligned} & \left| \begin{array}{cc} \epsilon_{2p} - E & t_1 e^{ika/2} + t_2 e^{-ika/2} \\ t_1 e^{-ika/2} + t_2 e^{+ika/2} & \epsilon_{2p} - E \end{array} \right| \\ &= (\epsilon_{2p} - E)^2 - (t_1^2 + t_2^2 + 2t_1 t_2 \cos ka) \\ &= 0. \end{aligned} \quad (11.9)$$

The solution of Eq. (11.9) yields the dispersion relations

$$E_{\pm}(\vec{k}) = \epsilon_{2p} \pm \sqrt{t_1^2 + t_2^2 + 2t_1 t_2 \cos ka}, \quad \left(-\frac{\pi}{a} < k < \frac{\pi}{a} \right), \quad (11.10)$$

which are plotted in Fig. 11.2 for the values of $t_1 = -1.1$ and $t_2 = -0.9$. Comparing Figs. 11.2 and 2.2, we see that an energy gap of $2|t_1 - t_2| = 8\alpha x_0 = 0.4$ is opened at $k = \pm\pi/a$ because of the bond alternation. The electronic energy of those electrons which are in the occupied valence energy band (E_+ band in Fig. 11.2), decreases by opening the energy gap. On the other hand, the elastic energy increases by

$$E_{sp} = 4Kx_0^2 \quad (11.11)$$

where K is a spring constant, and thus the optimized value of x_0 is given by minimizing the total energy. Putting $t_1 = t_0 - 2\alpha x_0$ and $t_2 = t_0 + 2\alpha x_0$ into Eq. (11.10), the energy difference of the electronic energy is given by

$$E_{el}(x_0) = \frac{a}{\pi} \int_{-\pi/a}^{\pi/a} dk \{ E_+(k)|_{x_0=x_0} - E_+(k)|_{x_0=0} \}. \quad (11.12)$$

Thus the total energy $E_{tot} = E_{el} + E_{sp}$ has a minimum, $\partial E_{tot}/\partial x_0 = 0$ when

$$8Kx_0 = \frac{a}{\pi} \int_{-\pi/a}^{\pi/a} dk \frac{\partial}{\partial x_0} \sqrt{A + B \cos ka}, \quad (11.13)$$

*It is noted that $t_{nm}^0 < 0$ and $\alpha > 0$ in Eq. (11.7).

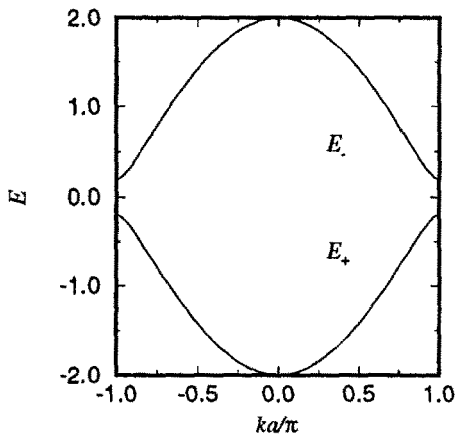


Fig. 11.2: The energy dispersion relation $E_{\pm}(\vec{k})$ for bond-alternating polyacetylene given by Eq. (11.10) using values for the parameters $\epsilon_{2p} = 0$, $t_1 = -1.1$ and $t_2 = -0.9$. The energy gap at $k = \pm\pi/a$ arising from the bond alternation has a value of $2|t_1 - t_2| = 8\alpha x_0 = 0.4$ in these units.

where A and B denote $A = 2t_0^2 + 8\alpha^2 x_0^2$ and $B = 2t_0^2 - 8\alpha^2 x_0^2$, respectively. The integration of Eq. (11.13) is given analytically by

$$\frac{\pi |t_0| K}{4 \alpha^2} = \frac{1}{z^2} [\mathcal{K}(z) - \mathcal{E}(z)] \quad (11.14)$$

where $\mathcal{K}(z)$, and $\mathcal{E}(z)$ are, respectively,[†] the complete elliptical integrals of the first and the second kind defined by,

$$\mathcal{K}(z) = \int_0^{\pi/2} \frac{d\theta}{\sqrt{1 - z^2 \sin^2 \theta}}, \text{ and } \mathcal{E}(z) = \int_0^{\pi/2} d\theta \sqrt{1 - z^2 \sin^2 \theta}. \quad (11.15)$$

In Eq. (11.14) z is a function of x_0 which is given by

$$z^2 = \frac{2B}{A+B} = 1 - 4 \left(\frac{\alpha x_0}{t_0} \right)^2. \quad (11.16)$$

To solve Eq. (11.14), we use the mathematical formula $\cos 2\theta = 1 - 2\sin^2 \theta$, and obtain a solution for x_0 over a reasonable range of $\alpha > 0$.

[†]When $|z| < 1$ we can expand $\mathcal{K}(z)$ and $\mathcal{E}(z)$ around $k = 0$ to obtain:

$$\mathcal{K}(z) = \frac{\pi}{2} \left\{ 1 + \left(\frac{1}{2} \right)^2 z^2 + \left(\frac{1 \cdot 3}{2 \cdot 4} \right)^2 z^4 + \dots \right\},$$

and

$$\mathcal{E}(z) = \frac{\pi}{2} \left\{ 1 - \left(\frac{1}{2} \right)^2 z^2 + \left(\frac{1 \cdot 3}{2 \cdot 4} \right)^2 \frac{z^4}{3} + \dots \right\},$$

respectively.

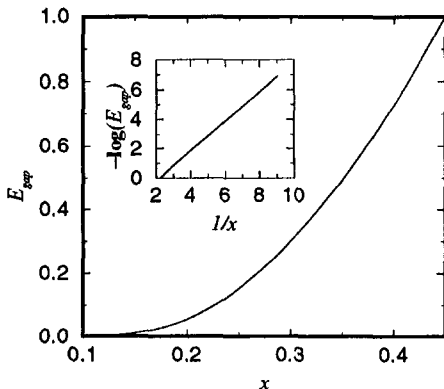


Fig. 11.3: The normalized energy gap of polyacetylene, which is the solution of Eq. (11.14), $E_{\text{gap}} \equiv 8\alpha x_0/|t_0|$, is plotted as a function of the normalized electron-phonon interaction $x \equiv 4\alpha^2/(\pi|t_0|K)$. The inset shows a linear dependence of $-\log(E_{\text{gap}})$ as a function of $1/x$.

In Fig. 11.3 we plot the normalized energy gap, $E_{\text{gap}} \equiv 8\alpha x_0/|t_0|$, as a function of the normalized electron-phonon interaction $x \equiv 4\alpha^2/(\pi|t_0|K)$. In the inset of Fig. 11.3 we plot $-\log(E_{\text{gap}})$ as a function of $1/x$, clearly showing a linear dependence of $-\ln(E_{\text{gap}})$ on $1/x$ which is numerically fitted by

$$E_{\text{gap}} = 9.12e^{-1.015/x}. \quad (11.17)$$

The functional form of the energy gap is similar to that for the superconducting energy gap according to BCS theory.

Because of this lowering of the total energy, bond alternation is always found in a one-dimensional metal. The corresponding lattice deformation is called the Peierls distortion. In a molecule which has degenerate and partially-occupied levels associated with the high symmetry of the molecular geometry, the degenerate states become unstable under a lattice distortion, which lowers the symmetry and splits the degenerate levels so as to open an energy gap between the filled and unoccupied states. This effect which is similar to the Peierls instability is called the Jahn-Teller effect in quantum chemistry. The Peierls instability is thus a kind of Jahn-Teller effect which occurs in the solid state.^t In higher dimensions, this instability does not always occur, simply because the energy gain in a small region around the Fermi energy is not always larger than the energy loss associated with the elastic energy.^s In a carbon nanotube,

^tThe Peierls instability is sometimes called a band Jahn-Teller effect.

^sThere are no pure one or two dimensional solids in three dimensional space. The Peierls instability occurs when the shape of the Fermi surface is close to that of a one-dimensional

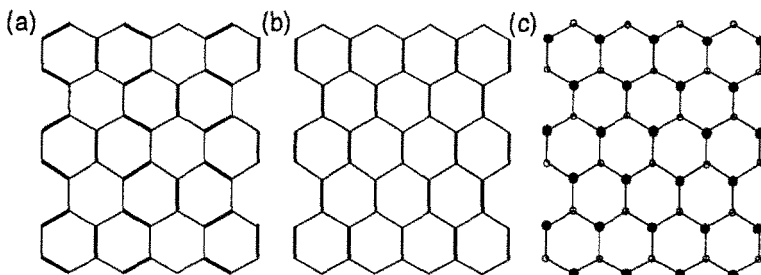


Fig. 11.4: Possible bond alternation for a honeycomb lattice. (a) a Kekulé type in-plane bond alternation, (b) a quinoid type in-plane bond alternation, and (c) an out-of-plane bond alternation. In the case of in-plane bond alternations, thick and thin lines, respectively, denote shrunk and elongated bonds, while solid and open circles in the out-of-plane bond alternation denote deformations in the $+z$ and $-z$ directions, respectively.

although the geometry is one-dimensional, the electronic structure becomes close to that of graphite as the diameter increases. Thus a dimensional crossover associated with bond alternation occurs at 0 K, as described in Sect. 11.3.2.

11.3.2 Peierls Distortion of graphite and carbon nanotubes

In chapter 2 we show that two-dimensional graphite has no energy gap between the bonding and antibonding π bands because there are two equivalent carbon atoms in the unit cell which give rise to a symmetry-imposed degeneracy at the Brillouin zone corner. If the two atoms were not equivalent to each other, an energy gap would appear, thereby lowering the electronic energy. Whether this symmetry-lowering distortion does occur or not depends on the strength of the electron-phonon coupling constant, which we will discuss in this section.

In the honeycomb lattice we can consider three kinds of lattice deformations as shown in Fig. 11.4; (a) a Kekulé type of in-plane bond alternation, (b) a quinoid type in-plane bond alternation, and (c) an out-of-plane bond alternation. In Fig. 11.4(a) and (b), thick and thin lines, respectively, denote shrunk and

surface, or when two Fermi surfaces are parallel to each other over large areas in the Brillouin zone (the nesting condition).

elongated bonds. In the case of an out-of-plane deformation, the *A* and *B* sites in the unit cell deform in the $+z$ and $-z$ directions, respectively. After deformation, the unit cell becomes twice as large as the original unit cell in the case of in-plane deformations, while the unit cell for out-of-plane deformations does not change. Thus for simplicity we consider the case of an out-of-plane deformation.

Even if we deform the lattice by an out-of-plane deformation, all C–C bonds are still equivalent to each other, and thus there is no relative difference in the transfer energy between the *A* and *B* sites. When the site energies have different values for the *A* and *B* sites, the two sites are not equivalent. For example the *A* and *B* sites are inequivalent in three-dimensional graphite, in which the *A* sites have carbon atoms above and below the atom but the *B* sites do not.* In a single layer of graphite, there is no relative difference in the site energy between the *A* and *B* sites. However, in the case of a single layer carbon nanotube, there is a difference between the inner and outer directions.

If we assume that the site energy for the *A* and *B* carbon atoms is shifted by $\pm\alpha z_0/2$ in which α is the electron-phonon coupling constant per distortion z_0 , the energy dispersion of the distorted π bands of graphite is given by solving the perturbation Hamiltonian,

$$\mathcal{H} = \begin{pmatrix} \alpha z_0 & tf(k) \\ tf(k)^* & -\alpha z_0 \end{pmatrix}, \quad (11.18)$$

where t and $f(k)$ are defined by Eq. (2.24) and Eq. (2.25), respectively. Here we neglect the effect of the overlap matrix S and we put $\epsilon_{2p} = 0$ in Eq. (2.26) for simplicity. When the distortion is included, the calculated energy dispersion $E(\mathbf{k})$ becomes

$$E(\mathbf{k}) = \pm t \sqrt{\left(\frac{\alpha z_0}{t}\right)^2 + 1 + 4 \cos \frac{\sqrt{3}k_x a}{2} \cos \frac{k_y a}{2} + 4 \cos^2 \frac{k_y a}{2}}. \quad (11.19)$$

This relation implies an energy gap of $2\alpha z_0$ at the K point. The value of z_0 is obtained by minimizing the total energy which is given by the sum of the

*In the SSH Hamiltonian they consider only the change of the transfer energy by the lattice deformation. Here we consider only the change of the site energy by the lattice deformation. Generally, the electron-lattice interaction affects both the transfer integral and site energies. See, for example, R. Saito and H. Kamimura, J. Phys. Soc. Japan 52, (1983) 407.

electronic energy and potential energy of the lattice. No distortion from the honeycomb lattice is observed in crystalline graphite because the density of states at the Fermi level is zero in the case of two-dimensional graphite. This situation is explained below as the limit of a carbon nanotube.

Let us consider the Peierls instability of a carbon nanotube. Here we consider only out-of-plane distortions for the case of a zigzag carbon nanotube, $(n, 0)$, for simplicity. Since the size of the unit cell does not change in the case of an out-of-plane distortion, the electronic structure of a distorted $(n, 0)$ zigzag nanotube is obtained by zone-folding as discussed in Eq. (4.7). The $4n$ energy dispersion relations of the distorted $(n, 0)$ zigzag nanotube, $E_{z_0}^q(k)$, are expressed as

$$E_{z_0}^q(k) = \pm t \sqrt{\left(\frac{\alpha z_0}{t}\right)^2 + 1 \pm 4 \cos\left(\frac{\sqrt{3}ka}{2}\right) \cos\left(\frac{q\pi}{n}\right) + 4 \cos^2\left(\frac{q\pi}{n}\right)},$$

$$\left(-\frac{\pi}{\sqrt{3}} < ka < \frac{\pi}{\sqrt{3}}\right), \quad (q = 1, \dots, n). \quad (11.20)$$

Taking account of the potential energy of the lattice as $Kz_0^2/2$ per unit cell of graphite, in which K is a spring constant, we obtain the following gap equation for the $(n, 0)$ zigzag nanotube

$$-\frac{Kt}{\alpha^2} = \frac{1}{2\pi n} \sum_{q=1}^n \frac{1}{\sqrt{A_q + B_q}} K \left(\sqrt{\frac{2B_q}{A_q + B_q}} \right), \quad (11.21)$$

in which $K(x)$ is the complete elliptical integral of the first kind defined in Eq. (11.14), and A_q and B_q are given by

$$A_q = \left(\frac{\alpha z_0}{t}\right)^2 + 1 + 4 \cos^2\left(\frac{q\pi}{n}\right) \quad \text{and} \quad B_q = \left|4 \cos\left(\frac{q\pi}{n}\right)\right|, \quad (11.22)$$

respectively, and Eq. (11.21) is obtained by use of the mathematical formula,

$$\int_{-\pi/2}^{\pi/2} d\theta \left\{ \frac{1}{\sqrt{a + b \cos \theta}} + \frac{1}{\sqrt{a - b \cos \theta}} \right\} = \int_0^{2\pi} \frac{d\theta}{a + b \cos \theta}$$

$$= \frac{4}{\sqrt{a+b}} K \left(\sqrt{\frac{2b}{a+b}} \right), \quad (a > b > 0), \quad (11.23)$$

which directly follows from the definition of K in the footnote of the previous subsection.

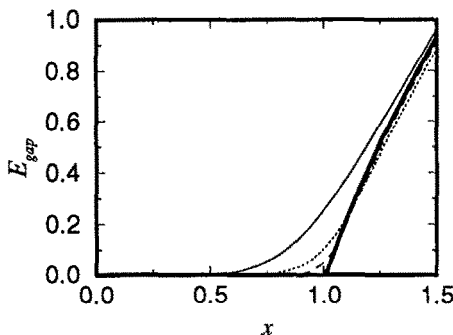


Fig. 11.5: The normalized energy gap $E_{\text{gap}} \equiv \alpha z_0 / |t_0|$ for metallic zigzag nanotubes, $(n, 0)$, is plotted as a function of the normalized electron-phonon interaction $x \equiv \alpha^2 / (K|t|)$ ($t < 0$) for special values of $n = 3, 6, 12$, and $999 (\sim \infty)$, which is essentially 2D graphite) denoted by solid, dotted, dashed, and bold solid lines, respectively.

In Fig. 11.5, we plot the energy gap $E_{\text{gap}} \equiv 2\alpha z_0 / |t_0|$, which is normalized by $|t_0|$, for metallic zigzag nanotubes $(n, 0)$, as a function of x which is the electron-phonon interaction α^2 normalized by $K|t_0|$ so that $x \equiv \alpha^2 / (K|t_0|)$ ($t_0 < 0$). The plot in Fig. 11.5 is made for special values of n that are multiples of 3, namely $n = 3, 6, 12$, and $999 (\sim \infty)$, corresponding to 2D graphite) denoted by solid, dotted, dashed, and bold solid lines, respectively. From the figure, we see that the dependence of the energy gap of the nanotube on the electron-phonon coupling constants is very close to that for the 2D case, and that an energy gap appears due to the finite values of the interaction. Actually in the case of zigzag nanotubes, the energy gap has non-zero values for small values of x , although these values can be exponentially small, as seen in Eq. (11.17). The difference between the application of Eq. (11.17) to polyacetylene and carbon nanotubes is that the factor appearing in the exponent of Eq. (11.17) depends on n for $(n, 0)$ zigzag nanotubes as $\propto \exp(-nA/x)$ (A is constant) [71]. Thus for large n a larger interaction x is necessary for opening an energy gap. The reason why we get the present results is that the electron energy gain comes only from two of the $4n$ energy bands which cross the Fermi energy, while the elastic energy loss comes from all of the $2n$ carbon atoms in the unit cell [71].

In the limit of $n \rightarrow \infty$, we obtain the two-dimensional case in which a non-zero value of z_0 appears only when $\alpha^2 / K|t_0| > 1.01$. Since there is no experimental distortion in 2D graphite, the normalized interaction of $\alpha^2 / K|t_0|$ satisfies $\alpha^2 / K|t_0| < 1.01$.

As for the other types of distortions of carbon nanotubes shown in Fig. 11.4, Harigaya et al.[233] and Viet et al.[235] independently calculated the energy gap

as a function of the chiral vector or the intensity of the electron-phonon interaction, using the SSH model for two-dimensional graphite. The calculated result shows a similar functional dependence of the energy gap on the electron-phonon interaction. A magnetic-induced distortion can however occur in a nanotube since the density of states at the Fermi energy is enhanced by the presence of a magnetic field by forming the $\ell = 0$ Landau level, as discussed in detail by Ajiki and Ando [160].

The electron-electron repulsion interaction, which is considered to be large in conjugate polymers, is also expected to be important in carbon nanotubes, since they are also low-dimensional materials. On-site ($U_0 n_{i\uparrow} n_{i\downarrow}$) and off-site electron interactions ($U_{ij} n_{i\sigma} n_{j\sigma}$) are taken into account in the SSH Hamiltonian, in which the two-body effect is calculated mostly within the Hartree-Fock approximation, while keeping self-consistency between the charge and the lattice distortion [233]. Within the reasonable range of $U \sim |t_0|$, the lattice distortion is determined by the electron-phonon interaction (α). For larger U , a spin-Peierls interaction may occur in which the interaction between the two spins is now a function of the deformation of the lattice: ($J \sim -|t|^2/U = J_0 + \alpha_J(x_n - x_{n+1})$).[†]

In conclusion, though metallic 1D energy bands are generally unstable under a Peierls distortion, the Peierls energy gap obtained for metallic nanotubes is found to be greatly suppressed by increasing the nanotube diameter. Thus the Peierls gap quickly approaches the zero-energy gap of 2D graphite [69, 71]. Thus if we consider finite temperatures or fluctuation effects, it is believed that such a small Peierls gap ($< 10^{-3}$ eV) cannot be observed experimentally. The coexistence of metallic and semiconducting carbon nanotubes, depending on the chirality of the carbon nanotube, is independent of the lattice deformation.

11.4 Properties of Multi-Wall Nanotubes

In this section, we list several interesting features that can be seen only in multi-wall nanotubes. Although multi-layer nanotubes have not been characterized in detail for their physical properties, because of the difficulty of making measurements on the individual shells of the nanotube and of sample preparation of

[†]There is an kinetic exchange interaction $J \sim -|t|^2/U$ which favors the antiferro-magnetic interaction. Since the transfer energy t in the SSH Hamiltonian is a function of $(x_n - x_{n+1})$, [see Eq. (11.7)], J depends on the deformation. This effect is known as the spin-Peierls distortion.

a well-defined and structurally characterized multi-wall nanotube, the co-axial nanotubes provide an interesting geometry, as shown below.

When we consider two coaxial nanotubes which share the same nanotube axis, the chiral vectors of the inner and outer nanotubes can be determined separately, which give the radii of the constituent nanotubes and the interlayer spacing between them. However, the structures of the two nanotubes will not be commensurate to each other in almost all concentric nanotubes, since their ratio of lengths in the circumferential direction is scaled by the ratio of the two diameters, but is not scaled in the direction of the nanotube axis. Further for (n, m) nanotubes, the length of the chiral vector $C_h = L$ is proportional to an irrational number $L = a\sqrt{n^2 + m^2 + nm}$. The only commensurate cases are the cases of the achiral co-axial nanotubes, since the translation vectors, T , are the same for two armchair nanotubes (n_1, n_1) and (n_2, n_2) (where $T = a$) or for two zigzag nanotubes $(n_1, 0)$, $(n_2, 0)$ (where $T = \sqrt{3}a$). Thus the lattice constant along the z axis has a 1 to 1 commensurate ratio. As for the circumferential direction, cyclic boundary conditions always imply a commensurate relation. In achiral nanotubes, the commensurate ratio is expressed by n_1/n_2 . It is clear that an armchair nanotube and a zigzag nanotube cannot be commensurate in the direction of the z axis, since the ratio of T is $1/\sqrt{3}$. In the case where the two are general chiral nanotubes, since the length of $T = \sqrt{3}L/d_R$ is an irrational number in units of a [see Eq. (3.8)], the ratio of the T vectors for the two nanotubes will be an irrational number. In the case of incommensurate co-axial nanotubes, no periodicity appears along the z axis. This means that when we put carbon atoms on the x axis, both for the inner and outer nanotubes, we will not see any two atoms in a line parallel to the x axis. When we slide the inner nanotube along the z axis relative to the outer nanotube, the elastic potential is, however, a periodic function, with a period that is the larger value of the T vectors for the constituent nanotubes. When the number of carbon atoms in the unit cell of the constituent nanotubes becomes large, the potential becomes flat, since the average of the inter-atomic potentials at different distances does not depend much on z . In this sense, the shear modes between two graphite layers, which is observed at 42 cm^{-1} in graphite, should be much reduced in the multi-wall nanotube. One nanotube may move smoothly with respect to the other in the attractive force between the two walls.

Since we have two degenerate shear modes in the x and y directions in

the graphitic plane, we can expect another shear mode in the nanotube which corresponds to the rotation around the z axis. Since there are two chiral vectors in a horizontal plane perpendicular to the nanotube axis, the rotation around the z axis has a periodicity of $2\pi/d_c$, where d_c is the common divisor of the four integers, n_1 , m_1 , n_2 , and m_2 for the (n_1, m_1) and (n_2, m_2) nanotubes. Thus, we expect the motion to be smoother, the smaller is the value of d_c . The normal mode for the shear displacement of the two constituents of a two-walled nanotube is a mixture of a translation and a rotation around the z axis. The direction of the normal mode displacements will be determined by the two chiral vectors. In all cases, we expect a downward shift for the shear stress between the adjacent walls of a multi-wall nanotube, relative to the shear mode in graphite.

Chandrabhas et al. [236], however, have reported an upshift of the two shear modes to 49 cm^{-1} and 58 cm^{-1} from the E_{2g_1} graphite shear mode at 42 cm^{-1} . The authors attributed the upshift to defects in the nanotube axis. Except for a few nanotubes with open ends, most nanotubes have end caps which prevent the sliding motion. In that case a vibrational mode can be expected to result from the sliding motion. If we could have an ideal coaxial multi-wall nanotube with open ends, it would be interesting to study the nano-forces associated with sliding the inner nanotube with respect to the outer nanotube, like the microscopic motion of a muscle.

The electronic structure of a multi-wall nanotube has been calculated for a commensurate double-wall carbon nanotube by a tight binding calculation [76]. In this calculation, the value used for the largest interlayer interaction in graphite associated with the overlap of the wave functions of the two π electrons was $\gamma_1 = 0.35\text{ eV}$ for the two A carbon atoms with a separation $(0, 0, c)$. In the tight-binding calculation, the interlayer interaction between two carbon atoms on two different nanotube shells with a separation r is assumed to be $\gamma_1 \exp(-Ar)$, where $A = 1/a$ is an empirical damping factor. The calculated results for the commensurate $(5,5)-(10,10)$ and $(9,0)-(18,0)$ nanotubes show an anti-crossing* of two energy dispersion curves with the same symmetry of wave functions belonging to the two different nanotubes. As for the wave functions with different symmetries, the energy dispersion relations can cross each other, since the wave functions remain orthogonal to each other even in the presence

*Anti-crossing means that two energy dispersion curves repel each other at the crossing point. Anti-crossing occurs as a result of the interaction between the two energy bands.

of the interlayer interaction. Although we take account of the interlayer interaction, the calculated result [76] shows that the electronic properties of a two-shell coaxial nanotube look like the sum of the electronic structure of the two independent nanotubes except for the anti-crossing phenomenon. Even when this anti-crossing appears near the Fermi energy, we do not see the onset of an energy gap at the Fermi energy for metal-metal and metal-semiconductor coaxial nanotubes. Thus the calculated results show that the constituent nanotubes of a coaxial nanotube remain either metallic or semiconducting, depending on the chirality of the constituent nanotube. From this result, we can expect that it will be possible to fabricate coaxial conducting wires or capacitors shielded by semiconducting nanotubes which are suggested in the literature [141, 237]. Since the energy gap of a BN nanotube is the same as that for the bulk BN semiconductor, a large energy gap of about 5 eV is expected for BN nanotubes. Thus when we cover a carbon nanotube by a BN nanotube, the nanotube complex will be more interesting than carbon-carbon coaxial nanotubes for device applications, since high insulation by the BN nanotube can be expected. The arc method of synthesis using a carbon rod with the materials for the BN nanotube included in the central portion of the carbon anode yields a coaxial multi-wall nanotube in which a several-wall BN nanotube is surrounded by a several-wall carbon nanotube on both the outside and the inside [137]. This observation suggests further possibilities for a variety of other nanotube complexes.

If the electronic structure of a multi-wall nanotube can be understood in terms of the electronic structure of the constituent single-wall nanotubes, it becomes easy to understand the topological STM and the transport STS experiments in which only the outermost nanotube contributes to the STM image and STS conductance measurements, respectively. In the STM experiment on single crystal graphite, a triangular lattice is observed because of the *ABAB* stacking of the graphite layers. In graphite, the electrons and holes near the Fermi energy mainly corresponds to *B* atom wavefunctions, which do not have a neighboring atom directly above or below them on the adjacent graphite layers. Thus when a small voltage is applied, the STM can only see the electrons and the holes at the *B* sites which form a triangular lattice. In a multi-wall nanotube and even in a single-wall carbon nanotube, a triangular pattern is observed in the STM image, which clearly shows that the *A* and *B* atoms are not equivalent to each other [54] in the nanotube plane, although the reason for this is still not clear.

A more sophisticated calculation was done for multi-layer nanotubes within the local density approximation to establish the optimum interlayer distance between an inner (5, 5) armchair nanotube and an outer armchair (10, 10) nanotube. The result of this calculation yielded a 3.39 Å interlayer separation [196, 238], with an energy stabilization of 48 meV/carbon atom. The fact that the interlayer separation is somewhat less than the 3.44 Å separation expected for turbostratic graphite may be explained by the interlayer correlation between the carbon atom sites both along the nanotube axis and the circumferential directions. A similar calculation for double-layered hyper-fullerenes has also been carried out, yielding an interlayer spacing of 3.524 Å between the two shells of C₆₀@C₂₄₀, with an energy stabilization of 14 meV/atom [147]. In addition, for two coaxial armchair nanotubes, estimates for the translational and rotational energy barriers of 0.23 meV/atom and 0.52 meV/atom, respectively, were obtained, suggesting significant translational and rotational interlayer mobility for individual shells of ideal nanotubes at room temperature. Detailed band calculations for various interplanar geometries for a two-layered coaxial armchair nanotube [196, 238] confirm the tight-binding results [76] mentioned above.

In the limit of large diameter, we can expect multi-wall carbon nanotubes to have the properties of graphite. In the multi-layer structure, the cross section of the hollow core becomes relatively small with increasing numbers of carbon layers, and thus the multi-wall structure would be advantageous for obtaining high strength per unit area in the nanotube axis direction. However, when the diameter increases to more than 10–20 nm, the multi-wall nanotube starts to exhibit a hexagonal pillar shape, similar to the occurrence of faceting in carbon fibers [9]. In the faceting, the curvature of the nanotubes becomes concentrated at the corners of the pillars as the interlayer correlation becomes established over a large area with a structure that is close to that of graphite. The faceting may occur in order to gain the cohesive energy of graphite through the ABAB stacking. By faceting the layers, the greatest part of the individual layers more quickly approach that of graphite than through the cylindrical growth of multi-wall nanotubes. It is important to note that the faceting is not generally found in pyrolytically generated, multi-layer carbon nanotubes [59], which is related to the growth of multi-wall nanotubes in the radial direction by an accretion method.

Appendix: Programs for a (n,m) carbon nanotube

In this Appendix, we show first a simple program for generating parameters of an (n,m) carbon nanotube, which is discussed in Chapter 3. The atomic coordinates for an (n,m) carbon nanotube are generated in the unit cell of the nanotube by the second program. The third program gives more coordinates for several unit cells. The source codes are written in Fortran 77. Any reader can use these codes by citing the book.

A-1 Parameters for an (n,m) carbon nanotube

The first program A-1 generates the characteristic vectors such as C_h , T , R and other related parameters. See details of the definitions given in Tables 3.2 and 3.3.

We show below an example of the input-output on a workstation. When you input n, m values for an (n,m) carbon nanotube using a standard input method, which generally means a keyboard, we obtain output for the parameters in a standard output format.

Example: Input and output of the program A-1

```
tube% a1.out
Enter n,m for C_h
10,10          <== input
C_h = ( 10, 10) ==> Chiral vector (n,m)
d =   10        ==> d is gcd(n,m)
d_R =   30       ==> d_R is gcd(2n+m,2m+n)
L/a = square root of 300 ==> Length of C_h
```

```

d_t = 13.56955AA   r_t = 6.78478AA ==> diameter and radius
T = ( 1, -1)      ==> Translation vector (t_1,t_2)
T/a = 1           ==> Length of T
N = 20            ==> Number of hexagon in the unit cell
R = ( 1, 0)       ==> Symmetry vector
M = 10            ==> number of T in N R

```

Here the diameter and the radius are in Å unit. The lengths of C_h and T are shown in units of a . Since these values are a square root of an integer in units of a , the output is shown above for convenience.

A-2 Coordinates for a (n,m) carbon nanotube

The program A-2 generates (x_i, y_i, z_i) ($i = 1, \dots, 2N$) coordinates in the unit cell for an (n, m) carbon nanotube. When n, m values are input in the same way as in the example for the A-1 program, the program generates two files:

Output files for A-2: (No Input file)

tube.xyz : $2N$ and coordinates (x_i, y_i, z_i) ($i = 1, \dots, 2N$)

en.xyz2 : work file which will be used in the program A-3.

The file tube.xyz includes the atomic coordinates of carbon atoms in the unit cell for the (n, m) nanotube. The other file en.xyz2 is a work file which will be used in the program A-3. The file tube.xyz has a format for the xmol program* which can display the structure in its xyz format and can convert the results to many formats consistent with other software. The first line of tube.xyz is the number of carbon atoms in the unit cell. After a blank line in the second line, the atomic symbol C and (x_i, y_i, z_i) coordinate in Å units are listed from the third line for the number of carbon atoms. The file input-output is specified by the OPEN statement of Fortran codes. The z axis is taken to be along the nanotube axis. The C-C bond distance is taken as 1.42Å. If you want to change

*xmol is a graphic software package with a Copyright by Research Equipment Inc. and dba Minnesota Supercomputer Center Inc.

this value, the parameter in the program should be changed.

A-3 Coordinates for several unit cells

The program A-3 reads the en.xyz2 which is generated by the A-2 program. When you enter the number of unit cells N_u from the keyboard, the program A-3 outputs a file tube1.xyz. Thus, before we run the A-3 program, we need to run the A-2 program. The file tube1.xyz has the same format as tube.xyz but the number of carbon atoms becomes $N_u \times 2N$.

Input and Output files for A-3:

en.xyz2 : (Input) the work file made by the program A-2.
tube1.xyz : (Output) the coordinates (x_i, y_i, z_i) ($i = 1, \dots, 2N \times N_u$)

If you want a large numbers of carbon atoms (more than 5000), the parameters in the program should be changed.

A-4 Source Codes

Here we list the source cords. Anybody that uses these source codes or their modified versions is required to cite the book.

A-1 Parameters for a (n, m) nanotube

```
c
c Parameters for a (n,m) nanotube
c
c Made by 10/16/95   R. Saito
c
c Reference: "Physical Properties of Carbon Nanotubes"
c           Imperial College Press,
c           by R. Saito, G. Dresselhaus, and M.S. Dresselhaus
c
c     dimension nnp(100),nnq(100)
c
c     itest=1
c     itest1=0
c
c     write(*,*) 'Enter n,m for C_h'
c     read(*,*) n,m
```

```

nd=igcm(n,m)
if(mod((n-m),3*nd).eq.0) then
ndr=3*nd
else
ndr=nd
endif
if(itest.eq.1) write(*,10) n,m
10 format(' C_h = (' ,i3,' ,',i3,')')
if(itest.eq.1) write(*,20) nd
20 format('   d = ',i3)
if(itest.eq.1) write(*,21) ndr
21 format(' d_R = ',i3)
c
a=sqrt(3.0)*1.421
eps=1.0e-5
c L
l2=n*n+m*m+n*m
if(l2.le.0) stop 'l2.le.0'
l=int(sqrt(float(l2))+eps)
if((l2-l**2).eq.0) then
if(itest.eq.1) write(*,30) l
30 format(' L/a = ', i4)
else
if(itest.eq.1) write(*,31) l2
31 format(' L/a = square root of ', i6)
endif
dt=a*sqrt(float(l2))/3.1415926525
rt=dt*0.5
if(itest.eq.1) write(*,32) dt,rt
32 format(' d_t = ', f10.5, '\AA'    r_t = ',f10.5, '\AA')
c T
nr=(2*m+n)/ndr
ns=-(2*n+m)/ndr
if(itest.eq.1) write(*,42) nr,ns
42 format('   T = (' ,i3,' ,',i3,')')
nt2=3*l2/ndr/ndr
nt=int(sqrt(float(nt2))+eps)
if((nt2-nt**2).eq.0) then
if(itest.eq.1) write(*,40) nt
40 format(' T/a = ', i3)
else
if(itest.eq.1) write(*,41) nt2
41 format(' T/a = square root of ', i6)
endif
c N
nn=2*l2/ndr
if(itest.eq.1) write(*,50) nn
50 format('   N = ', i4)
c R
ichk=0
if(nr.eq.0) then
n60=1
else
n60=nr
endif
c
itest2=0

```

```

c      do 60 np=-abs(n60),abs(n60)
c      do 61 nq=-abs(ns),abs(ns)
c      j2 = nr*nq - ns*np
c      if(j2.eq.1) then
c      j1 = m*np - n*nq
c      if(itest2.eq.1) write(*,67) n,m,nr,ns,np,nq,j1,j2
67    format('n,m,ns,np,nq,j1,j2=',6i4,2i6)
c      if( j1.gt.0 .and. j1.lt.nm ) then
c      ichk=ichk+1
c      nnp(ichk)=np
c      nnq(ichk)=nq
c      endif
c      endif
c      continue
61    continue
60    continue
c
c      if(ichk.eq.0) then
c      write(*,*) 'n,m,ns=',n,m,ns
c      stop ' not found p,q strange!!'
c      endif
c
c      itest3=1
c
c      if(ichk.ge.2) then
c      if(itest3.eq.1) then
c      write(*,*) 'n,m,ns=',n,m,ns
c      write(*,*) 'ichk=',ichk, 'ndr=', ndr
c      write(*,66) (nnp(i),nnq(i),(m*nnp(i)-n*nnq(i)),nn,i=1,ichk)
c      stop ' more than 1 pair of p,q strange!!'
c      endif
c
c      if(nr.ne.0 .and. ns.ne.0) then
c
c      if(itest1.eq.1) then
c      do 77 i=1,ichk
c      if((m*nnp(i)-n*nnq(i)).lt.nm) goto 777
77    continue
c      endif
c
c      write(*,*) 'n,m,ns=',n,m,ns
c      write(*,*) 'ichk=',ichk, 'ndr=', ndr
c      write(*,66) (nnp(i),nnq(i),(m*nnp(i)-n*nnq(i)),nn,i=1,ichk)
66    format(' (,i2,',',i2,) mp-nq = ', i3, ' N= ', i3)
c      stop ' more than 1 pair of p,q strange!!'
c      endif
c      endif
777  continue
c
c      if(itest.eq.1) write(*,62) nnp(i),nnq(i)
62    format(' R = (,i3,',',i3,)')
c M = mp-nq
c     mmm=m*nnp(i)-n*nnq(i)
c     write(*,69) mmm
69    format(' M = ',i3)
c     stop
c     end

```

```

c
c calculate the highest common divisor
c
    integer function igcm(ii,jj)
    i=abs(ii)
    j=abs(jj)
    if(j.gt.i) then
    iw=j
    j=i
    i=iw
    endif
    if(j.eq.0) then
    igcm=i
    return
    endif
10   continue
    ir=mod(i,j)
    if(ir.eq.0) then
    igcm=j
    return
    else
    i=j
    j=ir
    endif
    goto 10
end

```

A-2 Atomic Coordinates for a (n,m) nanotube in the unit cell

```

c
c Atomic Coordinates in the unit cell of a  $(n,m)$  nanotube
c
c Made by 10/31/95 by T. Takeya and R. Saito
c
c Reference: "Physical Properties of Carbon Nanotubes"
c           Imperial College Press,
c           by R. Saito, G. Dresselhaus, and M.S. Dresselhaus
c
c Input: n,m (from keyboard)
c Output: tube.xyz (coordinates. See detail in the above book.)
c          en.xyz2 (a work file for the program A-3)
c
c      implicit real*8(a-h,o-z)
c
c acc: C-C bond distance.
c
        parameter (acc = 1.42d0)
        parameter (nk=1300)
        dimension x(nk),y(nk),z(nk)
c
        write(*,*)' Enter n,m for C_h=(n,m)'
        read(*,*) n,m
c
        call gen11(n,m,np,nq,nr)
        write(*,*)' R = (' , np, ', ', nq , ', ')
c

```

```

c      a: the length of the unit vector
c      pi = 3.141592... sq3 = 1.732....
c
c      sq3=sqrt(3.0d0)
c      pi=4.0d0*atan(1.0d0)
c      a=sqrt(3.0d0)*acc
c
c      r;|R| , c;|C_h| , t;|T|
c
c      r=a*sqrt(dfloat(np*np+nq*nq+np*nq))
c      c=a*sqrt(dfloat(n*n+m*m+n*m))
c      t=sqrt(3.0d0)*c/dfloat(ndr)
c      write(*,*) 't=',t, dfloat(n*n+m*m+n*m)
c      write(*,190)c/2.0d0/pi
c 190  format(' radius =',f10.4)
c
c      nn: the number of hexagon in the unit cell N
c
c      nn=2*(n**2+m**2+m*n)/ndr
c
c      write(*,*) ' N =',nn*2
c
c      rs: radius of the tube
c
c      if(2*nn.gt.nk) stop 'parameter nk is too small'
c
c      rs=c/(2.0d0*pi)
c
c      q1: the chiral angle for C_h
c      q2: the 'chiral' angle for R
c      q3: the angle between C_h and R
c
c      q1=atan((sq3*dfloat(m))/dfloat(2*n+m))
c      q2=atan((sq3*dfloat(nq))/dfloat(2*np+nq))
c      q3=q1-q2
c
c      q4: a period of an angle for the A atom
c      q5: the difference of the angle between the A and B atoms
c
c      q4=2.0d0*pi/dfloat(nn)
c      q5=acc*cos((pi/6.0d0)-q1)/c*2.0d0*pi
c
c      h1:
c      h2: Delta z between the A and B atoms
c
c      h1=abs(t)/abs(sin(q3))
c      h2=acc*sin((pi/6.0d0)-q1)
c
c      write(*,*) 'q1: =',q1*180.0d0/pi
c      write(*,*) 'q2: =',q2*180.0d0/pi
c      write(*,*) 'q4: =',q4*180.0d0/pi
c      write(*,*) 'q5: =',q5*180.0d0/pi
c
c      Calculate 2*nn atoms in the unit cell.
c
c      The A atom
c

```

```

i=0
do 100 i=0,nn-1
  x1=0
  y1=0
  z1=0
  k=int(dfloat(i)*abs(r)/h1)
  x1=rs*cos(dfloat(i)*q4)
  y1=rs*sin(dfloat(i)*q4)
  z1=dfloat((dfloat(i)*abs(r)-dfloat(k)*h1))*sin(q3)
  kk2=abs(int(z1/t))+1

c Check the A atom is in the unit cell 0 < z1 < t
c
  if(z1.gt.t-0.02)then
    z1=z1-t*dfloat(kk2)
  endif
  if(z1.lt.-0.02) then
    z1=z1+t*dfloat(kk2)
  endif
  ii=ii+1
  x(ii)=x1
  y(ii)=y1
  z(ii)=z1

c The B atoms
c
  z3=(dfloat(i)*abs(r)-dfloat(k)*h1)*sin(q3)-h2
  ii=ii+1

c Check the B atom is in the unit cell 0 < z3 < t
c
  if((z3.ge.-0.02).and.(z3.le.t-0.02))then
c yes
    x2 =rs*cos(dfloating(i)*q4+q5)
    y2 =rs*sin(dfloating(i)*q4+q5)
    z2 =dfloat(dfloating(i)*abs(r)-dfloat(k)*h1)*sin(q3)-h2
    x(ii)=x2
    y(ii)=y2
    z(ii)=z2
  else
c no
    x2 =rs*cos(dfloating(i)*q4+q5)
    y2 =rs*sin(dfloating(i)*q4+q5)
    z2 =dfloat(dfloating(i)*abs(r)-dffloat(k+1)*h1)*sin(q3)-h2
    kk=abs(int(z2/t))+1
    if(z2.gt.t-0.01)then
      z2=z2-t*dfloat(kk)
    endif
    if(z2.lt.-0.01) then
      z2=z2+t*dfloat(kk)
    endif
    x(ii)=x2
    y(ii)=y2
    z(ii)=z2
    endif
  continue
c
  100

```

```

c Out put to the file tube.xyz
c
      open(60,file='tube.xyz')
      write(60,*)2*nn
      write(60,*)'
      do i=1,nn*2
          write(60,117)x(i),y(i),z(i)
      end do
117      format('C',3f10.5)
      close(60)

c Out put to the file en.xyz2
c
      open(60,file='en.xyz2')
      write(60,*)2*nn
      write(60,118)t,acc
118      format(2f25.5)
      do i=1,nn*2
          write(60,116)i,x(i),y(i),z(i)
      end do
116      format(ii5,3f25.20)
      close(60)
      stop
      end

c This subroutine calculates np,nq and ndr from n,m
c
      subroutine gen11(n,m,np,nq,ndr)
      dimension nnp(100),nnq(100)
c
      nd=igcm(n,m)
      if(mod((n-m),3*nd).eq.0) then
      ndr=3*nd
      else
      ndr=nd
      endif
c L
      l2=n*n+m*m+n*m
      if(l2.le.0) stop 'l2.le.0'
      l=int(sqrt(dfloat(l2))+eps)
      dt=a*sqrt(dfloat(l2))/3.1415926525
c T
      nr=(2*m+n)/ndr
      ns=-(2*n+m)/ndr
      nt2=3*l2/ndr/ndr
      nt=int(sqrt(dfloat(nt2))+eps)
c N
      nn=2*l2/ndr
c R
      ichk=0
      if(nr.eq.0) then
          n60=1
          else
          n60=nr
      endif
c
      itest2=1

```

```

c
do 60 np=-abs(n60),abs(n60)
do 61 nq=-abs(ns),abs(ns)
j2 = nr*nq - ns*np
if(j2.eq.1) then
j1 = m *np - n*nq
if( j1.gt.0 .and. j1.lt.nn ) then
ichk=ichk+1
nnp(ichk)=np
nnq(ichk)=nq
endif
endif
endif
61 continue
60 continue
c
if(ichk.eq.0) then
stop ' not found p,q strange!!'
endif
c
itest3=1
c
if(ichk.ge.2) then
if(itest3.eq.1) then
stop ' more than 1 pair of p,q strange!!'
endif

if(nr.ne.0 .and. ns.ne.0) then
c
if(itest1.eq.1) then
do 77 i=1,ichk
if((m*nnp(i)-n*nnq(i)).lt.nn) goto 777
continue
endif
c
endif
endif
777 continue
c
if(itest.eq.1) then
np=nnp(1)
nq=nnq(1)
endif
2 continue
return
1 continue
stop
end
c
c calculate the highest common divisor
c
integer function igcm(ii,jj)
i=abs(ii)
j=abs(jj)
if(j.gt.i) then
iw=j
j=i
i=iw

```

```

        endif
        if(j.eq.0) then
          igcm=i
          return
        endif
10      continue
        ir=mod(i,j)
        if(ir.eq.0) then
          igcm=j
          return
        else
          i=j
          j=ir
        endif
        goto 10
      end

```

A-3 Atomic Coordinates for several unit cells of a (n, m) nanotube

```

c
c Atomic Coordinates for several unit cells of a (n,m) nanotube
c
c Made by 10/31/95   by T. Takeya and R. Saito
c
c Reference: "Physical Properties of Carbon Nanotubes",
c             Imperial College Press,
c             by R. Saito, G. Dresselhaus, and M.S. Dresselhaus
c
c Input : n (from keyboard, the number of the unit cell.)
c         : en.xyz2 (a work file made by the program A-2)
c Output: tube1.xyz (atomic coordinates)
c
c     implicit real*8(a-h,o-z)
      parameter (nk=5000, aa=1.42)
      dimension x(nk),y(nk),z(nk)
      dimension iic(nk),ic(nk,3),iz(nk,3)
c
      write(*,*) 'enter the number of the unit cell N_u ='
      read(*,*)n
      open(61,FILE='en.xyz2')
      read(61,*)nn
      read(61,*)t
      do 10 i=1,nn
        read(61,*)j,x(i),y(i),z(i)
10      continue
      close(61,status='keep')
c
      write(*,*) 'Number of total atoms = ', n*nn
      if(n*nn.gt.nk) stop 'change parameter nk to a larger value'
c
      ii=nn
      do 20 i=1,nn
        do 21 jj=0,n-1
          iii=ii+i+jj*ii
          z(iii)=z(i)+dfloat(jj+1)*t
21

```

```
x(iii)=x(i)
y(iii)=y(i)
21 continue
20 continue
c
open(60,FILE='tube1.xyz')
write(60,*)n*nn
write(60,*)'
do 100 i=1,n*nn
  write(60,700)x(i),y(i),z(i)
100 continue
700 format('C',3f10.5)
close(60)
c
stop
end
```

References

1. T. A. Edison, US Patent 470,925 (1892). (issued March 15, 1892).
2. P. Schützenberger and L. Schützenberger, Compt. Rend. **111**, 774 (1890).
3. C. H. Pelabon, Compt. Rend. **137**, 706 (1905).
4. R. Bacon, J. Appl. Phys. **31**, 283–290 (1960).
5. C. Herring and J. K. Galt, Phys. Rev. **85**, 1060 (1952).
6. A. P. Levitt, in *Whisker Technology*, (Wiley-Interscience, New York, 1970).
7. A. W. Moore, A. R. Ubbelohde, and D. A. Young, Brit. J. Appl. Phys. **13**, 393 (1962).
8. L. C. F. Blackman and A. R. Ubbelohde, Proc. Roy. Soc. **A266**, 20 (1962).
9. M. S. Dresselhaus, G. Dresselhaus, K. Sugihara, I. L. Spain, and H. A. Goldberg, *Graphite Fibers and Filaments* (Springer-Verlag, Berlin, 1988), Vol. 5 of *Springer Series in Materials Science*.
10. T. Koyama, Carbon **10**, 757 (1972).
11. M. Endo, T. Koyama, and Y. Hishiyama, Jap. J. Appl. Phys. **15**, 2073–2076 (1976).
12. G. G. Tibbetts, Appl. Phys. Lett. **42**, 666 (1983).
13. G. G. Tibbetts, J. Crystal Growth **66**, 632 (1984).
14. M. Endo. *Mécanisme de croissance en phase vapeur de fibres de carbone (The growth mechanism of vapor-grown carbon fibers)*. PhD thesis, University of Orleans, Orleans, France, 1975. (in French).
15. M. Endo. PhD thesis, Nagoya University, Japan, 1978. (in Japanese).
16. A. Oberlin, M. Endo, and T. Koyama, Carbon **14**, 133 (1976).
17. A. Oberlin, M. Endo, and T. Koyama, J. Cryst. Growth **32**, 335–349 (1976).
18. R. Kubo, 1977. (private communication to M. Endo).

19. S. Iijima, *Nature (London)* **354**, 56 (1991).
20. H. W. Kroto, J. R. Heath, S. C. O'Brien, R. F. Curl, and R. E. Smalley, *Nature (London)* **318**, 162–163 (1985).
21. R. E. Smalley, DoD Workshop in Washington, DC (December 1990).
22. D. R. Huffman, DoD Workshop in Washington, DC (December 1990).
23. M. S. Dresselhaus, DoD Workshop in Washington, DC (December 1990).
24. M. S. Dresselhaus, G. Dresselhaus, and P. C. Eklund, University of Pennsylvania Workshop (August 1991).
25. J. H. Weaver, J. L. Martins, T. Komeda, Y. Chen, T. R. Ohno, G. H. Kroll, N. Troullier, R. E. Haufler, and R. E. Smalley, *Phys. Rev. Lett.* **66**, 1741–1744 (1991).
26. F. P. Bundy. In *Solid State Physics under Pressure: Recent Advance with Anvil Devices*, edited by S. Minomura, page 1, D. Reidel, Dordrecht, 1985.
27. F. P. Bundy, *J. Geophys. Res.* **85**, 6930 (1980).
28. F. P. Bundy, W. A. Bassett, M. S. Weathers, R. J. Hemley, H. K. Mao, and A. F. Goncharov, *Carbon* **34**, 141–153 (1996).
29. R. J. Lagow, J. J. Kampa, H. C. Wei, S. L. Battle, J. W. Genge, D. A. Laude, C. J. Harper, R. Bau, R. C. Stevens, J. F. Haw, and E. Munson, *Science* **267**, 362–367 (1995).
30. V. I. Kasatochkin, A. M. Sladkov, Y. P. Kudryavtsev, N. M. Popov, and V. V. Korshak, *Dokl. Chem.* **177**, 1031 (1967).
31. V. I. Kasatochkin, V. V. Korshak, Y. P. Kudryavtsev, A. M. Sladkov, and I. E. Sterenberg, *Carbon* **11**, 70 (1973).
32. A. G. Whittaker and P. L. Kintner, *Carbon* **23**, 255 (1985).
33. A. G. Whittaker and P. L. Kintner, *Science* **165**, 589 (1969).
34. A. G. Whittaker, *Science* **200**, 763 (1978).
35. A. G. Whittaker, E. J. Watts, R. S. Lewis, and E. Anders, *Science* **209**, 1512 (1980).
36. A. El Gorsey and G. Donnary, *Science* **363** (1968).
37. V. I. Kasatochkin, M. E. Kasakov, V. A. Savransky, A. P. Nabatnikov, and N. P. Radimov, *Dokl. Akad. Nauk, USSR* **201**, 1104 (1971).
38. R. B. Heimann, J. Kleiman, and N. M. Slansky, *Nature (London)* **306**, 164 (1983).
39. A. G. Whittaker and G. M. Wolten, *Science* **178**, 54 (1972).

40. A. G. Whittaker, G. Donnay, and K. Lonsdale, Carnegie Institution Year Book **69**, 311 (1971).
41. J. S. Speck, M. Endo, and M. S. Dresselhaus, J. Crystal Growth **94**, 834 (1989).
42. J. S. Speck, M. S. Dresselhaus, and M. Endo. In *Extended Abstracts of the Symposium on Graphite Intercalation Compounds at the Materials Research Society Meeting, Boston*, edited by M. Endo, M. S. Dresselhaus, and G. Dresselhaus, page 169, Materials Research Society Press, Pittsburgh, PA, 1988.
43. J. S. Speck, J. Appl. Phys. **67**, 495 (1990).
44. M. Endo, CHEMTECH **18**, 568 (1988). September issue.
45. C. Kittel, in *Introduction to Solid State Physics*, 6th ed., (John Wiley and Sons, New York, NY, 1986).
46. N. W. Ashcroft and N. D. Mermin, in *Solid State Physics*, (Holt, Rinehart and Winston, New York, NY, 1976).
47. R. S. Mulliken, in *Life of a Scientist*, (Springer-Verlag, New York, Berlin, 1989).
48. G. S. Painter and D. E. Ellis, Phys. Rev. B **1**, 4747 (1970).
49. R. A. Jishi, L. Venkataraman, M. S. Dresselhaus, and G. Dresselhaus, Phys. Rev. B **51**, 11176 (1995).
50. M. S. Dresselhaus, G. Dresselhaus, and R. Saito, Carbon **33**, 883–891 (1995).
51. S. J. Tans, M. H. Devoret, H. Dai, A. Thess, R. E. Smalley, L. J. Geerligs, and C. Dekker, Nature (London) **386**, 474 (1997).
52. C. Journet, W. K. Maser, P. Bernier, A. Loiseau, M. Lamy de la Chapelle, S. Lefrant, P. Deniard, R. Lee, and J. E. Fischer, Nature (London) **388**, 756 (1997).
53. M. R. Falvo, G. J. Clary, R. M. Taylor II, V. Chi, F. P. Brooks Jr, S. Washburn, and R. Superfine, Nature (London) **385** (1997).
54. C. Dekker, S. J. Tans, M. H. Devoret, L. J. Geerlings, R. J. A. Groeneveld, L. C. Venema, J. W. G. Wildöer, A. R. M. Verschueren, A. Bezryadin, A. Thess, H. Dai, and R. A. Smalley. In *Proc. of the Int. Winter School on Electronic Properties of Novel Materials: Molecular Nanostructures*, edited by H. Kuzmany, J. Fink, M. Mehring, and S. Roth, Springer-Verlag, New York, 1997. Kirchberg, Austria.

55. A. Thess, R. Lee, P. Nikolaev, H. Dai, P. Petit, J. Robert, C. Xu, Y. H. Lee, S. G. Kim, A. G. Rinzler, D. T. Colbert, G. E. Scuseria, D. Tománek, J. E. Fischer, and R. E. Smalley, *Science* **273**, 483–487 (1996).
56. J. M. Cowley, P. Nikolaev, A. Thess, and R. E. Smalley, *Chem. Phys. Lett.* **265**, 379–384 (1997).
57. C. H. Kiang, W. A. Goddard III, R. Beyers, and D. S. Bethune, *Carbon* **33**, 903 (1995).
58. S. Iijima and T. Ichihashi, *Nature (London)* **363**, 603 (1993).
59. M. Endo, K. Takeuchi, K. Kobori, K. Takahashi, H. Kroto, and A. Sarkar, *Carbon* **33**, 873 (1995).
60. P. M. Ajayan. In *Carbon Nanotubes: Preparation and Properties*, edited by T. Ebbesen, page 111, CRC Press, Inc., Boca Raton, Florida, USA, 1997. Chapter III.
61. P. M. Ajayan. In *Fullerenes and Nanotubes*, edited by Pierre Delhaès and P. M. Ajayan, page this volume, Gordon and Breach, Paris, France, 1998. Series: World of Carbon, volume 2.
62. S. Iijima. In *Fullerenes and Nanotubes*, edited by Pierre Delhaès and P. M. Ajayan, Gordon and Breach, Paris, France, 1998. Series: World of Carbon, volume 2.
63. Ph. Lambin and A. A. Lucas, *Phys. Rev. B* **56**, 3571 (1997).
64. W. Cochran, F. H. C. Crick, and V. Vand, *Acta Cryst.* **5**, 581 (1952).
65. C. H. Olk and J. P. Heremans, *J. Mater. Res.* **9**, 259–262 (1994).
66. K. Sattler, *Carbon* **33**, 915 (1995).
67. J. C. Charlier, X. Gonze, and J. P. Michenaud, *Europhys. Lett.* **28**, 403–408 (1994).
68. J. C. Charlier. In *Fullerenes and Nanotubes*, edited by Pierre Delhaès and P. M. Ajayan, Gordon and Breach, Paris, France, 1998. Series: World of Carbon, volume 2.
69. Riichiro Saito, Mitsutaka Fujita, G. Dresselhaus, and M. S. Dresselhaus, *Phys. Rev. B* **46**, 1804–1811 (1992).
70. M. S. Dresselhaus, G. Dresselhaus, R. Saito, and P. C. Eklund, in *C₆₀-Related Balls and Fibers*, chapter 18, pages 387–417, edited by J. L. Birman, C. Sébenne, and R. F. Wallis (Elsevier Science Publishers, B.V. 1992, New York, 1992). Balkanski Festschrift.

71. J. W. Mintmire, B. I. Dunlap, and C. T. White, Phys. Rev. Lett. **68**, 631–634 (1992).
72. J. W. Mintmire, D. H. Robertson, and C. T. White, J. Phys. Chem. Solids **54**, 1835 (1993).
73. T. Hamada, M. Furuyama, T. Tomioka, and M. Endo, J. Mater. Res. **7**, 1178–1188 (1992). *ibid.*, 2612–2620.
74. R. Saito, M. Fujita, G. Dresselhaus, and M. S. Dresselhaus. In *Electrical, Optical and Magnetic Properties of Organic Solid State Materials, MRS Symposia Proceedings, Boston*, edited by L. Y. Chiang, A. F. Garito, and D. J. Sandman, page 333, Materials Research Society Press, Pittsburgh, PA, 1992.
75. R. Saito, M. Fujita, G. Dresselhaus, and M. S. Dresselhaus, Appl. Phys. Lett. **60**, 2204–2206 (1992).
76. R. Saito, G. Dresselhaus, and M. S. Dresselhaus, J. Appl. Phys. **73**, 494 (1993).
77. M. S. Dresselhaus, R. A. Jishi, G. Dresselhaus, D. Inomata, K. Nakao, and Riichiro Saito, Molecular Materials **4**, 27–40 (1994).
78. R. A. Jishi, D. Inomata, K. Nakao, M. S. Dresselhaus, and G. Dresselhaus, J. Phys. Soc. Jpn. **63**, 2252–2260 (1994).
79. G. Dresselhaus and M. S. Dresselhaus, Phys. Rev. **140A**, 401 (1965).
80. G. Dresselhaus, M. S. Dresselhaus, and J. G. Mavroides, Carbon **4**, 433 (1966).
81. J. W. Mintmire and C. T. White, Carbon **33**, 893 (1995).
82. J. W. G. Wildöer, L. C. Venema, A. G. Rinzler, R. E. Smalley, and C. Dekker, Nature (London) **391**, 59–62 (1998).
83. A. M. Rao, E. Richter, S. Bandow, B. Chase, P. C. Eklund, K. W. Williams, M. Menon, K. R. Subbaswamy, A. Thess, R. E. Smalley, G. Dresselhaus, and M. S. Dresselhaus, Science **275**, 187–191 (1997).
84. H. Ajiki and T. Ando, J. Phys. Soc. Jpn. **62**, 2470–2480 (1993). Erratum: *ibid* page 4267.
85. M. L. Elert, C. T. White, and J. W. Mintmire, Mol. Cryst. Liq. Cryst. Sci. Technol., Sect. A **125**, 329 (1985).
86. C. T. White, D. H. Roberston, and J. W. Mintmire, (1995). unpublished.
87. X. Blase, L. X. Benedict, E. L. Shirley, and S. G. Louie, Phys. Rev.

- Lett. **72**, 1878 (1994).
- 88. J. C. Charlier, X. Gonze, and J. P. Michenaud, *Europhys. Lett.* **29**, 43–48 (1995).
 - 89. J. C. Charlier, X. Gonze, and J. P. Michenaud, *Carbon* **32**, 289–299 (1994).
 - 90. S. G. Louie. In *Progress in Fullerene Research: International Winter School on Electronic Properties of Novel Materials*, edited by H. Kuzmany, J. Fink, M. Mehring, and S. Roth, page 303, 1994. Kirchberg Winter School, World Scientific Publishing Co., Ltd., Singapore.
 - 91. X. Blase, A. Rubio, S. G. Louie, and M. L. Cohen, *Phys. Rev. B* **51**, 6868 (1995).
 - 92. N. G. Chopra, J. Luyken, K. Cherry, V. H. Crespi, M. L. Cohen, S. G. Louie, and A. Zettl, *Science* **269**, 966 (1995).
 - 93. Z. Weng-Sieh, K. Cherrey, N. G. Chopra, X. Blase, Y. Miyamoto, A. Rubio, M. L. Cohen, S. G. Louie, A. Zettl, and R. Gronsky, *Phys. Rev. B* **51**, 11229 (1995).
 - 94. D. S. Bethune, C. H. Kiang, M. S. de Vries, G. Gorman, R. Savoy, J. Vazquez, and R. Beyers, *Nature (London)* **363**, 605 (1993).
 - 95. B. I. Yakobson and R. E. Smalley, *American Scientist* **85**, 324 (1997).
 - 96. M. Yudasaka, T. Komatsu, T. Ichihashi, and S. Iijima, *Chem. Phys. Lett.* **278**, 102 (1997).
 - 97. P. C. Eklund et al., unpublished (1997). UK Workshop.
 - 98. J. M. Cowley and F. A. Sundell, *Ultramicroscopy* **68**, 1 (1997).
 - 99. H. Kataura, A. Kimura, Y. Maniwa, S. Suzuki, H. Shiromaru, T. Wakabayashi, S. Iijima, and Y. Achiba, unpublished (1997). in press.
 - 100. T. W. Ebbesen and P. M. Ajayan, *Nature (London)* **358**, 220 (1992).
 - 101. T. W. Ebbesen, H. Hiura, J. Fujita, Y. Ochiai, S. Matsui, and K. Tanigaki, *Chem. Phys. Lett.* **209**, 83–90 (1993).
 - 102. S. Seraphin, D. Zhou, J. Jiao, J. C. Withers, and R. Loufty, *Carbon* **31**, 685–689 (1993).
 - 103. Y. Saito and M. Inagaki, *Jpn. J. Appl. Phys.* **32**, L954 (1993).
 - 104. T. W. Ebbesen, *Annu. Rev. Mater. Sci.* **24**, 235–264 (1994).
 - 105. P. M. Ajayan and S. Iijima, *Nature (London)* **358**, 23 (1992).
 - 106. V. P. Dravid, X. Lin, Y. Wang, X. K. Wang, A. Yee, J. B. Ketterson, and R. P. H. Chang, *Science* **259**, 1601 (1993).

107. S. Iijima, Mater. Sci. Eng. **B19**, 172 (1993).
108. R. E. Smalley, Accounts Chem. Res. **25**, 98 (1992).
109. Y. Saito, T. Yoshikawa, M. Inagaki, M. Tomita, and T. Hayashi, Chem. Phys. Lett. **204**, 277 (1993).
110. M. Endo, K. Takeuchi, S. Igarashi, K. Kobori, M. Shiraishi, and H. W. Kroto, J. Phys. Chem. Solids **54**, 1841–1848 (1993).
111. J. J. Cuomo and J. M. E. Harper, IBM Tech. Disclosure Bulletin **20**, 775 (1977).
112. J. A. Floro, S. M. Rossnagel, and R. S. Robinson, J. Vac. Sci. Technol. **A1**, 1398 (1983).
113. Z. Ya. Kosakovskaya, L. A. Chernozatonskii, and E. A. Fedorov, JETP Lett. (Pis'ma Zh. Eksp. Teor.) **56**, 26 (1992).
114. A. Loiseau, (1998). private communication.
115. D. Laplaze, P. Bernier, W. K. Maser, G. Flamant, T. Guillard, and A. Loiseau, Carbon page xx (1997).
116. T. W. Ebbesen. In *Carbon Nanotubes: Preparation and Properties*, edited by T. Ebbesen, page 139, CRC Press, Inc., Boca Raton, Florida, USA, 1997. Chapter IV.
117. S. C. Tsang, P. J. F. Harris, and M. L. H. Green, Nature (London) **362**, 520 (1993).
118. P. M. Ajayan, T. W. Ebbesen, T. Ichihashi, S. Iijima, K. Tanigaki, and H. Hiura, Nature (London) **362**, 522 (1993).
119. H. Hiura, T. W. Ebbesen, and K. Tanigaki, Adv. Mater. **7**, 275 (1995).
120. F. Ikazaki, S. Oshima, K. Uchida, Y. Kuriki, H. Hayakawa, M. Yumura, K. Takahashi, and K. Tojima, Carbon **32**, 1539 (1994).
121. S. Bandow, (1997). private communication.
122. The mass spectra of the CS₂ extract show evidence for C₆₀ and C₇₀ in the normal ratio C₆₀:C₇₀≈7:1 and much higher concentrations of unknown molecular species or carbon clusters with masses in the range 107 < M < 361 amu.
123. For characterization by electron microscopy, the various samples were dispersed ultrasonically in ethanol and a drop of this solution was placed onto the carbon micro-grid. High resolution scanning electron microscopy (HRSEM) and transmission electron microscopy (TEM) measurements were carried out at 5 kV (Hitachi S-900) and 120 kV (Philips

- EM400), respectively. The low acceleration voltage was selected for HRSEM because it enhances the image contrast.
124. E. Dujardin, T. W. Ebbesen, H. Hiura, and K. Tanigaki, *Science* **265**, 1850 (1994).
 125. P. M. Ajayan and S. Iijima, *Nature (London)* **361**, 333 (1993).
 126. T. W. Ebbesen. In *Carbon Nanotubes: Preparation and Properties*, edited by T. Ebbesen, page 225, CRC Press, Inc., Boca Raton, Florida, USA, 1997. Chapter VII.
 127. C. Guerret-Picourt, Y. Le Bouar, A. Loiseau, and H. Pascard, *Nature (London)* **372**, 159 (1994).
 128. A. Loiseau and H. Pascard, *Chem. Phys. Lett.* **256**, 246 (1996).
 129. S. C. Tsang, Y. K. Chen, P. J. F. Harris, and M. L. H. Green, *Nature (London)* **372**, 159 (1994).
 130. J. Y. Yi and J. Bernholc, *J. Chem. Phys.* **96**, 8634 (1992).
 131. O. Zhou, R. M. Fleming, D. W. Murphy, C. H. Chen, R. C. Haddon, A. P. Ramirez, and S. H. Glarum, *Science* **263**, 1744 (1994).
 132. H. Hiura and T. W. Ebbesen, (1997). Unpublished.
 133. E. G. Gal'pern, I. V. Stankevich, A. L. Chistykov, and L. A. Chernozatonskii, *Chem. Phys. Lett.* **214**, 345 (1993).
 134. M. S. Dresselhaus and G. Dresselhaus, *Advances in Phys.* **30**, 139–326 (1981).
 135. A. M. Rao, P. C. Eklund, S. Bandow, A. Thess, and R. E. Smalley, *Nature (London)* **388**, 257 (1997).
 136. R. S. Lee, H. J. Kim, J. E. Fischer, A. Thess, and R. E. Smalley, *Nature (London)* **388**, 255 (1997).
 137. K. Suenaga, C. Colliex, N. Demonty, A. Loiseau, H. Pascard, and F. Willaime, *Science* **278**, 653 (1997).
 138. J. Goma and A. Oberlin, *Thin Solid Films* **65**, 221 (1980).
 139. M. Guigon, A. Oberlin, and G. Desarmot, *Fibre Sci. and Technol.* **20**, 55 (1984).
 140. M. Guigon, A. Oberlin, and G. Desarmot, *Fibre Sci. and Technol.* **20**, 177 (1984).
 141. Riichiro Saito, Mitsutaka Fujita, G. Dresselhaus, and M. S. Dresselhaus, *Materials Science and Engineering* **B19**, 185–191 (1993).
 142. M. Endo and H. W. Kroto, *J. Phys. Chem.* **96**, 6941 (1992).

143. S. Iijima, T. Ichihashi, and Y. Ando, *Nature (London)* **356**, 776 (1992).
144. R. Saito, G. Dresselhaus, and M. S. Dresselhaus, *Chem. Phys. Lett.* **195**, 537 (1992).
145. R. E. Smalley, *Mater. Sci. Eng.* **B19**, 1–7 (1993).
146. S. Iijima, private communication.
147. Y. Yosida, *Fullerene Sci. Tech.* **1**, 55 (1993).
148. M. S. Dresselhaus, G. Dresselhaus, and R. Saito, *Phys. Rev. B* **45**, 6234 (1992).
149. K. Tanaka, M. Okada, K. Okahara, and T. Yamabe, *Chem. Phys. Lett.* **191**, 469 (1992).
150. L. Langer, L. Stockman, J. P. Heremans, V. Bayot, C. H. Olk, C. Van Haesendonck, Y. Bruynseraeede, and J. P. Issi, *J. Mat. Res.* **9**, 927 (1994).
151. J. Heremans, C. H. Olk, and D. T. Morelli, *Phys. Rev. B* **49**, 15122 (1994).
152. X. K. Wang, R. P. H. Chang, A. Patashinski, and J. B. Ketterson, *J. Mater. Res.* **9**, 1578 (1994).
153. J. M. Luttinger, *Phys. Rev.* **84**, 814–817 (1951).
154. R. Saito, G. Dresselhaus, and M. S. Dresselhaus, *Phys. Rev. B* **50**, 14698 (1994).
155. D. R. Hofstadter, *Phys. Rev. B* **14**, 2239–2249 (1976).
156. F. A. Butler and E. Brown, *Phys. Rev.* **166**, 630 (1968).
157. J. W. McClure, *Phys. Rev.* **104**, 666 (1956).
158. H. S. M. Coxeter, in *Introduction to Geometry*, 2nd ed., (John Wiley and Sons, New York, NY, 1969).
159. M. Yoshida and E. Osawa, *Bulletin Chem. Soc. Jpn.* **68**, 2073 (1995).
ibid. p. 2083.
160. H. Ajiki and T. Ando, *J. Phys. Soc. Jpn.* **65**, 505 (1996).
161. B. I. Dunlap, *Phys. Rev. B* **49**, 5643 (1994).
162. B. I. Dunlap, *Phys. Rev. B* **50**, 8143 (1994).
163. M. Tsukada and N. Shima, *J. Phys. Soc. Jpn.* **56**, 2875 (1987).
164. P. A. Lee, A. D. Stone, and H. Fukuyama, *Phys. Rev. B* **35**, 1039 (1987).
165. L. Langer, V. Bayot, J. P. Issi, L. Stockman, C. Van Haesendonck, Y. Bruynseraeede, J. P. Heremans, and C. H. Olk, *Extended Abstracts*

- of the Carbon Conference page 348 (1995).
166. R. Landauer, IBM Journal of Research and Development **1**, 223 (1957).
 167. R. Landauer, Phil. Mag. **21**, 863 (1970).
 168. T. Nakanishi and T. Ando, J. Phys. Soc. Japan **66** (1997). in press.
 169. R. Tamura and M. Tsukada, Phys. Rev. B **55**, 4991 (1997). scaling law of nanotube conductance.
 170. T. Ando, Phys. Rev. B **44**, 8017 (1991).
 171. S. Ihara and S. Itoh, Carbon **33**, 931 (1995).
 172. S. Motojima, M. Kawaguchi, K. Nozaki, and H. Iwanaga, Carbon **29**, 379 (1991).
 173. V. Ivanov, J. B. Nagy, Ph. Lambin, A. A. Lucas, X. B. Zhang, X. F. Zhang, D. Bernaerts, G. Van Tendeloo, S. Amelinckx, and J. Van Lundenuyt, Chem. Phys. Lett. **223**, 329 (1994).
 174. J. Liu, H. Dai, J. H. Hefner, D. T. Colbert, R. E. Smalley, S. J. Tans, and C. Dekker, Nature (London) **385**, 780 (1997).
 175. Needed et al., (1992).
 176. K. Akagi, R. Tamura, M. Tsukada, S. Itoh, and S. Ihara, Phys. Rev. Lett. **74**, 2307 (1995).
 177. S. Datta, *Transport in mesoscopic systems* (Cambridge University Press, Cambridge, UK, 1995).
 178. B. J. Wees et al., Phys. Rev. Lett. **60**, 848 (1988).
 179. L. Chico, V. H. Crespi, L. X. Benedict, S. G. Louie, and M. L. Cohen, Phys. Rev. Lett. **76**, 971-974 (1996).
 180. D. Thouless, Phys. Rev. Lett. **39**, 1167 (1977).
 181. H. Kamimura and H. Aoki, in *The Physics of Interacting Electrons in Disordered Systems*, (Clarendon Press, Oxford, 1989).
 182. M. S. Dresselhaus, M. Endo, and J. P. Issi. In *Fluorine-Carbon and Fluoride-Carbon Materials: Chemistry, Physics and Applications*, edited by T. Nakajima, pages 95-186, Marcel Dekker, Inc, New York, 1994. Chapter IV.
 183. P. A. Lee and T. V. Ramakrishnan, Rev. Mod. Phys. **57**, 287 (1985).
 184. L. Langer, V. Bayot, E. Grivei, J. P. Issi, J. P. Heremans, C. H. Olk, L. Stockman, C. Van Haesendonck, and Y. Bruynseraeede, Phys. Rev. Lett. **76**, 479-482 (1996).
 185. T. W. Ebbesen, H. Hiura, M. E. Bisher, M. M. J. Treacy, J. L. Shreeve-

- Keyer, and R. C. Haushalter, Advanced Materials **8**, 155 (1996).
186. T. W. Odom, J. L. Huang, P. Kim, and C. M. Lieber, Nature (London) **391**, 62–64 (1998).
187. M. Bockrath, D. H. Cobden, P. L. McEuen, N. G. Chopra, A. Zettl, A. Thess, and R. E. Smalley, Science **275**, 1922–1924 (1997).
188. C. L. Kane and E. J. Mele, Phys. Rev. Lett. **78**, 1932 (1997).
189. C. A. Klein. In *Chemistry and Physics of Carbon*, edited by P. L. Walker, Jr., page 217. Marcel Dekker, Inc., New York, 1966. Vol. 2.
190. C. A. Klein, J. Appl. Phys. **33**, 3388 (1962).
191. A. A. Bright and L. S. Singer, Carbon **17**, 59 (1979).
192. V. Bayot, L. Piraux, J. P. Michenaud, and J. P. Issi, Phys. Rev. B **40**, 3514 (1989).
193. R. A. Jishi, L. Venkataraman, M. S. Dresselhaus, and G. Dresselhaus, Chem. Phys. Lett. **209**, 77–82 (1993).
194. T. Aizawa, R. Souda, S. Otani, Y. Ishizawa, and C. Oshima, Phys. Rev. B **42**, 11469 (1990).
195. C. Oshima, T. Aizawa, R. Souda, Y. Ishizawa, and Y. Sumiyoshi, Solid State Commun. **65**, 1601 (1988).
196. J. C. Charlier. *Carbon Nanotubes and Fullerenes*. PhD thesis, Catholic University of Louvain, Belgium, 1994. Department of Physics.
197. M. Tinkham, *Group Theory and Quantum Mechanics* (McGraw-Hill, New York, N. Y., 1964).
198. M. S. Dresselhaus, G. Dresselhaus, and P. C. Eklund, *Science of Fullerenes and Carbon Nanotubes* (Academic Press, New York, NY, 1996).
199. J. M. Holden, Ping Zhou, Xiang-Xin Bi, P. C. Eklund, Shunji Bandow, R. A. Jishi, K. Das Chowdhury, G. Dresselhaus, and M. S. Dresselhaus, Chem. Phys. Lett. **220**, 186 (1994).
200. T. Guo, C.-M. Jin, and R. E. Smalley, Chem. Phys. Lett. **243**, 49–54 (1995).
201. M. S. Dresselhaus and G. Dresselhaus, Light Scattering in Solids III **51**, 3 (1982). edited by M. Cardona and G. Güntherodt, Springer-Verlag Berlin, Topics in Applied Physics.
202. A. Kasuya, Y. Sasaki, Y. Saito, K. Tohji, and Y. Nishina, Phys. Rev. Lett. **78**, 4434 (1997). Raman experiment in carbon nanotubes.

203. M. S. Dresselhaus, G. Dresselhaus, and P. C. Eklund, *J. Raman Spect.* **27**, 351–371 (1995).
204. D. S. Knight and W. B. White, *J. Mater. Res.* **4**, 385 (1989).
205. S. Guha, J. Menéndez, J. B. Page, and G. B. Adams, *Phys. Rev. B* **53**, 13106 (1996).
206. G. W. Chantry, in *The Raman Effect*, vol. 1 ed., (Dekker, New York, NY, 1971).
207. D. W. Snoke, M. Cardona, S. Sanguinetti, and G. Benedek, *Phys. Rev. B* **53**, 12641 (1996).
208. R. Saito, T. Takeya, T. Kimura, G. Dresselhaus, and M. S. Dresselhaus, *Phys. Rev. B* (1998).
209. D. H. Robertson, D. W. Brenner, and J. W. Mintmire, *Phys. Rev. B* **45**, 12592 (1992).
210. P. C. Eklund, J. M. Holden, and R. A. Jishi, *Carbon* **33**, 959 (1995).
211. F. Tuinstra and J. L. Koenig, *J. Chem. Phys.* **53**, 1126 (1970).
212. T. C. Chieu, M. S. Dresselhaus, and M. Endo, *Phys. Rev. B* **26**, 5867 (1982).
213. P. Lespade, R. Al-Jishi, and M. S. Dresselhaus, *Carbon* **20**, 427 (1982).
214. M. J. Matthews, X. X. Bi, M. S. Dresselhaus, M. Endo, and T. Takahashi, *Appl. Phys. Lett.* **68**, 1078–1080 (1996).
215. M. S. Dresselhaus and R. Kalish, *Ion Implantation in Diamond, Graphite and Related Materials* (Springer-Verlag; Springer Series in Materials Science, Berlin, 1992). Volume 22.
216. R. Al-Jishi and G. Dresselhaus, *Phys. Rev. B* **26**, 4514 (1982).
217. K. Yoshizawa, K. Okahara, T. Sato, K. Tanaka, and T. Yamabie, *Carbon* **32**, 1517 (1994).
218. S. Krichene, J. P. Buisson, and S. Lefrant, *Synth. Metals* **17**, 589–594 (1986).
219. B. I. Yakobson, C. J. Brabec, and J. Bernholc, *Phys. Rev. Lett.* **76**, 2511 (1996).
220. R. S. Ruoff and D. C. Lorents, *Carbon* **33**, 925 (1995).
221. M. S. Dresselhaus, G. Dresselhaus, P. C. Eklund, and R. Saito, *Physics World* **10**(12) (December 1997).
222. J. Bernholc. Quantum molecular dynamics simulations of microtube bending (unpublished).

223. R. E. Peierls, in *Quantum Theory of Solids*, (Oxford University Press, London, 1955).
224. X. F. Zhang, X. B. Zhang, G. Van Tendeloo, S. Amelinckx, M. Op de Beeck, and J. Van Landuyt, *J. Cryst. Growth* **130**, 368–382 (1993).
225. M. Liu and J. M. Cowley, *Ultramicroscopy* **53**, 333 (1994).
226. B. T. Kelly, in *Physics of Graphite*, (Applied Science (London), 1981).
227. G. Overney, W. Zhong, and D. Tománek, *Z. Phys. D* **27**, 93 (1993).
228. J. Bernholc, J. Y. Yi, Q. M. Zhang, C. J. Brabec, E. B. Anderson, B. N. Davidson, and S. A. Kajihara, *Zeitschrift für Physik D: Atoms, Molecules and Clusters* **26**, 74 (1993).
229. M. M. J. Treacy, T. W. Ebbesen, and J. M. Gibson, *Nature (London)* **381**, 678 (1996).
230. K. Harigaya and M. Fujita, *Phys. Rev. B* **47**, 16563 (1993).
231. B. Friedman, *Phys. Rev. B* **45**, 1454 (1992).
232. K. Harigaya, *Phys. Rev. B* **45**, 13676 (1992).
233. K. Harigaya, *Synthetic Metals* **56**, 3202–3207 (1993).
234. W. P. Su, J. R. Schrieffer, and A. J. Heeger, *Phys. Rev. Lett.* **42**, 1698 (1979). see also *Phys. Rev. B* **22**, 2099 (1980).
235. N. A. Viet, H. Ajiki, and T. Ando, *J. Phys. Soc. Jpn.* **63**, 3036 (1994).
236. N. Chandrabhas, A. K. Sood, D. Sundararaman, S. Raju, V. S. Raghunathan, G. V. N. Rao, V. S. Satry, T. S. Radhakrishnan, Y. Hariharan, A. Bharathi, and C. S. Sundar, *PRAMANA-Journal of Phys.* **42**, 375–385 (1994).
237. M. S. Dresselhaus, G. Dresselhaus, and Riichiro Saito, *Materials Science and Engineering* **B19**, 122–128 (1993).
238. J. C. Charlier and J. P. Michenaud, *Phys. Rev. Lett.* **70**, 1858–1861 (1993).

Index

<i>1s</i> Core Orbitals.....	9	S_{ij}	29
<i>a_{C-C}</i>	25	σ bond	7
<i>c</i> -axis crystallite sizes L_c	89	$a_1 \ a_2$	38
C_N group	184	$b_1 \ b_2$	47
D_n group	184	$K_1 \ K_2$	47
D_n point group	48	R	41
d_R	39	T	39
d_t	38	C_h	37
E_{2g} optic mode	188	2D graphite	
K point	60	acoustic modes	170
$k \cdot p$ perturbation theory	106	Brillouin zone	25
k^2 dependence	170	force constant parameters	169
L	38	graphite	25
M -point mode	202	Landau level	106
N	40	optical modes	170
S -matrix	145	phonon dispersion relations	166
sp hybridization	5	reciprocal lattice unit vectors	25
sp^2 hybridization	7	unit cell	25
sp^3 hybridization	8	unit vectors	25
sp^n hybridization	5		
T_{HT}	89		
VH configurations	196		
VV configuration	196		
Γ^{vib}	185		
π bands of 2D graphite			
$\mathcal{H}_{jj'}$	26	AB effect	110
$\mathcal{S}_{jj'}$	27	ABAB stacking	87
energy dispersion relations	27	abundance of nanotubes	210
π bands	26	acetylene	7
π bond	7	additive property	148
ψ	41	Aharonov–Bohm effect	108
σ bands of 2D graphite	29	amorphous carbon	12
\mathcal{H}_{ij}	29	amorphous graphite	12
		Anderson localization	147
		angle of rotation around the	
		nanotube axis ψ	41

A

AB effect	110
ABAB stacking	87
abundance of nanotubes	210
acetylene	7
additive property	148
Aharonov–Bohm effect	108
amorphous carbon	12
amorphous graphite	12
Anderson localization	147
angle of rotation around the	
nanotube axis ψ	41

antibonding π^* bands	24
arc method	77
areal moment of inertia	211
armchair nanotube.....	36
atomic sites	185
axis of cone.....	121

B

ballistic transport	139
bamboo structure.....	81
band Jahn-Teller effect	216
bending angle	121
bending	81
benzene gas	80
bias window.....	157
bistability	156
Bloch's theorem	17
BN nanotube.....	224
bond alternation.....	213
bond polarization theory.....	192
bond-bending.....	167
bond-stretching.....	167
bonding π bands.....	24
breathing A_{1g} mode	172,190
Bright model	160
broad Raman peaks around the 1347 cm^{-1}	202
bulk modulus	15

C

C_2 absorption process.....	89
cantilever beam.....	211
capping.....	81
carbide	79
carbon arc synthesis	73
carbon fiber with high T_{HT}	147
carbon fibers.....	14,15
carbon nanotube	

beam rigidity	211
Brillouin Zone	45
circumferential length	38
curvature	70
density of states	66
diameter	38
dynamical matrix	173
electronic structure in a magnetic field	108
electronic structure	59
energy gap	66
growth rate	78
oxidation	84
parameters	46
Peierls instability	219
phonon dispersion relations ..	171
quantum transport	152
reciprocal lattice vectors	45
resistivity	157
solid state properties	66
strain energy	210
structure	35
the number of hexagons N	40
unit cell	45
carbon whisker	2,82
carbonization temperature	87
carbyne	13
catalytic chemical vapor deposition ..	2
CGS units	95
CH_x	22
channels	142
chemical potentials	142
chiral angle θ	39
chiral nanotube	36
chiral vector C_h	37
chirality	35
classic elastic theories	208
classical conductance	139
classical transport	144
classification	35

coaxial nanotubes 222
 cobalt catalyst 132
 coherence 138
 coiled carbon nanotubes 130
 electronic structure 134
 commensurate 222
 commensurate double-wall
 carbon nanotube 223
 complete elliptical integrals 215
 conductance $G[\mathcal{U}]$ 137
 conductance regimes 141
 conductance 127
 conductivity 137
 core electrons 5
 core orbitals 9
 Coulomb charging effect 155
 crystallite size along the
 c-axis L_c 89
 current operator 127
 CVD 2
 cyclotron frequency ω_c 95
 cyclotron radius r_c 95

D

de Broglie wavelength λ_B 138
 desorption temperature
 hydrogen 88
 oxygen 88
 diamagnetism for graphite 106
 diamond 11
 diffusion constant D 151
 diffusive motion 139
 dihedral angle 121
 dimensionless inverse magnetic
 length $L/2\pi\ell$ 112
 disorder in carbon fibers 202
 distorted columnar structures 89
 dynamical matrix $\mathcal{D}(\mathbf{k})$ 165

E

eccentricity 123
 edge states 126
 EELS 11
 effective mass 110
 Einstein relation 151
 elastic modulus C_{11} 210
 elastic scattering 138
 elastic thin film 210
 electron energy loss spectra 11
 electron-electron interaction 221
 electron-electron scattering 138
 electron-phonon coupling
 constant 213
 electronic polarization tensor 192
 electronic properties of a two-shell
 coaxial nanotube 224
 encapsulated metal cluster 79
 energy dispersion
 armchair and zigzag
 nanotubes 61
 energy stabilization 225
 enhanced backward scattering 152
 ensemble average 150
 envelope function 200
 equation of motion 163
 Euler theorem 132

F

facetting 225
 Fermi sphere 138
 Fermi wavelength λ_F 138
 finite size effect 202
 flux quantum 100
 focused-ion-beam-induced
 deposition 154
 force constant model 163
 correction of force constant .. 178

- force constant tensor 163, 167
 Fourier transform 164
 free electron in a magnetic field 95

G

- Gaussian broadening 124
 genus 132
 gerade 186
 graphitization temperature 87
 growth mechanism 89

H

- heat treatment temperature T_{HT} 202
 helical pitch 133
 helically coiled nanotube 131
 helix-shaped structure 132
 heptagonal defect 81, 116
 high strength per unit area 225
 highly oriented pyrolytic graphite 2
 hollow cylindrical cantilever 213
 HOPG 2
 hybridization 5

I

- Iijima 4
 in zero magnetic field 111
 in-phase motion 199
 in-plane bond alternation 217
 in-plane crystallite sizes L_a 89
 incommensurate co-axial
 nanotubes 222
 infrared-active modes 183
 interband coupling 107
 intercalated graphite
 with fluorine 147
 interlayer interaction 207
 inversion center 186

- irreducible representation 184

J, K

- Jahn-Teller effect 216
 joint density of states 191
 junction 115, 123
 shape of a junction 120
 Keating potential 211
 Kekulé structure 213

L

- Landau energy bands
 two-dimensional graphite 104
 carbon nanotube 111
 Landau gauge 95
 Landau radius 97
 Landau degeneracy 97
 Landauer formula 144
 laser vaporization method 74
 layer-by-layer removal 84
 length of cone axis 123
 linear k dispersion 107
 local density approximation 71
 localization length L_c 147
 localization phenomenon 147
 longitudinal acoustic mode 177
 Lorentz force 95

M

- magnetic-induced distortion 221
 McClure 106
 mean free path L_m 138
 mesophase pitch fibers 15
 mesoscopic systems 127, 138
 metal-metal coaxial nanotubes 224
 metal-metal junction 124

metal-semiconductor coaxial
 nanotubes 224
 metal-semiconductor junction 124
 methane 8
 MKS (SI) units 95
 molecular polarizabilities 193
 momentum relaxation length L_m 138
 momentum relaxation time t_m 139
 Mott localization 147
 multi-wall nanotubes 209, 221

N

nanotube junctions 116
 negative curvature 116
 negative magnetoresistance 151
 Landau level formation 160, 151
 Ni/Co catalyst 187
 non-symmorphic translational
 group 52
 non-zone-center phonon mode 202
 normal mode 192
 normalized electron-phonon
 interaction 216

O

open ends 89
 out-of-phase motion 199
 out-of-plane deformation
 dotfill 218
 overlap integral matrix 19
 oxidation 84

P

PAN (polyacrylonitrile) 15
 PAN fibers 14, 2
 parameters of 2D graphite
 tight binding method 32

Pauli exclusion principle 138
 Peierls distortion 216, 70
 Peierls instability 213
 pentagon 187
 PES 10
 phase-coherent motion 151
 phase diagram of carbon 12, 13
 phase relaxation time t_φ 139
 phase-relaxation length L_φ 138
 phonon density of states 171, 202
 phonon mode 163
 phonon occupation number 192
 photoelectron spectroscopy 10
 π bond 7, 207
 pitch fiber 14
 polarizability parameters 194
 polarization 192
 polyacetylene (CH_x) (see also
 trans-polyacetylene) 7, 22, 213
 normalized energy gap 215
 polyacrylonitrile 2
 power law for the A_{1g} mode 198
 projection operator 184

Q

quantized conductance G_0 143
 quantized current 143
 quantized resistance R_0 143
 quantum confinement 95

R

radial 167
 Raman experiment 187
 Raman mode of carbon nanotube
 atomic displacements 200
 higher frequency modes 198
 lower frequency modes 196
 medium frequency modes 201

Raman polarizability parameters .. 195
 Raman spectra
 angular dependence 205
 polarization dependence 197
 Raman-active modes 183
 random phase 150
 rare-earth metals 79
 Rayleigh scattering 190
 regular triangle 120
 resistance 137
 resistance of a mesoscopic wire R_w 144
 resistivity 137
 resolvent 127
 resonance tunneling 156
 resonant Raman effect 191
 Rh/Pd catalyst 187
 rope 187
 rotation angle ψ 43
 rotation around the z axis 203, 223

S

sample length L 139
 sample orientation dependence 203
 scaled force constant 181
 second-rank tensor 168
 secular equation 165, 20
 selection rules 186
 semi-metal 134
 semi-toroidal structure 130
 shear modes between two
 graphite layers 222
 σ -bonding 207
 sliding motion 223
 sound velocity 178
 sp^2 hybridization 7
 sp^3 hybridization 8
 space group symmetry operation
 $R = (\psi|\tau)$ 43
 spin-Peierls interaction 221

STM image 224
 strain energy per carbon atom 210
 strongly localized regime 147
 STS experiments 224
 Su-Schrieffer-Heeger (SSH) model 213
 sublattices 199
 superlattice 133
 symmetry assignment 205
 symmetry vector \mathbf{R} 41
 symmetry-lowering effects 202

T

(10,10) armchair nanotube 187
 thermal diffusion length L_T 151
 thermal vibration 212
 Thomas A. Edison 1
 tight binding approximation in a
 static magnetic field 98
 tight binding method 17
 $\mathcal{H}_{jj'}$ 19
 $\mathcal{S}_{jj'}$ 19
 tilt and twist boundaries 89
 time-reversed processes A_p^R 151
 toroidal carbon nanotube 133
 torus C_{360} 130
 tows 15
 trans-polyacetylene
 π -bands 22
 $\mathcal{H}_{JJ'}$ 23
 $\mathcal{S}_{JJ'}$ 24
 Bloch orbitals 22
 Brillouin zone 22
 energy dispersion relations 24
 reciprocal lattice vector 22
 unit vector 22
 transfer integral matrix 19
 transit time t_t 139
 transition metals 79
 translation τ 43

- translation in the direction of \mathbf{T} τ . 41
 translational vector \mathbf{T} 37
 transmission probability 144
 transport experiments 159
 transverse acoustic mode 177
 tube opening 85
 tubule axis length 123
 tunneling conductance 123
 turbostratic graphite 89
 twisted helical carbon nanotube 132
 twisting motion 169, 178
 two-band semimetal model 160
 two-dimensional cosine band in
 a magnetic field 100
 two-dimensional graphite (see 2D-graphite)
 two-dimensional van Hove
 singularities 125
 two-point resistance 155

U, V

- ungerade 186
 unitary matrix 168
 universal conductance
 fluctuations (UCF) 127, 148, 161
 valence electrons 5
 van-Hove singularities 191
 vapor grown carbon fiber 2, 14, 79
 vapor growth method 80
 vaporization temperature 77, 88
 vector potential 95
 voltage drop 127, 144

W

- wavy ribbons 89
 weakly localized regime 147
 wire frame model 123
 wrinkled layers 89

X, Y, Z

- XPS 9
 Young's modulus Y 211
 zero-gap semiconductor 64
 zigzag nanotube 36
 zone folding
 phonon mode 163, 172
 zone-center vibrations 183
 zone-folding
 Energy dispersion 59

